Application of Forward Modeling to Materials Characterization

Submitted in partial fulfillment of the requirements for

the degree of

Doctor of Materials Science and Engineering

in

Materials Science and Engineering

Saransh Singh

B.Tech., Metallurgical Engg. and Materials Sc., Indian Institute of Technology, Bombay
M.Tech., Metallurgical Engg. and Materials Sc., Indian Institute of Technology, Bombay
M.S., Materials Science and Engineering, Carnegie Mellon University

Carnegie Mellon University
Pittsburgh, PA

August, 2017

To my dog, who did not eat my homework $\cdots$

Abstract

The four pillars of material science and engineering namely structure, processing, properties and performance form the so-called *material paradigm*. At the heart of the material paradigm is materials characterization, which is used to measure and identify the relationships. Materials Characterization typically reconstructing the conditions giving rise to a measurement, a classic *inverse problem*. The solutions of these inverse problems are under or over determined and not unique. The solutions of these inverse problems can be greatly improved if accurate *forward models* exist for these characterization experiments. In this thesis, we will be focusing of developing forward models for electron diffraction modalities. Specifically, four different forward models for electron diffraction, namely the Electron Backscatter Diffraction, Electron Channeling Patterns, Precession Electron Diffraction and Transmission kikuchi Diffraction modalities are presented. Further, these forward models are applied to important materials characterization problems, including diffraction pattern indexing using the dictionary approach and forward model based orientation refinement. Finally, a novel pole figure inversion algorithm using the *cubochoric* representation and model based iterative reconstruction is also presented.

ACKNOWLEDGEMENTS

Derek Lau, Dr. Brian Decost, Tim Hsu and Yao-Yao. All of you have helped me in invaluable ways, from listening to my existential rants to helping me in my research.

I would like to thank the staff at the Department of Material Science and Engineering for making sure everything runs smoothly and efficiently. I would especially like to mention Marygrace Antkowski for helping me with all tasks administrative.

Finally, I would like to acknowledge my brother, Siddhartha and parents, Ramendra and Purnima Singh for supporting my career choices at every step of the way. The tiny things you did, be it hading me a popular science novel, or watching the discovery channel for a whole weekend with me, that initiated my interest in science. I will always be grateful for that.

Saransh Singh
Pittsburgh, PA
June 16, 2017

List of Publications Resulting from this Work

The following papers related to the work presented in this thesis have been published or submitted in peer reviewed journals (chronological order):

1. Brian E. Jackson, Jordan J. Christensen, **Saransh Singh**, Marc De Graef, David T. Fullwood, Eric R. Homer, Robert H. Wagoner: *Performance of Dynamically Simulated Reference Patterns for Cross-Correlation Electron Backscatter Diffraction.* Microscopy and Microanalysis 08/2016;22(4):789-802. DOI:10.1017/S143192761601148X

2. **Saransh Singh**, Marc De Graef: *Orientation sampling for dictionary-based diffraction pattern indexing methods.* Modelling and Simulation in Materials Science and Engineering 11/2016; 24(8). DOI:10.1088/0965-0393/24/8/085013

3. **Saransh Singh**, Marc De Graef: *Dictionary Indexing of Electron Channeling Patterns. Microscopy and Microanalysis* 02/2017;23(1):1-10. DOI:10.1017/S1431927616012769

4. Patrick G. Callahan, McLean Echlin, Tresa M. Pollock, **Saransh Singh**, Marc De Graef: *Three-dimensional texture visualization approaches: Theoretical analysis and examples.* Journal of Applied Crystallography 04/2017; 50(2). DOI:10.1107/S1600576717001157

5. Farangis Ram, Stuart Wright, **Saransh Singh**, Marc De Graef: *Error Analysis of the Crystal Orientations Obtained by the Dictionary Approach to EBSD Indexing.* Ultramicroscopy 04/2017; 181., DOI:10.1016/j.ultramic.2017.04.016

6. Katharina Marquardt, Marc De Graef, **Saransh Singh**, Hauke Marquardt, Anja Rosenthal, Sanae Koizuimi: *Qantitative electron backscatter diffraction data (EBSD) analyses using the dictionary indexing (DI) approach: overcoming indexing difficulties on geological materials.* American Mineralogist 01/2017; DOI:10.2138/am-2017-6062CCBYNCND

7. **Saransh Singh**, Farangis Ram, Marc De Graef: *Application of Forward Models to Orientation Refinement.* Journal of Applied Crystallography (submitted).

8. Patrick G. Callahan, McLean Echlin, Jean Charles Stinville, Tresa M. Pollock, **Saransh Singh**, Farangis Ram, Marc De Graef: *3D Texture Vizualization Approaches: Application to Nickel and Titanium Alloys.* Journal of Applied Crystallography (submitted).

The following papers related to the work presented in this thesis have been published or submitted in peer reviewed conference proceedings (chronological order):

1. **Saransh Singh**, Marc De Graef: *Automated Dictionary-based Indexing of Electron Channeling Patterns.* Microscopy and Microanalysis 08/2015; 21(S3):2041-2042., DOI:10.1017/S1431927615010983

2. **Saransh Singh**, Marc De Graef: *GPU-Based Defect Image Simulations using the Scattering Matrix Formalism.* Microscopy and Microanalysis 08/2015; 21(S3):2213-2214., DOI:10.1017/S1431927615011848

3. Michael Chapman, **Saransh Singh**, Marc De Graef: *Can EBSD Patterns Be Used for Determination of Grain Boundary Inclination?.* Microscopy and Microanalysis 08/2015; 22(S3):2039-2040. DOI:10.1017/S1431927615010971

4. **Saransh Singh**, Marc De Graef: *Automated Data Acquisition and Indexing of Electron Channeling Patterns using the Dictionary Approach.* Microscopy and Microanalysis 07/2016; 22(S3):1420-1421., DOI:10.1017/S1431927616007947

5. **Saransh Singh**, Marc De Graef: *Applications of Forward Modeling to Refinement of Grain Orientations.* Microscopy and Microanalysis 08/2017 (accepted).

6. Elena Pascal, **Saransh Singh**, Marc De Graef: *Dynamical Simulations of Transmission Kikuchi Diffraction (TKD) Patterns.* Microscopy and Microanalysis 08/2017 (accepted).

7. **Saransh Singh**, Katharina Marquardt, Marc De Graef: *Accurate Grain and Phase Boundary Location by Dictionary-Based Indexing of Geological EBSD Data.* Microscopy and Microanalysis 08/2017 (accepted).

8. **Saransh Singh**, Farangis Ram, Marc De Graef: *EMsoft: Open Source Software for Electron Diffraction/Image Simulations.* Microscopy and Microanalysis 08/2017 (accepted).

9. Joseph Tessmer, **Saransh Singh**, Yoosuf N. Picard, Marc De Graef: *Automated Acquisition and Analysis of Selected Area Electron Channeling Patterns in an FEG-SEM.* Microscopy and Microanalysis 08/2017 (accepted).

LIST OF TABLES

LIST OF FIGURES

TABLE OF CONTENTS

CHAPTER I

Introduction

Material science is an interdisciplinary field focusing on the study and design on new materials. The whole field can be described by the well known materials paradigm, which states that there is an inter-relationship between four pillars, namely structure, processing, properties and performance of a given material. At the heart of the materials paradigm is material characterization, a collection of tools for the study of a material's microstructure, both qualitatively and quantitatively.

The length scales of interest in material science has a wide variation, ranging from a fraction of a meter, for example in the study of failure analysis of large components, to an Å, such as in the study of the crystal structure and nanoparticles. This constitutes a variation by 10 orders of magnitude. To accurately resolve features at a particular length scale, the probe used to study those features needs to have an equal or smaller size. Thus, the probes used for materials characterization are as varied in length scales as the features we are interested in. Some of the well known probes are photons (X-rays, optical microscopy etc.), neutrons, positrons etc. One of the most important and widely used class of materials characterization methods is based on electron scattering. These methods involve scattering of electrons from the material of interest, observing the outcome and trying to reconstruct the conditions which led to the observed outcome. This is a classic *inverse problem* and significant advances have been made in solving this problem [2, 3].

Electron microscopy, broadly speaking, comes in two flavors, the transmission or forescatter mode (Transmission Electron Microscopy) and the scanning or backscatter mode (Scanning Electron Microscopy). While there are striking similarities in the physics of both of

these microscopy techniques, there are significant differences in how quantitative these techniques are perceived to be. The TEM community has been quantitative in all its analysis for a long time; the SEM community still has, by and large, a fairly qualitative approach to materials characterization. The central goal of this dissertation is to make progress towards elevating SEM based methods to the same footing as TEM based methods in terms of their quantitative aspects.

Conventional TEM has a whole host of diffraction and imaging modalities, including but not limited to spot diffraction, precession electron diffraction (PED), convergent beam electron diffraction (CBED), dark field/bright field imaging, weak beam imaging etc. Similarly, the SEM has its own set of diffraction and imaging modalities, including Electron Backscatter Diffraction (EBSD), Electron Channeling Patterns (ECP), Electron Channeling Contrast Imaging (ECCI), Transmission Kikuchi Diffraction (TKD) etc. The choice of which modality to use for characterization depends on the nature of the information we are seeking. In this thesis, we will attempt to solve the *forward problem* of electron scattering for crystalline materials for both the backscatter and forescatter geometry and apply the solutions to the problem of materials characterization. The forward problem can be stated as follows: *Given the crystal structure and microscope conditions, can we predict what the outcome of the experiment will be?* A more abstract and detailed analysis on forward models will be presented in chapter III. We will try to use the forward models to make the techniques more quantitative. For this dissertation, we will specifically be applying the forward model for mapping grain orientations, which are of particularly important for the macroscopic properties of a material. The remainder of the chapter is organized as follows: Section 1.1 discusses the importance of mapping grain orientation and its implications on the properties of the material. Section 1.2 states the hypothesis of this study. Finally, section 1.3 gives the outline of this thesis.

1.1 Texture-Property relationship

One of the main goals of material science is to optimize the properties of various engineering materials. Optimizing properties stems from the need to reduce material utilization and cost, increase the efficiency, improve safety etc. In order to do so, it is important to

understand and quantify the effect of different parameters on the properties of materials.

Engineering materials are usually crystalline, but most often in poly-crystalline form. They consist of multiple grains having different crystal orientations. While the microscopic properties of these grains are anisotropic due to the crystalline nature, the macroscopic property of the whole crystal depends on the relative fractions of each of these grain orientations, or the *texture*. Texture also provides information about the thermo-mechanical processing history of materials and can be used to reconstruct the conditions leading to the microstructure, for example in geological rocks. Thus, it can be seen that texture is paramount in understanding the structure-processing-properties relationship.

Crystallographic texture is represented using the orientation distribution function (ODF), which describes the fraction of occurrence of any given orientation over the whole of orientation space. If orientation is represented by the symbol $\mathbf{g}$, then the ODF is defined as the volume fraction of the grains with this orientation. Mathematically,

$$f(\mathbf{g}) = \frac{1}{V_0} \frac{\mathrm{d}V(\mathbf{g})}{\mathrm{d}\mathbf{g}}. \tag{1.1}$$

Here, V_0 represents the total volume of the sample and $V(\mathbf{g})$ represents the volume of grains with the orientation $\mathbf{g}$. It is important to note that ODF differs from a probability distribution function in its normalization. If the orientation dependent property $\chi(\mathbf{g})$ for a material system is known, we can calculate the average macroscopic property $\langle \chi \rangle$ as an average given by the expression:

$$\langle \chi \rangle = \int_{\mathbf{g}} \chi(\mathbf{g}) f(\mathbf{g}) \mathrm{d}\mathbf{g}. \tag{1.2}$$

Some of the properties of interest can be electrical and thermal conductivity, strength, chemical reactivity, corrosion resistance etc. Calculating the ODF requires knowledge of the crystal orientation for all the grains. Therefore, we need a robust and reliable way to map orientations. There has been a lot of work in the past to extract orientations from EBSD patterns using the Hough transform [4, 5] and PED patterns using cross-correlation [6]; both have led to commercial implementations that have been very successful in mapping

the orientation as a function of spatial position. However, there are obvious challenges and drawbacks with each method which will be discussed in the following chapter. The majority of this thesis will be focused on unifying the notion of "indexing" diffraction patterns, which means assigning an orientation **g** to a diffraction pattern. Instead of extracting linear features from the diffraction patterns like the band positions, we will use every available pixel to index the patterns in the hopes of making the technique more robust to noise.

1.2 Hypothesis

This thesis has the following hypotheses:

- Forward models can be used to extract information from diffraction patterns that goes beyond the traditional orientation measurement.

- The dictionary-based indexing approach is more robust to the presence of noise than the traditional approaches to pattern indexing. The indexing success rate for the dictionary method will be at least 50% when the traditional method fails completely.

Usually, when performing orientation mapping using EBSD, the diffraction patterns are discarded and only the inverse pole figure (IPF) is reported as the final result. However, considerable information is thrown out in the process. We propose to save *all* diffraction patterns and extract the relevant quantity of interest as a post-processing step. Comparing the results from our approach to measurement of the same quantity using a different technique will serve to verify or reject our hypothesis.

The second hypothesis will require us to compare the indexing results by our approach to the current indexing approach for all three diffraction modalities. Based on the success rate of the indexing of the two techniques, we will consider the hypothesis verified or rejected.

1.3 Thesis outline

Our discussion of applying forward models to orientation mapping will begin with a brief overview of the different diffraction techniques used for this study in chapter II. Specifically, the geometry and detector systems for EBSD, ECP, PED and TKD modalities and the as-

sociated indexing techniques will be discussed. The chapter will also discuss the limitations
and challenges associated with each of them.

Chapter III will lay out the theoretical framework used in the rest of the dissertation.
The chapter starts off by discussing some important orientation representations in mate-
rial science, including Euler angles, Rodrigues vectors and unit quaternions. The concept
of fundamental zone, which is the asymmetric unit of orientation space for a given crystal
symmetry, is introduced. Next, we introduce various 2-D and 3-D mapping used in this dis-
sertation for data storage, sampling, analysis and visualization. The chapter also discusses
the quantum mechanical theory of dynamical diffraction in a periodic potential. This sec-
tion also discusses stochastic inelastic scattering using Monte Carlo simulations, which form
the background signal in the diffraction pattern. Finally, the section introduces the con-
cept of a generalized forward projector (GFP). The concept of a GFP, which is based on
the dynamical diffraction theory, together with a modality specific detector model, is used
to complete the forward model for the four modalities. The notion of a master pattern is
introduced, which serves as an important computational tool to make realistic pattern sim-
ulations computationally tractable. Finally, some results are presented for each one of the
diffraction modality.

Chapter IV introduces the novel cubochoric sampling method for both orientation and
misorientation space. The chapter builds on the sampling techniques and forward mod-
els outlined in previous chapters to introduce the "dictionary" based method for index-
ing of diffraction patterns. The chapter begins by summarizing the general algorithm for
dictionary-based indexing, which is a unified method to index all diffraction patterns. Next,
we describe how to estimate the experiment-specific detector parameters using optimiza-
tion algorithms necessary for the dictionary approach. The following section will discuss
the image processing routines used for the dictionary approach.

Chapter V presents the results of indexing and a comparison with results from current
techniques together with the accuracy and precision of the new approach for the EBSD
and PED modality. Indexing results for ECP modality for a poly-Silicon sample is also
presented. The forward models for electron scattering are used to develop an orientation
refinement algorithm which can be used to improve the angular accuracy of the diffraction

modalities using highly binned patterns. A novel formulation of the pole figure inversion using the cubochoric representation and Bayesian model based approach is presented. Some preliminary results of this new method on both simulated and experimental texture is shown. Finally, we will end with some concluding remarks about the use of forward model in the field of materials characterization.

We end the dissertation by a brief discussion of the anticipated impact of this work and proposing several different directions for future work in chapter VI.

CHAPTER II

Current Technique Overview

The first electron microscope was invented by Ernst Ruska and Max Knoll in 1931. The main motivation for designing it was to overcome the limitations placed on resolution by the wavelength of visible light. At that time, the electron microscope had a resolution barely matching that of optical microscopes. There has been considerable progress in every aspect of this field, mostly resulting in an improved instrument resolution. This includes brighter electron sources (LaB_6, Field Emission Guns), more stable power sources, improvements to the electron optical lenses etc. Nowadays, the Transmission Electron Microscopes can routinely reach atomic resolution and the Scanning Electron Microscope can achieve a resolution close to 1 nm. Alongside the hardware and instrumentation development, theoretical models for image contrast formation have been developed to enable quantitative interpretation of features in micrographs. The advent of fast computers has also enabled the computation of these contrast features and direct comparison with observations.

With improving instrumentation and a better understanding of the underlying physics, the scope of electron microscopy has considerably widened. Initially, the instrument was only used for defect imaging, fractography etc. Over time, the instrument has evolved to include analytical techniques such as energy dispersive x-ray spectra (EDXS), electron energy loss spectroscopy (EELS), energy filtered imaging etc. to name just a few. In this chapter, we will limit our discussion to four specific electron diffraction techniques namely, Electron Backscatter Diffraction (EBSD), Electron Channeling Patterns (ECP), Precession Electron Diffraction (PED) and Transmission Kikuchi Diffraction (TKD). Section 2.1 describes the EBSD technique in an SEM. This section also discusses the current pattern indexing algo-

rithm implemented in commercial software and the associated drawbacks and limitations. Section 2.2 explains the ECP technique and its application to defect imaging. The section also discusses indexing ECPs using the same technique as EBSD and the associated challenges. Section 2.3 discusses PED, which is a TEM based method for high spatial resolution orientation mapping. The section also describes the indexing algorithm and possible improvements to it. Finally, section 2.4 discusses the recently developed TKD modality in the scanning electron microscope.

2.1 Electron Backscatter Diffraction

Electron backscatter diffraction or EBSD is used interchangeably for both the SEM-based diffraction technique and the accessory system that can be attached to the instrument to record these patterns. The technique provides quantitative information about the grain size, grain boundary character, grain orientation, texture and phase identity of the sample. The spatial resolution of the technique is about 30 nm, while the angular resolution is reported to be about $0.5°$.

The fundamental discovery of bright and dark lines in an electron micrograph, which forms the basis for EBSD, can be traced back to Nishikawa and Kikuchi in 1928. They directed a 50 kV electron beam on a cleavage face of calcite at a grazing angle of $6°$ [7]. The patterns were recorded on photographic plates. The first serious investigation of the formation mechanism was carried out by Alam et al. [8]. The introduction of the first commercial SEM in 1965 led to rapid development in the field, with the first true EBSD pattern observed by Venables and Harland [9]. They used a combination of a phosphor screen and TV camera to record the pattern.

Dingley and co-workers extended the work done by Venables using the phosphor screen and TV camera by adding computer-aided indexing [10–12]. This was the first prototype of the modern-day EBSD system. The big breakthrough in the utility of this technique came with the work of Krieger-Lassen, Conradsen, and Juul-Jensen, who used the Hough transform [13] to automate the indexing of diffraction patterns [4]. This led to the developement of the first fully automated EBSD system [14].

The technique requires a dedicated EBSD detector, which attaches in one of the available

ports of the SEM chamber. The modern EBSD camera consists of a scintillator screen, which is optically connected through a fibre-optic bundle or lens to a charge coupled device (CCD) camera sitting behind the scintillator. The first use of a slow scan charge coupled device (SSCCD) was reported in [15]. The phosphor screen converts the electronic signal into light, which is transferred by the optical system to the CCD camera. This can be further displayed on a screen. Departures from these detection schemes have included an investigation of microchannel plates [16] and the adoption of a retarding electrostatic field for energy filtering [17]. Recently, there have been a few successful efforts to rid the camera system of the optical intermediaries, leading to direct electron detectors [18]. A comprehensive overview of EBSD techniques and practices can be found in [19–21]. A timeline of important developments in the field is presented in Table 2.1.

1928	First observation of bright and dark line in electron micrograph by Nishikawa and Kikuchi.
1954	First proposed formation mechanism by Alam et al.
1973	First EBSD observation in a SEM by Venables and Harland.
1984	On-line assisted indexing of EBSD patterns by Dingley.
1986	First commercial EBSD system by Oxford Instruments.
1992	Use of Hough transform for indexing EBSD pattern by Kreiger-Lassen et al.
1993	Fully automated EBSD system by Adams et al.
1993	First use of a slow-scan charged couple device video camera (SSCCD) by Michael and Goehner.
2013	First use of direct electron detectors for EBSD by Wilkinson et al.

Table 2.1: Important developments for EBSD modality.

A schematic of the EBSD setup is shown in Fig. 2.1(a). The setup consists of a flat, polished sample tilted to typically $70°$. The electrons are usually accelerated to energies of $5 - 30$ keV, with lower voltages used for higher spatial resolution. Electron diffraction occurs from an interaction volume around the illumination point. A fraction of all diffracted electrons are captured by the scintillator screen leading to the diffraction contrast. A typical EBSD pattern from a Si sample is shown in Fig. 2.1(b). The band edges are the gnomonic projection of the Kossel cones on the detector plane. The microscope geometry along with Bragg's law and the sample crystallography and orientation can be used to calculate these band positions. This algorithm has been automated in a number of commercial packages. The details of this method are discussed later in this section.
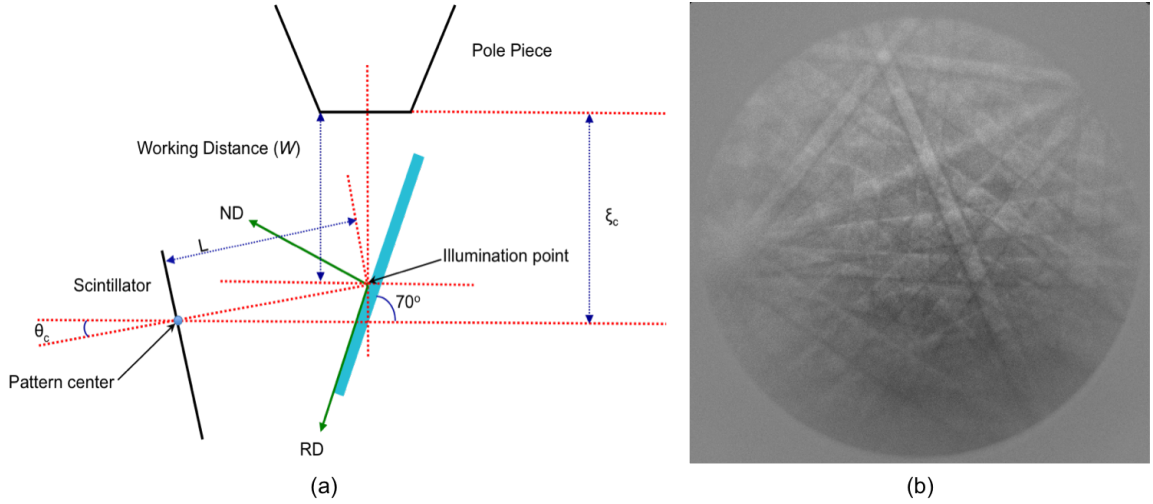
Figure 2.1: (a) Schematic of the EBSD setup (b) Typical EBSD pattern from Si.

The first automated indexing of electron backscattered diffraction patterns using the Hough transform was performed by Krieger-Lassen, Conradsen, and Juul-Jensen in 1992 [4]. Initially the technique could index one pattern in a few seconds. With the advent of high speed computers and faster cameras, there has been an exponential increase in the indexing speeds of commercial EBSD systems [22], which can now index up to a thousand patterns per second. In the following sub-sections, we will discuss in detail the Hough transform algorithm to index EBSD patterns. We will also define and discuss various components of the output from two commercial EBSD systems. These parameters will later be redefined for the new indexing algorithm proposed in this dissertation. Finally, we will give examples of cases where the commercial software lacks in performance. We shall come back to these same datasets later in the dissertation to illustrate the efficacy of the new indexing algorithm.

2.1.1 Hough Tansform

The Hough transform is an image processing algorithm to detect straight lines in an image. It belongs to the family of Radon transforms and converts a straight line in image space to a single point in Hough space. More specifically, the intensity in $x - y$ image coordinates are transformed to the $\rho - \theta$ Hough coordinates, where ρ represents the distance of a line from the origin, taken as the center of the image, and θ represents the counter-clockwise angle the normal to the line from the origin makes with the positive $x-$axis. This is illustrated in Fig. 2.2(a). The operation takes two parameters, which define the resolution of the
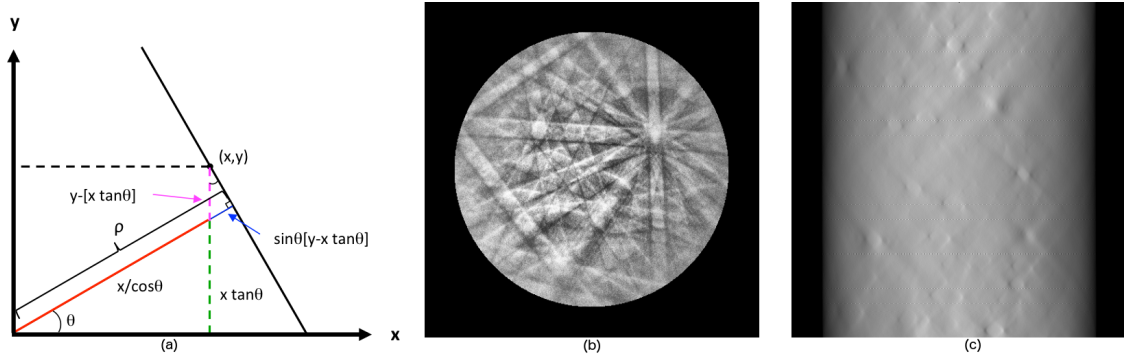
Figure 2.2: (a) Definition of ρ and θ for the Hough transform. (b) A typical EBSD pattern from Si and (c) the Hough transform of the EBSD pattern showing peaks correspond to various bands in the diffraction pattern.

transform, $\Delta\rho$ and $\Delta\theta$.

Numerically, the transform is performed by calculating ρ for each image pixel (x_i, y_i) and different values of θ using the following equation

$$\rho_j = x_i \cos\theta_j + y_i \sin\theta_j \tag{2.1}$$

Each pixel gives rise to a sinusoidal curve in $\rho - \theta$ space. The intensity of the sinusoid is the same as the intensity at (x_i, y_i) in the image space. This process is repeated for all pixels in the image and the intensities are accumulated, which gives rise to peaks in Hough space. A typical processed EBSD pattern and its Hough transform are shown in Fig. 2.2(b)-(c) respectively. Since the bands are not a single pixel wide, the Hough peaks are diffuse. The peak detection algorithm must be able to segment out these peaks from the background. In practice, only $\Delta\theta$ is the parameter and $\Delta\rho$ is chosen to maintain a square aspect ratio for the Hough peaks. The contrast of the Hough transform is also enhanced by convolving the Hough image with a "butterfly" mask. The typical size of the butterfly kernel is 9×9, but higher/lower sizes are used depending on the quality of the patterns.

2.1.2 Orientation Mapping

As described above, the Hough transform detects the Kikuchi bands in an EBSD pattern. There are two leading methods to identify the orientation of the sample after the bands have been detected: the triplet voting scheme used in the EDAX OIM™ package and minimizing

the "fit" between the experimental pattern and a computationally determined orientation, which is implemented in the Oxford Aztec^{TM} package. While the details of the process constitute proprietary information, both algorithms have the following basic ingredients:

- Determine plane normal direction (normals to detected Kikuchi bands).

- Measure inter-planar angles using all pairs of plane normals.

- Compare computed angles between planes to a look-up table for the given material system and phases.

- Identify best matching lattice planes using the look-up table.

- Extract the orientation using the identified lattice planes along with the sample geometry

The details can be found in [23]. If more than one phase is present in the field of view, then a similar process is repeated for the other phases and the best match is used to report the phase as well as the orientation. Thus, the EBSD system can identify both the phase and orientation simultaneously.

Calculating the plane normal direction requires an accurate knowledge of the pattern center and the screen-to-scintillator distance. Several methods are used to calibrate the EBSD system, including using a calibration sample of known orientation, iterative methods, which require an initial guess, moving the camera and measuring the shift in specific pattern features and most recently the use of direct electron detectors [24–27]. Care must be taken in calibrating the pattern center appropriately since an error in the initial calibration will lead to errors in the final solution, or no solution at all.

The EBSD system calculates certain parameters for the confidence of the indexing, pattern quality etc. These parameters are defined differently for different vendors. Here we list some of the salient ones for both the TSL and HKL systems. These definitions have been taken from the respective manuals of the two EBSD systems. Later we will redefine these for the new proposed indexing method. For the TSL system, these are:

- Confidence Index: The confidence index (CI) can be calculated in one of two ways. The first way is $CI = (V_1 - V_2)/V_{IDEAL}$ where V_1 and V_2 are the number of votes for

the best and second best solutions and V_{IDEAL} is the total possible number of votes from the detected bands. The second way is to change the denominator to be based on the total possible number of votes for the maximum number of bands set on the Hough page (Maximum Peak No.). The latter method has an advantage in that if only three bands are found then the CI will be smaller than the case where more than three bands were detected (assuming the Maximum Peak No. is set greater than 3).

- Image Quality: The IQ parameter is defined as the average height of the detected peaks in the Hough transform. The quality of diffraction patterns is dependent on strain in the diffraction volume of material, the phase of the material, the presence of impurities among other factors. It should be noted that this parameter is not purely orientation dependent. Some bands have higher structure factors than others and some orientations may produce patterns with a higher line length fraction of these bands than other orientations. This results (along with other factors) in the IQ parameter not being an absolute measure of the quality of a pattern.

- Fit: The fit parameter defines the average angular deviation between the recalculated bands and the detected bands. This is done by calculating where the bands should appear based on the orientation obtained from the voting procedure.

- d-spacing Fit: This is the average difference between the widths of the detected bands as determined from the Hough transform and the widths of the recalculated bands.

For the HKL system, the relevant parameters are:

- Mean Angular Deviation: This number expresses how well the simulated diffraction pattern overlays the experimental pattern. A smaller number means that the solution is a better fit. The mean angular deviation (MAD) is given in degrees specifying the averaged angular misfit between detected and simulated Kikuchi bands.

- Band Contrast: This quantity derived from the Hough transform describes the average intensity of the Kikuchi band compared to the overall intensity in the diffraction pattern. A higher number signifies more contrast in the image. This is analogous to the image quality parameter for the TSL system.
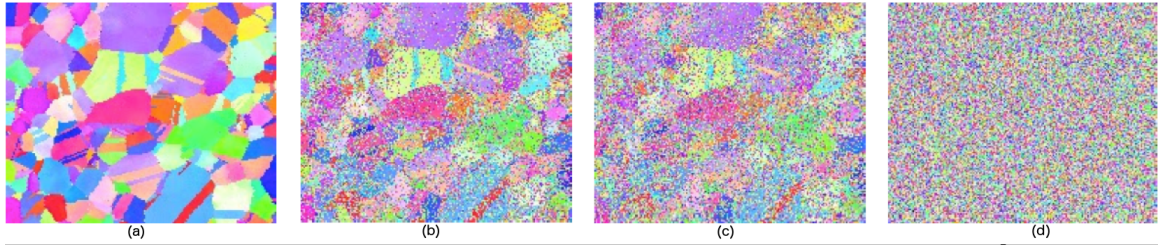
Figure 2.3: IPF from a Ni sample from the same region with varying gain and exposure time to maintain a constant exposure level. The pattern quality decreases as we move from left to right. (Gain in dB, exposure time in msec)(a) Gain = 18.01, exposure time = 0.94 (b) Gain = 30.4, exposure time = 0.2 (c) Gain = 31.53, exposure time = 0.17 and (d) Gain = 36, exposure time = 0.1.(Data courtsey Dr. Stuart Wright, EDAX)

- Band Slope: This is yet another image quality indicator derived from the Hough transform, which represents the maximum intensity gradient at the edges of the Kikuchi bands. Similar to band contrast, a higher number represents higher pattern quality.

2.1.3 Limitations and Challenges

The current indexing algorithms have been widely successful across a plethora of material systems and crystal structures. However, there are obvious limitations and challenges associated with them. By design, the algorithms only use a subset of all available pixels in the diffraction pattern for indexing. Most of the pixels which do not lie on or near the band edges are thrown out. Thus, the algorithm is expected to perform poorly as the noise in the pattern increases. This is shown in Fig. 2.3(a)-(d). Four scans were performed on a Nickel sample in the same region with different gain and exposure time setting to maintain a constant exposure level at 90%. The indexing was performed using the commercial using the commercial EDAX OIM$^{\text{TM}}$ package. As we move from the left panel to the right, the gain increases and the exposure time decreases. This is reflected in the quality of the EBSD pattern as well as the subsequent indexing as shown in the figure.

The spatial resolution of EBSD is closely related to the material system under investigation (atomic number) as well as microscope acquisition conditions and has been studied using both experimental techniques as well as Monte Carlo electron trajectory simulations [28–32]. The spatial resolution is very strongly correlated with the microscope voltage with the best spatial resolution obtained at lower voltages. Monte Carlo trajectory simulations were performed for Mg in the EBSD geometry at different microscope acceleration
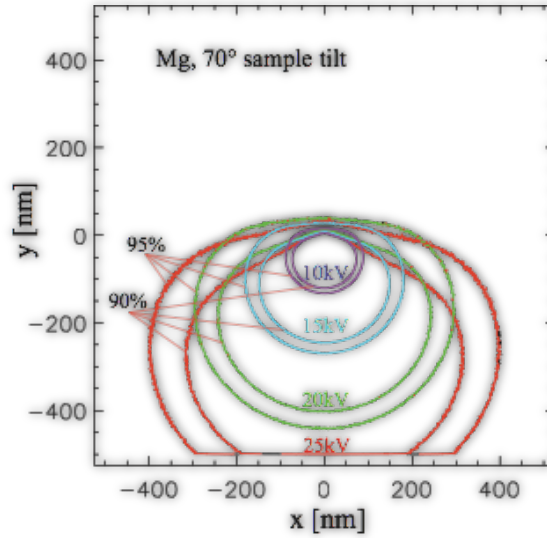
Figure 2.4: Monte Carlo trajectory simulations showing iso-surfaces with 90 and 95% of all backscattered electron in the EBSD geometry for different acceleration voltages. The interaction volume and consequently the effective spatial resolution increases from $\sim$ 50nm at 10 keV to $\sim$ 400 nm at 25 keV. Simulations were carried out for Mg tilted at 70°

voltages. Fig. 2.4 shows the iso-surface for 90 and 95% of all backscattered electrons. The effective spatial resolution changes from $\sim$ 50 nm at 10 keV to $\sim$ 400 nm at 25 keV.

Thus, study of fine microstructural features requires the use of low acceleration voltages. However, the quality of the EBSD pattern deteriorates progressively with decreasing acceleration voltages making high spatial resolution orientation mapping using the commercial packages problematic. Fig. 2.5(a)-(b) shows the IPF-Z map for a low and high gain acquisition respectively. The patterns were indexed using the commercial Aztec$^{\text{TM}}$ package. The Hough based method performs poorly close to the grain boundaries as well as the shot peened region for the low gain acquisition. For the high gain acquisition, the commercial methods fails completely with less than 5% indexing success rate.

Fig. 2.6(a) shows the raw IPF map for an orthorhombic forsterite crystal showing significant noise in the indexing. The IPF-Z map after performing data clean up is shown in Fig. 2.6(b). The clean up procedure introduces artifacts in the final IPF such as unphysical "phantom" grains and unphysical grain boundaries as shown by insets 2 and 3. The indexing was performed using the commercial EDAX OIM$^{\text{TM}}$ package.

Finally, Fig. 2.7(a) shows an IPF for a multi-phase geological sample containing clinopyroxene (monoclinic), garnet (cubic) and melt (amorphous). The IPF (overlaid with the sec-
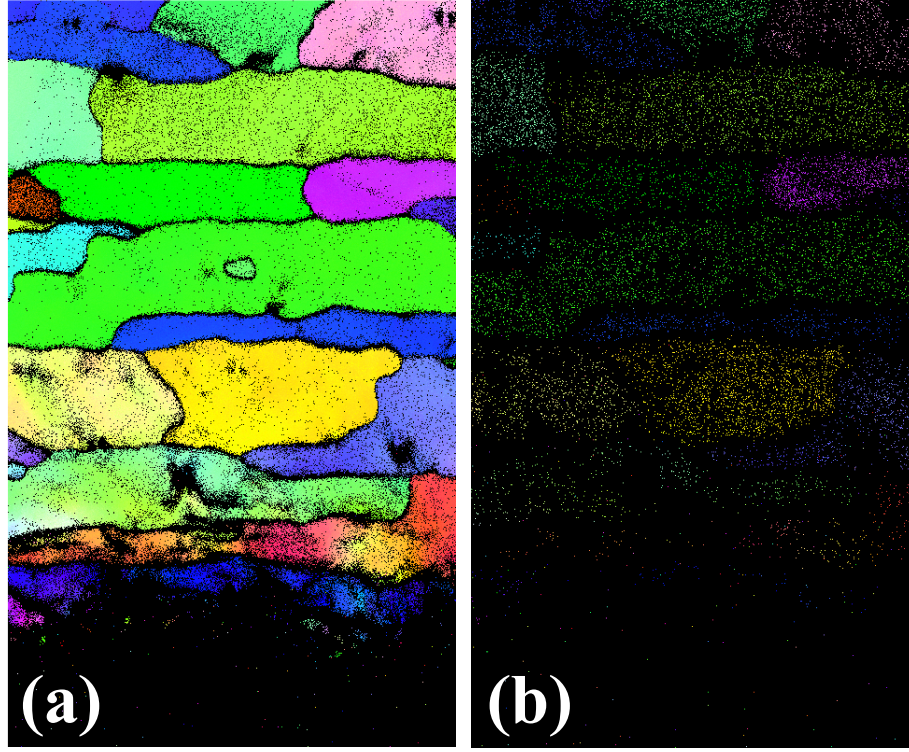
Figure 2.5: IPF from a shot peened Aluminum dataset at 5 kV microscope acceleration voltage at (a) low gain and (b) high gain acquisition.(Data courtesy Dr. Tim Burnett, Univ. of Manchester)
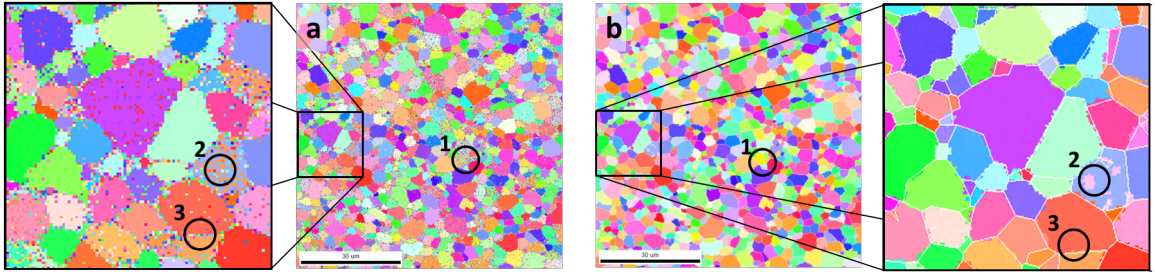
Figure 2.6: IPF-Z for an orthorhombic forsterite crystal (a) raw map and (b) after cleanup.(Data courtsey Dr. Katharina Marquardt, Univ. of Bayreuth)

ondary electron image) clearly shows poor indexing of low symmetry multi-phase systems, even though the patterns are of a reasonably good quality, as shown in Fig. 2.7(b)-(c). Additionally, clean up procedures for such a system are not recommended due to the presence of the amorphous melt phase. The indexing was performed using the the commercial Aztec$^{\text{TM}}$ package. Thus, it can be seen that the current indexing scheme has its drawbacks and fails to adequately perform for noisy patterns and certain material systems. This motivates our study of a new indexing scheme capable of handling such datasets.
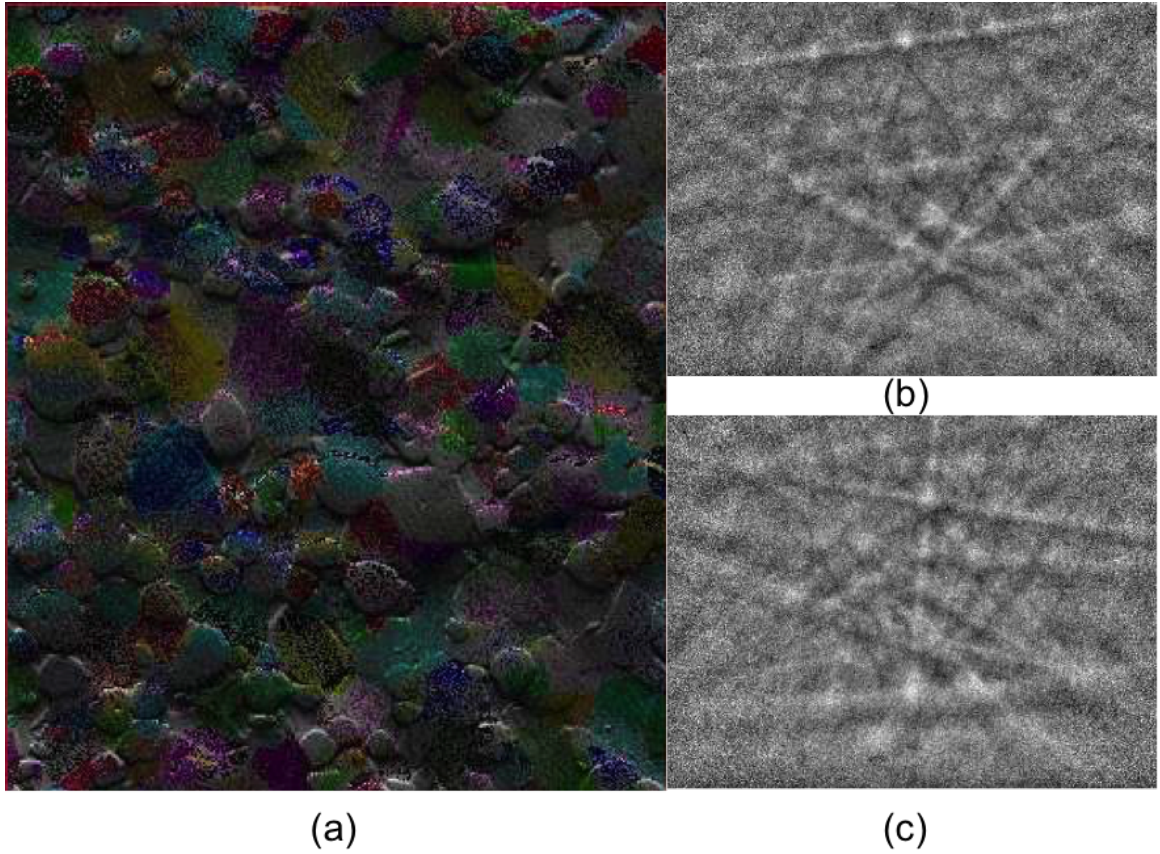
Figure 2.7: (a) IPF overlayed with secondary electron image for for clinopyroxene-garnet-melt multi-phase system (b) typical diffraction pattern from the clinopyroxene phase and (c) typical diffraction pattern from the garnet phase.(Data courtsey Dr. Katharina Marquardt, University of Bayreuth)

2.2 Electron Channeling Pattern

Electron channeling patterns capture the variation in backscatter yield as a function of beam orientation. While there are subtle differences between electron channeling patterns (ECP) and EBSD, they are related to each other by the reciprocity theorem. The channeling patterns contain much of the same information as an EBSD pattern, including orientation, lattice strains etc. However, since the variation of backscatter intensity is being studied as a function of the relative orientation of the beam and the crystal lattice, the technique has a much lower spatial resolution. The best systems can achieve a spatial resolution of about 10 μm.

"Kikuchi-like" bands were first observed by Coates in 1967 while studying single crystals in low magnification under a conventional SEM [33]. The origin of these contrast features was interpreted as superposition of Bloch waves by Booker et al. in the same year [34].

However, the first dynamical diffraction calculation was not performed until 1971 by Clarke and Howie and Spencer et al. [35, 36]. It was hypothesized in the latter publication that it was possible to observe lattice defects using electron channeling. However, the actual observation of dislocations using electron channeling in the SEM was not made until 1977 [37, 38]. The signal to noise ratio (SNR) were very high for channeling contrast and hence a high tilt configuration $(50° − 70°)$ and high acceleration voltage $40 − 50$ kV had traditionally been used. Thus a high-energy filter located in front of a scintillator detector, to remove lower energy BSEs in order to increase the SNR was used for defect imaging. Further progress was made with the use of digital signal processing to enhance the weak channeling signal on top of a huge background [39]. The currently used low-tilt configuration using a conventional backscatter detector was first demonstrated in [40]. Since the first dynamical diffraction theory of Clarke and Howie and Spencer et al. major advances have been made in the theoretical development and realistic pattern simulation of channeling pattern and its associated imaging modality known as Electron Channeling Contrast Imaging (ECCI) [41–45]. ECPs have been used in the area of crystallographic orientation mapping, lattice strain measurements and grain contrast measurements [46]. Initially, ECPs were used for determining crystal orientation. However, the ECPs were limited by a low spatial resolution, needed extra coils to rock the beam about a point and were much slower compared to EBSD pattern acquisition thereby making EBSD the technique of choice for phase and orientation identification.

Defect analysis using a SEM, commonly known as Electron Channeling Contrast Imaging (ECCI), has received much attention in the recent past. Traditional defect analysis has for decades relied on TEM modalities, such as the bright field-dark field and weak beam imaging, and Scanning Transmission Electron Microcopy (STEM) diffraction contrast imaging methods. While the spatial resolution of ECCI is somewhat lower than that of the TEM based methods, ECCI provides more flexibility in sample preparation, data acquisition from bulk samples and larger viewing area for better statistics. ECCI involves tilting and rotating the sample such that the Bragg condition for one of the lattice planes is exactly satisfied. The microscope is then switched back to scanning mode. This technique allows for measuring the backscatter yield as a function of spatial location. Lattice defects, which represent
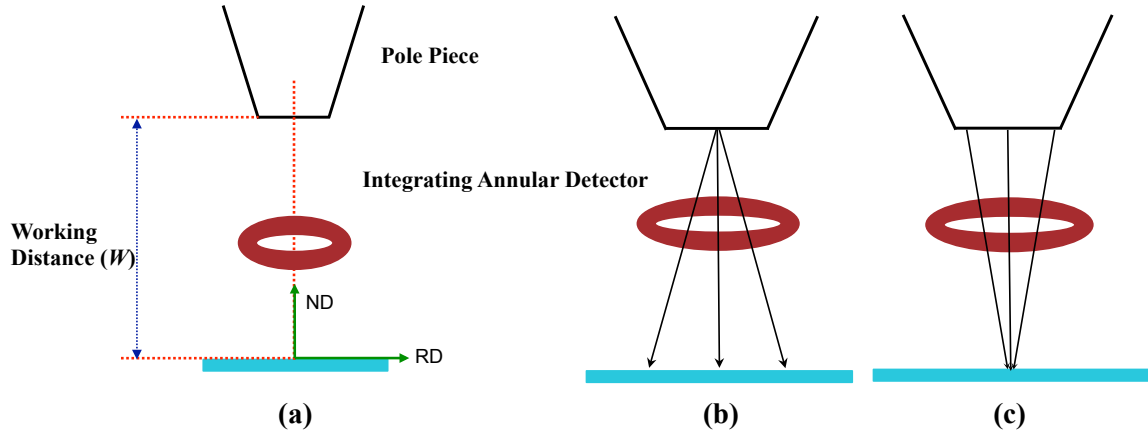
Figure 2.8: (a)Schematic for the ECP setup for 0 sample tilt (b)regular channeling mode and (c) selected area channeling mode.

a deviation from the regular crystal lattice, have a different backscatter yield and consequently show contrast variation in the acquired micrographs. It has been shown in [47] that the $\mathbf{g} \cdot \mathbf{b}$ and the $\mathbf{g} \cdot \mathbf{b} \times \mathbf{u}$ analysis, which have been extensively used in the TEM, is still valid for ECCI [48]. Thus, quantitative defect characterization can be performed on the SEM, provided the orientation of the sample is accurately known. A comprehensive review of electron channeling and ECCI can be found in [46, 49]. A timeline of the important developments for the ECP modality is presented in Table 2.2.

1967	First observation of channeling patterns by Coates.
1967	First dynamical theory by Booker.
1971	First calculation of dynamical channeling contrast by Clarke and Howie.
1977	First successful attempt to image dislocations in bulk samples by using channeling contrast by Pitaval et al.
1990	First use of digital signal processing to improve signal to noise ratio by Czernuszka et al.
1999	First demonstration of low tilt configuration and use of conventional backscatter detector by Simkin and Crimp.

Table 2.2: Important developments for ECP modality.

A schematic of the ECP setup is shown in Fig. 2.8(a). The setup consists of an annular integrating backscatter detector, which sums up the signal from all backscattered electrons captured by the detector. The typical inner and outer radii for the detector is of the order of a few millimeter. Typical acceleration voltages range from $5 - 30$ keV. The incident beams lie inside a conical volume, with the pivot point being in one of the lenses for regular ECP
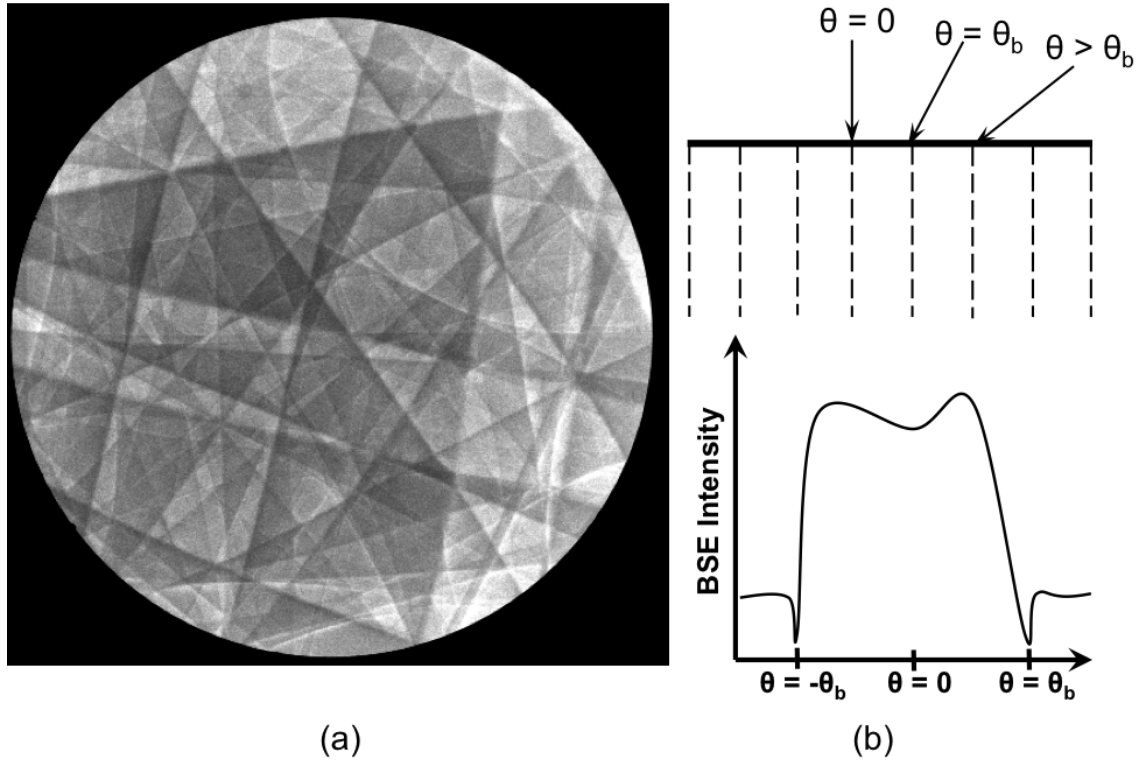
Figure 2.9: (a)Typical electron channeling pattern for Si and (b)schematic of variation in intensity versus beam tilt

mode or on the sample for selected area or beam rocking mode. The two modes are shown in Fig. 2.8(b) and (c) respectively. A typical ECP from a Si sample is shown in Fig. 2.9(a). Bragg's law is satisfied on the band edges leading to a large contrast variation. A schematic of the intensity versus beam tilt angle is shown in Fig. 2.9(b).

There have been a number of attempts to automate the indexing of channeling patterns. Schmidt and Olesen were the first to simulate kinematical patterns and use them to index ECPs for all seven crystal systems [50]. However, the process was not automated. Automatic band detection using the Hough transform pioneered by Krieger-Lassen, Conradsen, and Juul-Jensen can be used to detect the bands in ECPs. However, geometrical considerations limit the angular range in the diffraction patterns to about $\pm 10°$ and makes the automation unreliable. The method might work for certain special cases, but is no sufficiently general method to index channeling patterns in an automated fashion. While there have been efforts to integrate ECCI with the Electron Backscatter Diffraction (EBSD) method [51] for orientation mapping, it would be convenient if the orientation determination

could be performed without the use of extra hardware.

With the advent of fully scriptable microscopes for stage control and data acquisition, it has become possible to automate the data collection process for rapid ECCI-based defect characterization and analysis. Ideally, data acquisition in ECCI mode should be automated by controlling both the stage and detector (secondary and backscatter). The ultimate aim of this exercise is to automate data collection in the ECCI modality at different Bragg conditions by autonomous navigation in orientation space using sample tilt and rotation. This will enable high-throughput collection of large numbers of defect images from different regions in the sample. This motivates our efforts to design an indexing algorithm, which is sufficiently general to index any ECP for any one of the seven crystal systems.

2.3   Precession Electron Diffraction

Precession Electron Diffraction (PED) was initially designed by Vincent and Midgley in 1994 to be a substitute for x-rays for *ab-initio* structure determination [52]. The first TEM precession interfaces were developed at University Oslo [53,54], University of Bologna [55,56] and Northwestern University [57]. However, the first commercially available system ("spinning star"), which could be retrofitted to any modern TEM was not introduced until 2004. The x-ray based method is severely limited by the spatial resolution and can only "solve" structures for samples larger than a few μm. Since then, the technique has also been applied to symmetry determination [58–60], solving difficult unknown crystal structures [61, 62]. In this section we will focus on only one aspect, namely high spatial-resolution orientation mapping, similar to the EBSD system. For a spherical aberration corrected microscope, the spatial resolution can easily be better than 1 nm. This method can also be used for highly deformed samples where the Kikuchi bands in EBSD patterns are very faint or non-existent and the Hough transform based method fails.

The schematic of beam precession in the TEM is shown in Fig. 2.10. The beam is tilted using a deflection coil at a fixed angle ϕ, with the pivot point lying on the sample, and precesses along the cone. The diffracted beams are refocused to the back-focal plane using a set of descan coils. The resulting diffraction pattern is obtained by summing up the signal while the beam is precessing. The Ewald sphere, which is attached to the beam, also
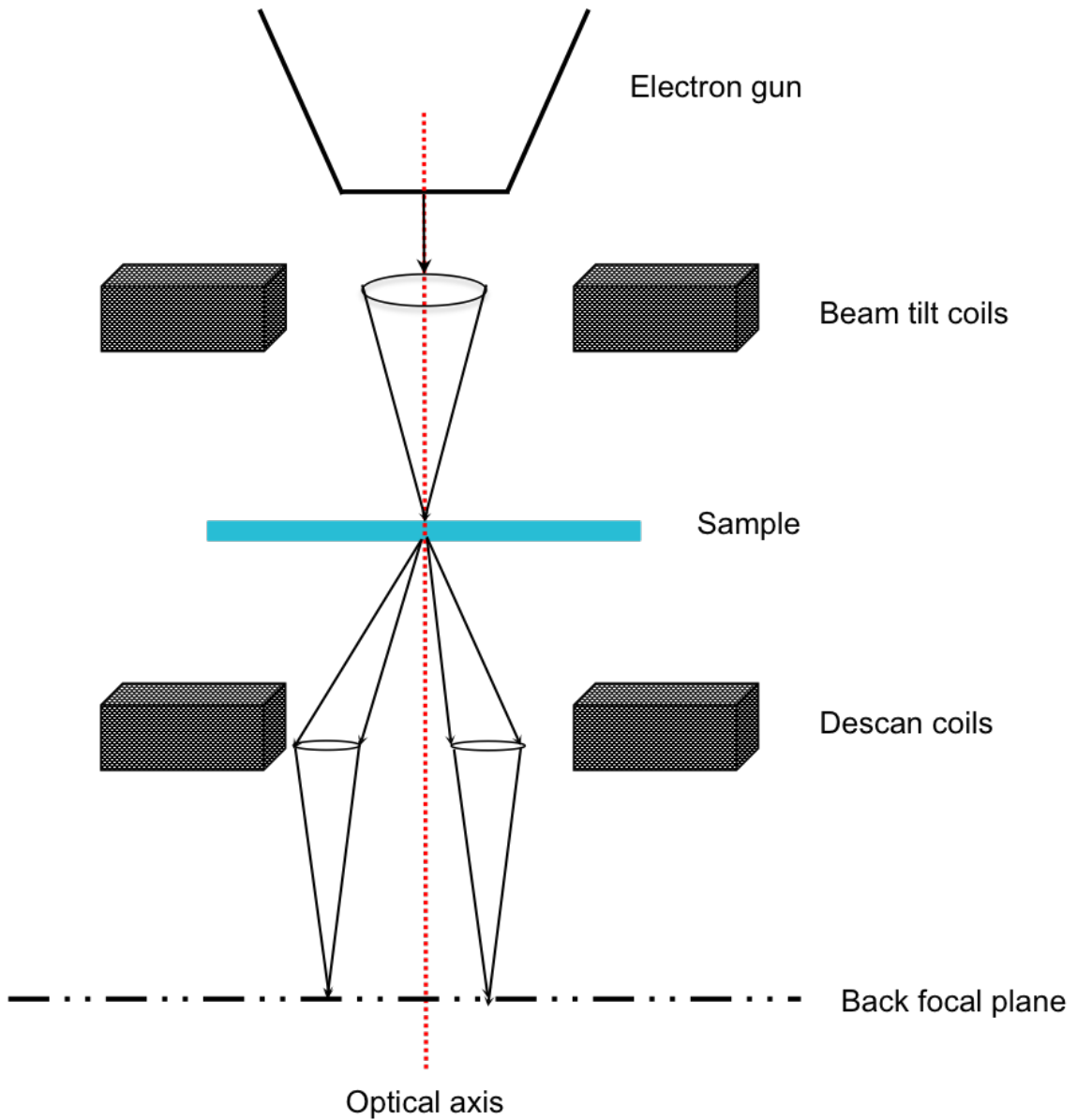
Figure 2.10: Schematic of the PED setup. The incoming parallel beam is precessed around a cone using a set of beam tilt coils. The diffracted beams are later refocused using a set of descan coils.

precessed with along with the beam. Therefore, the resulting diffraction pattern covers a wider range of reciprocal space. The beam is then rastered across the sample and diffraction patterns are recorded at each location.

It is well known that due to the strong interaction of electron with matter, the intensities in diffraction patterns are not kinematic, but dynamical in nature, with the beam scattering multiple times. The dynamical nature of scattering can be reduced in a number of ways, such as using an ultra-thin sample and using very high acceleration voltages. However,

these techniques have their own drawbacks in terms of beam damage. The precession of the electron beam to integrate the diffraction intensity offers two main advantages which make the analysis of diffraction patterns easier:

- The precession action leads to more reflections, both from the ZOLZ and HOLZ compared to conventional electron diffraction. This is because the Ewald sphere, attached to the beam, is also precessed and satisfies the Bragg's condition for a larger set of reciprocal lattice vectors.

- The integration over an angular range minimizes the dynamical effects but still maintains the geometry of the zone-axis.

Even though a higher precession angle is desirable for greater number of spots from HOLZ, typical precession angles of less than 1° are used. This is because the spatial resolution of the instrument is directly related to the precession angle. An instrument with spherical aberration coefficient given by C_s, for precession angle of ϕ and beam convergence angle of α will have the diameter of the circle of least confusion, d given by

$$d \sim 4C_s\phi^2\alpha \tag{2.2}$$

The first precession system for measurement of integrated diffraction intensities was invented by Vincent and Midgley in 1994 [52]. The first study of automating the data acquisition by using an external source for beam scanning was reported by Rauch et al., in 2008 [63] leading to the eventual introduction of the precession-assisted crystal orientation mapping technique (PACOM) commercially, ASTAR system. The added advantage of this method was that any TEM could be retrofitted with the unit needed for scanning the beam. The data acquisition rate for a typical PED system with a dedicated external CCD camera is in excess of 100 patterns/sec. However, unlike the EBSD system, the indexing of the acquired patterns is done off-line. A timeline of the important developments for orientation imaging using PED modality is presented in Table 2.3

1994	First PED system developed by Vincent and Midgley.
2004	First commercial PED system capable of being retrofit to any TEM by NanoMEGAS .
2008	First scanning variant of PED developed by Rauch et al.
2008	Introduction of precession-assisted crystal orientation mapping technique (PACOM) commercially, ASTAR

Table 2.3: Important developments for PED modality.
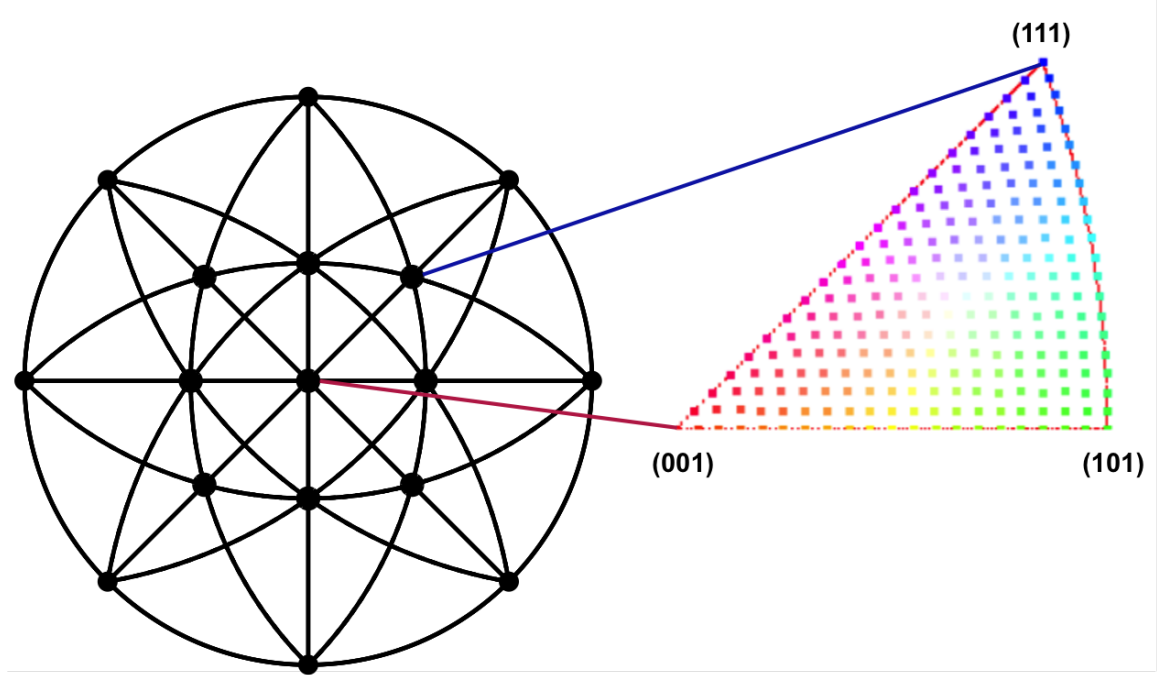
Figure 2.11: Stereographic projection of crystal having cubic symmetry. The inset shows the standard stereographic triangle (SST) and sampling of points from the SST for template matching.

2.3.1   Orientation Mapping and Limitations

Precession electron diffraction patterns are indexed off-line, using a "template" of kinematically precomputed patterns. The only a priori information required for the sample is its crystal structure, which includes its space group and the atom positions in the asymmetric part of the unit cell. The template is calculated for various points on the asymmetric unit in the stereographic projection of the crystal. For example, for a cubic crystal the asymmetric unit is the standard stereographic triangle. The matching is done using a normalized cross-correlation approach, where the cross-correlation coefficient, σ_{ij}, between the ith experimental and j^{th} template pattern is given by

$$\sigma_{ij} = \left\langle \frac{e_i - \bar{e}}{||e_i - \bar{e}||}, \frac{t_j - \bar{t}}{||t_j - \bar{t}||} \right\rangle \tag{2.3}$$

where, $\langle , \rangle$ denotes the inner product, $\bar{e}$ and $\bar{t}$ represents the mean of the experimental and template patterns respectively and e_i and t_j are the ith experimental and j^{th} template pattern respectively. The sampling of the asymmetric unit of the stereographic projection is done at a fixed angular resolution, typically $1°$ or less. This is shown in the inset of Fig. 2.11. The cross-correlation index for each of the sampling points is calculated as a map and the point with the highest index is chosen as the solution. If there is more than one phase present, then the template matching is done for both the phases and the one with the higher cross-correlation index is picked to be the correct solution. The software also calculates the Reliability Index, R, which is analogous to the confidence index for EBSD. It is defined as

$$R = 100 \left(1 - \frac{\sigma_1}{\sigma_2} \right) \tag{2.4}$$

Here, σ_1 and σ_2 are the highest and second highest cross-correlation coefficients for the set of sampled points on the stereographic projection. The software also calculates a virtual bright field image of the scanned area by placing a virtual aperture on the transmitted beam and summing the intensities in the acquired diffraction pattern. The resulting images are helpful in recognizing the scanned area in the sample and are less sensitive to diffraction contrast and curvature effects, which makes observation of features such as in-grain precipitates or stacking faults easier [64]. Complementary dark field images can also be acquired by shifting the virtual aperture to one of the diffracted beams. A comprehensive review of PED and its associated techniques can be found in [65] and specifically for orientation mapping in [66].

As we will see later, the dictionary approach works on the same general principles as the template matching algorithm with two key differences:

- The dictionary approach uniformly samples the whole of orientation space, instead of just the asymmetric unit in the stereographic projection. Thus, no cross-correlation needs to be performed on the dictionary "templates". Sampling only the stereographic projection also leads to different angular resolutions for different components of the
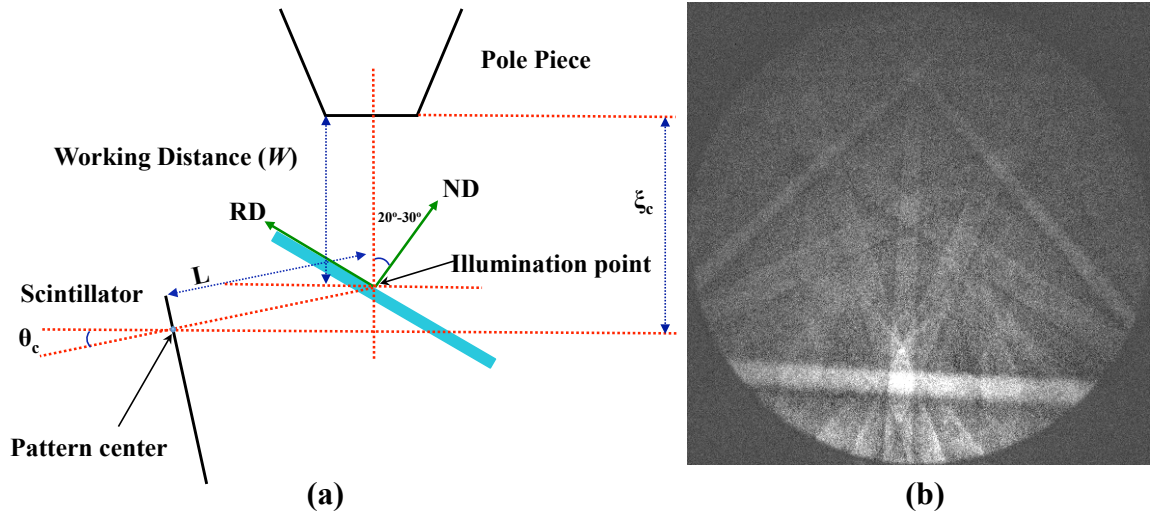
Figure 2.12: (a) Traditional configuration of TKD modality with the camera close to vertical and sample tilted to $20° - 30°$ from optical axis away from the camera and (b) typical TKD pattern from nano-grained Aluminum (pattern courtesy Dr. Patrick Callahan, University of California at Santa Barbara).

Euler angles.

- In the template matching algorithm, the cross-correlation is done on the patterns after a thresholding operation. The dictionary approach uses a different set of image processing routines to supress noise.

We will present preliminary results for a 50% cold rolled Cu as a proof of concept of the dictionary approach to indexing precession electron diffraction patterns.

2.4 Transmission Kikuchi Diffraction

Transmission Kikuchi Diffraction (TKD), sometimes erroneously referred to as Transmission Electron Backscatter Diffraction (t-EBSD) or transmission Electron Forward Scatter Diffraction (t-EFSD) is a very recently developed electron diffraction technique, using the same hardware and software as the EBSD modality to perform orientation mapping with very high spatial resolution. This development happened simultaneously at National Institute of Standards and Technology (NIST) [67] and The University of Sydney [68]. The primary motivation of this work was to improve the spatial resolution of orientation mapping in the SEM. While the EBSD modality had a spatial resolution of the order of 50 nm, the TKD modality offered a spatial resolution better than 10 nm [69–71]. For the TKD
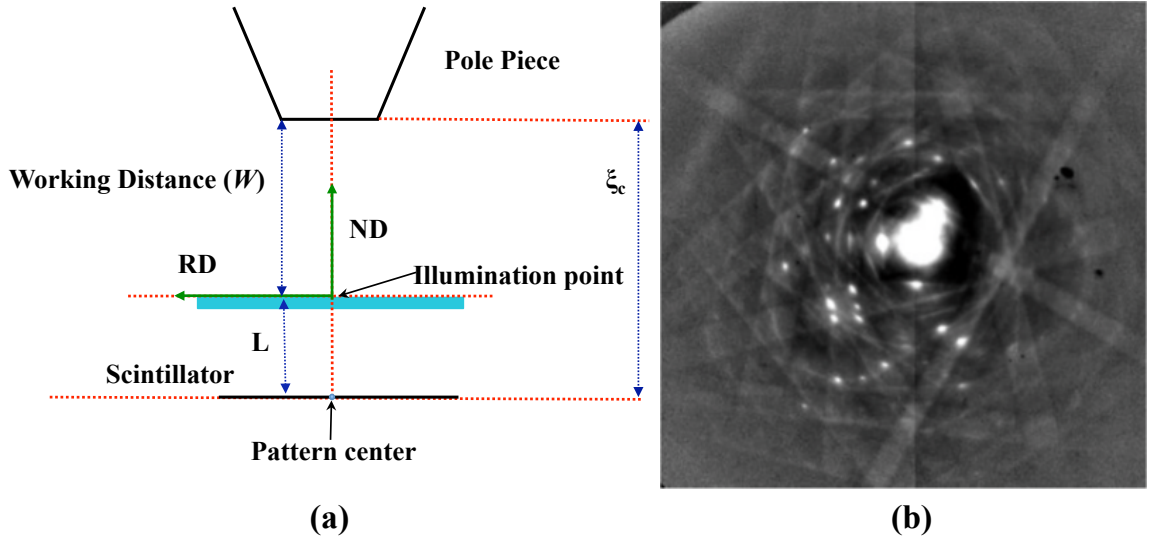
Figure 2.13: On-axis configuration of the TKD modality with the camera horizontal and sitting underneath the sample and (b) typical pattern in this configuration with the coherent diffraction spots intercepted along with the regular kikuchi bands (pattern taken from [1]).

modality, the sample is electron transparent and is tilted to $20° − 30°$ from optical axis away from the camera. The camera itself is a regular EBSD camera and intercepts the electrons scattered at high angles as shown in Fig. 2.12(a). A typical TKD patern from nano-grained Aluminum is shown in Fig. 2.12(b).

An alternate geometry for this technique was also proposed in which the sample was not tilted and the camera was placed on the optical axis below the sample [1]. This is illustrated in Fig. 2.13(a). The intensity of the transmitted electrons is higher for electrons scattered by smaller angles. However, since the camera is placed directly below the sample, for thinner samples the diffraction patterns include coherent diffraction spots in addition to the Kikuchi bands. A typical TKD pattern in this configuration is shown in Fig. 2.13(b). This geometry enables the camera to intercept electrons scattered by small angles and decreases the acquisition time, probe size and probe current and potentially improving the spatial resolution even further. This configuration is also geometrically simpler and more flexible than the traditional one.

A timeline for the important developments for the TKD modality is presented in Table 2.4.

The indexing of these diffraction patterns is done using the same Hough transform based

2012	First demonstration of TKD (reported as t-EBSD) by Keller and Geiss.
2015	Orientation mapping by transmission SEM using on-axis detector by Fundenberger et al.
2015	First commercial TKD system by Bruker Nano.

Table 2.4: Important developments for TKD modality.

method and software as the EBSD modality and will be not repeated again here.

CHAPTER III

Background

This dissertation makes use of numerous theoretical and simulation techniques, both well known and newly developed during the course of this study. This chapter serves as a brief collection of the pertinent methods. The chapter is organized as follows: Section 3.1 introduces some of the orientation representation important in material science. Section 3.1.4 introduces the concept of fundamental zones for various crystallographic symmetry. Specifically, we will be looking at fundamental zones in Rodrigues space. Section 3.2 introduces the various bijective projection method from a sphere which are used in this study. This includes the well-known equal area Lambert projection and its generalization to higher dimensions, the so-called homochoric mapping. This will then be used to define some new projections which aid in data storage, analysis and visualization. Section 3.3 discusses the scattering of electrons by an arbitrary crystal. Both elastic or dynamical scattering and inelastic or stochastic scattering is introduced. The formal solution to the elastic scattering problem is presented using two different approaches and a Monte Carlo approach is introduced for inelastic scattering. Finally, sections 3.4.1, 3.4.2, 3.4.3 and 3.4.4 discuss the generalized forward projectors for EBSD, ECP, PED and TKD modalities respectively with example simulations and comparison with experimental patterns.

3.1   Orientation Repersentations

Rotation or orientation representation defines a set of transformation rules to go from one Cartesian reference frame to a different one. For 3-D rotations, three independent numbers are required. There are many representations of orientation, some of which include the
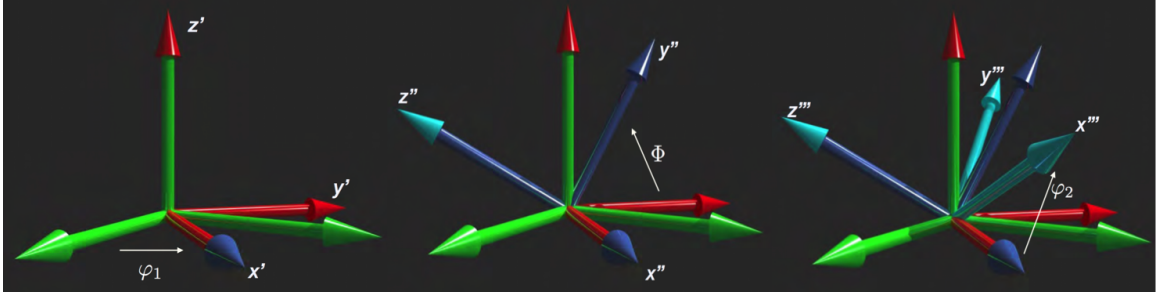
Figure 3.1: Schematic for the three rotations in the Bunge Euler angle representation about the Z-X'-Z" axis.

axis-angle pair, rotation matrix, Euler angles, Rodrigues vectors, unit quaternions, Cayley-Hamilton representation etc. In this section we will discuss three representation which are popular in material science, namely Bunge Euler angles, Rodrigues vectors and unit quaternions.

3.1.1 Bunge Euler angles

The Bunge Euler angles is given as a set of three angles, (ϕ_1, Φ, ϕ_2). These angles describe the rotation about the Z-X'-Z" axis respectively. This is shown schematically in Fig. 3.1. While the Bunge Euler angles are intuitive, there are significant drawbacks associated with them. Some of these include the gimbal lock and curved boundaries of the fundamental zones.

3.1.2 Rodrigues Vectors

Rodrigues vectors, $\mathbf{r}$ are vectors with magnitude equal to the tangent of half the rotation angle and direction coinciding with the rotation axis. Mathematically,

$$\mathbf{r} = \tan \frac{\omega}{2} \hat{\mathbf{n}}. \tag{3.1}$$

Here, ω is the rotation angle and $\hat{\mathbf{n}}$ is the rotation axis. The drawback with this representation is that 180° rotations have infinite magnitude. However, as we will see in the next section, the fundamental zones in Rodrigues space have planar boundaries making it particularly useful in numerical procedures and visualization.

3.1.3 Unit Quaternions

Quaternions are extensions of complex numbers to 4 dimensions. The quaternion is composed of a scalar part, r and a vector part, $\vec{v}$. Mathematically, they are represented as

$$q \equiv (r, \vec{v}) \equiv (q_0 + \mathrm{i}q_1 + \mathrm{j}q_2 + \mathrm{k}q_3), \tag{3.2}$$

with i,j and k satisfying the following identity

$$\mathrm{i}^2 = \mathrm{j}^2 = \mathrm{k}^2 = \mathrm{ijk} = -1 \tag{3.3}$$

Unit quaternions, sometimes referred to as *versors*, are quaternions with unity norm. Unit quaternions are isomorphic with the rotation space SO(3) and represent rotations in 3 dimensions. For a rotation and ω and rotation axis, $\hat{\mathbf{n}}$, the unit quaternion is given by

$$q = \cos\frac{\omega}{2} + \sin\frac{\omega}{2}\hat{\mathbf{n}}. \tag{3.4}$$

Quaternions avoid the problem of gimbal lock and are numerically the most stable. However, quaternions reside in $\mathbb{R}^4$ are non-intuitive to visualizes and represent in graphically.

3.1.4 Fundamental Zones

Diffraction patterns which arise from crystals are a function of the orientation of the crystal with respect to an external reference frame. However, due to crystal symmetry, not all possible points in orientation space lead to a unique diffraction patterns. The presence of symmetries in the crystal limits the range of orientations required to uniquely identify each one of the diffraction patterns. This set of unique points, which represent distinct orientations of a crystal, are referred to as the fundamental zone. While there will be many choices of fundamental zones for different crystal symmetries, we will always refer to the one which has the set of point closer to the origin than any other symmetrically equivalent set. Also, we will limit our discussion to the fundamental zones in Rodrigues space, since the bounding surfaces for this space are planar. We will discuss the fundamental zone of the orientation space for all possible 3-D rotation groups. Finally, we will conclude the section

with a discussion of uniform sampling of the Fundamental Zones and iso-misorientation surfaces using the cubochoric approach.

Fundamental Zones in Rodrigues space

It has been shown in [72] that the set of points equidistant from the origin and an arbitrary Rodrigues vector $\mathbf{r}$ form a plane at a distance of $\tan(\omega/4)$ on either side of the origin, where $\tan(\omega/2) = |\mathbf{r}|$ is the modulus of the arbitrary Rodrigues vector. This can be used to show that each rotational crystal symmetry element, $\mathbf{c}_i = \tan(\omega_i/2)\mathbf{I}_i$, bounds the Rodrigues space by the a pair or parallel planes at a distance of $\tan(\omega_i/4)$ on either side of the origin. Thus, depending on the rotational group of the crystal, the Fundamental zone may either be bound in some directions and open in others, or may form a closed polyhedron. Fundamental zones for individual symmetries are as follows

1. *Cyclic symmetries*: For the cyclic symmetry $\mathcal{C}_n$, the Rodrigues space is bound perpendicular to the n-fold axis at a distance of $\tan(\pi/2n)$ on either side of the origin, while the space is unbounded for the other two orthonormal basis directions. Notice that for $\mathcal{C}_1$, the fundamental zone coincides with the whole Rodrigues space. Examples include the rotation group $1, 2, 4, 6$.

2. *Dihedral symmetries*: For the dihedral symmetry $\mathcal{D}_n$, the fundamental zone is a prism with $2n$ sided polygons at a distance of $\tan(\pi/2n)$ on either side of the origin as the prism base and $2n$ square prism faces at distance 1. The base is perpendicular to the n-fold axis and the square faces are perpendicular to the 2-fold axis. Examples include the rotation groups 222, 32, 422 and 622.

3. *Tetrahedral symmetries*: For tetrahedral symmetry, the fundamental zone is a regular octahedron, with the faces at a distance of $\tan(\pi/6)$ from the origin. The faces are all perpendicular to the 3-fold symmetry axes. The rotational group 23 displays this fundamental zone.

4. *Octahedral symmetries*: For octahedral symmetries, the fundamental zone is a truncated cube, with the octagonal faces at distance $\tan(\pi/8)$ from origin and the triangular faces at a distance of $\tan(\pi/6)$ from origin. The octagonal faces are perpendicular

to the 4-fold axes and the triangular faces are all perpendicular to the 3-fold axes. The rotational group 432 displays such a fundamental zone.

3.2 Projections

This study makes extensive use of various 2-D and 3-D mappings for data storage, sampling, analysis and visualization. This chapter will be a brief overview of all the relevant projections used in this thesis. We shall be using the following notation to describe the various shapes used subsequently in this chapter

- $\mathbb{S}_r^n = \{\mathbf{x} \in \mathbb{R}^{n+1}, ||x|| = r\}$ - the n-dimensional sphere of $\mathbb{R}^{n+1}$ of radius r;

- $\mathbb{B}_r^n = \{\mathbf{x} \in \mathbb{R}^n, ||x|| \leq r\}$ - the n-dimensional ball of $\mathbb{R}^n$ of radius r;

- $\mathcal{C}_a^n = \{\mathbf{x} \in \mathbb{R}^n, ||x_i|| \leq \frac{a}{2}\}$ - the n-dimensional "cube" of $\mathbb{R}^n$ of edge length a,

where, the symbol $|| \cdot ||$ represents the Euclidean norm. The first item represents all points on the surface of a sphere of radius r in $\mathbb{R}^{n+1}$. For $n = 2$, this would represent all points on a circle, for $n = 3$, it would be all points on the surface of a sphere and so on. The second item represents all points on or inside a ball of radius r in $\mathbb{R}^n$. Similar to the last case, for $n = 2$, this would represent all points on or inside a circle (a disk) and the case $n = 3$ represents all points on or inside a sphere (a ball) etc. Finally, the last item represents all points on or inside a "cube". For $n = 2$, the cube would be a square etc. The following subsections describe isomorphisms between the various shapes that have been described above.

3.2.1 Equal area Lambert Projection

The well known equal area Lambert projection is a smooth isomorphism (diffeomorphism) between $\mathbb{S}_r^2$ i.e. points on a sphere to $\mathbb{B}_{2r}^2$ i.e. points on a disk of radius $2r$. In Cartesian coordinates with (x, y, z) on a unit sphere and (X, Y) on the disk of radius 2, the forward

and inverse transformation are given by

$$
\begin{aligned}
(X, Y) &= \left(\sqrt{\frac{2}{1-z}}x, \sqrt{\frac{2}{1-z}}y \right); \\
(x, y, z) &= \left(\sqrt{1 - \frac{X^2 + Y^2}{4}}X, \sqrt{1 - \frac{X^2 + Y^2}{4}}Y, -1 + \frac{X^2 + Y^2}{2} \right). \quad (3.5)
\end{aligned}
$$

3.2.2 Modified Lambert Projection

This is an extension of the previously defined equal area Lambert projections, where the ball (disk) $\mathbb{B}^2_{\sqrt{2}r}$ is further mapped onto $\mathcal{C}^2_{2r\sqrt{\pi}}$ i.e., a square with edge length $2r\sqrt{\pi}$. Thus, we effectively have an equal-area isomorphism between $\mathbb{S}^3_r$ and $\mathcal{C}^2_a$. As will be discussed further, this mapping is used to uniformly sample points on a sphere. Since this is an equal area mapping, this allows for further refinement of the grid. This approach is also used for the purpose of storing data on the surface of a sphere in a square grid, which is supremely convenient since arrays are naturally rectangular in shape. This approach also makes interpolation of data on a sphere much easier. In this scheme, a sphere $\mathbb{S}^2_r$ maps onto a "cube" $\mathcal{C}^2_{2r\sqrt{\pi}}$. For a unit sphere, which represents the set of unit vectors in 3-D, the forward relation which maps a point (x, y) in $\mathcal{C}^2_{2\sqrt{\pi}}$ to a point (a, b, c) in $\mathbb{S}^2_1$ is given by the following equations [73]

- For $0 \le |y| \le |x| \le \sqrt{\pi}$,

$$
(a, b, c) = \left(\frac{2x}{\pi}\sqrt{\pi - x^2}\cos(\frac{y\pi}{4x}), \frac{2x}{\pi}\sqrt{\pi - x^2}\sin(\frac{y\pi}{4x}), \frac{2x^2}{\pi} - 1 \right); \quad (3.6)
$$

- For $0 \le |x| \le |y| \le \sqrt{\pi}$,

$$
(a, b, c) = \left(\frac{2y}{\pi}\sqrt{\pi - y^2}\sin(\frac{x\pi}{4y}), \frac{2y}{\pi}\sqrt{\pi - y^2}\cos(\frac{x\pi}{4y}), \frac{2y^2}{\pi} - 1 \right). \quad (3.7)
$$

The inverse relation, which maps a point (a, b, c) in $\mathbb{S}^2_1$ to a point (x, y) in $\mathcal{C}^2_{2\sqrt{\pi}}$ is given by

- For $0 \le |b| \le |a|$,

$$
(x, y) = \text{sgn}(a)\sqrt{2(1+c)}\left(\frac{\sqrt{\pi}}{2}, \frac{2}{\sqrt{\pi}}\arctan\frac{b}{a} \right); \quad (3.8)
$$

- For $0 \leq |a| \leq |b|$,

$$(x, y) = \text{sgn}(b)\sqrt{2(1+c)}\left(\frac{2}{\sqrt{\pi}}\arctan\frac{a}{b}, \frac{\sqrt{\pi}}{2}\right). \tag{3.9}$$

While these equations are theoretically valid both for the Northern and Southern hemisphere, in practice, the projections for each hemisphere are applied separately to avoid severe distortions near the poles, which are an artifact of the equal-area Lambert projection. The use of this projection method to store and interpolate from the so-called Electron Backscatter Diffraction and Electron Channeling master patterns will be presented in later chapters.

3.2.3 Cubochoric Projection

The previous subsection presented results for an isomorphism between $\mathbb{S}^2_1$, which represents the set of unit vectors in 3 dimensions, and $\mathcal{C}^2_{2\sqrt{\pi}}$, which is a square. The cubochoric projection is a generalization of this last result for one higher dimension i.e., an isomorphism between $\mathbb{S}^3_1$, which represents the set of unit quaternions in 4 dimensions or alternatively the set of orientations in 3 dimensions, and $\mathcal{C}^2_{\pi^{2/3}}$, which is a cube. The cubochoric projection method preserves all the useful properties of the modified equal-area projection, namely that it is an equal-volume projection, hierarchical, easy to store and visualize etc. The cube is divided into six square pyramids, with the apex at the center. Each pyramid is mapped onto a corresponding curved pyramid on the sphere. The schematic is shown in Fig. 3.2. The forward and inverse relations are given as a series of three operations $\mathcal{M}_1, \mathcal{M}_2$ and $\mathcal{M}_3$. The points on the ball are further mapped onto the sphere $\mathbb{S}^3_1$ using the generalization of the Lambert equal-area mapping, formally called the *homochoric* mapping. For the pyramid with the primary symmetry axis aligned with the positive z direction, these are given by the following three steps [74]:

- *Step 1.* Isotropic scaling from $\mathcal{C}^3_{a'} \to \mathcal{C}^3_a$

$$\mathcal{M}_1(x, y, z) = \frac{a}{a'}(x, y, z). \tag{3.10}$$
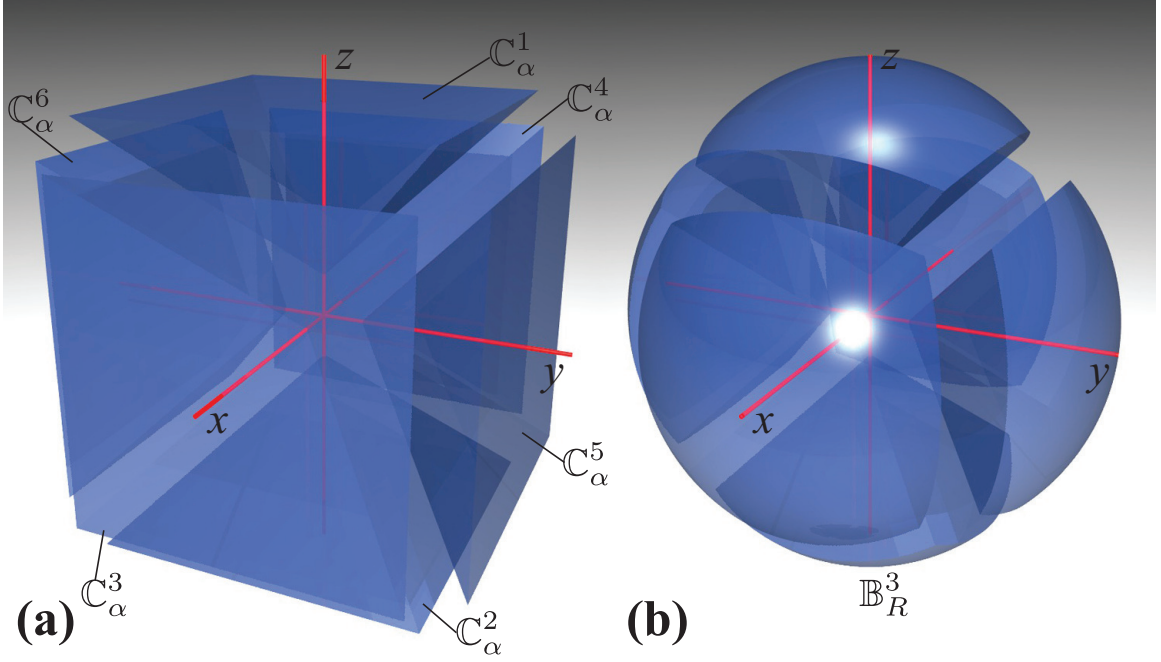
Figure 3.2: (a) Cube divided into six pyramids and (b) each pyramid mapped on to a curved pyramid

Here, a is the edge length of the cube $\mathcal{C}_a^3$ having the same surface area as a sphere of radius R $\mathbb{S}_R^2$ and a' is the edge length of the cube $\mathcal{C}_{a'}^3$ having the same volume as a ball of radius R $\mathbb{B}_R^3$. Thus,

$$
\begin{aligned}
a &= \sqrt{\tfrac{2\pi}{3}}R; \\
a' &= \sqrt[3]{\tfrac{4\pi}{3}}R.
\end{aligned}
\tag{3.11}
$$

- *Step 2.* Area preserving transformation of each square slice on the pyramid to a curved square slice, i.e. $\mathcal{C}_a^2 \to \widetilde{\mathcal{C}_a^2}$ [75]

$$
\mathcal{M}_2(x,y,z) = (T_1(x,y), T_2(x,y), z),
\tag{3.12}
$$

The transformation, $T_1(x,y)$ and $T_2(x,y)$ are given by the expressions (with $\beta = \sqrt{\pi/6}$):

– For $|y| \leq |x|$

$$(x, y) \to (X, Y) = \frac{2^{1/4} x}{\beta \sqrt{\sqrt{2} - \cos \frac{y\pi}{12x}}} \left(\sqrt{2} \cos \frac{y\pi}{12x} - 1, \sqrt{2} \sin \frac{y\pi}{12x} \right); \qquad (3.13)$$

– For $|x| \leq |y|$

$$(x, y) \to (X, Y) = \frac{2^{1/4} y}{\beta \sqrt{\sqrt{2} - \cos \frac{x\pi}{12y}}} \left(\sqrt{2} \sin \frac{x\pi}{12y}, \sqrt{2} \cos \frac{x\pi}{12y} - 1 \right). \qquad (3.14)$$

- *Step 3.* Mapping the curved pyramid $\widetilde{\mathcal{C}_a^2}$ onto the ball $\mathbb{B}^3_{\rho(\alpha)}$ by mapping each slice of the pyramid onto the portion of the sphere $\mathbb{S}^2_{\rho(\alpha)}$, using the inverse Lambert azimuthal equal area projection with respect to the North pole of $\mathbb{S}^2_{\rho(\alpha)}$

$$\mathcal{M}_3\left(x, y, \frac{\alpha}{2}\right) = \left(\sqrt{1 - \frac{x^2 + y^2}{4\rho^2(\alpha)}}\, x, \sqrt{1 - \frac{x^2 + y^2}{4\rho^2(\alpha)}}\, y, \rho(\alpha) - \frac{x^2 + y^2}{2\rho(\alpha)} \right). \qquad (3.15)$$

In deriving the final expression for the transformation, we choose $\alpha = 2z$, so that $\rho(\alpha) = \sqrt{\frac{6}{z}}$. While these relations are only valid for one of the pyramids, the transformations for other pyramids can be found by appropriate permutation of the symbols. The overall transformation, $\mathcal{P}_1$, from the cube $\widetilde{\mathcal{C}_a^3}$ to the ball $\mathbb{B}^3_R$ is given by the concatenation of the three steps

$$\mathcal{P}_1 = \mathcal{M}_1 \circ \mathcal{M}_3 \circ \mathcal{M}_3. \qquad (3.16)$$

This transformation is volume preserving only if the Jacobian of the transformation is equal to one. It can be shown that the Jacobian of the overall transformation, $\mathcal{J}(\mathcal{P}_1)$ is given by

$$\mathcal{J}(\mathcal{P}_1) = \mathcal{J}(\mathcal{M}_1)\mathcal{J}(\mathcal{M}_2)\mathcal{J}(\mathcal{M}_3) = 1. \qquad (3.17)$$

The final step in obtaining the mapping from $\mathcal{C}_a^3$ (with $a = (\pi^5/6)^{1/6}$) to the Northern hemisphere of the unit sphere $\mathbb{S}^3_+$ is carried out by using the generalization of the Lambert equal-area projection in 3 dimensions. It can be shown that this mapping is equivalent to the well known homochoric coordinates. There is no closed form solution for the transformation

and we have to resort to numerical methods to find the approximate solutions. Details of this projection method can be found in [74].

3.3 Electron Scattering

3.3.1 Dynamical Diffraction

Electrons are elementary particles and their behavior is inherently quantum mechanical in nature. Any theoretical description or experiment concerning these particles must hence be based on quantum mechanics. Also, the typical acceleration voltages used in a SEM are of the order of tens of kilovolts, so that the electrons are traveling at a significant fraction of the speed of light. For example, at 20 keV, the electrons are traveling at $0.272c$. In a TEM, the acceleration voltages, and subsequently the electron velocity, are even higher. At such high velocities, the rules of special relativity apply, and thus the relativistic nature of the electrons has to be taken into account while constructing a theory of electron scattering in a SEM. Electron microscopy is thus, quintessentially, a relativistic quantum mechanical experiment where the sample is illuminated with electrons, and a scattered intensity is observed.

The general description of the elastic-inelastic scattering of the electrons has been discussed in the papers by Dudarev et al. [76–79]. They used a quantum mechanical density matrix formalism to study the redistribution of electrons from the incoming state into elastic and inelastic final states. While this theory is very general, it is also extremely complicated. Thus, we will use a simplification where we treat the elastic and the inelastic parts of the scattering separately. This makes the theory more usable in practical situations.

In 1926, Schrödinger constructed a wave theory of matter. Dirac extended the theory to include special relativity. Thus, the Dirac equation should be the starting point for the theoretical study. However, it was shown by Fujiwara in [80] that for high energy electrons, the spin of the electrons and the time dependence of the wavefunction can be neglected. The Dirac equation then reduces to a time independent Schrödinger-like equation called the Klein-Gordon equation, in which the electron wavelength and mass are replaced by their relativistically correct values. Thus, the governing equation for a relativistic electron in an

arbitrary potential is

$$\Delta\Psi + 4\pi^2\mathbf{k}_0^2\Psi = -4\pi^2 U(\mathbf{r})\Psi \tag{3.18}$$

Here, Δ is the Laplacian operator operating on the wavefunction Ψ, $\mathbf{k}_0 = \frac{1}{\lambda}$ is the relativistic wavenumber, and $U(\mathbf{r}) = \frac{2meV_c(\mathbf{r})}{h^2}$ is the modified periodic potential $V_c(\mathbf{r})$, inside the illuminated crystal. To phenomenologically take absorption into account, the crystal potential is written as a complex potential $V_c(\mathbf{r}) = V(\mathbf{r}) + iW(\mathbf{r})$ [81]. Since the crystal potential will have the periodicity of the lattice, it can be expanded in a Fourier series along all points in reciprocal lattice. This leads to the following expression for the crystal potential

$$V_c(\mathbf{r}) = V_0 + V^{'}(\mathbf{r}) + iW(\mathbf{r}) = V_0 + \sum_{\mathbf{g}\neq 0} V_{\mathbf{g}}e^{2\pi i\mathbf{g}\cdot\mathbf{r}} + i\sum_{\mathbf{g}\neq 0} W_{\mathbf{g}}e^{2\pi i\mathbf{g}\cdot\mathbf{r}} \tag{3.19}$$

The frequency independent part of the potential, V_0, is the mean inner potential of the crystal. This accelerates the electrons and slightly changes the relativistic acceleration potential. This is similar to refraction from an optically denser to a less dense medium. If this expression of the potential is substituted in eq. 3.18, one obtains

$$\Delta\Psi + 4\pi^2 k_0^2\Psi = -4\pi^2[U(\mathbf{r}) + iU^{'}(\mathbf{r})]\Psi, \tag{3.20}$$

where,

$$U(\mathbf{r}) = \frac{2me}{h^2}\sum_{\mathbf{g}\neq 0} V_{\mathbf{g}}e^{2\pi i\mathbf{g}\cdot\mathbf{r}};$$

$$U^{'}(\mathbf{r}) = \frac{2me}{h^2}\sum_{\mathbf{g}} W_{\mathbf{g}}e^{2\pi i\mathbf{g}\cdot\mathbf{r}}. \tag{3.21}$$

Equation 3.20 is ultimately the equation that we are trying to solve. The formal and numerical methods to solve the equation is discussed in the next section . The atomic scattering factors, which can be used to compute periodic complex potentials for an arbitrary crystal, for different elements have been computed and parametrized as atomic scattering factors in the form of power series or exponential expansion by a number of authors [82–85]. In this work, we use the Weickenmeier and Kohl parametrization. For details, the reader is

referred to [86].

3.3.2 Formal solution

The previous section introduced the governing equation for electron scattering by an arbitrary potential. Apart from a few special cases, it is not possible to compute the exact solution to this equation and we have to resort to numerical approximations. While it is possible to numerically tackle this equation using a variety of differential equation solvers, such as the fourth order Runge-Kutta method etc., these methods are computationally very intensive. Progress can be made using physically motivated assumptions about the scattering process. In this section, we will discuss two important approaches to reduce the order of the equation by one and formally solve it, namely the scattering matrix and the Bloch wave approach. While methods exist to solve this equation in real space, both these methods described here rely on the use of Fourier space.

Scattering Matrix Approach

From Bragg's law, we know that any diffracted beam has a wave vector $\mathbf{k}' = \mathbf{k}_0 + \mathbf{g}$, where $\mathbf{k}_0$ is the initial wave vector and $\mathbf{g}$ is any reciprocal lattice vector which lies on the Ewald sphere. It is also known that plane waves are momentum eigenfunctions for the Schrödinger equation. Hence, it is assumed that the wave function of the electron at the exit plane is a linear superposition of plane waves, with their wave vectors dictated by Bragg's law. Therefore, the *Ansatz* is

$$\Psi(\mathbf{r}) = \sum_{\mathbf{g}} \psi_{\mathbf{g}} e^{2\pi i (\mathbf{k}_0 + \mathbf{g}) \cdot \mathbf{r}}. \tag{3.22}$$

After substitution of eq. 3.22 into eq. 3.20 and some mathematical manipulations, we obtain

$$\sum_{\mathbf{g}} [\Delta \psi_{\mathbf{g}} + 4\pi i (\mathbf{k}_0 + \mathbf{g}) \cdot \nabla \psi_{\mathbf{g}} + 4\pi^2 \left\{ \mathbf{k}_0^2 - (\mathbf{k}_0 + \mathbf{g})^2 \right\} \psi_{\mathbf{g}}] e^{2\pi i (\mathbf{k}_0 + \mathbf{g}) \cdot \mathbf{r}} =$$
$$-4\pi^2 \sum_{\mathbf{g}} [U + iU'] \psi_{\mathbf{g}} e^{2\pi i (\mathbf{k}_0 + \mathbf{g}) \cdot \mathbf{r}}. \tag{3.23}$$

In 1976, Van Dyck [87] showed that the first term in eq. 3.23, i.e. the Laplacian, is negligible for high energy electrons. This involves a formal solution to the full second order equation and neglecting the back-scattered waves; this is the forward scattering approximation. Fur-

thermore, as we are considering samples which are infinite in the lateral dimensions, the Fourier coefficients of the wavefunction $\psi_{\mathbf{g}}$ cannot depend on these coordinates, so they are only a function of depth. Using the general definition of the dot product, we have:

$$(\mathbf{k}_0 + \mathbf{g}) \cdot \nabla \psi_{\mathbf{g}} = |\mathbf{k}_0 + \mathbf{g}| \cos \alpha \frac{d\psi_{\mathbf{g}}}{dz}. \tag{3.24}$$

Using eq. 3.24 along with eqs. 3.21 introduced earlier, the equation reduces to

$$\sum_{\mathbf{g}} \left[\frac{d\psi_{\mathbf{g}}}{dz} - 2\pi i \frac{\mathbf{k}_0^2 - (\mathbf{k}_0 + \mathbf{g})^2}{2|\mathbf{k}_0 + \mathbf{g}| \cos \alpha} \psi_{\mathbf{g}} \right] e^{2\pi i (\mathbf{k}_0 + \mathbf{g}) \cdot \mathbf{r}} = \sum_{\mathbf{g}} \left[\pi i \sum_{\mathbf{g}'} \frac{(U_{\mathbf{g}-\mathbf{g}'} + iU'_{\mathbf{g}-\mathbf{g}'})}{|\mathbf{k}_0 + \mathbf{g}| \cos \alpha} \psi_{\mathbf{g}'} \right] e^{2\pi i (\mathbf{k}_0 + \mathbf{g}) \cdot \mathbf{r}} \tag{3.25}$$

Eq. 3.25 must hold everywhere inside the crystal, therefore the equality has to be valid for individual terms in the summation. This results in the equations:

$$\frac{d\psi_{\mathbf{g}}}{dz} - 2\pi i \frac{\mathbf{k}_0^2 - (\mathbf{k}_0 + \mathbf{g})^2}{2|\mathbf{k}_0 + \mathbf{g}| \cos \alpha} \psi_{\mathbf{g}} = \pi i \sum_{\mathbf{g}'} \frac{(U_{\mathbf{g}-\mathbf{g}'} + iU'_{\mathbf{g}-\mathbf{g}'})}{|\mathbf{k}_0 + \mathbf{g}| \cos \alpha} \psi_{\mathbf{g}'} \tag{3.26}$$

The coefficient of $\psi_{\mathbf{g}}$ in the second term on the left side of eq. 3.26 is known as the deviation parameter, $s_{\mathbf{g}}$, or excitation error. Equation 3.26 explains that the variation of the wave function with depth depends both on the geometry of diffraction ($s_{\mathbf{g}}$) and amplitude of all other waves. The strength of coupling between different diffracted waves is defined by the crystal potential ($U_{\mathbf{g}-\mathbf{g}'}$). Additional substitutions in eq. 3.26 simplify the equation. The Fourier components of the potential are split into their magnitude and phase, and new quantities called the extinction ($\xi_{\mathbf{g}}$) and absorption ($\xi'_{\mathbf{g}}$) distance are defined as

$$\frac{1}{\xi_{\mathbf{g}}} = \frac{|U_{\mathbf{g}}|}{|\mathbf{k}_0 + \mathbf{g}| \cos \alpha}; \tag{3.27}$$

$$\frac{1}{\xi'_{\mathbf{g}}} = \frac{|U'_{\mathbf{g}}|}{|\mathbf{k}_0 + \mathbf{g}| \cos \alpha}. \tag{3.28}$$

For convenience, both quantities can be represented by one complex quantity $q_{\mathbf{g}}$ defined as

$$\frac{1}{q_{\mathbf{g}}} = \frac{1}{\xi_{\mathbf{g}}} + i \frac{e^{i\beta_{\mathbf{g}}}}{\xi'_{\mathbf{g}}}. \tag{3.29}$$

where $\beta_{\mathbf{g}}$ is the difference in the phase angles of $\xi_{\mathbf{g}}$ and $\xi'_{\mathbf{g}}$. Substitutions of eqs. 3.27 and 3.28 along with the definition of $s_{\mathbf{g}}$ produces the final form of the Darwin-Howie-Whelan (DHW) equations [86]:

$$\boxed{\frac{\mathrm{d}\psi_{\mathbf{g}}}{\mathrm{dz}} - 2\pi \mathrm{i} s_{\mathbf{g}} \psi_{\mathbf{g}} = \mathrm{i}\pi \sum_{\mathbf{g}'} \frac{e^{\mathrm{i}\theta_{\mathbf{g}-\mathbf{g}'}}}{q_{\mathbf{g}-\mathbf{g}'}} \psi'_{\mathbf{g}}.}$$ (3.30)

The DHW equations can be further simplified by the substitution

$$\psi_{\mathbf{g}} = S_{\mathbf{g}} e^{\mathrm{i}\theta_{\mathbf{g}}} e^{\frac{\pi z}{\xi'_0}}.$$ (3.31)

This is done because the phase factor evaluates to unity after taking the squared modulus of the wavefunction. After substitution and further simplification using the Kronecker delta function, the following equation is obtained:

$$\frac{dS_{\mathbf{g}}}{dz} = \mathrm{i}\pi \sum_{\mathbf{g}} \left[2s_{\mathbf{g}'}\delta(\mathbf{g} - \mathbf{g}') + \frac{1 - \delta(\mathbf{g} - \mathbf{g}')}{q_{\mathbf{g}-\mathbf{g}'}} \right] S_{\mathbf{g}'}.$$ (3.32)

This equation can be rewritten in the form of a matrix equation,

$$\frac{d\mathbf{S}}{dz} = \mathrm{i}\mathcal{A}\mathbf{S}.$$ (3.33)

The $\mathcal{A}$ matrix is referred to as the *structure matrix*. The diagonal entries of the matrix contain information about the geometry of diffraction through the excitation errors. The off diagonal entries describe how the beams interact with each other through the crystal potential. This equation has a well known solution of the form

$$\mathbf{S}(z_0) = e^{\mathrm{i}\mathcal{A}z_0}\mathbf{S}(0).$$ (3.34)

Here, $\mathbf{S}(0)$ refers to the initial condition of the electron beam. The exponential of the matrix is typically referred to as the *scattering matrix*. There are numerous ways to calculate the exponential of a matrix. The scaling and squaring method to pre-condition the matrix followed by either the Padé approximation or the optimized Taylor method is used in this work [88].

Bloch Wave Approach

While deriving the DHW equations, it was assumed that the only allowed wave vectors at the exit plane are the ones which follow Bragg's law. This is valid for an observer outside the crystal but need not be true inside. If it is of interest to calculate the wavefunctions inside the crystal, then the DHW equation are no longer appropriate. We need an alternate approach to calculate the wavefunctions. The only waves allowed inside a periodic lattice should have the periodicity of that lattice i.e., should follow Bloch's theorem [89]. One such Bloch wave is given by:

$$C(\mathbf{r})e^{2\pi i \mathbf{k} \cdot \mathbf{r}} = \sum_{\mathbf{g}} C_{\mathbf{g}} e^{2\pi i (\mathbf{k}+\mathbf{g}) \cdot \mathbf{r}}. \tag{3.35}$$

The term $C(\mathbf{r})$ has the same periodicity as the crystal and hence, can be expanded as a Fourier sum along the reciprocal lattice points. The important difference from the previous *Ansatz* is that the $\mathbf{k}$ wave vector used here is not the same as the $\mathbf{k}_0$ wave vector, which is the wave vector of the incident electrons. The *Ansatz* will be a superposition of all such Bloch waves and reads as

$$\Psi(\mathbf{r}) = \sum_{j} \alpha^{(j)} \sum_{\mathbf{g}} C_{\mathbf{g}}^{(j)} e^{2\pi i (\mathbf{k}^{(j)}+\mathbf{g}) \cdot \mathbf{r}}. \tag{3.36}$$

Furthermore, it has been shown in [90] that only the normal component of the wave vector changes, and the tangential component is invariant. Therefore, it is convenient to write the wave vector in the Bloch waves formalism as

$$\mathbf{k}^{(j)} = \mathbf{k}_0 + \gamma^{(j)} \mathbf{n}. \tag{3.37}$$

Using equations 3.36, 3.37 and 3.20 together with the high energy approximation (no back-scattered waves), the following system of equations is obtained

$$2\mathbf{k}_0 s_{\mathbf{g}} C_{\mathbf{g}}^{(j)} + \sum_{\mathbf{h} \neq \mathbf{g}} U_{\mathbf{g}-\mathbf{h}} C_{\mathbf{h}}^{(j)} = 2k_n \left(1 + \frac{g_n}{k_n}\right) \gamma^{(j)} C_{\mathbf{g}}^{(j)}. \tag{3.38}$$

Here g_n and k_n represent the normal components of the respective vectors. Usually, $g_n <<$ k_n and their ratio in eq. 3.38 can be neglected. This final equation can be rewritten in the

form of an eigenvalue problem

$$\bar{\mathcal{A}}\mathbf{C}^{(j)} = 2k_n\gamma^{(j)}\mathbf{C}^{(j)}. \tag{3.39}$$

The diagonal entries of $\bar{\mathcal{A}}$ contain the geometry of diffraction, i.e., the excitation error terms. The off-diagonal terms contain the interaction with the crystal. This is very similar to the form of the structure matrix, as defined in the previous section. From the knowledge of the eigenvalues and eigenvectors, the individual Bloch waves can be calculated. The weight factors $\alpha^{(j)}$ are calculated using the boundary conditions at the entrance plane.

3.3.3 Stochastic Scattering

The previous sub-section discussed the elastic scattering processes, during which the energy of the electron does not change. This, however, is an approximation of the actual physical process. As the electron travels through the material, it can exchange energy with the atom lattice using a variety of mechanisms. These processes are grouped under the umbrella of *inelastic scattering*. Some of the mechanisms include *Bremsstrahlung*, plasmon excitations, phonon excitations etc. The full treatment of electron scattering by a crystal involves solving the time-dependent relativistic Schrödinger's equation, which is a considerable challenge. In this work, we incorporate the effects of inelastic scattering separately using Monte Carlo simulation, which compute the electron trajectories and energy losses as the electron passes through the crystal. The model uses the single scattering approach, which accurately represents the interaction of high energy electrons with solids over a wide range of conditions and materials. There are two major assumptions in this model

1. Only the elastic or Rutherford scattering events are responsible for changing the trajectory of electrons. Thus, only elastic collisions are responsible for the spatial interaction and angular distribution of the electrons. The inelastic scattering events only represent a loss in the energy of the electrons.

2. While there are a few mechanisms, such as *Bremsstrahlung* where the electrons can lose energy continuously, in reality most of the energy loss comes from discrete inelastic collision events. However, it is assumed that the electron loses energy at a continuous

rate along its path. This assumption results from an averaging of all the discrete inelastic steps along the trajectory of the electron and leads to significant simplification. This is known as the continuous slowing down approximation or CSDA.

The elastic or Rutherford cross section in cm^2/atom for electron scattering is given by [91]

$$\sigma_E = 5.21 \times 10^{-21} \frac{Z^2}{E^2} \frac{4\pi}{\alpha(1+\alpha)} \left(\frac{E+511}{E+1024}\right)^2, \tag{3.40}$$

where, Z is the average atomic number of the target, E is the energy of the incident electron and α, is the screening factor to account for the fact that the electron does not see all of the nuclear charge. The screening factor, α is given by the expression

$$\alpha = 3.4 \times 10^{-3} \frac{Z^{0.67}}{E} \tag{3.41}$$

The scattering cross section given above defines a mean free path for electron scattering, which is the average distance traveled by the electron be fore it undergoes a scattering event. The expression for the mean free path (in cm) is given by

$$\lambda = \frac{A}{N_A \rho \sigma_E}, \tag{3.42}$$

where λ is the mean free path, A is the average atomic weight of the target in gm/mole, N_A is Avogadro's constant and ρ is the density of the target in g/cm^2. The actual distance traveled by the electron between each successive collision is random and is calculated by sampling from an exponential distribution, with λ as the "survival parameter". Concretely, the path length between successive collisions is given by $s = \lambda \log r$, where r is a random number from a uniform distribution. The scattering angle is similarly sampled using the differential form of the scattering cross section and is given as $\cos\phi = 1 - \frac{2\alpha r}{1+\alpha-r}$, where ϕ is the scattering angle and r is again a random number generated from a uniform distribution. The azimuthal angle of scattering is sampled uniformly in the range $[0, 2\pi]$.

As mentioned before, the energy losses for the electrons are accounted for using the CSDA. It was shown in [92] that the energy loss per unit path length, referred to as the

stopping power, is given by the expression

$$\frac{\mathrm{d}E}{\mathrm{d}s} = -78500 \times \frac{Z}{AE} \log\left(\frac{1.166E}{J}\right), \tag{3.43}$$

where the symbols have their usual meaning and J is the mean ionization potential representing the effective energy loss per interaction between the electron and the target. This single parameter incorporates all the energy loss mechanisms. J has been parametrized empirically using experimental data and has the following form (in units of keV):

$$J = \left[9.76Z + \frac{58.5}{Z^{0.19}}\right] \times 10^{-3}. \tag{3.44}$$

Again, the symbols have their usual meaning. However, we are using a modified version of the stopping power, which has been given by Joy and Luo [93]. The modified expression fits the stopping power data better at lower energies of the electron and is given by

$$\frac{\mathrm{d}E}{\mathrm{d}s} = -78500 \times \frac{Z}{AE} \log\left(\frac{1.166(E + 0.85J)}{J}\right). \tag{3.45}$$

Further details about the implementation of this algorithm can be found in [91]. This concludes our discussion of the inelastic scattering of electron by a solid.

3.4 Forward Models for Electron Diffraction Modalities

As has been stated before, the field of material science relies on a plethora of characterization techniques to study the structure-property-processing-performance relationship for the system of interest. The technique of choice depends on the information being sought. A generalized view of the characterization process is depicted in Fig. 3.3. The system of interest has some geometry characterized by its shape function, $D(\mathbf{r})$. We are seeking information about some property of interest. This might be a scalar field, such as density, electric potential etc., a vector field, such as magnetization, polarization, etc. or a tensor field, such as stress, strain etc. These fields are represent by the symbols $s(\mathbf{r})$, $\mathbf{v}(\mathbf{r})$ and $t(\mathbf{r})$ respectively.

The system is typically studied using some probe, $\mathcal{P}$ having a point spread function $\mathcal{T}$.
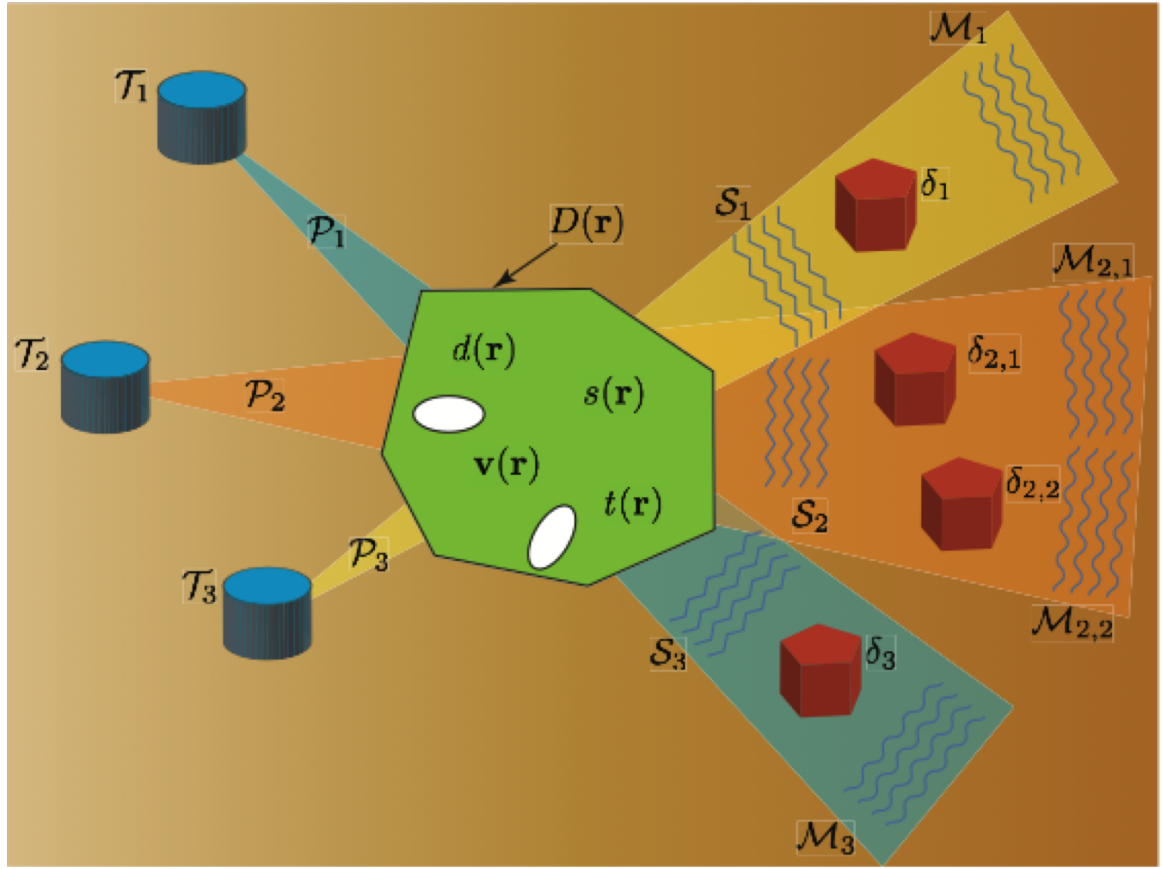
Figure 3.3: A generalized view of materials characterization.

The probe interacts with the system and has a response denoted by $\mathcal{S}$, which is detected using an array of detectors characterized by their point spread function, δ. The detector modifies the response to give us the measured signal, $\mathcal{M}$. This step is the system *parameterization* and describes the minimal set of model parameters necessary to completely characterize the system. In material science, a typical problem would be reconstructing the field of interest, given a set of measurements. This falls in the general class of problems called the *inverse problems*. The inverse problem consists in using the results of actual observations to infer the values of the parameters, which best characterizes the system under investigation. Mathematically, this can be written as

$$[s(\mathbf{r}), \mathbf{v}(\mathbf{r}), t(\mathbf{r})] = \mathcal{F}^{-1}(\mathcal{M}_i | \mathcal{P}_i, \mathcal{T}_i, \delta_i, ...). \tag{3.46}$$

Here $\mathcal{F}^{-1}$ represents the operator which describes the explicit relationship between mea-

surements and the quantity of interest, given the parameters describing the probe, detector etc. Inverse problems are ubiquitous in science and engineering and their solution allows us to extract parameters about the system under study that can not be easily obtained from direct observations. A few important inverse problems in material science include structure determination and phase reconstruction using synchrotron x-ray, determination of magnetic structure using neutron scattering, elemental analysis using electron diffraction (EDX) etc. Even orientation mapping using EBSD, discussed in chapter II, can be posed as an inverse problem. Inverse problems are difficult to solve for two main reasons:

- Different sets of model parameters may be consistent with the data. In other words, an inverse problem can have multiple solutions, or no solution at all.

- Discovering the correct values of the model parameters may require exploring a huge parameter space. This might make the problem intractable.

The inverse of this problem is the *forward problem*. The forward problem involves the prediction of observations, given the values of the parameters defining the model. Mathematically, we can write this as

$$\mathcal{M}_i = \mathcal{F}_i[D(\mathbf{r}), s(\mathbf{r}), \mathbf{v}(\mathbf{r}), t(\mathbf{r}), \delta_i, ...].$$
(3.47)

Here, $\mathcal{F}$ denotes the operator which describes the explicit relationship between model parameters and measurements. While the inverse problem may or may not use prior information of the physical processes involved in the experiment, the forward model is a physics-based model, compatible with known laws and principles of physics. Also, contrary to the inverse problem, the forward problem will always have a unique solution. The accuracy and precision of the prediction will depend on the validity of the model, but a unique solution is always guaranteed.

In this section we will discuss forward models for electron scattering, specifically for four modalities: Electron Backscatter Diffraction, Electron Channeling Patterns, Precession Electron Diffraction and Transmision Kikuchi Diffraction. The forward model for all four diffraction modalities will consist of two distinct parts; dynamical diffraction, which is common to all four modalities and a detector model, which decides what signals are being

measured. We will also discuss the concept of a master pattern, which is a computational tool to make the forward model numerically efficient. We will conclude each section with a comparison of the results of the forward model with actual experimental patterns.

3.4.1   Electron Backscatter Diffraction

The background for this section has already been laid in section 3.3. In that section, we discussed how to calculate the wavefunction of the electron in a periodic potential. For the EBSD modality, we are interested in calculating the backscatter yield as a function of different channeling directions. The dynamical contribution to backscattering is superimposed on a stochastic signal, which makes up the background of the diffraction pattern. In this sub-section, we will discuss the computation of the backscatter yield for electron having a wave vector $\mathbf{k}$. We will also incorporate stochastic scattering in this model through a depth and energy dependent weight factor.

Scattering Theory

Dynamical Scattering   As the electrons travel through a layer of crystalline material before leaving the surface, they undergo dynamic scattering events. Since the electrons can originate from a range of depths, the effective signal on the detector will be the integral of signals over the depth range. Since the electron is backscattered at one of the lattice sites, this is equivalent to calculating the thickness integrated probability of inelastic scattering from all sites in the unit cell. [94,95]. The cross-section of inelastic scattering is proportional to the square of the atomic number and the Debye-Waller factor, which needs to be properly accounted for in the model [96,97]. We also introduce the term $\lambda(E, z)$, which is an energy and thickness dependent weight factor to account for the relative fractions of backscattered electrons with given energy and originating at a given depth. As will be discussed later, $\lambda(E, z)$ is calculated using Monte Carlo electron trajectory simulations. The thickness-integrated backscatter yield in a direction $\mathbf{k}$ is given by

$$\mathcal{P}(\mathbf{k}, E, z_0(E)) = \sum_n \sum_{i \in S_n} \frac{Z_n^2}{z_0(E)} \int_0^{z_0(E)} \lambda(E, z) |\Psi_\mathbf{k}(\mathbf{r}_i)|^2 \mathrm{d}z. \tag{3.48}$$

The first sum runs over the asymmetric unit, n in the unit cell and the second sum runs over all equivalent positions S_n for each element n. The wavefunction of the electron can be calculated by either the scattering matrix or the Bloch wave approach. For the Bloch wave formalism, the wavefunction is given by

$$\Psi(\mathbf{r}) = \sum_j \alpha^{(j)} \sum_{\mathbf{g}} C_{\mathbf{g}}^{(j)} e^{2\pi i (\mathbf{k}_0 + (\gamma^{(j)} + iq^{(j)})\mathbf{n} + \mathbf{g}) \cdot \mathbf{r}}. \tag{3.49}$$

After substituting equation 3.49 in 3.48 and some algebra, we end up with the following equations for the backscatter yield

$$
\begin{aligned}
\mathcal{P}(\mathbf{k}, E) &= \langle e | S \circ L | e \rangle \\
S_{\mathbf{gh}} &= \sum_n \sum_{i \in S_n} Z_n^2 e^{M_{\mathbf{h}-\mathbf{g}}^{(n)}} e^{2\pi i (\mathbf{h}-\mathbf{g}) \cdot \mathbf{r}} \\
L_{\mathbf{gh}} &= \sum_i \sum_j \alpha^{(j)*} C_{\mathbf{g}}^{(j)*} \mathcal{I}_{jk}(E) \alpha^{(k)} C_{\mathbf{h}}^{(k)}.
\end{aligned}
\tag{3.50}
$$

Here, $\circ$ denotes the Hadamard (element-wise) product of the two matrices and e is a column vector with all entries equal to 1. The notation is just a convenient way to represent summing all elements of the matrix $S \circ L$. The matrix $\mathcal{I}_{jk}$ is defined by the integral

$$\mathcal{I}_{jk}(E) = \frac{1}{z_0(E)} \int_0^{z_0(E)} \lambda(E, z) e^{-2\pi(\alpha_{jk} + i\beta_{jk})z} \mathrm{d}z, \tag{3.51}$$

where,

$$
\begin{aligned}
\alpha_{jk} &= q^{(j)} + q^{(k)} \\
\beta_{jk} &= \gamma^{(j)} - \gamma^{(k)},
\end{aligned}
\tag{3.52}
$$

where γ and q are the real and imaginary parts, respectively, of the Bloch wave eigenvalues. The matrix S can be regarded as a structure factor, while the matrix L contains the dynamical scattering information. The thermal motion of atoms is described by the term $M_{\mathbf{g}}^{(n)} = B_n |\mathbf{g}|^2 / 4$, where B_n is the Debye-Waller factor at room temperature for the element n. We can compute a similar expression using the scattering matrix formalism. In

that case, the wavefunction is written as

$$\Psi(\mathbf{r}) = \sum_{\mathbf{g}} \psi_{\mathbf{g}}(\mathbf{r}) e^{2\pi i(\mathbf{k}_0 + \mathbf{g}) \cdot \mathbf{r}}. \tag{3.53}$$

Here, $\mathbf{k}_0$ is the wave vector of the incident electron. It is implicitly assumed that the scattered plane waves travel in directions dictated by Bragg's law. As previously stated, the Fourier coefficients, $\psi_{\mathbf{g}}$ can be calculated by repeated multiplication of the scattering matrix with the initial state of the incoming beam. The equations for backscatter yield in the scattering matrix formalism can be written in the same form as in the Bloch wave formalism as

$$
\begin{aligned}
\mathcal{P}(\mathbf{k}, E) &= \langle e | S \circ L^S | e \rangle \\
S_{\mathbf{gh}} &= \sum_{n} \sum_{i \in S_n} Z_n^2 e^{M_{\mathbf{h-g}}^{(n)}} e^{2\pi i(\mathbf{h-g}) \cdot \mathbf{r}} \\
L_{\mathbf{gh}}^S &= \frac{1}{z_0(E)} \int_0^{z_0(E)} \lambda(E, z) \psi_{\mathbf{g}}^* \psi_{\mathbf{h}} dz
\end{aligned} \tag{3.54}
$$

The superscript S in matrix L^S refers to the scattering matrix approach. Note that the matrix S remains unchanged in the scattering matrix formalism. This completes our discussion of the dynamical diffraction theory for EBSD pattern simulation.

Stochastic Scattering The Monte Carlo based algorithm for stochastic electron scattering has already been discussed in chapter III. The incident beam current used for an EBSD experiment is of the order of 1 nA, which corresponds to 6.24×10^9 electrons per second. Thus, the Monte Carlo simulations typically considers a few billion electrons in order to obtain sufficient statistics. For EBSD, we are only interested in backscattered electrons. From these simulations, we can obtain the energy, depth and angular distributions of backscattered electrons. The simulations were performed for 4×10^9 electrons. Fig. 3.4(a)-(f) shows the angular distribution of backscattered electrons for different energy ranges as stereographic projections. The higher energy electrons are concentrated near the lower edge of the detector, showing near specular reflection, while the lower energy electrons are distributed more evenly over the whole detector. The cumulative angular distribution is shown
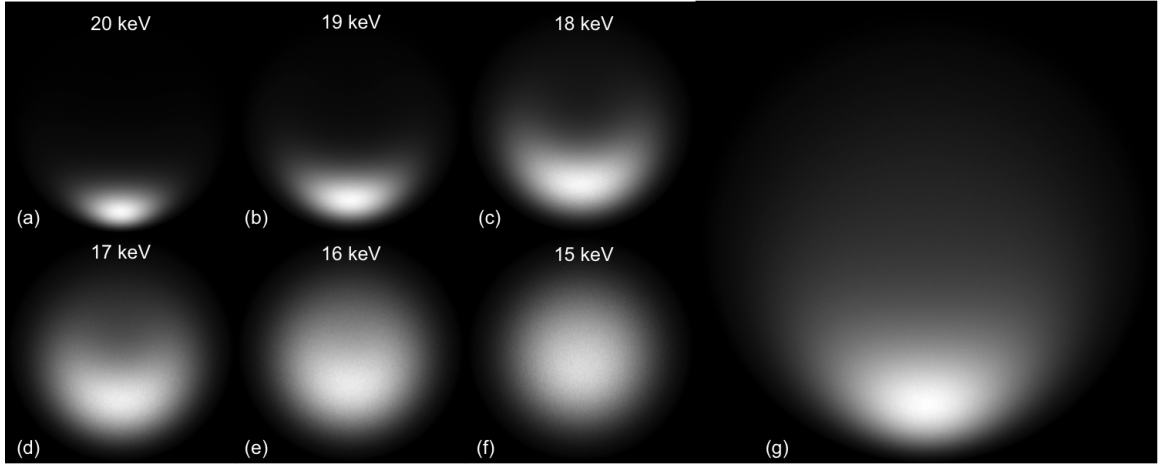
Figure 3.4: (a)-(f) Stereographic projection of backscattered electrons for different exit energy of electrons indicated in the figure. Higher energy electrons follow near specular reflection, while lower energy electrons have a more even angular distribution(g) cumulative angular distribution of all backscattered electrons; majority of electrons follow near specular reflection with the intensity peak near the edge of the stereographic circle. Simulations were performed for Nickel, tilted at $70°$ and incident beam energy of 25 keV.

in Fig. 3.4(g), which indicates that a higher fraction of backscattered electrons are low energy loss electrons. This is also reflected in Fig. 3.5(a), which shows the energy histogram for the fraction of backscattered electrons. The depth histograms for fractions of backscattered electrons for various energies are shown in Fig. 3.5(b), which shows that most of the backscattered electrons originate from the first 10 nm or so in the sample. Note that the histogram for the 20 keV electron is significantly lower than all the other curves. These curves also serve as input to extract the function $\lambda(z, E)$ for the dynamical simulation. The integration limit, $z_0(E)$ for the dynamical scattering is estimated from the Monte Carlo simulation as the 95% exit depth for different exit energy, i.e. the depth from with 95% of the electrons originate for a particular exit energy. This is shown in Fig. 3.5(c). The energy histogram for fraction of backscattered electrons for various exit depths is shown in Fig. 3.5(d). The histogram looks similar to the cumulative energy histogram (Fig. 3.5(a)), with most of the electrons originating from the first few nm.

Master EBSD Pattern

As discussed in section 3.4.1, the dynamical backscatter yield for each exit direction **k** is calculated using either the Bloch wave or the scattering matrix approach. To calculate a single EBSD pattern, the backscatter yield needs to be determined for a set of channeling
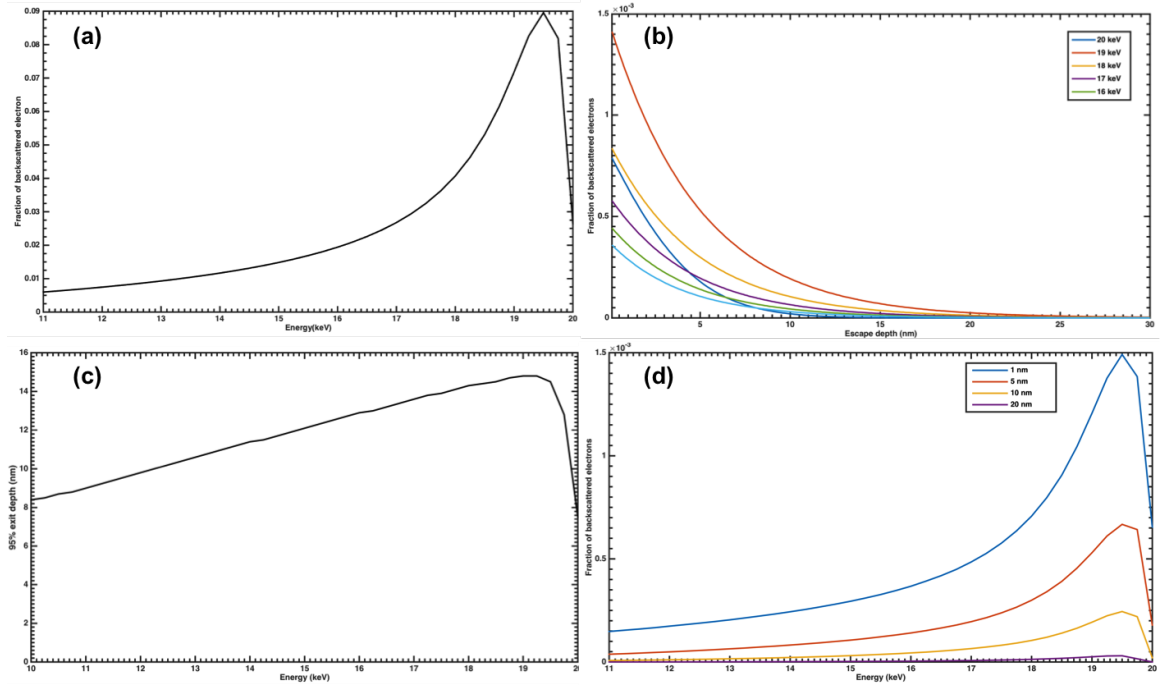
Figure 3.5: (a) Energy histogram for fraction of backscattered electrons (b) depth histogram for fraction of backscattered electrons for various exit energies (c) 95% exit distance for electrons with different exit energies and (d) energy histogram for fraction of backscattered electrons from originating at different depths.

directions, which depends on the crystal orientation. This is shown in Fig. 3.7. Since the dynamical scattering calculation is the computational bottleneck in our model, it is computationally more efficient to compute the dynamical contribution for a uniformly distributed set of **k**-vectors sampled from the unit sphere $\mathbb{S}_1^2$.

The uniform sampling is performed using the modified Lambert projection outlined in section 3.2.2. The resulting dynamical contributions are also saved in a square modified Lambert grid, with each pixel representing one direction on the unit sphere. Since Friedel's law is not necessarily valid for dynamical scattering, the calculation is performed for the asymmetric unit of the stereographic projection, taking the proper point group symmetry of the crystal in account (instead of the Laue group, which assumes inversion symmetry). This results in potentially different intensities for the Northern and Southern hemisphere. The resulting stereographic projection for the Northern and Southern hemisphere along with their Lambert projection for $\beta-$Mn (space group # 213; no inversion symmetry) is shown in Fig. 3.6. The acceleration voltage was set to 20 keV. The master pattern serves
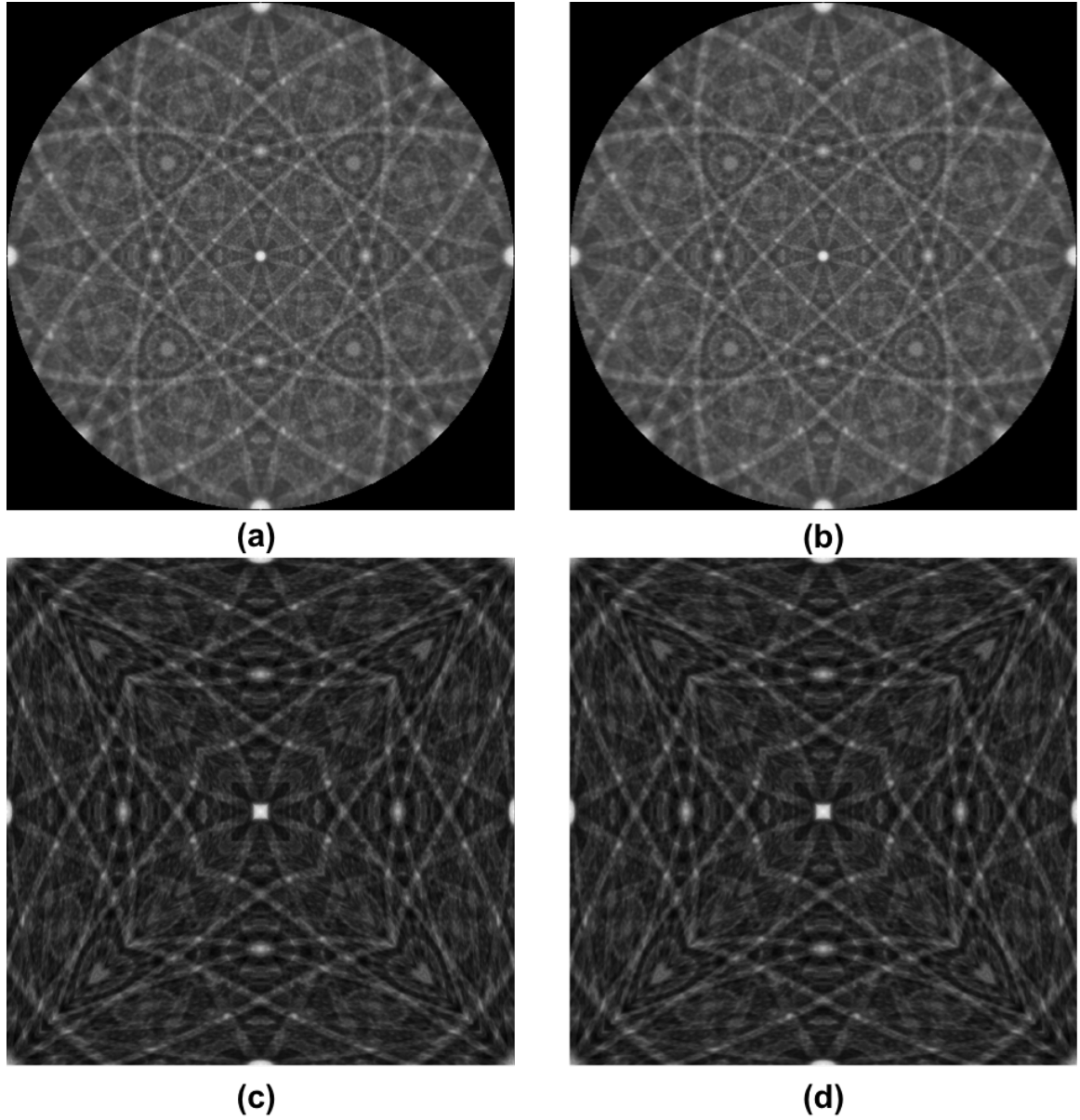
Figure 3.6: Stereographic projection of master pattern for $\beta-$Mn (a) Northern and (b) Southern hemisphere. Equivalent modified Lambert projections of (c) Northern and (d) Southern hemisphere. The acceleration voltage was set to 20 keV.

as a look-up table for dynamical backscatter intensity for individual pattern simulation.

Detector Model

The Monte Carlo and master pattern, once calculated for a given crystal and incident beam energy, are valid for all detector geometries. The geometry is only used in the final step to interpolate intensities from the Monte Carlo and master patterns. There are three distinct
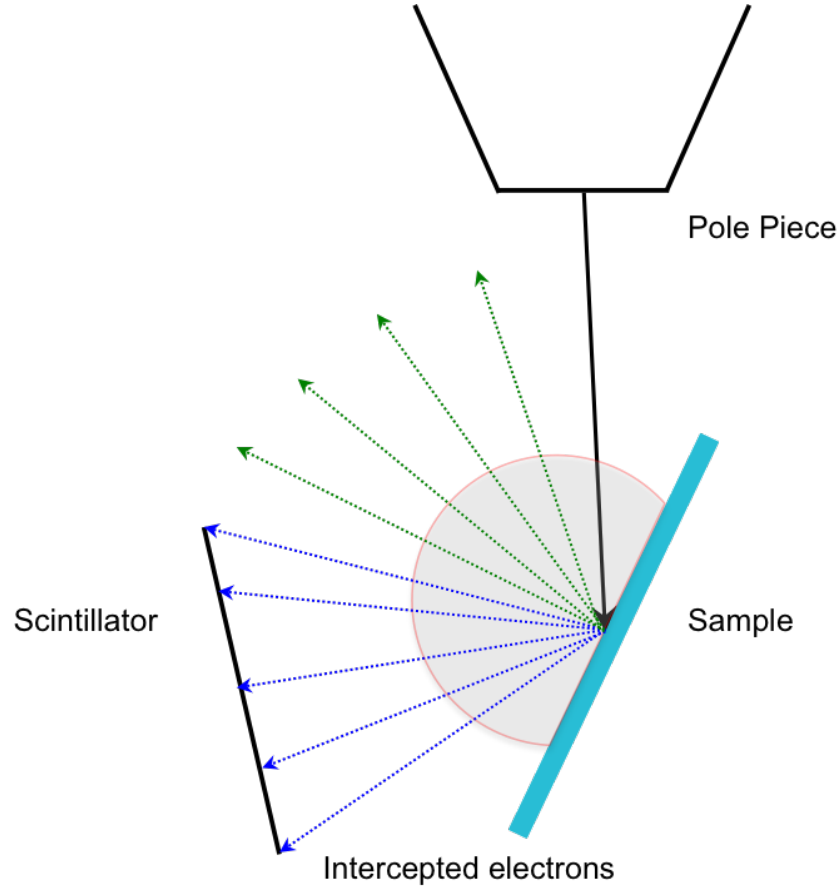
Figure 3.7: Electrons are backscattered in all possible direction. The EBSD signal is formed by a subset of these electrons, which are intercepted by the detector.

frames of reference for the EBSD geometry: the reference frame attached to the scintillator, the one attached to the sample and the crystal reference frame. The EBSD geometry is parametrized as follows:

- Illumination point to scintillator distance, L (in μm).

- Inclination angle of the scintillator with respect to the horizontal plane, θ_c.

- Inclination of the sample with respect to the horizontal plane, σ (typically set to 70°).

- Pattern center coordinates, $(x_{pc}, y_{pc}, 0)$ in the scintillator frame, which is the point which remains invariant when the scintillator is translated along its length.

- Out of plane tilt of sample, ω with respect to the rolling direction of the sample. This is typically close to 0 for a properly mounted sample.

- Size of each pixel on the scintillator, δ (in μm) and number of pixels in x and y dimension.

An arbitrary point $(x_s, y_s, 0)$ in the scintillator frame is converted to the sample frame using the following equations

$$
\begin{aligned}
\mathbf{r}_g^x &= [(y_{pc} - y_s)\cos\alpha + (L\cos\omega - (x_{pc} - x_s)\sin\omega)\sin\alpha] \\
\mathbf{r}_g^y &= [(x_{pc} - x_s)\cos\omega + L\sin\omega] \\
\mathbf{r}_g^z &= [-(y_{pc} - y_s)\sin\alpha + (L\cos\omega + (x_{pc} - x_s)\sin\omega)\cos\alpha].
\end{aligned}
\tag{3.55}
$$

Here, $\alpha = \pi/2 - \sigma + \theta_c$. The length of the vector is given by

$$
|\mathbf{r}_g| = \sqrt{L^2 + (x_{pc} - x_s)^2 + (y_{pc} - y_s)^2}.
\tag{3.56}
$$

The unit vector for an arbitrary point $(x_s, y_s, 0)$ in the sample frame is given by

$$
\hat{\mathbf{r}}_g = \frac{\mathbf{r}_g}{|\mathbf{r}_g|}.
\tag{3.57}
$$

The unit vector $\hat{\mathbf{r}}_g$ can be converted to the crystal frame by any one of several orientation transformation rules, such as quaternion multiplication, Rodrigues' rotation formula, orientation matrix, etc. These directions in the crystal frame correspond to the different channeling directions, which need to be interpolated from the master pattern and the Monte Carlo simulations. Special care must be taken when interpolating the background intensity from the Monte Carlo simulation, since the "effective pixel size" changes as a function of position. This is illustrated in Fig. 3.8. We seek a correction term such that the area subtended on a flat detector by a cone of opening angle β away from the pattern center location has an equal area as the area subtended at the pattern center. If $\hat{\mathbf{r}}_g^{pc}$ is the unit vector for the pattern center in the sample frame, then for any unit vector, $\hat{\mathbf{r}}_g$ the correction factor is given by

$$
\gamma(\hat{\mathbf{n}}) = \frac{[\cos^2\beta + (\hat{\mathbf{r}}_g^{pc} \cdot \hat{\mathbf{r}}_g)^2 - 1]^{3/2}}{\cos^3\beta}
\tag{3.58}
$$

The details of this calculation can be found in Appendix B.
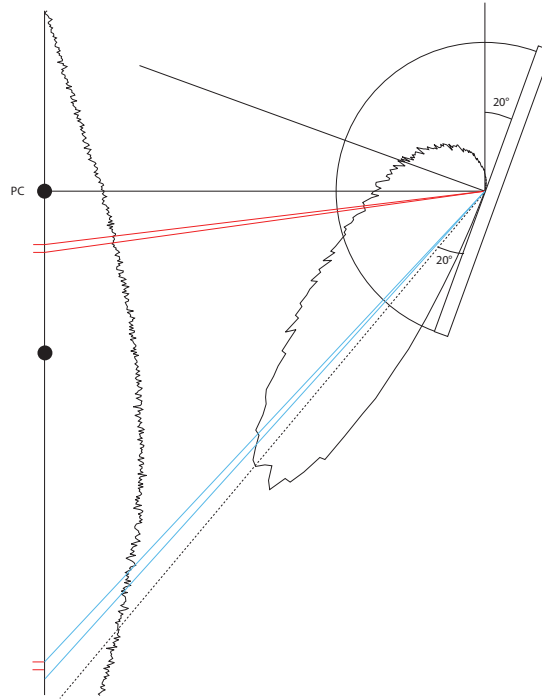
Figure 3.8: Schematic to illustrate necessity of a correction factor for background interpolation. The effective pixel size for interpolation is same at the unit hemisphere but larger for vectors away from the pattern center. The curve on the detector is the intensity profile after interpolation from Monte Carlo simulations.The other curve at the illumination point is a polar plot of intensity showing a maxima close to near specular reflection.
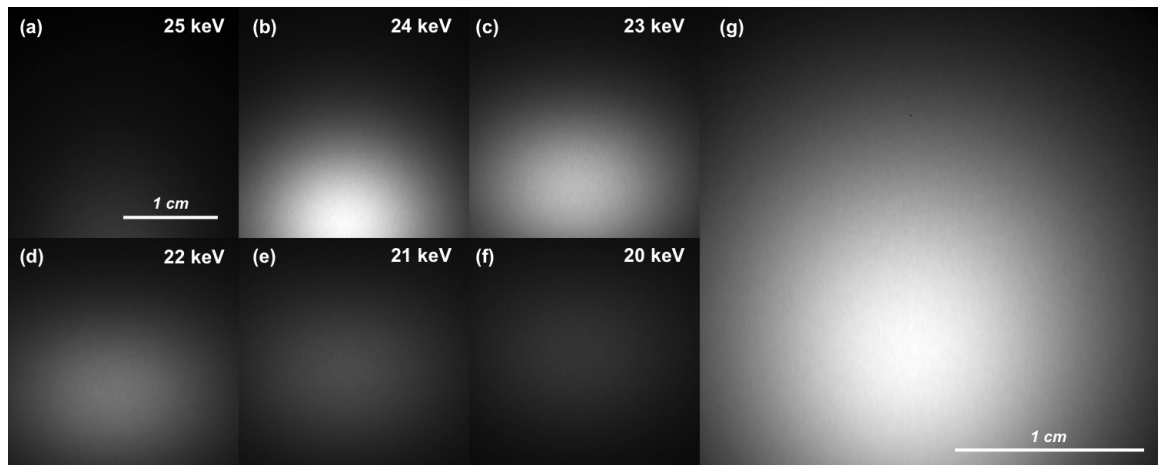
Figure 3.9: Simulated background interpolated from Monte Carlo simulation with the correction factor for (a) 25 keV (b) 24 keV (c) 23 keV (d) 22 keV (e) 21 keV (f) 20 keV and (g) overall intensity. The detector parameters for interpolation are stated in the text.

Pattern Interpolation

The final step in simulating realistic EBSD patterns consists of interpolating from the master pattern and Monte Carlo simulation for a given microscope geometry. Bilinear
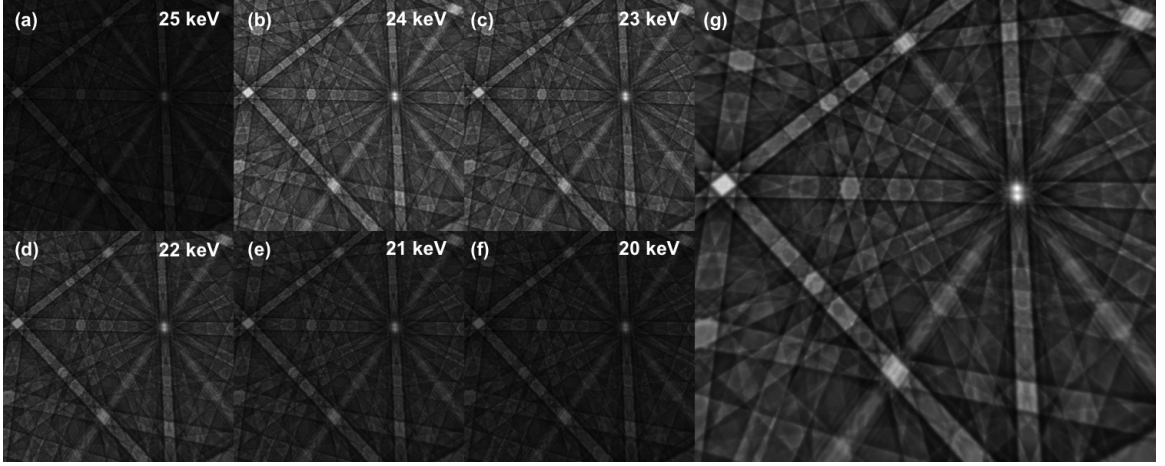
Figure 3.10: Simulated dynamical intensity interpolated from Monte Carlo simulation with the correction factor for (a) 25 keV (b) 24 keV (c) 23 keV (d) 22 keV (e) 21 keV (f) 20 keV.The overall signal is shown in (g). The detector parameters for interpolation are stated in the text.

interpolation is a convenient and fast interpolation scheme, since the results are saved on an equal-area square Lambert grid. Let $\mathcal{M}(\kappa, X, Y)$ represent the energy-dependent master pattern, where the first index labels the energy bins and the (X, Y) indicates the position on the master pattern. The position dependent energy histogram is represented as $\epsilon(\kappa, x_s, y_s)$, where the first index again labels the energy bins and (x_s, y_s) are arbitrary points on the scintillator. The number of backscattered electrons at the position (x_s, y_s) can be expressed by the energy weighted sum over all n_E energy bins:

$$I_{bse}(x_s, y_s) = \sum_{\kappa=1}^{n_E} \epsilon(\kappa, x_s, y_s) \mathcal{M}(\kappa, X(x_s, y_s, \tilde{q}), Y(x_s, y_s, \tilde{q})). \qquad (3.59)$$

where $\tilde{q}$ is a quaternion representing the crystal orientation and the coordinates (X, Y) are calculated by applying equations 3.55 and 3.57 together with the modified Lambert transformation given by equation 3.8 and 3.9. The interpolation from the Monte Carlo simulation for a Si sample and different energy bins are shown in Fig. 3.9(a)-(f) and the overall background is shown in Fig. 3.9(g). The interpolation from the master pattern for the respective energy bins is shown in Fig. 3.10(a)-(f), with the overall dynamical signal shown in Fig. 3.10(g).

The final energy weighted EBSD pattern is shown in Fig. 3.11(a), with the corresponding experimental pattern shown in 3.11(b). The microscope parameters and Euler angles are as
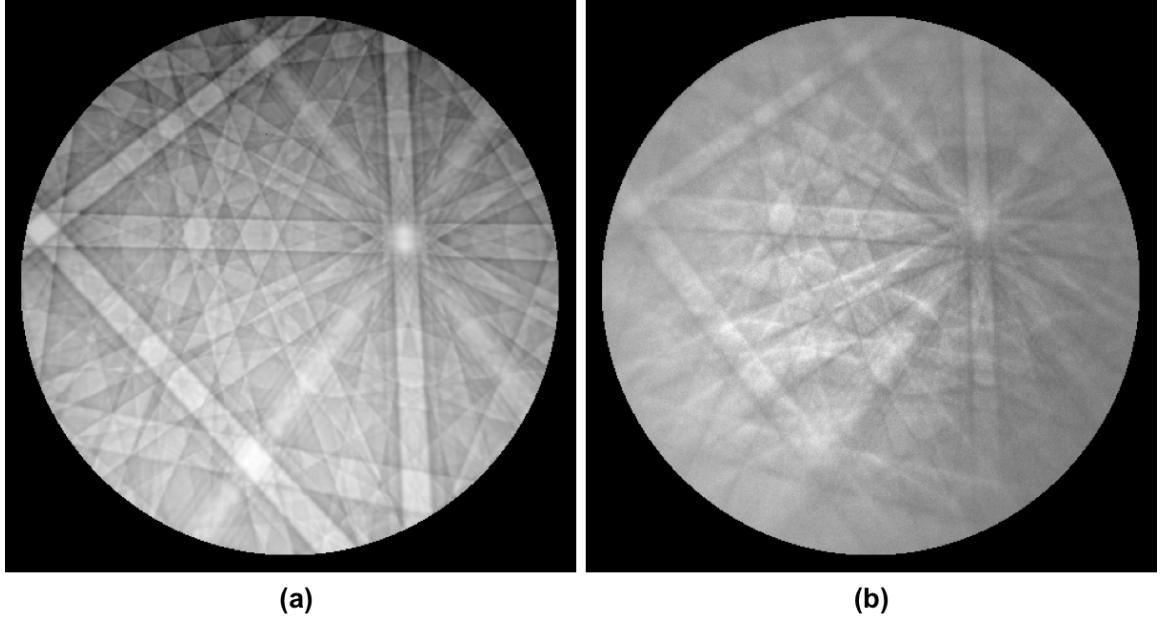
Figure 3.11: (a) Simulated EBSD pattern as sum of weighted patterns for individual energy bins with gamma correction and (b) Experimental EBSD pattern. The detector parameters and Euler angles are stated in the text.

follows: $L = 18100$ μm, $(x_{pc}, y_{pc}) \equiv (-20.0, 130.0)$, $\theta_c = 7°$, $\delta = 50\mu$m, $n^x_{scin} = n^y_{scin} = 488$, $(\phi_1, \Phi, \phi_2) \equiv (340.3°, 109.7°, 46.5°)$. The pattern center coordinates are in units of pixels, with the center pixel having the coordinates $(0.0, 0.0)$ and n^x_{scin}, n^y_{scin} represent the number of pixels on the scintillator in the x and y direction respectively.

3.4.2 Electron Channeling Patterns

For the ECP modality, we classify the backscattered electron as BSE1 or the BSE2 type. BSE1s are the electrons which have undergone backscattering as the first inelastic scattering event, while BSE2 are the electrons which have undergone multiple scattering events. Since the BSE1s undergo little or no energy loss, the energy of these electrons is almost the same as that of the incident beam. This has important consequences in depth distribution of the electrons and defect imaging in the SEM. The BSE1s carry the channeling signal and therefore the diffraction contrast, while the BSE2s make up the background signal. Monte Carlo simulations reveal that the typical ratio of BSE1s to BSE2 is of the order of $10^{-3} - 10^{-4}$ [98]. Thus, the desired channeling signal is a small fluctuation on top of a huge background. This situation is shown in Fig. 3.12(a). There are many strategies
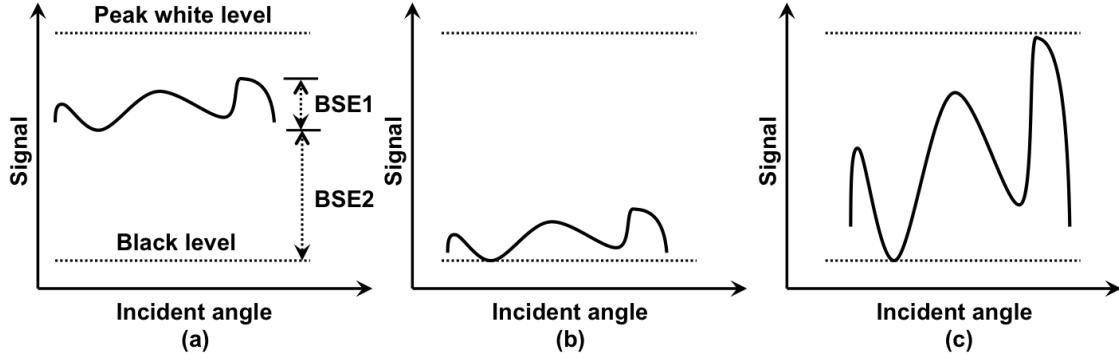
Figure 3.12: Schematic for the signal processing in the ECP modality.(a) The initial signal with both an BSE1 and BSE2 component (b) subtracting off the BSE2 component and (c) amplification of signal to fill all gray levels.

to enhance the contrast, such as signal differentiation and differential signal amplification. Signal differentiation looks at the time derivative of the original signal. This technique effectively acts as a high pass filter and filters out the low frequency signals in between the bands and amplifies the signal at the band edges. However, this technique results in a loss of fine signal from between the bands. The more popular approach for contrast enhancement is differential signal amplification. This technique first subtracts off the BSE2 component from the signal and amplifies the resulting signal to fill all gray levels [46]. This process is schematically shown in Fig. 3.12(b)-(c).

Scattering Theory

Dynamical Scattering The dynamical theory for the ECP modality is very similar to EBSD, with a few subtle differences. For the EBSD modality the electron undergoes scattering and finally channels while exiting the sample. Therefore, the final signal is composed of electrons in the complete energy range. On the other hand, for the ECP modality the electron channels on its way in and immediately is backscattered. Therefore, the final signal is composed of only electrons which have lost little or no energy at all. The two modalities are also related through the *reciprocity theorem* [86]. In this sense, ECP can be interpreted as an energy-filtered EBSD pattern. The expressions for the dynamical contribution to the intensity are very similar to EBSD, except for the energy dependence of the weight-factors

and exit depth. For the Bloch wave formalism, the expressions are

$$
\begin{aligned}
\mathcal{P}(\mathbf{k}) &= \langle e | S \circ L | e \rangle \\
S_{\mathbf{gh}} &= \sum_{n} \sum_{i \in S_n} Z_n^2 \mathrm{e}^{M_{\mathbf{h-g}}^{(n)}} \mathrm{e}^{2\pi \mathrm{i}(\mathbf{h-g}) \cdot \mathbf{r}} \\
L_{\mathbf{gh}} &= \sum_{i} \sum_{j} \alpha^{(j)*} C_{\mathbf{g}}^{(j)*} \mathcal{I}_{jk} \alpha^{(k)} C_{\mathbf{h}}^{(k)}.
\end{aligned}
\tag{3.60}
$$

The symbols have their usual meaning. Note that the S matrix is unaltered, whereas the $\mathcal{I}$ matrix and consequently, the L matrix have no explicit energy dependence. The $\mathcal{I}_{jk}$ matrix is defined by

$$
\mathcal{I}_{jk} = \frac{1}{z_0} \int_0^{z_0} \lambda(z) \mathrm{e}^{-2\pi(\alpha_{jk} + \mathrm{i}\beta_{jk})z} \mathrm{d}z.
\tag{3.61}
$$

Again, the symbols have their usual meaning. For the scattering matrix approach, the equations are given by

$$
\begin{aligned}
\mathcal{P}(\mathbf{k}) &= \langle e | S \circ L^S | e \rangle \\
S_{\mathbf{gh}} &= \sum_{n} \sum_{i \in S_n} Z_n^2 \mathrm{e}^{M_{\mathbf{h-g}}^{(n)}} \mathrm{e}^{2\pi \mathrm{i}(\mathbf{h-g}) \cdot \mathbf{r}} \\
L_{\mathbf{gh}}^S &= \frac{1}{z_0} \int_0^{z_0} \lambda(z) \psi_{\mathbf{g}}^* \psi_{\mathbf{h}} \mathrm{d}z
\end{aligned}
\tag{3.62}
$$

The depth histogram, $\lambda(z)$, is again given by Monte Carlo trajectory simulations.

Stochastic Scattering The stochastic scattering for the ECP modality follows the same algorithm as for the EBSD modality, except that only the BSE1 electrons are counted. Since the backscatter yield of the BSE1 electrons is much lower by a factor of $10^{-3} - 10^{-4}$, the simulations are performed for a larger number of electrons (typically 10^{10}) to obtain good statistics. Such computations are only possible if the process is massively parallelized. Since no interaction is assumed between two different electrons, graphical processing units (GPUs) are an ideal candidate for these computations. The Monte Carlo simulations are performed for BSE1 electrons for different incident angles, typically ranging from $0° - 20°$ in steps of $2°$. This variation in BSE1 yield as a function of incident beam direction is used to simulate the effect of sample tilt. In this study, we are only considering a single tilt stage,
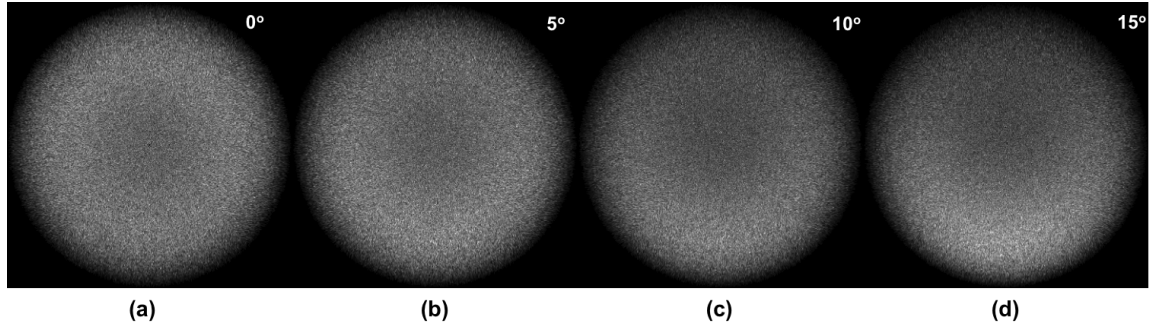
Figure 3.13: Stereographic projection of BSE1 electrons for different incidence angles (indicated on the figure). The acceleration voltage was set 30 kV.

with the tilt angle denoted by ω. Fig. 3.13(a)-(d) shows the stereographic projection of the backscattered electron distribution for different incident beam angles with respect to the optical axis.

Master ECP Pattern

Similar to EBSD, the dynamical backscatter yield is calculated as a function of the set of possible channeling directions, sampled uniformly from the unit sphere. This serves as a look-up table for fast interpolation of individual channeling patterns. The stereographic and modified Lambert projection for the Northern and Southern hemisphere for Si and beam acceleration voltage of 30 kV is shown in Fig. 3.14(a)-(d). Since Si is centrosymmetric, the intensities in the Northern and Southern hemispheres are identical.

Detector Model and Sample Geometry

Similar to the EBSD modality, the ECP modality requires the computation of the stochastic and dynamic contributions for all exit directions. The geometry of the detector is only used in the final step for pattern interpolation. For the ECP modality, the detector is an annular integrating detector. The detector is parametrized using two parameters: inner radius, R_{in} and outer radius, R_{out} of the annular detector. Not all the backscattered electrons are captured by the annular detector. As schematic of this is shown in Fig. 3.15. It can be seen from Fig. 3.13(a) that for normal incidence, more BSE1 electrons escape at higher angle than lower angle. Depending on R_{in} and R_{out}, the working distance should be set such that the detector captures most of these BSE1 electrons, which predominantly exit at $60° - 70°$
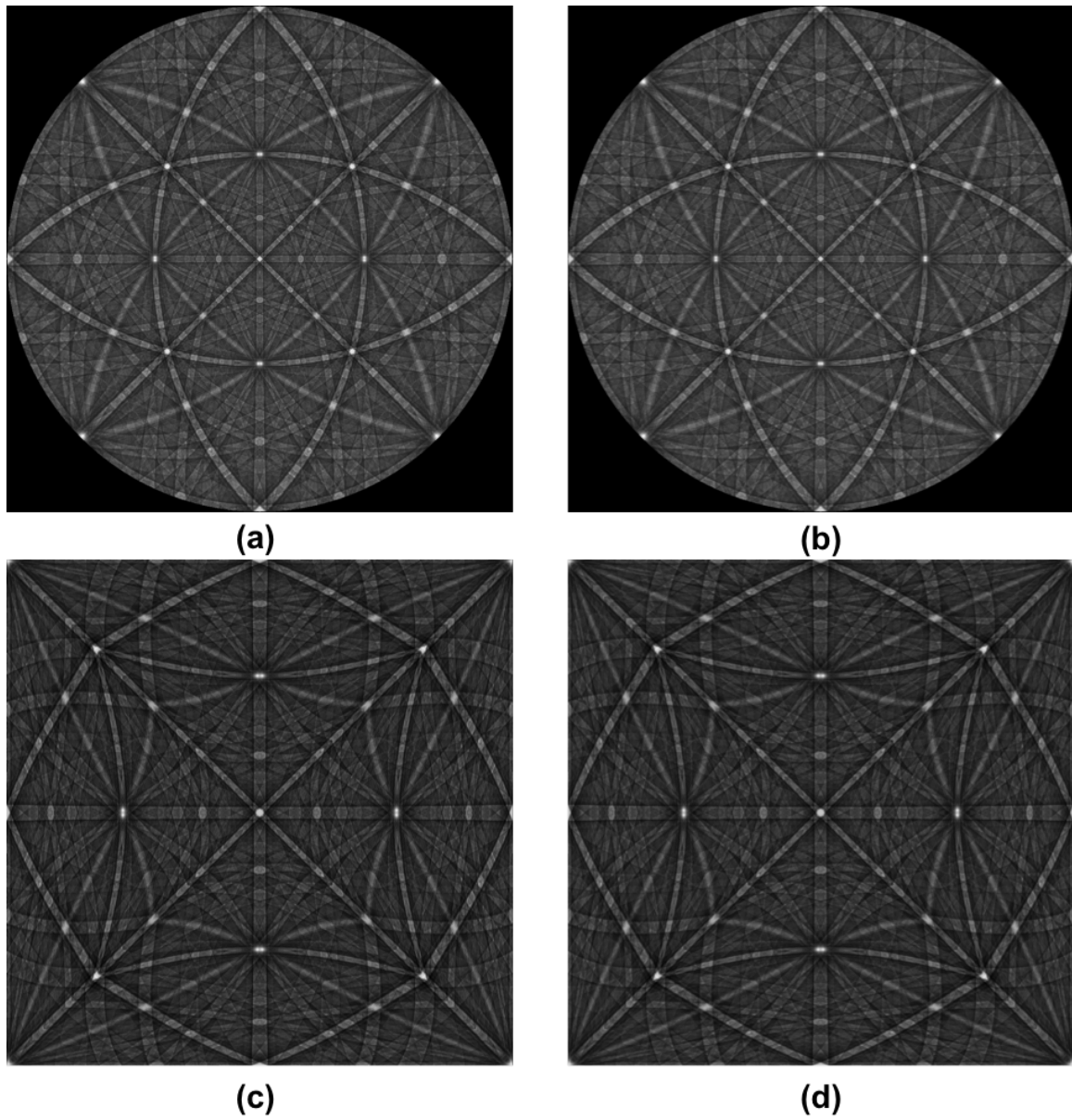
Figure 3.14: Stereographic projection of BSE1 yield for Si (a) Northern and (b) Southern hemisphere along with the respective modified Lambert projections of (c) Northern and (d) Souther hemisphere. The acceleration voltage was set 30 kV.

from the normal. The working distance, together with the detector dimensions also limits the angular range of the incident directions. For modern microscopes, with beam rocking apparatus, the typical limit on the half-angle of the incident cone is about 15°.
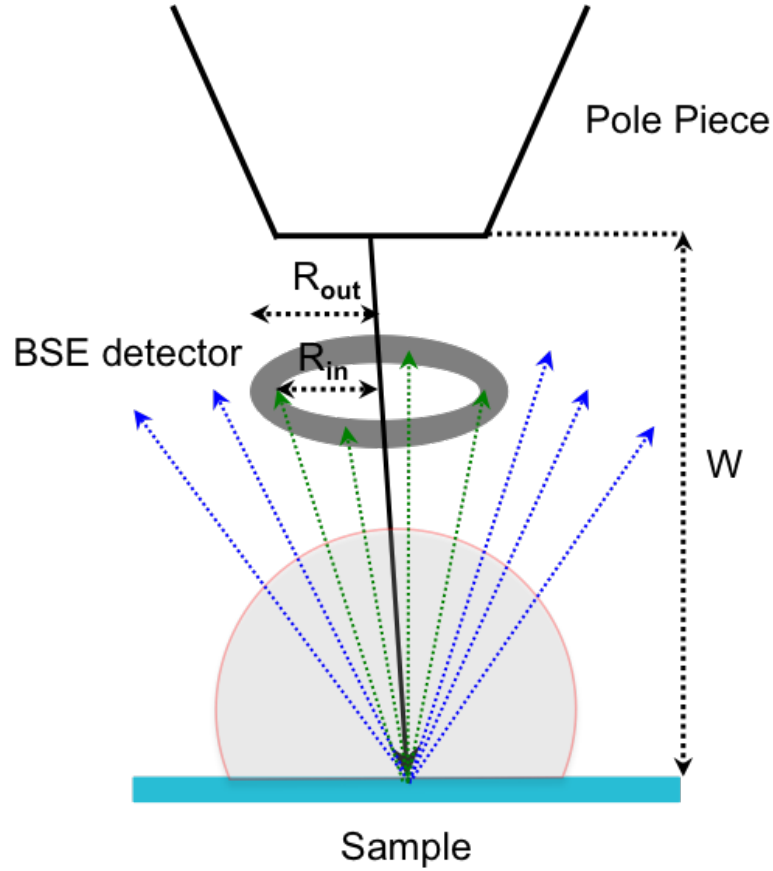
Figure 3.15: Electrons backscatter in all possible directions. Only a fraction of it is intercepted by the annular detector, depending on the inner and outer radius of the detector together with the working distance.

Detector Model and Aberrations

A channeling pattern is recorded by measuring the backscattered signal as a function of the incident beam direction. Monte Carlo simulations for BSE1 electrons reveal that the majority of BSE1s are scattered at a large angle with respect to the incident beam direction, typically in the range 50°-70°. Fig. 3.16(a) shows the stereographic projection of the BSE1 exit direction distribution for 20 keV electrons scattered from a Si sample. A polar plot of the BSE1 intensity as a function of angle with respect to the sample normal is shown in Fig. 3.16(b). The maximum intensity is at an exit angle of 58.1°. Since it is desirable to capture a large portion of the backscattered electrons to enhance the already weak BSE1 cumulative signal, an annular integrating backscatter detector is used, as shown in the schematic of Fig. 3.17(a). The inner and outer radii of the detector and the sample to
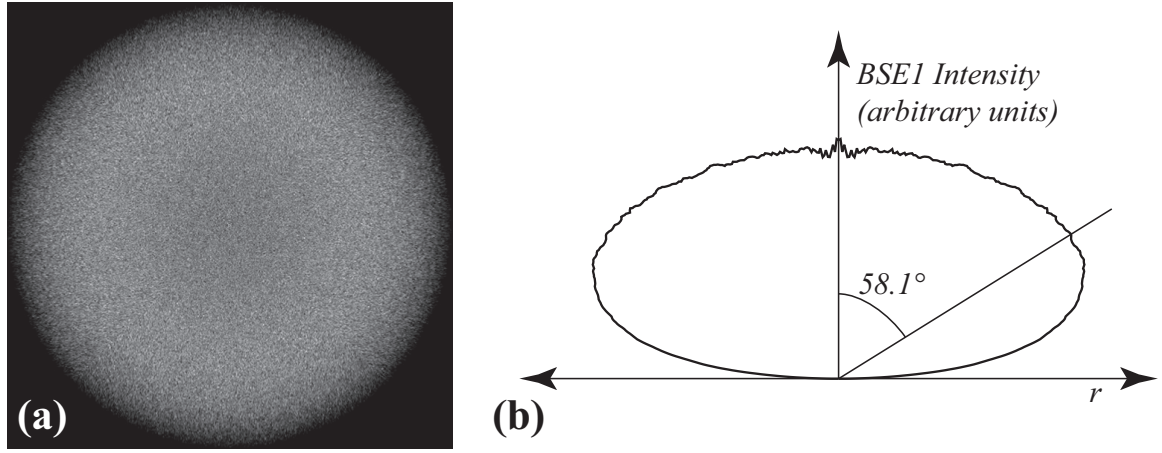
Figure 3.16: Monte Carlo simulation for 20 keV beam acceleration voltage for Si (a) stereographic projection of BSE1 electrons and (b) polar plot of backscatter yield as a function of angle from sample normal with the maximum at 58.1°.

detector distance, ξ are adjusted such that the detector captures a significant fraction of the total backscattered electron flux. For defect imaging, on the other hand, the sample is usually tilted to be close to a Bragg orientation. As a result, the background intensity will no longer have rotational symmetry around the incident beam direction. This asymmetry can be taken into account when the dynamical backscatter intensities are merged with the BSE1 results from stochastic Monte Carlo simulations.

The Monte Carlo simulations are performed for a range of incident beam angles, typically from $0° - 20°$ in steps of $1°$, resulting in the BSE1 backscatter yield as a function of exit direction and incidence angle, $\mathbf{Y}(\theta, \hat{\mathbf{n}})$. The inner and outer radius of the annular detector, together with the working distance, are used to calculate the solid angle range over which the Monte Carlo simulations need to be integrated. The detector is discretized with a polar and azimuthal angular step size of $1°$, producing a set of exit directions $\{\mathbf{e}_i\}$. For every incidence angle, θ_j from $0° - 20°$, the effective weight factor is then calculated by summing the backscatter yield over the calculated solid angle range; mathematically, we have:

$$w(\theta; R_{in}, R_{out}, \xi) = \sum_{\{\mathbf{e}_i\}} \mathbf{Y}(\theta, \hat{\mathbf{n}}). \tag{3.63}$$

For a realistic detector geometry with inner radius, $R_{in} = 5.0$ mm, outer radius, $R_{out} = 13.0$ mm and a working distance of WD $= 5.0$ mm, the fraction of electrons captured by the
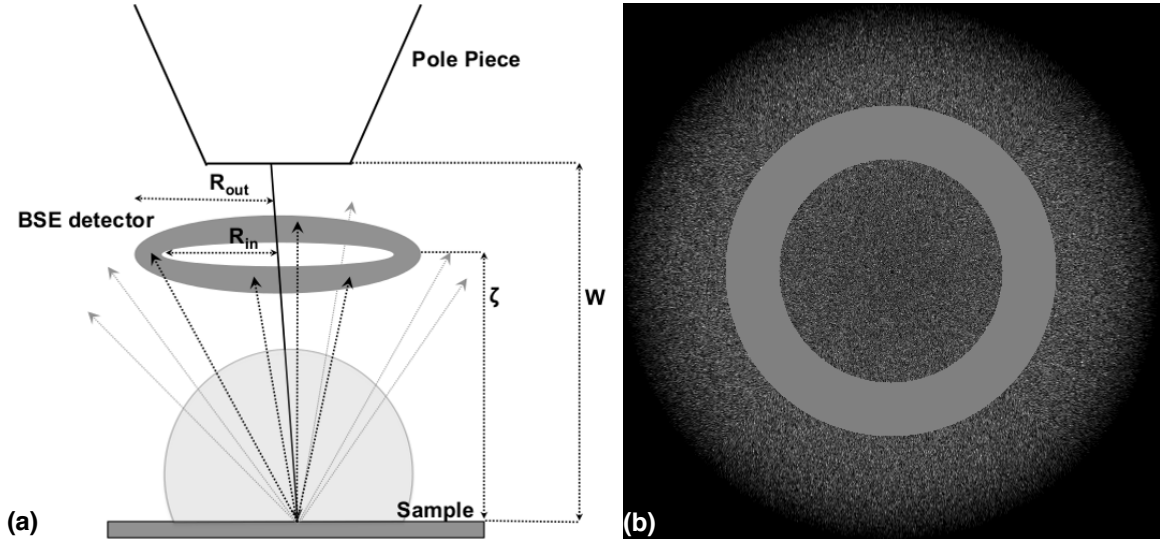
Figure 3.17: (a) Schematic of the ECP setup. Only a small fraction (black dashed) of the BSE1 electrons get captured by the annular detector and (b) stereographic projection of BSE1 exit direction for 20 keV acceleration voltage on Si sample superimposed with the stereographic projection of all exit directions for which the electron is captured by the detector (detector geometry in text).

detector is shown in Fig. 3.17(b). The weight factor for an arbitrary incidence angle is calculated by linear interpolation using weight factors of the known angles. For a grain with orientation described by a unit quaternion, $\tilde{q}$, each pixel (i, j) in the channeling pattern corresponds to an incident wave vector $\mathbf{k}_{ij}$ in the microscope reference frame; the intensity in the corresponding direction is interpolated from the Monte Carlo and master patterns and is given by the expression

$$I_{\mathrm{BSE}} = w(\theta; R_{in}, R_{out}, \xi)\mathcal{M}(\mathbf{k}_{ij}; \tilde{q}), \tag{3.64}$$

where θ is the angle between the wave vector $\mathbf{k}_{ij}$ and the sample normal and $\mathcal{M}(\mathbf{k}_{ij})$ is extracted from the master pattern using bi-linear interpolation.

Aberrations in the channeling patterns arise from the fact that the incident electron beam is scanned at a relatively large angle (10–15°) with respect to the optical axis. The primary (Seidel) aberrations of the objective lens (spherical aberration, coma, astigmatism, field curvature, and distortion) combine with the aberrations of the deflection system to introduce a significant amount of distortion in the high angle portion of the ECPs. We model the distortion in the following way: if P_i represents a point in the image plane corresponding

to a point P_0 in the object plane, then we assume that the location of P_i is given by $u_i + \Delta u_i$, where $\Delta u_i = (D + id)|u_0|^2 u_0$; u_0 is a complex number representing the location of point P_0, and D and d are the real and imaginary parts of the distortion coefficient. Depending on the sign of D, the distortion is either referred to as a barrel distortion ($D > 0$) or a pin-cushion distortion ($D < 0$). Note that the displacement field only depends on the position in the object plane, which makes the computation of the distortion field relatively straightforward. More details about this and various other lens aberrations can be found in [99], [100] and [101]. The Poisson noise is also accounted for in pattern simulations, since channeling patterns have relatively small currents and short exposure times. Fig. 3.18(a) shows an experimental pattern from a Si sample and acceleration voltage set to 30 kV. Fig. 3.18(b)-(d) shows the corresponding simulated patterns with no noise and distortion, with only distortion and with both noise and distortion respectively. The parameters and Euler angles for the simulation are as follows: $W = 4$ mm, $R_{in} = 3$ mm, $R_{out} = 7$ mm, $\theta_c = 14.36°$, $\omega = 0.0°$, $D = 7.7 \times 10^{-7} - i5.6 \times 10^{-7}$ and $(\phi_1, \Phi, \phi_2) \equiv (302.98°, 37.91°, 63.27°)$. Note that the adaptive histogram equalization algorithm (details in chapter IV) was applied to all patterns for contrast enhancement.

3.4.3 Precession Electron Diffraction

Scattering Theory

Dynamical Theory For diffraction patterns in transmission mode, we are interested in the wavefunction at the exit plane. The intensity of a particular diffracted beam is proportional to the square of its coefficient in the plane wave expansion, i.e.,

$$I_{\mathbf{g}} \propto |\psi_{\mathbf{g}}|^2. \tag{3.65}$$

For the Bloch wave approach, the Fourier coefficients can be calculated by summing over the Bloch waves. As stated previously in equation 3.49, the wavefunction is given by

$$\Psi(\mathbf{r}) = \sum_j \alpha^{(j)} \sum_{\mathbf{g}} C_{\mathbf{g}}^{(j)} e^{2\pi i (\mathbf{k}_0 + (\gamma^{(j)} + iq^{(j)})\mathbf{n} + \mathbf{g}) \cdot \mathbf{r}}. \tag{3.66}$$
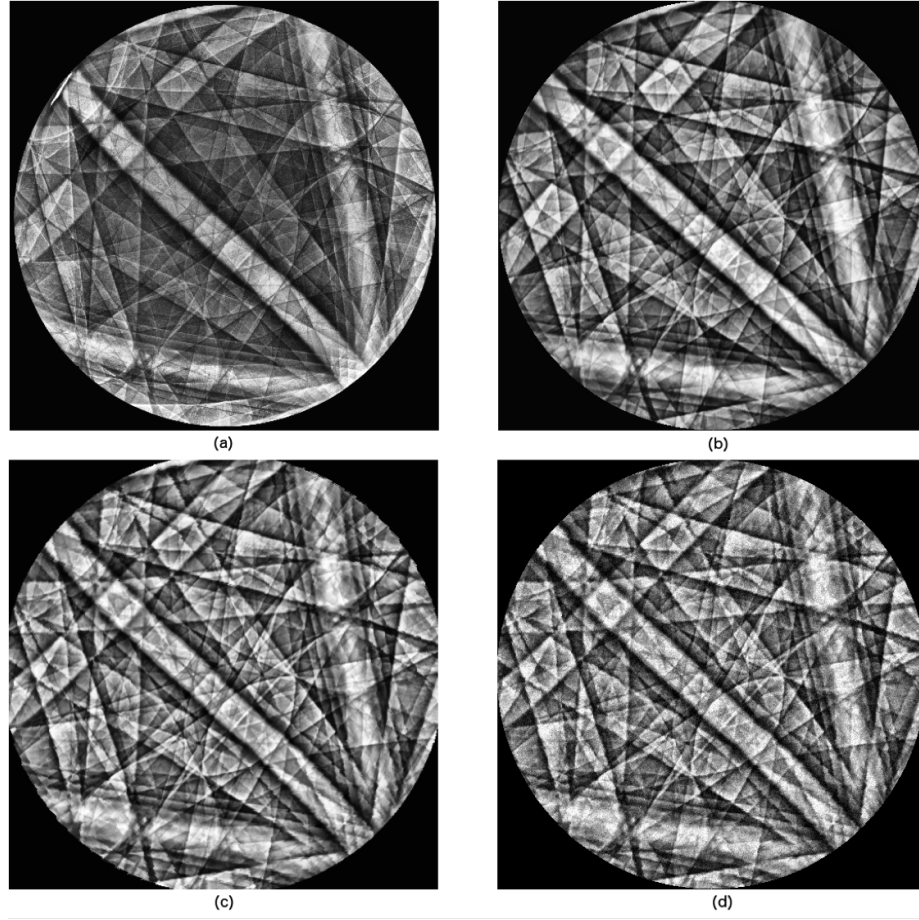
Figure 3.18: (a) Experimental Si pattern. Corresponding simulated patterns (a) with no noise or distortion (c) only distortion and (d) both noise and distortion applied. Adaptive histogram equalization was used for contrast enhancement. The parameters and Euler angles are mentioned in the text.

Since this equation is a linear superposition of different Bloch waves, represented by (j), over all reciprocal lattice vectors, represented by $\mathbf{g}$, the order of summations can be interchanged. After some rearrangement, the expression for the wavefunction can be written as

$$
\begin{aligned}
\Psi(\mathbf{r}) &= \sum_{\mathbf{g}} \left[\sum_{j} \alpha^{(j)} C_{\mathbf{g}}^{(j)} e^{2\pi i (\gamma^{(j)} + i q^{(j)}) z} \right] e^{2\pi i (\mathbf{k}_0 + \mathbf{g}) \cdot \mathbf{r}}; \\
&= \sum_{\mathbf{g}} \psi_{\mathbf{g}}(z) e^{2\pi i (\mathbf{k}_0 + \mathbf{g}) \cdot \mathbf{r}}.
\end{aligned}
\tag{3.67}
$$

The intensity of a beam diffracted in the direction $\mathbf{g}$ is given by

$$
I_{\mathbf{g}} = \sum_{i} \sum_{j} \alpha^{(i)*} \alpha^{(j)} C_{\mathbf{g}}^{(i)*} C_{\mathbf{g}}^{(j)} e^{2\pi i \left([\gamma^{(j)} - \gamma^{(i)}] + i [q^{(j)} - q^{(i)}] \right) z}
\tag{3.68}
$$

For the scattering matrix approach, the Fourier components are directly calculated by propagating the incident wave through the crystal thickness. For the crystal subdivided into n different layers, with each layer of thickness given by ϵ, the Fourier component of the outgoing wave vector is given by

$$\psi_{\mathbf{g}} = S_{\mathbf{g}} e^{i\theta_{\mathbf{g}}} e^{-\pi n\epsilon/\xi_0'}, \tag{3.69}$$

where the terms $S_{\mathbf{g}}$ are components of the column vector, $\mathbf{S}(z)$ given by

$$
\begin{aligned}
\mathbf{S}(z) &= [e^{i\mathcal{A}\epsilon}]^n S(0); \\
&= [\mathcal{S}(\epsilon)]^n \mathbf{S}(0). \tag{3.70}
\end{aligned}
$$

Here, $\mathcal{A}$ is the structure matrix and $\mathcal{S}(\epsilon)$ is the scattering matrix, $\theta_{\mathbf{g}}$ is the phase factor for the Fourier coefficient corresponding to $\mathbf{g}$ in the real part of the electrostatic lattice potential and ξ_0' is the normal absorption length and is common to all beams. Thus, the intensity of beam corresponding to the reciprocal lattice vector $\mathbf{g}$ is given by

$$I_g = |S_{\mathbf{g}}|^2 e^{-2\pi n\epsilon/\xi_0'}. \tag{3.71}$$

Note that the intensity of the beam is an exponentially decaying function of the thickness of the crystal, with the characteristic length scale given by ξ_0'. The overall intensity for a precessing electron beam will be the sum of intensities for each incident beam direction.

Kinematic approximation   As mentioned in section 2.3, the precession pattern is closer to kinematic diffraction patterns than dynamic patterns. Therefore, we can simplify the analysis performed above by using the two-beam approximation for which the intensities are analytically known. For a kinematic two-beam case with only the direct beam and one diffracted beam, the intensity of the scattered beam, I_S is given by the expression

$$I_S = \pi^2 z_\xi^2 \frac{\sin^2(\pi w z_\xi)}{(\pi w z_\xi)^2} = \pi^2 z_\xi^2 \mathrm{sinc}^2(\pi w z_\xi), \tag{3.72}$$
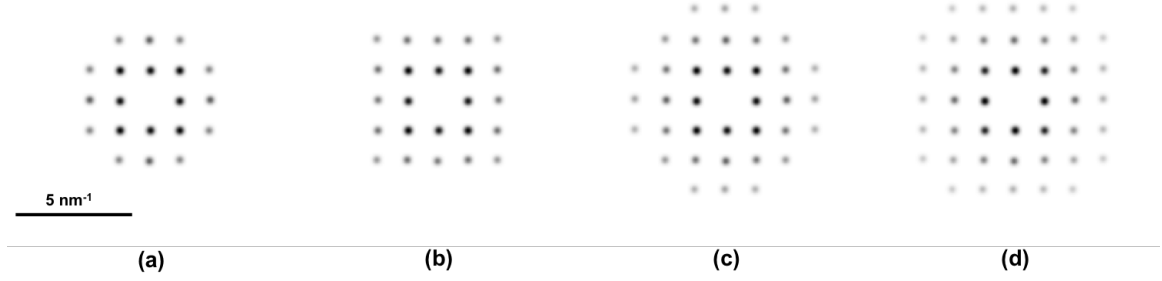
Figure 3.19: Simulated precession electron diffraction patterns (reverse contrast) for (001) zone axis Cu for different precession angles (a) $0.25°$ (b) $0.50°$ (c) $0.75°$ and (d) $1.0°$. The microscope acceleration voltage was set to 200 keV.

where the dimensionless parameter, w is given by

$$w = s_{\mathbf{g}} \xi_{\mathbf{g}}. \tag{3.73}$$

Further, the dimensionless parameter, z_{ξ}, referred to as the *reduced thickness*, is given by

$$z_{\xi} = \frac{z}{\xi_g}. \tag{3.74}$$

$s_{\mathbf{g}}$ and $\xi_{\mathbf{g}}$ are respectively the excitation error and extinction distance for the diffracted beam.

Detector Model

The PED pattern has a very simple detector geometry. Only one parameter is sufficient to define the scaling of the diffraction pattern. This parameter, μ represents the reciprocal nanometers per pixel and can be used to convert the length of vectors in reciprocal space to an equivalent pixel coordinate. This parameter will depend on the camera length and pixel density of the CCD screen. The value of μ together with the number of pixels, n_{pix} in the detector also decides the maximum length of the **g**-vector ($\mathbf{g}_{max} = \mu n_{pix}/\sqrt{2}$) which can be observed in the precession diffraction pattern. Each diffracted beam is plotted as a Gaussian peak of fixed width. The dimension gives the size of the diffraction spot and the standard deviation decides how quickly the intensity falls off from the kinematic intensity. Both of these parameters are specified by the user.
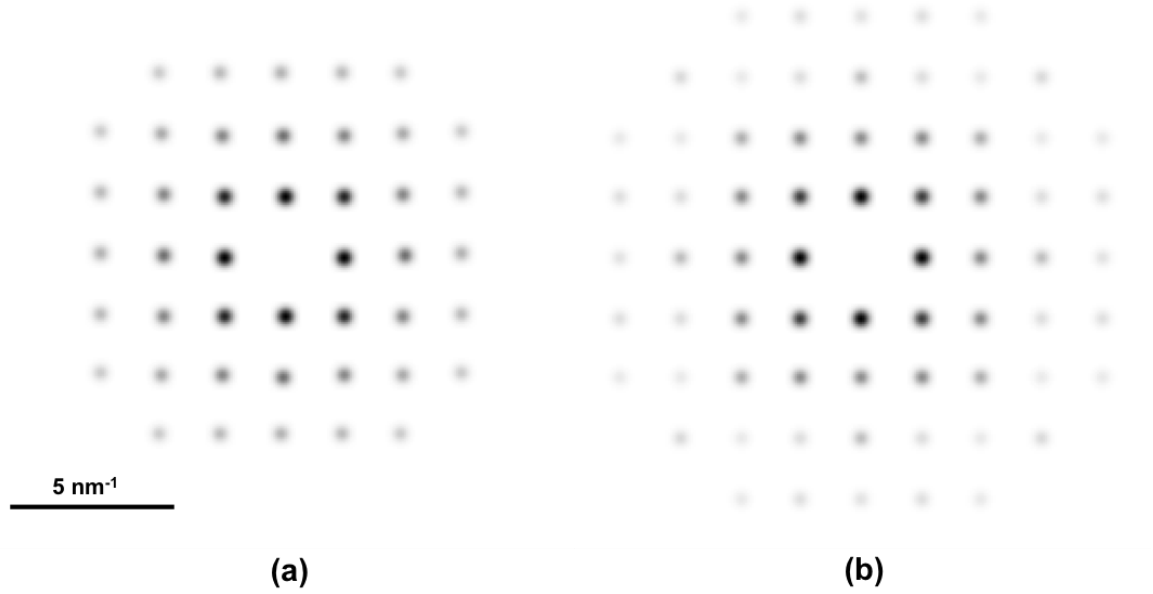
Figure 3.20: Comparison of simulated (a) dynamical (precession angle $= 1.0°$) and (b) kinematic precession electron diffraction patterns (reverse contrast) for (001) zone axis Cu. The microscope acceleration voltage was set to 200 keV.

Pattern Simulation

The scattering theory along with the detector model can be used to simulate diffraction patterns for precession electron diffraction. Fig. 3.19(a)-(d) shows the PED patterns (reverse contrast) for precession angle varying from $0.25° - 1°$ in steps of $0.25°$ for (001) zone axis copper. The microscope acceleration voltage is set to 200 keV. More HOLZ reflections becomes visible as the precession angle increases, which is a direct consequence of the Ewald sphere sweeping a higher volume in reciprocal space. Fig. 3.20(a)-(b) shows a dynamic (precession angle $= 0.75°$) and kinematic diffraction pattern (reverse contrast) respectively for the same sample and microscope conditions. While there are subtle differences in the intensity of diffracted spots, the overall geometry of the pattern is very similar. Fig. 3.21(a)-(b) shows the kinematic and experimental pattern (reverse contrast) for copper. The pattern has $\mu = 0.122$ nm^{-1}/pixel, $n_{pix} = 144$ and Euler angles in Bunge convention are given by $(\phi_1, \Phi, \phi_2) \equiv (327.22°, 3.56°, 0.78°)$. The acceleration voltage was set to 200 keV. Note that the direct beam is absent in the simulated pattern.
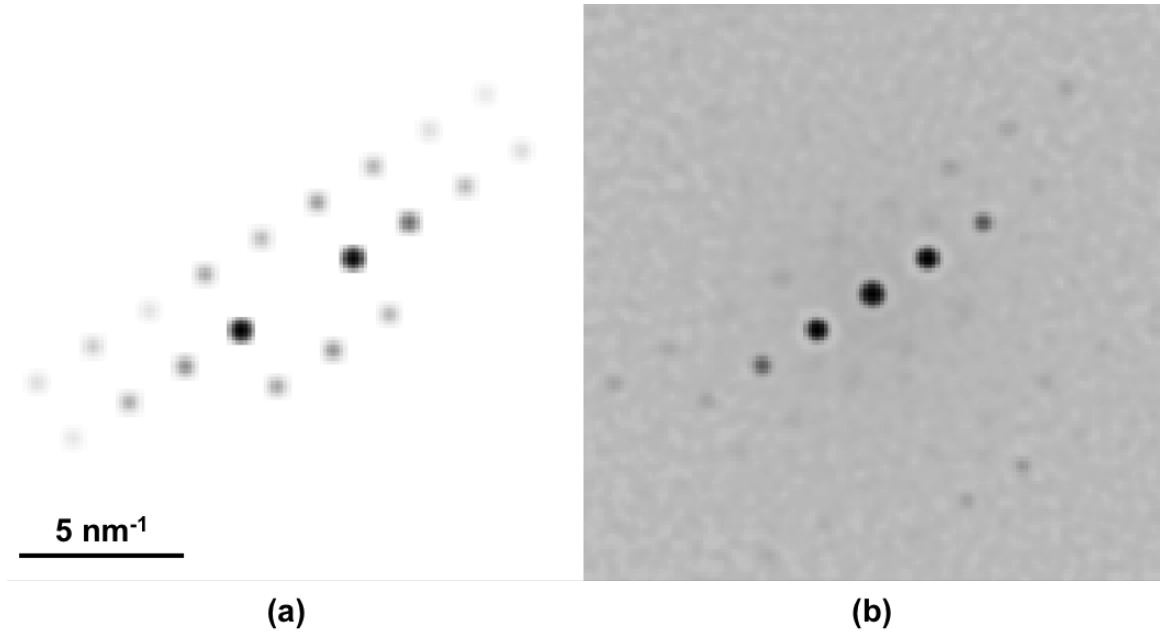
Figure 3.21: Comparison of (a) kinematically simulated and (b) experimental precession electron diffraction patterns (reverse contrast) for Cu. Parameters stated in text.

3.4.4 Transmission Kikuchi Diffraction

In the TKD modality, while the detector is still a position sensitive scintillator, the electrons are observed in the transmission mode instead of backscatter mode. As mentioned previously in chapter II, the sample is typically tilted by about $20° - 30°$ away from the detector, with the detector placed at the regular EBSD position. In some commercial systems, the detector is placed directly below the sample such that the coherent reflections are intercepted along with the Kikuchi bands. Fig. 3.22 shows a schematic of the TKD geometry. The incident electrons undergo both elastic and inelastic scattering in the sample. Following the example of EBSD modality, the elastic and inelastic contributions are treated separately. The electrons which undergo an elastic scattering event as their final scattering event before leaving the sample constitutes the dynamical diffraction signal. Thus, similar to the EBSD modality, the electron channels on its way out of the sample. Thus, there are striking similarities between the mechanism of EBSD and TKD signal generation. In this section we will highlight these similarities and point out the subtle differences between the two modalities.
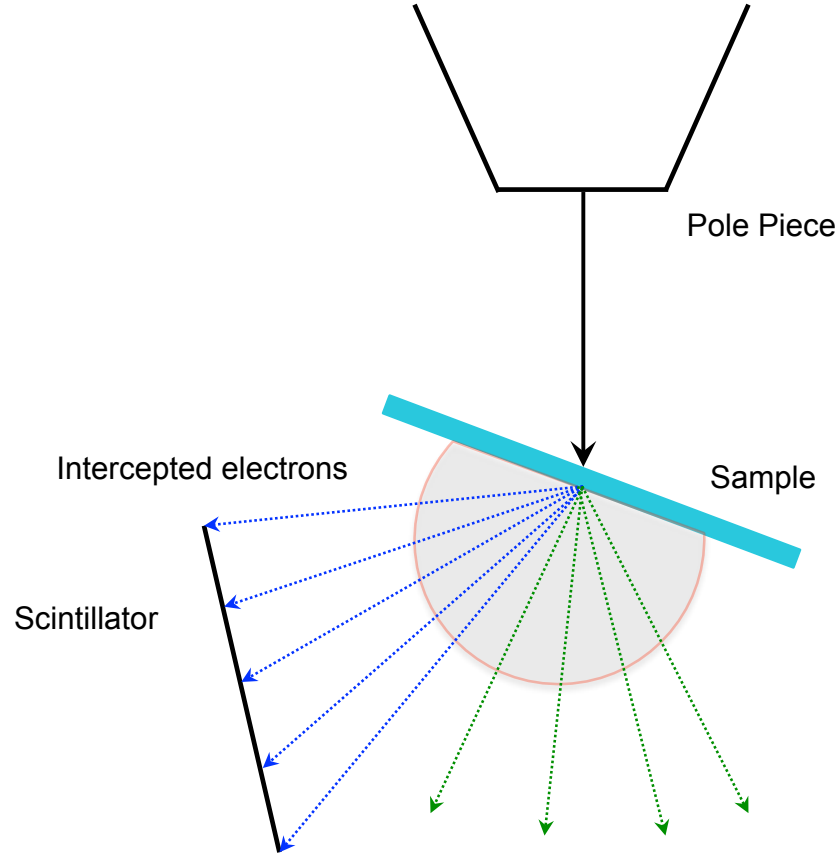
Figure 3.22: Schematic of Transmission Kikuchi Diffraction with the scintillator away from the sample showing the intercepted electrons.

Scattering Theory

Dynamical Theory   In the EBSD geometry the electron gets backscattered and the exit surface of the electrons is the same as the entrance surface. In contrast, the TKD transmission geometry has different entry and exit surfaces. However, the electrons undergo an elastic scattering event as their final event and can originate from a range of depths from the exit surface. Therefore, the overall signal for an exit direction $\mathbf{k}$ and electron energy, E and maximum escape depth z_0 will be an average of the signal from these depths and is very similar to eq. 3.48 with the only difference in the depth and energy dependent weight factor $\lambda(E, z)$. This weight factor needs to be calculated for the specific TKD geometry of interest. The rest of the methodology to compute the dynamical diffraction signal is exactly similar to the EBSD modality and will not be repeated here.

Stochastic Scattering The Monte Carlo algorithm for simulating the stochastic scatter-
ing has already been discussed in section 3.3. The same algorithm is now used to simulate
the energy, depth and angular distribution of electrons in the transmission mode of TKD
geometry. Fig. 3.23(a) shows the energy distribution of the transmitted electrons for differ-
ent film thicknesses (note that the x-axis has a log scale). The simulations were performed
for Nickel and 30 keV incident beam energy and $-20°$ sample tilt. As expected, the en-
ergy distribution shifts to the left with increasing film thickness indicating that the exit
electrons lose more energy. It is also interesting to note that the distribution gets tighter
with increasing film thickness. Most of the electrons contributing to the final signal lie in
a narrower energy window for thicker samples. Fig. 3.23(b) shows the depth distribution
of transmitted electrons (log scale on x-axis) for different electron exit energies. Again,
the simulations were performed for Nickel at 30 keV incident beam energy, $-20°$ sample
tilt and a film thickness of 0.2μm. The "attenuation length" of the electrons, given by the
slope of the curves are very similar for different energies. However, the curves are shifted
with respect to each other depending on the contribution of each energy to the final sig-
nal. Finally, Fig. 3.23(c) shows the overall depth distribution for all transmitted electrons
for different film thickness. Again, simulations are performed for Nickel at 30 keV incident
beam energy and $-20°$ sample tilt. It is interesting to note that the overall depth distri-
bution of transmitted electrons does not depend significantly on the thickness of the foil.

Fig. 3.24(a)-(f) shows the angular distribution of transmitted electrons for different exit
energies as a stereographic projection. Electrons which have lost little energy are scattered
by small angles whereas the electrons with larger energy loses are scattered by larger angles.
The bias on one side of the stereographic projection is due to the negative sample tilt.
Finally, the overall angular distribution of transmitted electrons is shown in Fig. 3.24(g).
The simulations are performed for Nickel at 30 keV incident beam energy, $-20°$ sample tilt
and film thickness of 0.2μm.
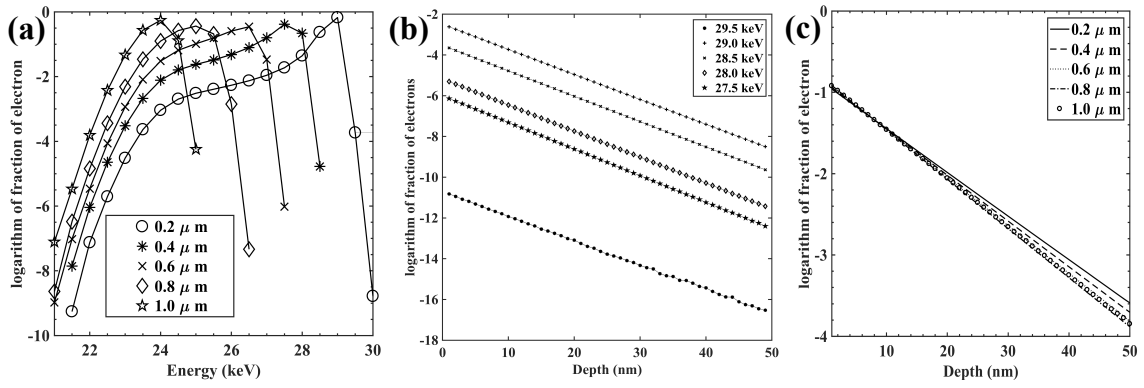
Figure 3.23: (a) Logarithm of the fraction of total transmitted electrons as a function of electron exit energy for different foil thickness and (b) logarithm of the number of transmitted electrons as a function of distance from the exit surface for different energies (foil thickness of 0.2μm) and (c) logarithm of the number of transmitted electrons as a function of depth from exit surface for various film thickness. Simulations were carried out for Nickel at 30 keV incident electrons.
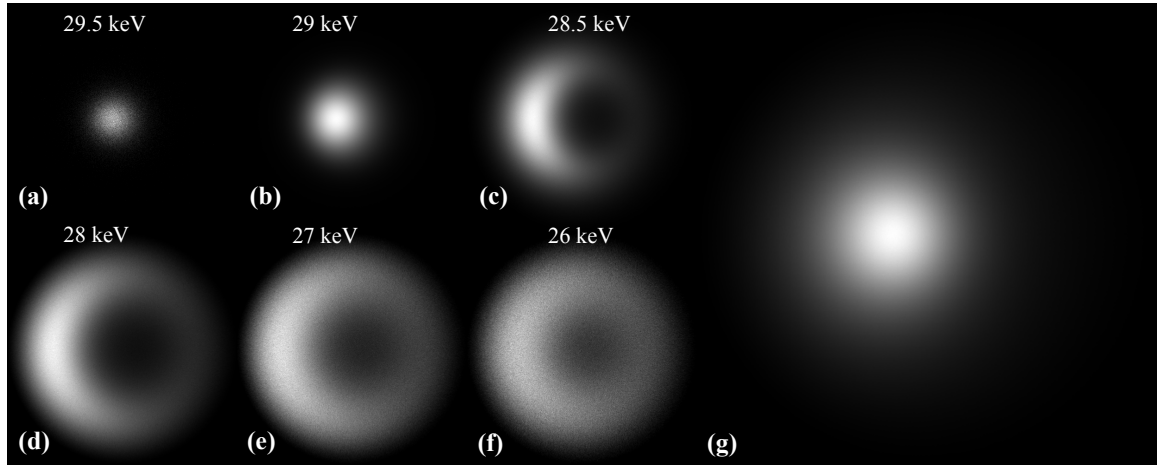
Figure 3.24: (a)-(f) Stereographic projection of transmitted electrons for different exit energies indicated in the figure. Higher energy electrons scatter by smaller angles whereas the electrons which have lost more energies gets scattered by large angles. (g) cumulative angular distribution of transmitted electrons. Most of the electrons are scattered by smaller angles. Simulations were performed for Nickel at 30 keV incident electron and a sample tilt of 20 keV.

Master TKD Pattern

Similar to the EBSD and ECP modality, the dynamical diffraction calculation for the TKD modality is carried out for a set of uniformly sampled exit directions. Fig. 3.25(a)-(b) shows the master TKD patterns for Nickel at 30 keV incident electron beam energy for the northern and southern hemispheres respectively. The corresponding modified Lambert projections are shown in Fig. 3.25(c)-(d) respectively.
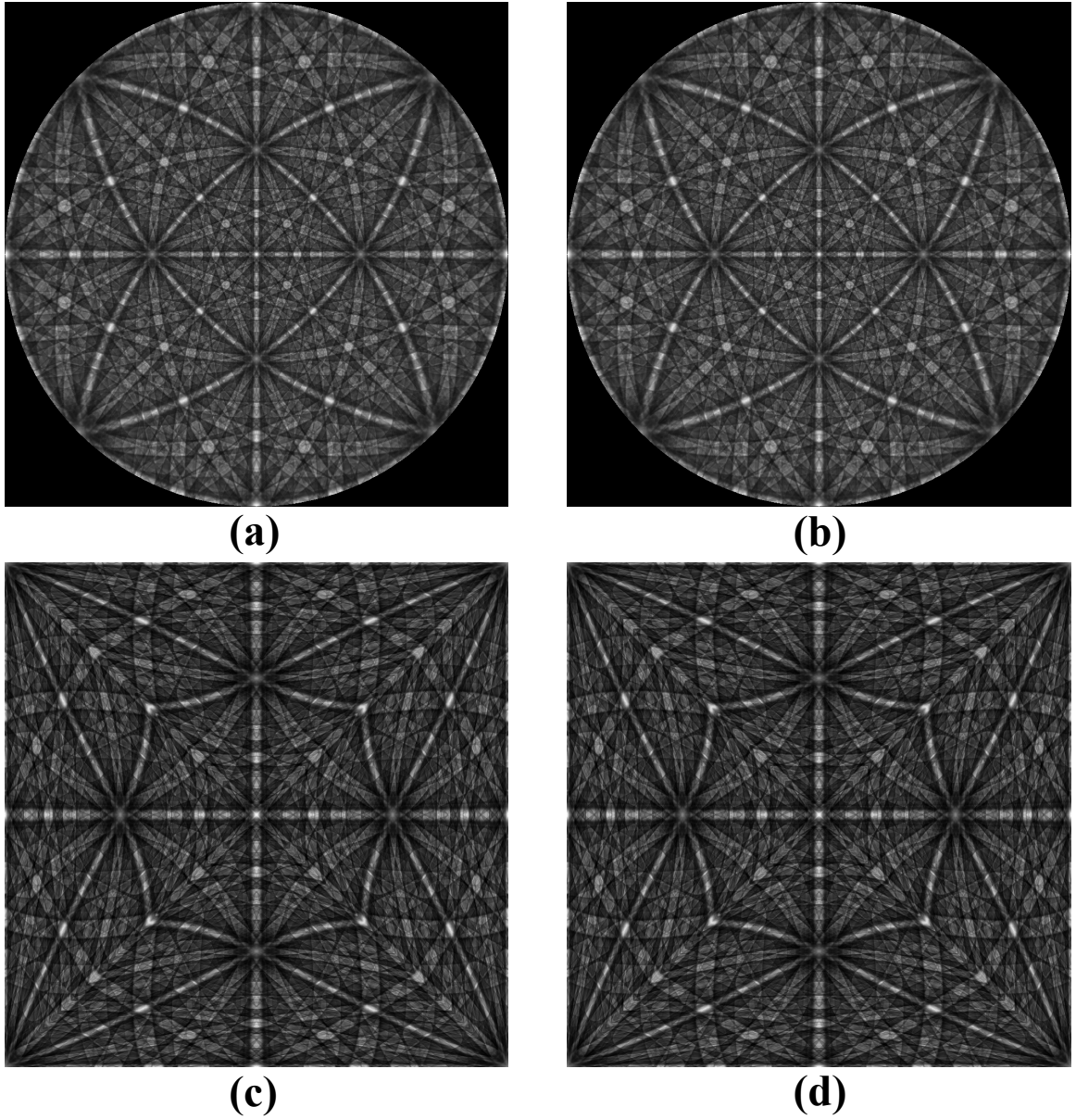
Figure 3.25: Stereographic projection of master pattern for Ni (a) northern and (b) southern hemisphere. Equivalent modified Lambert projections of (c) northern and (d) southern hemisphere. Incident electrons energy was set to 30 keV.

Detector Model and Pattern Interpolation

Since the parametrization and pattern interpolation for the TKD modality uses the same set of variables and equations as for the EBSD modality listed in 3.4.1 and equations 3.55 and 3.59, they will not be listed here again. It is interesting to note that the pattern centers for the TKD modality might lie outside the detector. Fig. 3.26(a)-(b) shows the interpolated background for two different energies from the Monte Carlo simulations. The
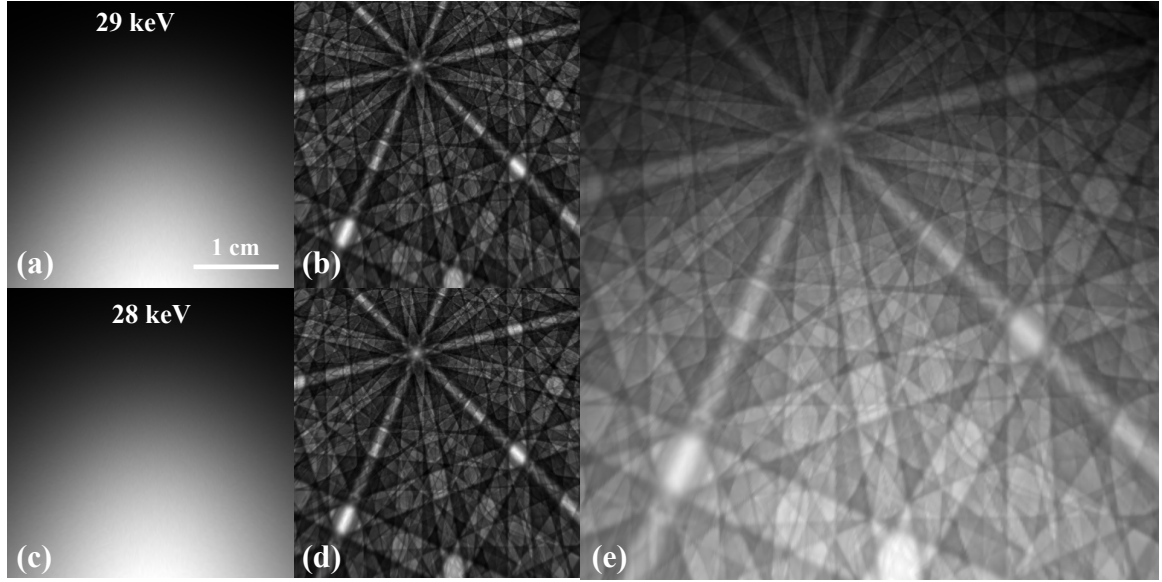
Figure 3.26: (a) Simulated background and (b) dynamical diffraction signal for electron in the energy range 29 − 30 keV. (c) and (d) shows the background and dynamical signal respectively for electron in the energy range 28 − 29 keV. The overall signal is shown in (e). The detector parameters for interpolation are stated in the text.

dynamical signal for the corresponding energies are shown in Fig. 3.26(c)-(d) respectively. The overall signal after gamma correction is shown in Fig. 3.26(e). The simulations were performed for Nickel with 30 keV incident energy and the following parameters: Euler angles $\equiv (198.60°, 54.26°, 219.44°)$, $L = 23471.46\mu$m, $\theta_c = 10.0°$, $\sigma = -20°$, $\delta = 70.0\mu$m, $(x_{pc}, y_{pc}) \equiv (6.44, 264.19)$. Fig. 3.27(a)-(b) show the comparison of TKD patterns for two different experimental patterns (left panel) and simulated patterns (right panel) from nanocrystalline Aluminum at 30 keV incident beam energy. The detector parameters for the two patterns were as follows: $L = 23471.46\mu$m, $\theta_c = 10.0°$, $\sigma = -24°$, $\delta = 70.0\mu$m, $(x_{pc}, y_{pc}) \equiv (6.44, 264.19)$, $n^x_{scin} = n^y_{scin} = 480$. The Euler angles for the two patterns are $(198.60°, 54.26°, 219.44°)$ and $(115.987°, 54.1689°, 242.170°)$ respectively. The pattern center coordinates are in units of pixels, with the center pixel having the coordinates $(0.0, 0.0)$ and n^x_{scin}, n^y_{scin} represent the number of pixels on the scintillator in the x and y direction respectively.
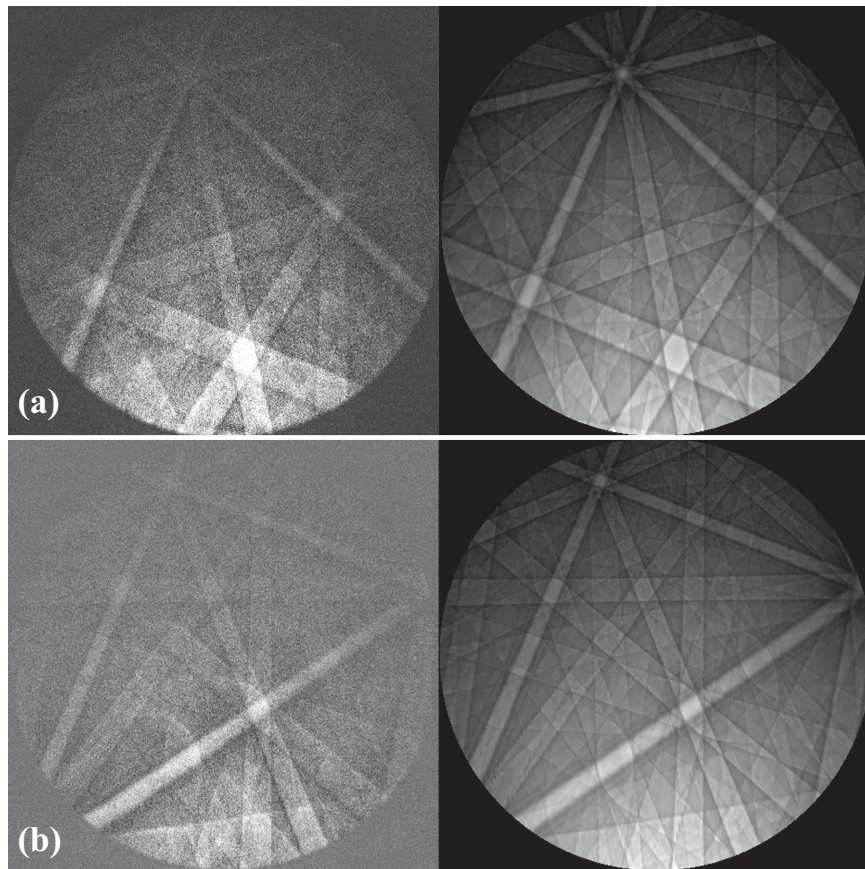
Figure 3.27: Comparison of experimental (left panel) and simulated (right panel) TKD patterns for two different orientations. Parameters for the simulations stated in text (Patterns courtesy Dr. Patrick Callahan, Univ. of California at Santa Barbara).

CHAPTER IV

Dictionary-based Indexing of Diffraction Patterns

Dictionary-based indexing of diffraction patterns refers to a class of techniques in which the diffraction pattern as a whole is matched against a library of pre-computed patterns. The details of each individual pattern, such as spot positions, band orientations, and so on, are not extracted from the pattern at all, but instead the entire pattern is considered to contain orientation information. The success of dictionary indexing approach will depend on the quality of the forward model for the diffraction modality. The forward models have already been shown to accurately reproduce experimental patterns in chapter III. We will use these models to compute the library of reference diffraction patterns; we will refer to such a library as a pattern dictionary.

In general terms, dictionary-based indexing can be described by means of the schematic in Fig. 4.1. The main ingredients are a physics-based forward model for the diffraction process (blue boxes), a geometric detector model, including detection noise (yellow) and an algorithm to sample orientation space (orange box with red border). The combination of these components is used to compute a pattern dictionary (left green box). In addition, a pattern matching engine is needed (middle green box), which compares the experimental patterns (light purple box) against the pattern dictionary, using any of a series of matching algorithms, some of which are the dot product or mutual information. As shown in Fig. 4.4, the dot product is a good metric for pattern matching. The pattern matching engine produces, for each experimental pattern, a ranking of the dictionary patterns according to the matching parameter; for instance, the dictionary patterns can be ranked in order of decreasing dot product, keeping only the top N matches, where N is specified by the user

and typically of order 30–40. It should be noted that each dictionary pattern is associated with one particular orientation and the top match is considered to be the orientation solution. Once all experimental patterns are indexed, a series of additional post-processing steps can be performed (upper right), including orientation refinements, error analysis and other statistics. The indexed orientations can then be used in traditional visualization programs to obtain orientation maps, direct and inverse pole figures, density plots of the orientation distribution function, and so on.

The dictionary approach as described in Fig. 4.1 is quite generic and should be capable of indexing patterns from many different diffraction modalities. Since the pattern matching algorithm typically uses all the pattern pixels, dictionary matching is expected to perform well for diffraction modalities in which the scattered intensity is distributed across the entire detector, instead of being focused in a few discrete diffraction spots. For the latter case, one may have to introduce a pre-processing step in which all patterns are converted to continuous intensity distributions before the matching step is carried out. In the case of precession electron diffraction (PED) patterns, for instance, a simple Hough transform of the spot pattern produces a pattern of sinusoidally curved bands, somewhat similar to an EBSD pattern with nearly straight Kikuchi bands. In general, the pre-processing step(s) should be carried out both on the experimental patterns and on the dictionary patterns, to avoid introduction of artifacts that might negatively affect the indexing process.

We have already introduced the forward models for four diffraction modalities. In the following sections, we will discuss the missing ingredients of the algorithm. Section 4.1 introduces the concept of uniform sampling of the fundamental zones introduced in the previous section. This section introduces the cubochoric vector, which is an alternate representation of 3D orientation. This section also introduces a new method to uniformly sample iso-misorientation surfaces using a combination or Rodrigues and cubochoric representations. Section 4.2 uses the iso-misorientation sampling discussed in the previous section to establish dot product as a robust proxy from misorientation. Section 4.3 discusses the accurate determination of detector parameters. Section 4.4 discusses the pre-processing of diffraction patterns. We will also re-define the various parameters used by different vendors for the dictionary approach in section 4.5. We will present results of applying these
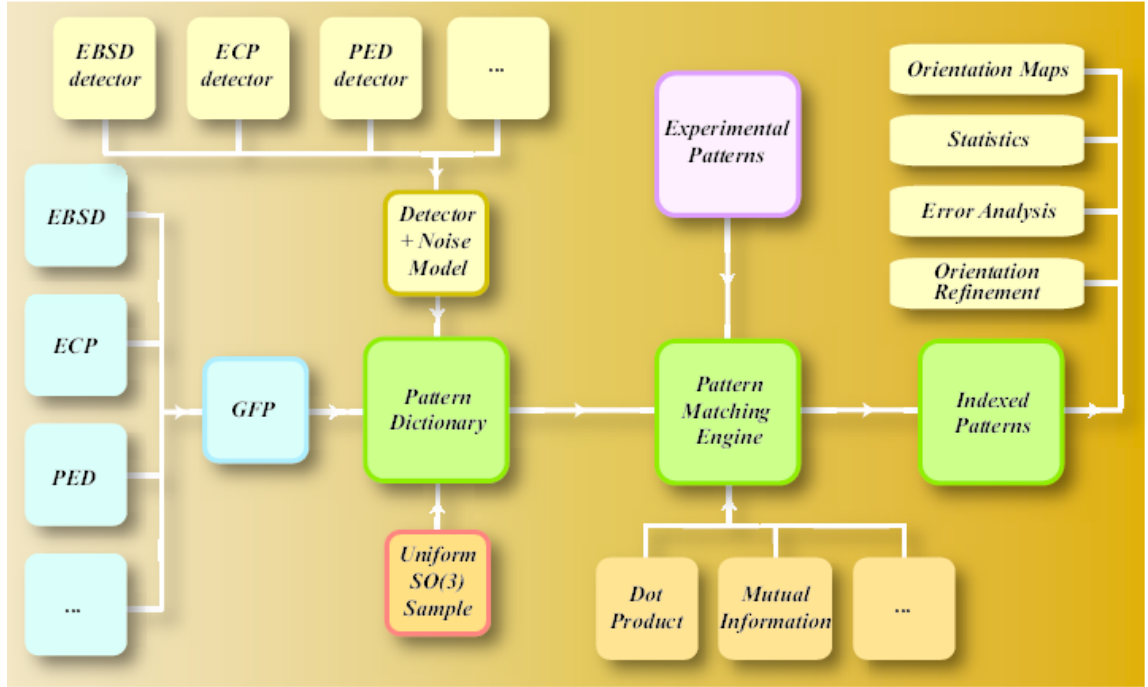
Figure 4.1: Schematic representation of dictionary-based approach for indexing diffraction patterns.

algorithm to different diffraction modalities.

4.1 Sampling of Fundamental Zone

The uniform sampling is of pivotal importance since it is paramount that all regions of the fundamental zone be represented equally. It might also be of interest for some applications to uniformly sample the set of all points which are a constant misorientation away from a given Rodrigues vector. Later, we will use this to show that dot products are a robust proxy for misorientations for dictionary based indexing methods. In this sub-section, we will discuss the uniform sampling of the Rodrigues fundamental zone and misorientation iso-surfaces starting from the cubochoric representation. We will also give empirical relations for the number of sampling points along the semi-edge of the cubochoric cube for a desired average angular misorientation of the generated dictionary. Further, using the concept of Riesz energies, we will show that the cubochoric approach leads to near optimal sampling of orientation space.

The cubochoric representation of 3D rotations was designed to provide a convenient tool to obtain uniform samples of 3D rotations. It is straightforward to create a uniform

sampling inside the cube C. Since the mapping from this cube to the quaternion unit hemisphere, $\mathbb{S}^3_+$, is an equal volume mapping (carried out in two steps via the intermediate homochoric representation), a uniform sampling of C must provide a uniform sampling of $\mathbb{S}^3_+$, which is isomorphic with $SO(3)$. The simplest uniform sampling of C is a cubical grid $(i, j, k)\delta$, where (i, j, k) is a triplet of integers and δ the grid spacing; the range of the integers is such that the grid points must lie completely inside or on the surface of C. For a given grid spacing δ, an infinite number of distinct grids can be generated that differ from each other by a constant translation vector $\mathbf{t} = \delta\boldsymbol{\tau}$, with $-1/2 < \tau_i \leq 1/2$; we will represent the resulting set of grid points by the symbol $S_{\boldsymbol{\tau}}(N)$, where N is the largest integer in the following set of six values:

$$N = \max\left\{\left\lfloor\frac{a_c}{2\delta} - \tau_i\right\rfloor, \left|\left\lceil-\frac{a_c}{2\delta} - \tau_i\right\rceil\right|\right\}, \qquad (i = 1\ldots3), \tag{4.1}$$

where $\lfloor\ \rfloor$ and $\lceil\ \rceil$ are the floor and ceiling functions and vertical bars indicate absolute values.

Amongst all possible unique grids, two types occupy a special role. The grids of the type $S_{000}(N)$ (i.e., $\mathbf{t} = \mathbf{0}$) are the only grids that contain the origin (the identity rotation). Grids of the type $S_{\frac{1}{2}\frac{1}{2}\frac{1}{2}}(N)$ are also special in the sense that their grid points lie at a maximum distance from all the grid points in $S_{000}(N)$; in fact, for a given value of N, each grid point of $S_{\frac{1}{2}\frac{1}{2}\frac{1}{2}}(N)$ lies at the center of the cubes of grid points of $S_{000}(N)$ and vice versa, so that $S_{000}(N)$ and $S_{\frac{1}{2}\frac{1}{2}\frac{1}{2}}(N)$ are dual grids. The number of grid points in $S_{000}(N)$ is equal to $(2N+1)^3$, whereas for $S_{\frac{1}{2}\frac{1}{2}\frac{1}{2}}(N)$ we have $8N^3$ grid points. It is also possible to define grids that are rotated with respect to the cubochoric reference frame; we will not consider such grids in this thesis.

For a given grid, $S_{\boldsymbol{\tau}}(N)$, it is of interest to know what the average disorientation, $\langle\theta\rangle$, is between nearest neighbor grid points. We define the disorientation θ between two orientations represented by quaternions $p = [p_0, \mathbf{p}]$ and $q = [q_0, \mathbf{q}]$ as:

$$\theta(p, q) = 2\arccos z_0 \quad \text{with} \quad z = pq^* \tag{4.2}$$

where the asterisk denotes the conjugate quaternion, and the regular quaternion product is assumed. For the cubochoric sampling, we take for each grid point $\mathbf{c}_{ijk}$ the set of nearest neighbors on the cubical grid, i.e., $\{\mathbf{c}_{i\pm1jk}, \mathbf{c}_{ij\pm1k}, \mathbf{c}_{ijk\pm1}\}$ and determine the average disorientation as

$$
\begin{aligned}
\langle\theta\rangle_{ijk} \;=\; & \frac{1}{6}\left[\theta(p_{ijk}, p_{i-1jk}) + \theta(p_{ijk}, p_{i+1jk}) + \theta(p_{ijk}, p_{ij-1k})+\right.\\
& \left.\theta(p_{ijk}, p_{ij+1k}) + \theta(p_{ijk}, p_{ijk-1}) + \theta(p_{ijk}, p_{ijk+1})\right],
\end{aligned}
\tag{4.3}
$$

where p_{ijk} is the quaternion corresponding to the cubochoric vector $\mathbf{c}_{ijk}$. For points on the cube faces, we adjust the computation of the average accordingly.

Table 4.1 lists $\langle\theta\rangle$ (in degrees) along with its standard deviation and full-width-at-half-maximum (FWHM) for a range of N values for grid type $S_{000}(N)$. The corresponding disorientation distributions are shown as histograms in Fig. 4.2(a) for N values that are multiples of 20; the histograms are shown in alternating colors to more clearly distinguish them. Fig. 4.2(b) shows the relation between the number of sampling points N and the average disorientation $\langle\theta\rangle$; the average values are indicated by red symbols, and the vertical lines through each symbol indicate a range of one standard deviation. The dashed lines are guide lines to indicate how many sampling points should be selected to obtain a given average disorientation.

It should be noted that uniform sampling of the quaternion unit sphere $\mathbb{S}^3_+$ leads to a range of disorientations, not a single value of the disorientation. This is related to the equal-volume nature of the mapping; an equal-volume map onto a spherical surface can not at the same time be angle preserving. This is also the case for projections from the sphere $\mathbb{S}^2$ onto a plane: the projection is either angle-preserving (stereographic) or area preserving (Lambert), and it can be shown that it is not possible to construct a mapping that preserves both angles and areas. The same is true for the uniform (equal-volume) mapping of the quaternion unit hemisphere $\mathbb{S}^3_+$, so that such a uniform map will always have a distribution of disorientation values.

The average disorientation can be parameterized as a function of N by fitting a hyper-

N	$(2N+1)^3$	$\langle\theta\rangle$	σ_θ	FWHM ($^\circ$)
20	68,921	6.598	0.243	3.998
40	531,441	3.380	0.128	0.326
60	1,771,561	2.273	0.088	0.235
80	4,173,281	1.712	0.066	0.178
100	8,120,601	1.373	0.054	0.143
120	13,997,521	1.146	0.045	0.116
140	22,188,041	0.984	0.039	0.100
160	33,076,161	0.861	0.034	0.088
180	47,045,881	0.766	0.030	0.079
200	64,481,201	0.690	0.027	0.071
220	85,766,121	0.628	0.025	0.065
240	111,284,641	0.576	0.023	0.060
260	141,420,761	0.531	0.021	0.054
280	176,558,481	0.494	0.020	0.051
300	217,081,801	0.461	0.018	0.047

Table 4.1: Average disorientation $\langle\theta\rangle$ (in degrees) along with standard deviation σ_θ and FWHM values for a cubochoric sampling of N equidistant points along the semi-edge of the cubochoric space. [sampling grid type $S_0(N)$]

bolic function to the data in Table 4.1, resulting in:

$$\langle\theta\rangle = 0.03732 + \frac{131.97049}{N}; \tag{4.4}$$

the nearest integer (nint) N for a given value of $\langle\theta\rangle$ is then given by:

$$N = \text{nint}\left[\frac{131.97049}{\langle\theta\rangle - 0.03732}\right]. \tag{4.5}$$

For instance, if an average disorientation of 1° is needed, then the cubochoric space should be sampled with N about equal to 137, resulting in a total of $20,796,875$ unique sampling points. The results for grid $S_{\frac{1}{2}\frac{1}{2}\frac{1}{2}}(N)$ are shown in Table 4.2, using the same conventions as for $S_{000}(N)$. Note that the values for the average disorientation of the two grid types are very similar; differences are largest for small numbers of sampling points. The disorientation histograms are nearly identical to those for grid $S_0(N)$ shown in Fig. 4.2; a fit of $\langle\theta\rangle$ vs. N based on Table 4.2 results in

$$\langle\theta\rangle = 0.07127 + \frac{125.70471}{N}. \tag{4.6}$$

N	$8N^3$	$\langle\theta\rangle$	σ_θ	FWHM (°)
20	64,000	6.285	0.212	3.998
40	512,000	3.296	0.119	0.318
60	1,728,000	2.234	0.083	0.212
80	4,096,000	1.690	0.064	0.165
100	8,000,000	1.359	0.052	0.135
120	13,824,000	1.136	0.044	0.115
140	21,952,000	0.976	0.038	0.098
160	32,768,000	0.856	0.033	0.087
180	46,656,000	0.762	0.030	0.077
200	64,000,000	0.686	0.027	0.070
220	85,184,000	0.625	0.024	0.063
240	110,592,000	0.573	0.022	0.058
260	140,608,000	0.529	0.021	0.054
280	175,616,000	0.492	0.019	0.051
300	216,000,000	0.459	0.018	0.047

Table 4.2: Average disorientation $\langle\theta\rangle$ along with standard deviation σ_θ and FWHM values for a cubochoric sampling of N equidistant points along the semi-edge of the cubochoric space. [sampling grid type $S_{\frac{1}{2}\frac{1}{2}\frac{1}{2}}(N)$]

4.1.1 Uniform sampling constrained by crystallographic symmetry

The above results for the average disorientation $\langle\theta\rangle$ are in principle only valid for the triclinic symmetry case, for which the cubochoric cube C represents the complete fundamental zone (FZ). In the presence of crystallographic symmetry, only a subset of the complete grid is needed, namely those points that result in Rodrigues vectors that lie inside the corresponding FZ. While we do not expect large changes in the average disorientation values when only a subset of the cubochoric space is considered, it is valuable to compare the results for all the rotational symmetry groups and corresponding FZs. Table 4.3 lists the average disorientation values for each of the 11 rotational point group symmetries. The values were computed in the same way as before, but grid points are taken into account only if the corresponding Rodrigues-Frank vector $\boldsymbol{\rho}$ ends inside the Rodrigues FZ. The changes in the average disorientation values are small, and the average values are all smaller than those for the absence of crystallographic symmetry. The values in Table 4.3 indicate that the parameterized expressions in eqs. 4.4 and 4.6 can be used for all crystallographic symmetries.

N	$\langle\theta\rangle^1$	$\langle\theta\rangle^2$	$\langle\theta\rangle^{222}$	$\langle\theta\rangle^4$	$\langle\theta\rangle^{422}$	$\langle\theta\rangle^3$	$\langle\theta\rangle^{32}$	$\langle\theta\rangle^6$	$\langle\theta\rangle^{622}$	$\langle\theta\rangle^{23}$	$\langle\theta\rangle^{432}$
20	6.598	6.484	6.460	6.418	6.395	6.442	6.426	6.375	6.352	6.379	6.490
40	3.380	3.315	3.303	3.282	3.269	3.295	3.285	3.264	3.246	3.254	3.311
60	2.273	2.227	2.218	2.205	2.196	2.214	2.206	2.193	2.180	2.185	2.224
80	1.712	1.677	1.670	1.660	1.653	1.667	1.661	1.652	1.641	1.645	1.674
100	1.373	1.345	1.339	1.331	1.325	1.337	1.332	1.325	1.316	1.319	1.342
120	1.146	1.122	1.118	1.111	1.106	1.116	1.111	1.106	1.098	1.101	1.120
140	0.984	0.963	0.959	0.954	0.949	0.957	0.954	0.949	0.942	0.944	0.961
160	0.861	0.843	0.840	0.835	0.831	0.838	0.835	0.831	0.825	0.827	0.841
180	0.766	0.750	0.747	0.743	0.739	0.746	0.743	0.739	0.734	0.736	0.748
200	0.690	0.676	0.673	0.669	0.666	0.672	0.669	0.666	0.661	0.662	0.674
220	0.628	0.614	0.612	0.608	0.605	0.611	0.608	0.605	0.601	0.602	0.613
240	0.576	0.563	0.561	0.558	0.555	0.560	0.558	0.555	0.551	0.552	0.562
260	0.531	0.520	0.518	0.515	0.513	0.517	0.515	0.513	0.509	0.510	0.519
280	0.494	0.483	0.481	0.478	0.476	0.480	0.478	0.476	0.473	0.474	0.482
300	0.461	0.451	0.449	0.447	0.444	0.448	0.447	0.444	0.441	0.442	0.450
320	0.432	0.423	0.421	0.419	0.417	0.420	0.419	0.417	0.414	0.415	0.422

Table 4.3: Average disorientations $\langle\theta\rangle$ (in degrees) for the 11 different types of Rodrigues fundamental zones as a function of the number of cubochoric sampling points N. The superscript on $\langle\theta\rangle$ indicates the rotational point group symbol. [sampling grid type $S_{000}(N)$]

4.1.2 Uniform sampling of iso-misorientation surfaces

It may also be of interest for some applications to uniformly sample points which are at a constant misorientation away from a given point in $SO(3)$. It is shown in Appendix A that the iso-misorientation surface about a point in Rodrigues space has the general form $(\mathbf{x}-\mathbf{v})^{\mathrm{T}}\mathcal{A}(\mathbf{x}-\mathbf{v}) = 1$, where $\mathcal{A}$ is a symmetric matrix with two degenerate eigenvalues. The sign of the eigenvalues of the matrix $\mathcal{A}$ determines whether the iso-misorientation surface is open or closed. If we are seeking an iso-surface at a constant misorientation angle μ around a point $\boldsymbol{\rho} = \tan\left(\frac{\omega}{2}\right)\hat{\mathbf{n}}$ in Rodrigues space, then the eigenvalues and orthonormal eigenvectors of $\mathcal{A}$ are given by the following expressions:

$$\lambda_1 = \lambda_2 = \mathrm{sign}\left(\pi - (\omega + \mu)\right);\sqrt{\frac{1 - \cos(\mu)}{\cos(\mu) + \cos(\omega)}};$$
$$\lambda_3 = \left|\frac{\sin(\mu)}{\cos(\mu) + \cos(\omega)}\right|. \tag{4.7}$$

and, denoting $\gamma_{xz} = \sqrt{n_x^2 + n_z^2}$:

$$\begin{aligned}
\hat{\mathbf{e}}_1 &= \frac{1}{\gamma_{xz}}\left(-n_z, 0, n_x\right); \\
\hat{\mathbf{e}}_2 &= \frac{1}{\gamma_{xz}}\left(-n_x n_y, \gamma_{xz}^2, -n_y n_z\right); \\
\hat{\mathbf{e}}_3 &= (n_x, n_y, n_z).
\end{aligned} \tag{4.8}$$

where $\hat{\mathbf{n}} = (n_x, n_y, n_z)$. If all three eigenvalues are positive $(\omega + \mu < \pi)$, then the iso-surface is a spheroid. When $\omega + \mu > \pi$, then the iso-surface is a two-sheet hyperboloid; for the special case $\omega + \mu = \pi$, the iso-surface is a spheroidal paraboloid (with circular cross section normal to the third eigenvector), with a single singular point at $\tan\frac{\pi}{2}\hat{\mathbf{n}}$. For the special case $\boldsymbol{\rho} = \mathbf{0}$, the iso-surface is a sphere of radius $\tan\left(\frac{\mu}{2}\right)$ centered at the origin. It is interesting to note that this sphere maps onto the surface of a centered cube inside the cubochoric cube; the semi-edge length of this centered cube is $(\pi(\mu - \sin(\mu)))^{\frac{1}{3}}$. This suggests a straightforward method to uniformly sample the iso-misorientation surface using the following approach:

- Uniformly sample the surfaces of a cube of appropriate semi-edge length centered in cubochoric space;

- Map this uniform grid from cubochoric space to a uniform grid on a sphere centered at the origin in Rodrigues space.

- Transform the sphere to an appropriate quadratic surface around the selected point $\boldsymbol{\rho}$.

The process is illustrated in Fig. 4.3 for a misorientation angle of $\mu = 25°$; in (a), the surface of a centered cube of semi-edge length $(\pi(\mu - \sin\mu))^{\frac{1}{3}}$ is sampled uniformly, with $N = 10$ sampling points along each edge, leading to a total of $6N(N-1) + 2 = 542$ sampling points. The points along the cube edges are highlighted in green, and the corner points in red. In Fig. 4.3(b), these sampling points have been converted to Rodrigues vectors and they lie on a sphere centered at the origin; the sphere is an iso-misorientation surface with respect to the identity orientation, and has radius $\tan(\mu/2)$. The other five

iso-surfaces shown in the figure correspond to a misorientation of $\mu = 25°$ with respect to the orientations $\boldsymbol{\rho} = (\pm 1, 0, 0)$, $(0, \pm 1, 0)$ and $(0, 0, 1)$ (the axes labels are the same as in part (a) of the figure); the coordinates of the sampling points on the iso-surfaces were computed by applying the Rodrigues formula for the composition of rotations. If $\boldsymbol{\sigma}$ represents the Rodrigues vector of any of the sampling points on the centered sphere, then the corresponding sampling point with respect to $\boldsymbol{\rho}$ can be computed from:

$$\boldsymbol{\rho}^{mis} = \frac{\boldsymbol{\sigma} - \boldsymbol{\rho} + \boldsymbol{\sigma} \times \boldsymbol{\rho}}{1 + \boldsymbol{\sigma} \cdot \boldsymbol{\rho}}. \tag{4.9}$$

As noted in Appendix A, special care must be taken of the points for which the denominator vanishes.

It should also be noted that the iso-misorientation surfaces themselves rotate when the rotation angle ω is changed. This is illustrated in the lower portion of Fig. 4.3(b); the red corner points (with negative z_c coordinate) of the centered sphere will move along the trajectories indicated by the dotted red lines when the rotation angle of $\boldsymbol{\rho}$ is increased (the increment is $4°$ in this figure). This results in a gradual rotation of all the sampling points as the rotation angle of $\boldsymbol{\rho}$ in increased. For the iso-surfaces shown in Fig. 4.3(b), the rotation angle is $\omega = \pi/2$, leading to an overall rotation of the iso-surface by an angle of $\pi/4$ with respect to the points on the centered sphere (for which $\omega = 0$).

4.1.3 Verification of the sampling uniformity

In this final section, we provide evidence for the uniformity of the cubochoric sampling approach by computing the so-called Riesz energies of the points in the sampling sets. For a set of distinct unit quaternions $S_M = \{q_1, q_2, \ldots, q_M\}$ on $\mathbb{S}^3$, we define the Riesz energy of the set as:

$$E_s(S_M) \equiv \sum_{1 \leq i < j \leq M} ||q_i - q_j||^{-s}, \quad (s > 0) \tag{4.10}$$

where

$$||q_i - q_j|| = \sqrt{\sum_{k=0}^{3} (q_{i,k} - q_{j,k})^2}, \tag{4.11}$$

and $q_{i,k}$ represent the components of the quaternion q_i. The sum in equation (4.10) covers the complete quaternion sphere, not just the hemisphere $\mathbb{S}^3_+$, i.e., both q and $-q$ are included in the summation.

For a given number of points M in the set S_M, the optimal (or extremal) Riesz energies are known for hyper-spheres of arbitrary dimension d; the optimal Riesz energy $\mathcal{E}_s(S_M)$ for $s > 0$ is given by [102]:

$$\mathcal{E}_s(S_M) = \gamma_{s,d} \begin{cases} M^2, & s < d \\ M^2 \ln M, & s = d. \end{cases} \tag{4.12}$$

In this relation, we have:

$$\gamma_{s,d} = \frac{\Gamma\left(\frac{d+1}{2}\right)\Gamma(d-s)}{2\Gamma\left(\frac{d-s+1}{2}\right)\Gamma\left(\frac{2d-s}{2}\right)}, \quad s < d \tag{4.13}$$

$$\gamma_{d,d} = \frac{\Gamma\left(\frac{d+1}{2}\right)}{2d\sqrt{\pi}\Gamma\left(\frac{d}{2}\right)}, \tag{4.14}$$

where $\Gamma(x)$ is Euler's complete gamma function. For the quaternion unit sphere $\mathbb{S}^3$ we have $d = 3$, so that the optimal Riesz energies are given by:

$$\mathcal{E}_1(S_M) = \frac{4M^2}{3\pi}; \quad \mathcal{E}_2(S_M) = \frac{M^2}{2}; \quad \mathcal{E}_3(S_M) = \frac{M^2 \ln M}{3\pi}. \tag{4.15}$$

Table 4.4 lists the Riesz energies for sample sets based on the cubochoric sampling method. For several values of N (the number of steps along the semi-edge of the cubochoric cube) we list M (the total number of points in the set S_M) and the corresponding Riesz energies $E_s(S_M)$ for $s = 1, 2, 3$. The numbers r_s represent the ratios of the computed energies to the optimal energies, i.e.,

$$r_s = \frac{E_s(S_M)}{\mathcal{E}_s(S_M)}. \tag{4.16}$$

It is clear from the table that all three values r_s converge (slowly) towards unity, indicating that the cubochoric sampling produces near optimal coverings of the quaternion sphere. As will be discussed in the chapter IV, for most dictionary indexing applications the value of N will be at least 90, for which there are $M = 11\,664\,000$ sampling points on the quaternion

N	M	$E_1(S_M)$	r_1	$E_2(S_M)$	r_2	$E_3(S_M)$	r_3
2	128	6777.2	0.9746378	7004.7	0.8550704	9771.9	1.1585340
4	1024	441 757.1	0.9926469	481 761.1	0.9188863	823 011.3	1.0672140
6	3456	5051 586.5	0.9965324	5637 049.5	0.9439182	10 796 536.7	1.0455966
8	8192	28 424 815.5	0.9979962	32 121 693.1	0.9573010	66 533 795.9	1.0369665
10	16 000	108 508 403.8	0.9986988	123 594 380.5	0.9655810	271 470 938.2	1.0324373
12	27 648	324 130 765.3	0.9990884	371 195 731.3	0.9711929	854 093 164.1	1.0296451
14	43 904	817 531 389.3	0.9993264	939 918 596.7	0.9752412	2246 913 907.0	1.0277355
16	65 536	1821 897 041.1	0.9994822	2100 876 601.6	0.9782969	5187 077 559.8	1.0263336
18	93 312	3693 904 543.6	0.9995897	4269 470 926.2	0.9806839	10 839 282 418.0	1.0252506
20	128 000	6951 270 140.0	0.9996670	8049 455 329.5	0.9825995	20 941 609 836.3	1.0243817
22	170 368	12 315 305 438.9	0.9997243	14 282 899 411.7	0.9841704	37 974 765 607.1	1.0236642
24	221 184	20 758 479 938.5	0.9997680	24 106 050 118.1	0.9854818	65 355 178 966.9	1.0230581
26	281 216	33 556 990 135.3	0.9998021	39 011 091 482.4	0.9865930	107 652 357 113.5	1.0225367
28	351 232	52 348 335 209.3	0.9998292	60 913 802 608.5	0.9875464	170 830 854 694.4	1.0220814
30	432 000	79 193 899 297.9	0.9998511	92 227 113 901.4	0.9883735	262 517 186 433.0	1.0216790

Table 4.4: Riesz energies for cubochoric sampling of the quaternion unit sphere for a rangle of N-values. M indicates the total number of points on $\mathbb{S}^3$, and the Riesz energies $E_s(S_M)$ as well as the ratios r_s are listed for each N.

unit sphere $\mathbb{S}^3$; computing the Riesz energy sums in Eq. (4.10) and normalizing by the optimal Riesz energies of Eq. (4.15) then results in $r_s = (0.9999834, 0.9961179, 1.0170389)$. Therefore, we can have confidence that the cubochoric sampling approach guarantees $SO(3)$ sampling uniformity for dictionary-based indexing applications.
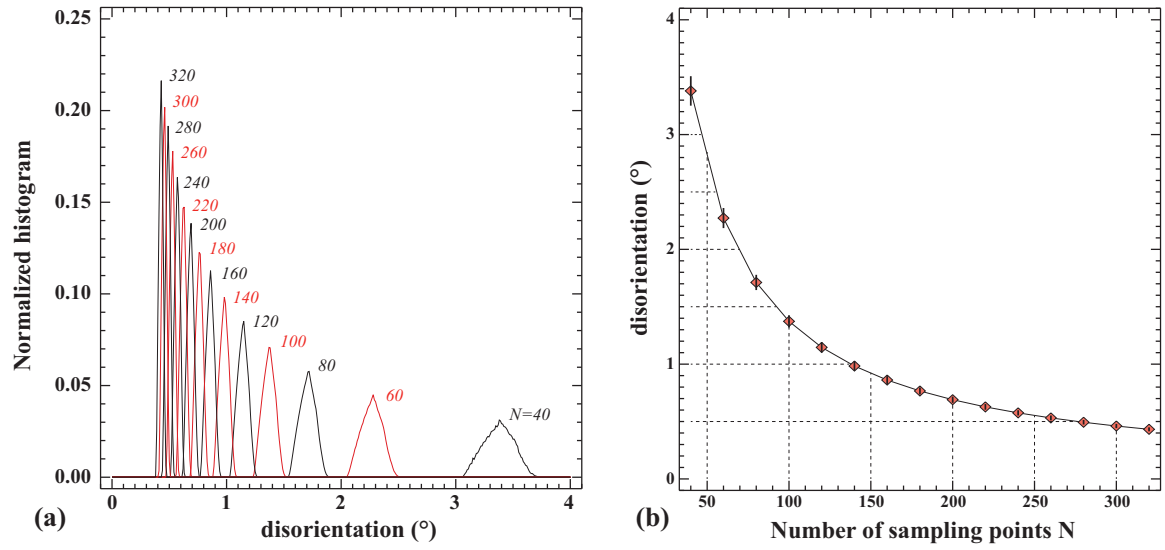
Figure 4.2: (a) normalized histograms of the disorientation for different numbers of sampling points; (b) average disorientation vs. the number of sampling points.
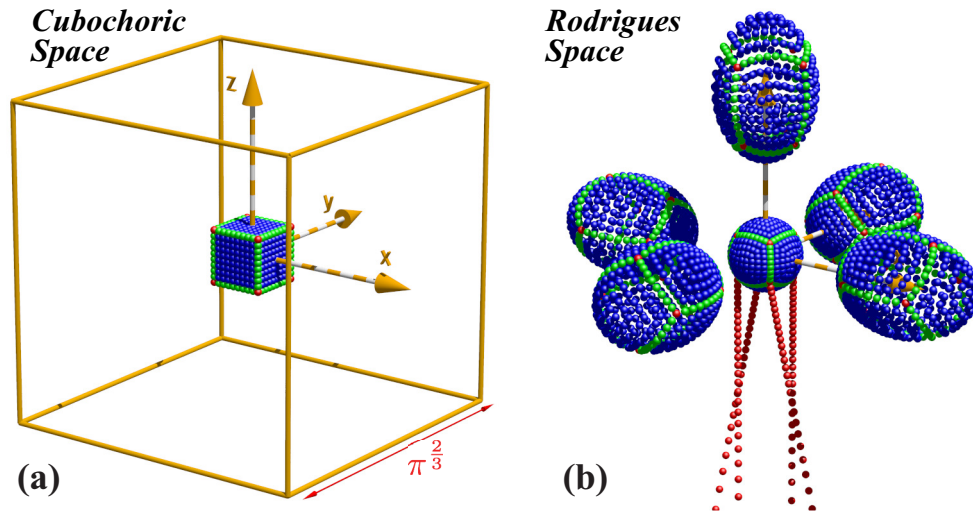
Figure 4.3: Uniform sampling of an iso-misorientation surface: (a) shows a uniform sampling of a cube surface inside the cubochoric cube; in (b) these points are mapped onto a sphere entered at the origin, as well as onto five spheroids corresponding to the rotations $\boldsymbol{\rho} = (\pm 1, 0, 0)$, $(0, \pm 1, 0)$ and $(0, 0, 1)$. The red dotted lines at the bottom of the figure are explained in the text.

4.2 Dot Product Proxy for Misorientation

Having the ability to uniformly generate orientations with a given misorientation with respect to a reference orientation is of importance for the analysis of the accuracy and precision of dictionary-based indexing approaches. In the dictionary-based approach to indexing diffraction patterns, the dot product serves as a proxy for the misorientation. The relation between the misorientation angle and the average dot product is shown in Fig. 4.4. A total of 15 random orientations were selected, and for each orientation an EBSD pattern was calculated for a set of realistic detector parameters. For each misorientation value in the set $\{1°, 2°, 3°, 4°, 5°, 7°, 9°, 11°, 15°\}$ a spherical iso-misorientation surface was sampled using the approach described in chapter III with a total of 488 sampling points (Rodrigues space). For each of the 15 starting orientations, the Rodrigues composition formula in eq. 4.9 was applied to obtain an iso-misorientation surface centered on the starting orientation. The EBSD forward model was used to compute the corresponding patterns, and, after normalization, the dot products of these patterns with the central pattern were computed. The plot in Fig. 4.4 shows the average dot product (averaged over 488 dot products) for each of the eight misorientation values. It is clear from this curve that the dot product decreases sharply with increasing misorientation angle until the angle is about 3°; beyond this value, the average dot product no longer depends on the misorientation angle. This result suggests that for a given experimental pattern and a dictionary with an angular step size of 1.5° (vertical dashed line in Fig. 4.4), there should always be at least one entry in the dictionary for which the dot product with the experimental pattern is significantly above the background dot-product level, taking into account the standard deviations of the dot product values. An angular step size of 1.5° requires, according to eq. 4.5, at least $N = 90$ as the number of samples along the semi-edge of the cubochoric cube.
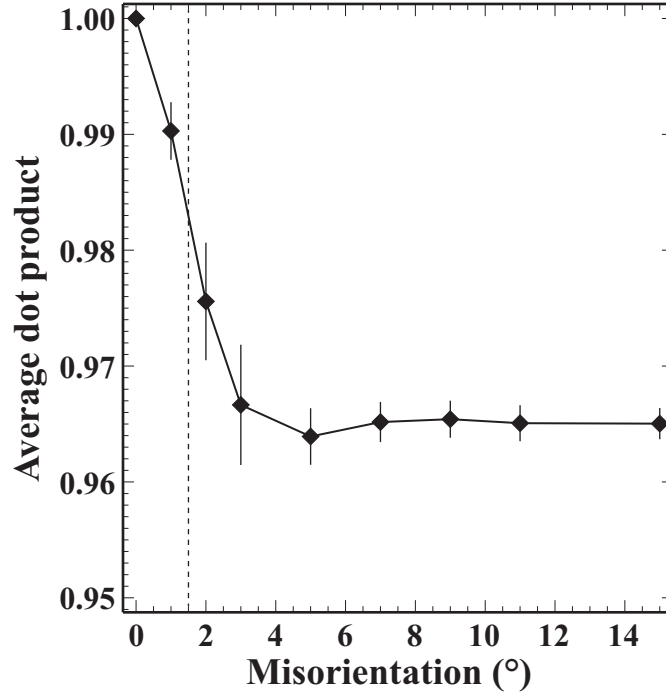
Figure 4.4: Average dot product vs. the misorientation angle; the vertical bars represent one standard deviation.

4.3 Detector Parameter using Derivative Free Optimization

One of the inputs the dictionary method requires is a set of accurate detector parameters to generate the list of all possible diffraction patterns. Since the parameter space for the diffraction modalities is large, standard search algorithms are expected to perform poorly. Also, the derivatives of the backscatter intensity with respect to the detector parameters are not known analytically. The Derivative Free Optimization (DFO) class of algorithms, which only requires function evaluations and no gradient information, represent an attractive approach to solve such a problem. The algorithm to estimate the detector parameters is shown in Fig. 4.5. The true detector parameters are those which maximize the dot product between an experimental pattern and the simulated pattern. Note that the algorithm requires an initial guess for the detector parameters. Since the dot product is highly non-linear with respect to the parameters, it is important to start off reasonably close to the true values. For this dissertation, we have evaluated two DFO algorithm, namely the Nelder-Mead (downhill-simplex) algorithm [103] and the Bound Optimization by Quadratic Approximation or the BOBYQA algorithm [104]. An in-depth review of some of the ma-

Initial guess for detector parameters and euler angles

Experimental diffraction pattern

Generalized Forward Projector

Evaluate dot product

Update detector parameters and euler angles using DFO

Convergence?

Yes

Terminate

No
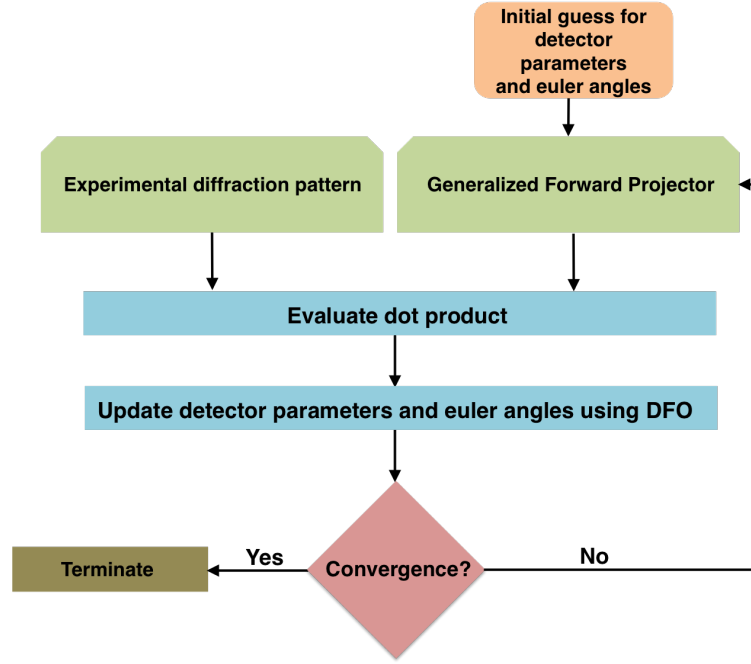
Figure 4.5: Algorithmic flow chart for estimating detector parameters in the dictionary approach

jor DFO techniques and their performance can be found in [105]. Fig. 4.6(a)-(b) shows the convergence behavior of the Nelder-Mead and BOBYQA methods, respectively. The tests were performed on an experimental 480×480 Si EBSD pattern (courtsey Dr. David Fullwood, BYU) with calibrated pattern centers. Three different initial guesses, amounting to 0.42%, 1.04% and 2.08% error in all three pattern centers, were used for the study. The BOBYQA algorithm converged to the same values for all three initial guesses, while the Nelder-Mead converged to a different set of parameters for one of the initial guesses. The BOBYQA algorithm converges faster since a lower number of function evaluations, which is the computational bottleneck, is required. Note that only the pattern centers were refined and no refinement was performed on the Euler angles. Fig. 4.7 shows the performance of these two algorithms compared to the calibrated values. Both algorithms converged reasonably close to the scan values, usually within one pixel.(Detector pixel size, $\delta = 140 \mu$m)
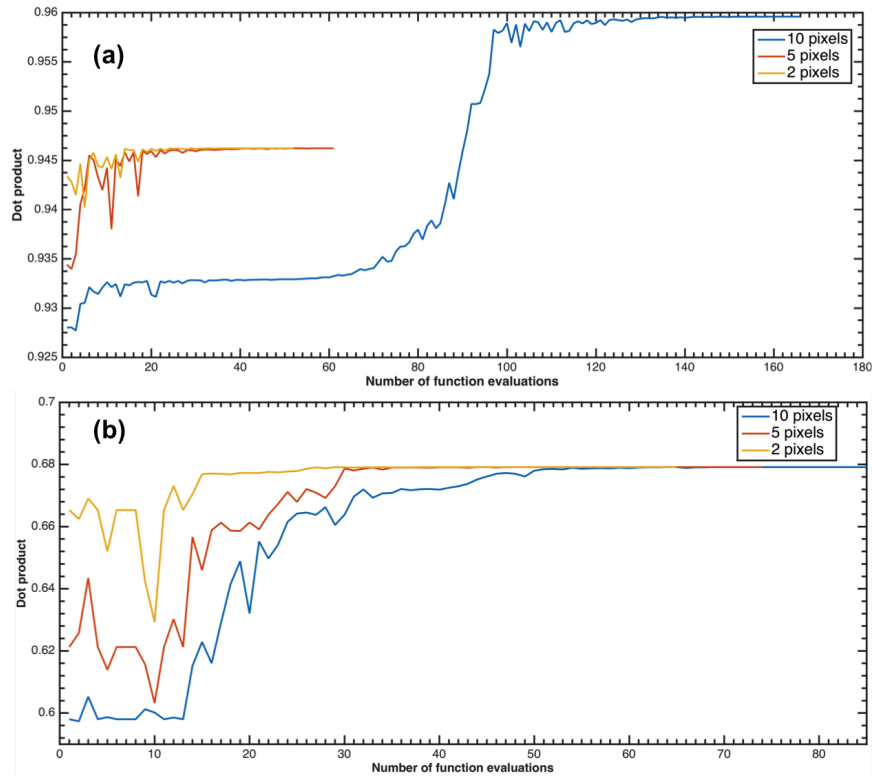
Figure 4.6: Convergence of dot product vs number of function evaluations for different errors in initial guesses of pattern centers for (a) Nelder-Mean and (b) BOBYQA.
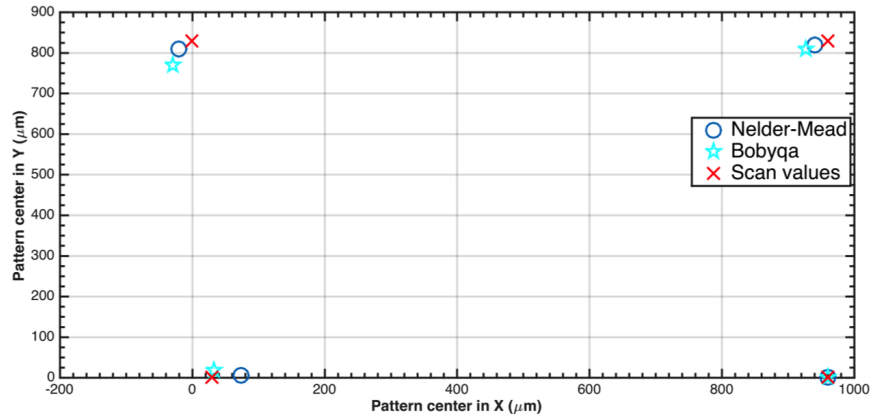
Figure 4.7: Performance of Nelder-Mead and BOBYQA methods to determine pattern centers against a calibrated Si sample. (Initial data courtsey Dr. David Fullwood, Brigham Young University)

4.4 Pre-Processing Diffraction Patterns

The dictionary indexing approach uses various image processing algorithms to either enhance contrast or suppress noise and background in the diffraction patterns for better indexing. As mentioned previously, these pre-processing routines are typically applied to

both the experimental and simulated patterns to avoid introduction of any artifacts. The pre-processing routines includes

- High-Pass Filter: This method filters out the low frequency component i.e., the background, from the diffraction pattern.

- Adaptive Histogram Equalization (AHE): This technique adjusts the histogram in an image locally and enhances the contrast in the image.

- Maximum a posteriori (MAP) estimate: This technique is used to clean image from noisy data using a given noise model. For electron scattering, the noise is Poisson or shot noise.

We will discuss each one of these pre-processing algorithms in this section. We will also present results of applying these image processing tools to experimental diffraction patterns.

4.4.1 High-Pass Filter

The High-Pass filter are a class of frequency filters which processes images in the Fourier domain. This class of technique is used for image enhancement, noise reduction etc. In our case, we use this frequency domain filter to suppress the background signal in the diffraction pattern. The image, $\mathbf{X}$, is transformed using the Fast Fourier Transform (FFT) to obtain the corresponding image in the frequency domain, $\mathcal{F}(\mathbf{X})$. The Fourier transform of the image is then multiplied by an inverted Gaussian mask, $\mathbf{H}$, to suppress the low frequency components in the image. The resulting image is transformed back to the spatial domain using the inverse Fourier transform to obtain the filtered image. The final filtered image, $\mathbf{Y}$, is given by

$$\mathbf{Y} = \mathcal{F}^{-1}[\mathcal{F}(\mathbf{X}) \circ \mathbf{H}]. \tag{4.17}$$

The $\circ$ operator represents the Hadamard (element-wise) product of the two matrices. Fig. 4.4.2 shows the application of a high-pass filter to an experimental EBSD pattern. The background signal is suppressed and the resulting image shows sharper bands.
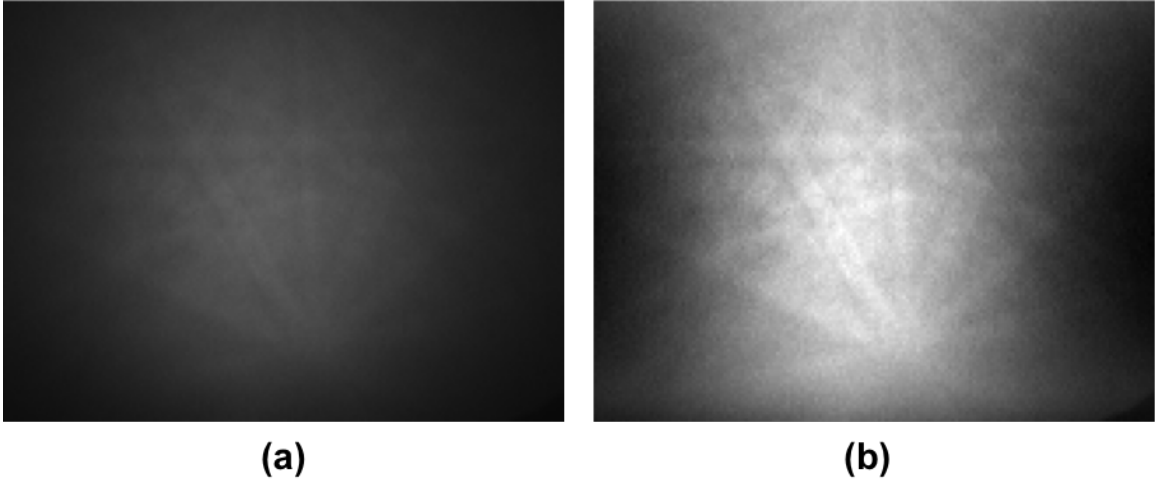
Figure 4.8: Application of high-pass filter algorithm described above to an experimental EBSD pattern in Co. (Pattern courtsey Dr. Bart Winiarski and Dr. Tim Burnett, University of Manchester.)

4.4.2 Adaptive Histogram Equalization

Adaptive Histogram Equalization (AHE) is a contrast enhancement tool for images. It differs from regular histogram equalization in that the method computes a number of histograms, each corresponding to different sections of the image, and uses them to redistribute intensity in the image, while the regular histogram equalization uses the histogram of the entire image. Since this method only looks at the neighborhood of a pixel, it works locally and enhances the edge definition in an image. In this section, we will first introduce the algorithm for regular histogram equalization and extended it to AHE. We will also discuss methods for efficient implementation of the algorithm.

Consider a grayscale image, $\mathbf{X}$, with L (typically 256) gray levels, which has n_i number of pixels for each gray level, i in the image. If there are n total pixels in the image, then the probability of a pixel having gray level i is given by

$$p_{\mathbf{X}}(i) = \frac{n_i}{n}, \qquad 0 \leq i \leq L.$$

$p_{\mathbf{X}}(i)$ is the probability distribution function for the gray levels in the image. The cumulative distribution function, $C_{\mathbf{X}}$, for $p_{\mathbf{X}}(i)$ is given by

$$C_{\mathbf{X}}(i) = \sum_{j=0}^{i} p_{\mathbf{X}}(j).$$

The goal of histogram equalization is to transform the original image, $\mathbf{X}$, by a function, $\mathcal{T}$, such that the resulting image, $\mathbf{Y} = \mathcal{T}(\mathbf{X})$, has a constant probability distribution function $p_{\mathbf{Y}}(i)$. The cumulative distribution function for the image $\mathbf{Y}$, $C_{\mathbf{Y}}$, will be linearly dependent on the gray scale level up to a constant, i.e., $C_{\mathbf{Y}}(i) = iK$. For a pixel in $\mathbf{X}$ having gray level ν, the transformed gray level is given by

$$\mathcal{H}(\nu) = \left\lfloor \frac{C_{\mathbf{X}}(\nu) - C_{\mathbf{X}}^{min}}{n - C_{\mathbf{X}}^{min}}(L-1) \right\rfloor. \tag{4.18}$$

Here, $C_{\mathbf{X}}^{min}$ is the minimum non-zero value of the cumulative distribution function and $\lfloor . \rfloor$ is the floor function. The histogram equalization effectively spreads out the information in the image to all available gray levels, thereby enhancing contrast.

The Adaptive Histogram Equalization technique is just a variation of the regular histogram equalization in which the cumulative distribution function used is computed only for a section of the image and not the entire image. The size of this region is a user input in this variation. This is shown schematically in Fig. 4.9. For an image, $\mathbf{X}$, only a small sub-region, $\mathbf{S}$, is considered around each pixel. The gray value is update according to equation 4.18, with $C_{\mathbf{X}}$ replaced by C_S, the cumulative distribution function of the sub-region $\mathbf{S}$. Note that pixels near the image boundary have to be treated separately, because their neighborhood does not lie completely within the image.

While the AHE offers advantages over the regular histogram equalization, there is a substantial computational cost associated with it. For the regular histogram equalization, only one cumulative distribution function is calculated. In the AHE variation, the number of histograms to be calculated is equal to the number of pixels in the image. Therefore, an approximate method, which is computationally more efficient is required. This is done through an interpolation scheme schematically shown in Fig. 4.10. The image, $\mathbf{X}$, is divided into a number of smaller sub-regions, $\mathbf{S}_i$, marked by solid black lines. The cumulative histogram for each one of the sub-regions is computed. These cumulative histograms are appropriate for the center pixel (solid black squares) of the sub-region $\mathbf{S}_i$. The value for an arbitrary pixel (marked in yellow) is computed by bilinear interpolation from the nearest four sub-regions (shaded blue). If the pixel is close to an edge (shaded green) such that it
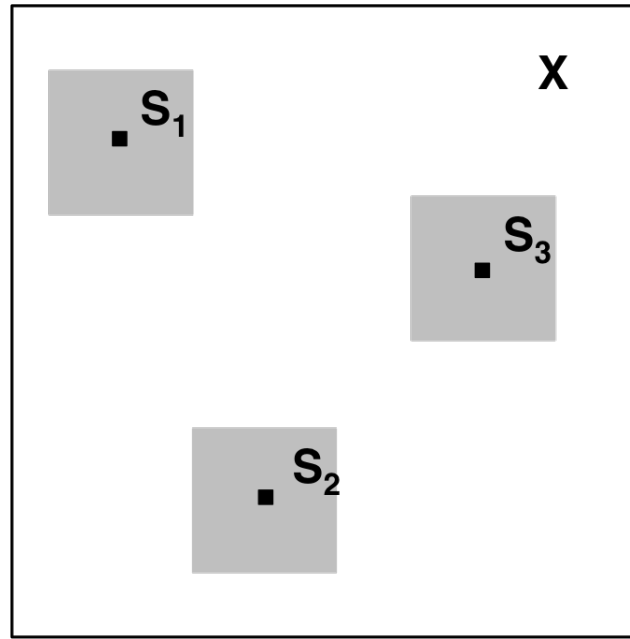
Figure 4.9: Schematic representation of adaptive histogram equalization algorithm.
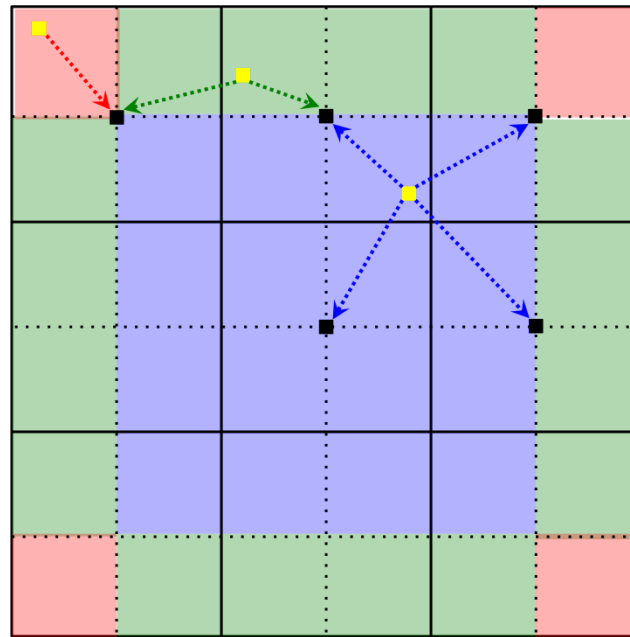
Figure 4.10: Schematic representation of a computationally efficient adaptive histogram equalization algorithm using interpolation.

only has two neighboring sub-regions, then linear interpolation is used. If the pixel is close to the corner (shaded red), then the cumulative distribution function of the corner tile is used.

A disadvantage of the method is that it is indiscriminate; it increases the contrast of
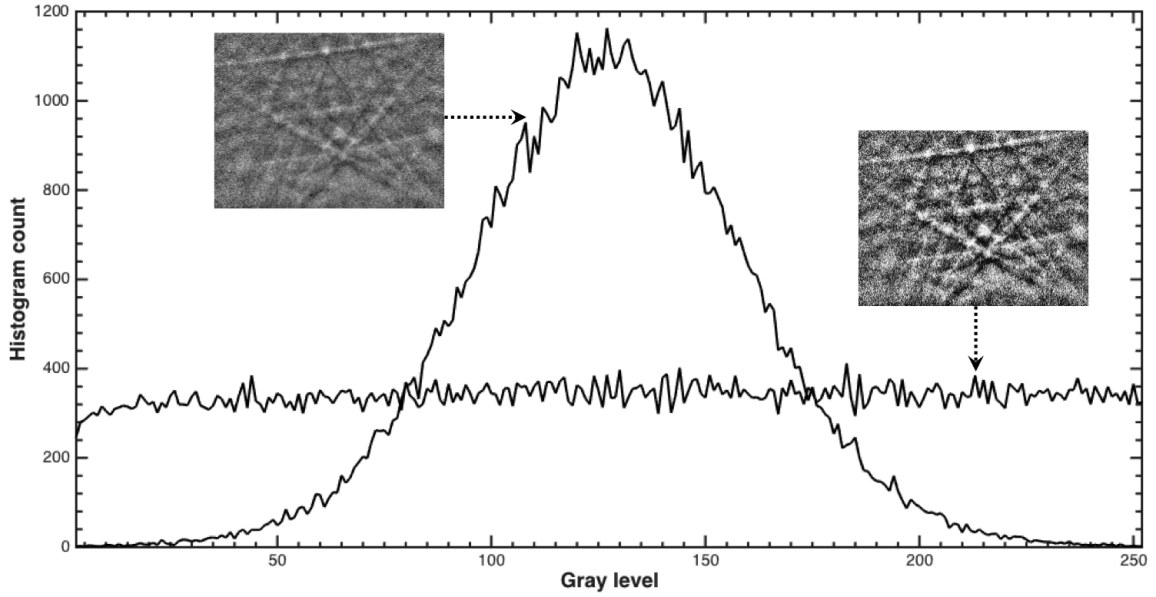
Figure 4.11: Histogram and diffraction pattern before and after AHE operation for a clinopyroxene sample. Tile size was 6×6 pixels.(Patterns courtsey Dr. Katharina Marquardt, University of Bayreuth.)

both signal and noise. There are other variations of the algorithm to address this issue, such as the *Contrast Limited* AHE etc., variations can be found in [106]. An example of AHE applied to a typical EBSD pattern from clinopyroxene is shown in Fig. 4.11. Note that the band edges have more contrast in the processed image.

4.4.3   MAP estimate with Poisson noise model

The maximum a posteriori or MAP estimator uses Bayesian statistics to define the probability of an event that cannot be repeated numerous times. In very general terms, a prior model for the system of interest is assumed and the model is updated based on the observed data, in accordance with Bayes theorem. Mathematically, Bayes theorem can be stated as

$$p(x|y) = \frac{p(x)p(y|x)}{p(y)},$$

where, $p(x|y)$ is the a posteriori probability of x, given y, $p(x)$ is the probability of x and represents the prior model and $p(y|x)$ is the likelihood estimator, which denotes the probability of y given x. $p(x)$ can be interpreted as our prior model of the system and $p(y|x)$ is the observed data. Once the data is observed, our prior model is updated to $p(x|y)$ using Bayes theorem stated above. The problem of de-noising an image is formulated as follows:

(a) **(b)**
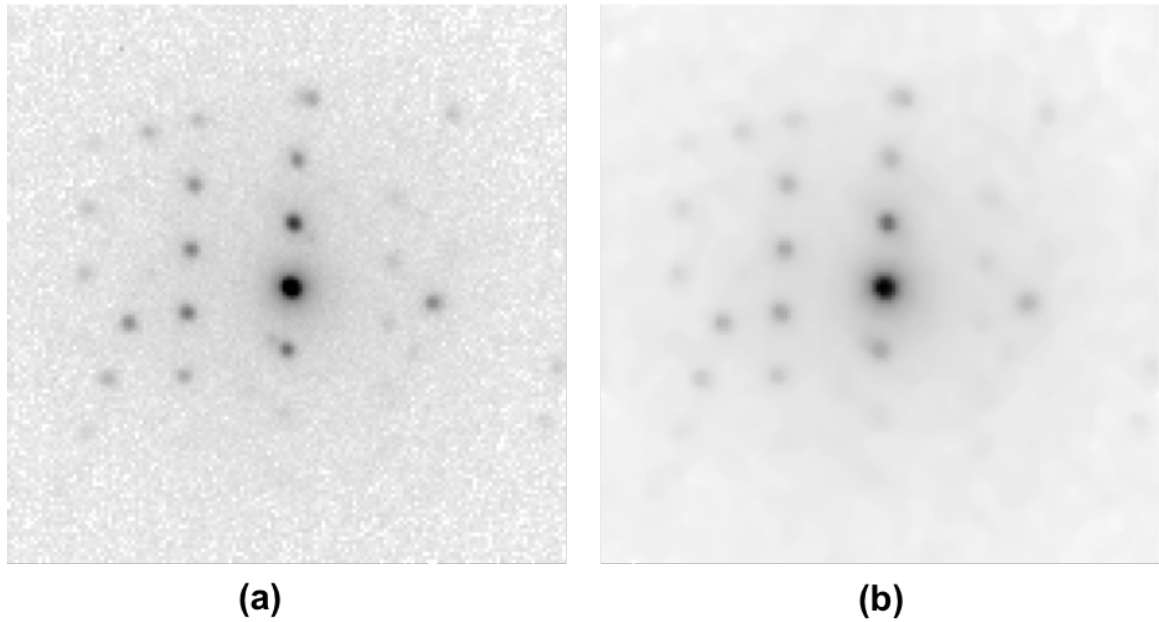
Figure 4.12: Typical zone axis precession diffraction pattern in reverse contrast from a Cu sample (a) prior and (b) post MAP estimate.(Pattern courtsey Asher Leff and Dr. Mitra Taheri, Drexel University.)

the diffraction pattern is assumed to be a sum of a"clean" image and independent and identically distributed (i.i.d) noise such that

$$Y = X + W$$

For electron diffraction, the noise, W, is Poisson noise. The goal of the MAP estimator is to approximate X as closely as possible. The prior model, $p(x)$, is modeled by the Q-generalized Gaussian Markov random field (GGMRF) model, whereas the noise, which is the likelihood estimator, $p(y|x)$, is estimated using a normalized Poisson distribution. The maximization of the a posteriori probability, $p(x|y)$, is done using the iterative coordinate descent (ICD) method. Details of image filtering using MAP estimate can be found in [107–110]. Fig. 4.12 shows an actual experimental pattern (reverse contrast) prior to and post the MAP estimate operation. The background noise towards the edge of the PED pattern is suppressed, while all the diffraction spots are intact.

4.5   Maps from Dictionary-based indexing

The various parameters for EBSD indexing using commercial packages, introduced in chapter II, are calculated in Hough space. The dictionary based approach fundamentally differs from the Hough transform based methods and much of the parameters derived from the Hough based method needs to be re-defined. In this section, we will revisit those definitions and re-define them. We will also introduce some new parameters that can be extracted from the dictionary approach.

- Confidence Index: The confidence index (CI) for each experimental pattern is taken as the highest dot product value.

- Image Quality: The image quality (IQ) is re-defined to capture the sharpness of the pattern. It is given by [23]

$$IQ = 1 - \frac{J}{J_{res} w_{tot}}. \tag{4.19}$$

If $w(k_x, k_y)$ denotes the power spectrum of the EBSD image, then J, J_{res} and w_{tot} are defined as

$$
\begin{aligned}
J &= \sum_{k_x=-N/2}^{N/2} \sum_{k_y=-N/2}^{N/2} w(k_x, k_y)(k_x^2 + k_y^2) \\
J_{res} &= \frac{1}{N^2} \sum_{k_x=-N/2}^{N/2} \sum_{k_y=-N/2}^{N/2} (k_x^2 + k_y^2) \\
w_{tot} &= \sum_{k_x=-N/2}^{N/2} \sum_{k_y=-N/2}^{N/2} w(k_x, k_y).
\end{aligned}
\tag{4.20}
$$

The new parameters defined in the dictionary approach for the EBSD modality are

- Average Dot Product Map (DP Map): This parameter is calculated from just the processed experimental patterns. The average dot product of an experimental pattern with its four nearest neighbor is plotted as a map. Similar neighbor patterns, for instance in the grain interior, leads to higher dot products, whereas dis-similar patterns, for instance near grain boundaries, lead to lower dot products, thereby leading to contrast. This helps delineate the different phases and boundaries in the sample.

Note that special care must be taken for points near the edge.

- Orientation Similarity Map (OSM): The dictionary method saves the top N (typically $30 - 40$) matches. The average common matches from the list of these N orientations with its four nearest-neighbor is plotted as a map. For grain interiors, the average number of matches is high, leading to bright regions. However, close to the grain boundaries, this parameter is smaller leading to contrast. This map is helpful in delineating the grain boundaries. Again, note that points close to the edge need to be treated separately.

CHAPTER V

Application of Forward Models

In this chapter we will look at several applications of forward modeling to materials characterization problems. Specifically, we will be looking at dictionary indexing of electron diffraction modalities, application of forward modeling to orientation refinement and finally the use of cubochoric representation along with a model based iterative reconstruction technique to formulate the pole figure inversion problem as a standard tomography problem. We will compare and contrast the results of the newly proposed techniques with the existing methods and outline the advantages/disadvantages for each them.

5.1 Dictionary Indexing of Diffraction Modalities

In this section, we present the results of the dictionary indexing approach for the three electron diffraction modalities: Electron Backscatter Diffraction, Electron Channeling Patterns and Precession Electron Diffraction. For the EBSD modality, we will be presenting indexing results for four different cases where the traditional method struggles: a Nickel dataset with varying acquisition conditions, a shot peened Aluminum dataset acquired at low microscope acceleration voltage, a low symmetry orthorhombic forsterite and a challenging mixture of monoclinic clinopyroxene, cubic garnet and amorphous melt. For the ECP modality, a proof of concept of the dictionary method is shown for poly-Silicon. Furthermore, the dictionary method is applied to generate the first inverse pole figure using channeling patterns for the same poly-Silicon sample. Finally, for the PED modality, we will consider the case of highly deformed cold rolled Cu sample.

Scan	Gain (dB)	Exposure Time (msec)	Indexing Success rate (%)
1	18.02	0.94	99.1
2	30.4	0.20	37.3
3	31.53	0.17	19.4
4	36.0	0.1	0.1

Table 5.1: Gain, exposure time and indexing success rate for the four scans shown in Fig. 5.1.

5.1.1   Electron Backscatter Diffraction

Fast acquisition/High gain: Nickel

10 EBSD scans were performed on the same area on the sample with varying detector gain and exposure time to obtain a constant exposure level of 90% (Courtesy Dr. Stuart Wright, EDAX). With increasing gain and decreasing exposure time, the pattern quality decreases and so does the fraction of successfully indexed points. The patterns for all the scans were saved and re-indexed using the dictionary approach. Fig. 5.1 shows IPFs using the TSL software (top row) for four of these scans. From left to right, the gain, exposure time and indexing success rate are shown in Table 5.1. The Hough mask was 9×9 with $2°$ θ step and 85% ρ fraction. 9 bands were considered for indexing and the patterns were binned 8×8. The bottom row shows the indexing of the same scans using the dictionary approach. The dictionary approach still gives near perfect indexing for the third scan when the Hough based method (conventional ISR^{CI}; threshold CI of 0.1) has close to 20% success rate. If the indexing success metric is changed to less than $5°$ disorientation from a reference pattern, then the result improves to about 40% success rate (conventional ISR^{RK}). When the conventional Hough based method completely breaks down with almost a 0% indexing success rate, the dictionary method still produces a reasonably clean IPF. The indexing rates of the different methods are shown in Fig. 5.2. The dictionary method has close to 80% successful indexing rate for the noisiest patterns. The efficacy of the traditional Hough transform based method can be improved using either cleanup procedures or compromising the spatial resolution by averaging the diffraction pattern with its nearest neighbors to improve the signal to noise ratio (NPAR).
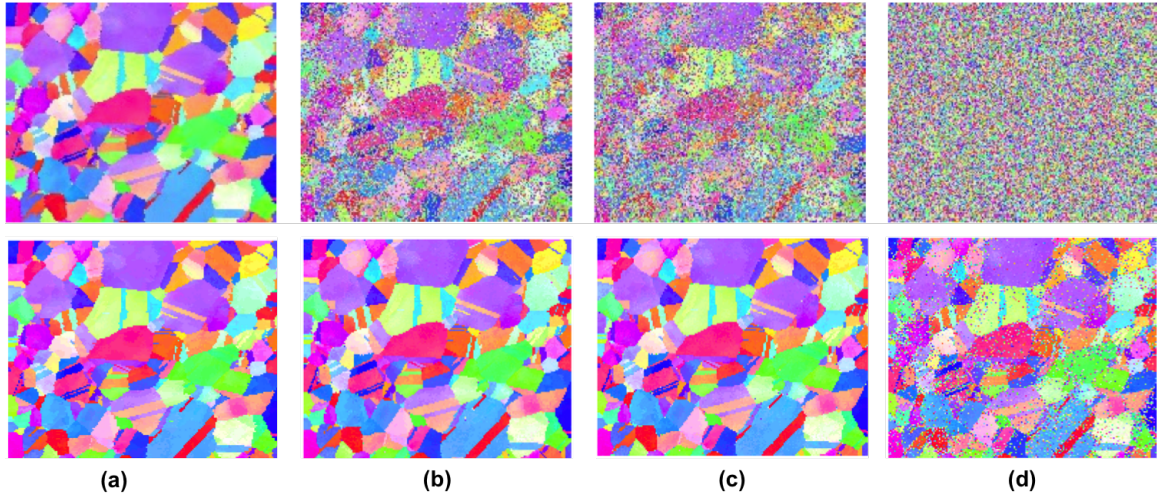
Figure 5.1: Comparison of Hough transform based indexing (top panel) to dictionary based indexing (bottom panel) for Nickel sample with varying noise levels. Parameters detailed in the text.
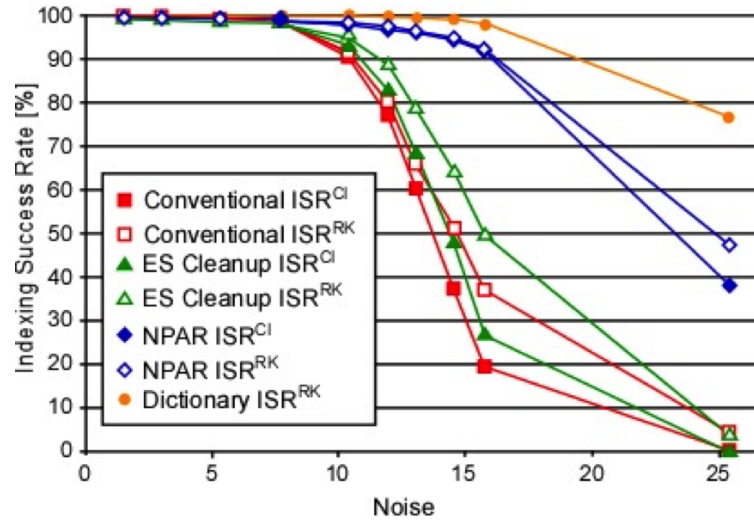
Figure 5.2: Comparison of indexing success rates with varying noise levels for different techniques.(Plot courtsey Dr. Stuart Wright, EDAX)

Low keV: Shot-peened Aluminum

Shot peened Aluminum has very small grains with high orientation gradient close to the shot peened surface and serves as an ideal candidate to study the efficacy of the dictionary method for low keV EBSD. Fig. 5.3(a) shows the secondary electron image of such a sample with the region of interest (ROI) indicated by the arrow (data courtsey Dr. Tim Burnett and Dr. Bart Winiarski, University of Manchester). The patterns were acquired at 5 keV acceleration voltage and a step size of 120 nm using both high and low gain. Fig. 5.3(b) shows the Orientation Similarity Map (OSM) (using the top 20 matches) of the ROI showing
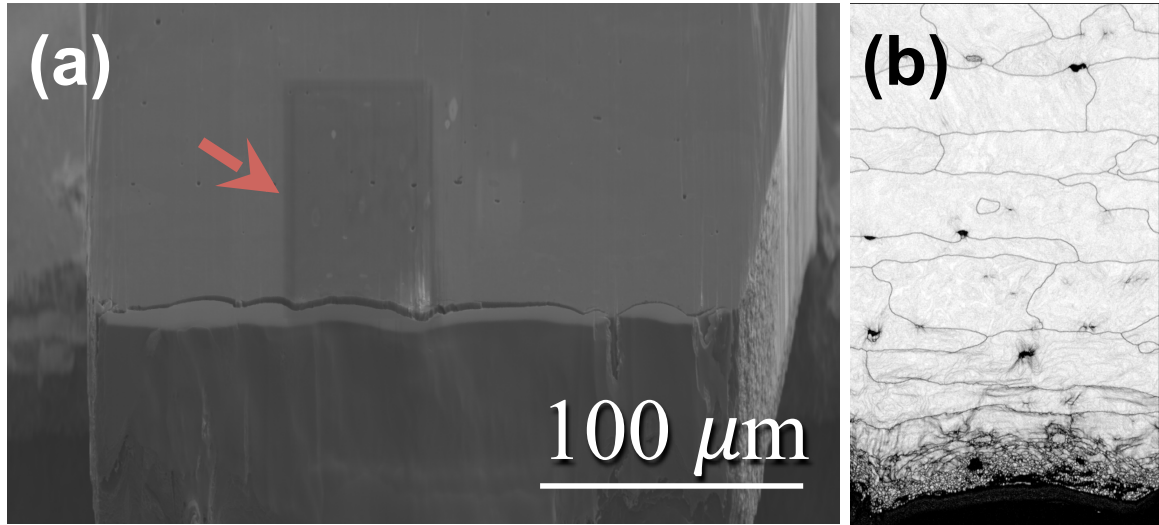
Figure 5.3: (a) Secondary electron image of the shot peened area with the region of interest (ROI) marked with the arrow and (b) Orientation Similarity Map (OSM) of the ROI showing relevant features.

the fine features close to the shot peened surface.

The IPF-Z map of the ROI for the low gain acquisition using the dictionary method (top panel) and commercial Aztec^{TM} package (bottom panel) is shown in Fig. 5.4(a). The dictionary method gives superior results close to the grain boundaries. The dictionary method also captures the fine orientation gradients in each grain due to severe plastic deformation during the shot peening. Finally, the dictionary method close to the shot peened surface shows the microstructure and orientation gradient in exquisite detail whereas the commercial package largely fails in this region. The corresponding IPF-Z map for high gain acquisition is shown in Fig. 5.4(b). While the dictionary method fails to index patterns close to the shot peened surface, the region away from the surface is accurately indexed. The commercial package produces a map with less than 5% indexing success rate.

Finally, Fig. 5.5(a) shows the OSM (using top 20 matches) for another dataset acquired at 10 keV with 25 nm step size and low gain conditions close to the shot peened surface. The IPF-Z map using the dictionary method and the Aztec^{TM} software is shown in Fig. 5.5(b)-(c) respectively. The fine features in the microstructure which are not identified using the commercial package are very clearly delineated using the dictionary method. The fine microstructural features are hypothesized to be the recrystallization centers during heat treatment and these results can have broad implications in studying the role of crystal
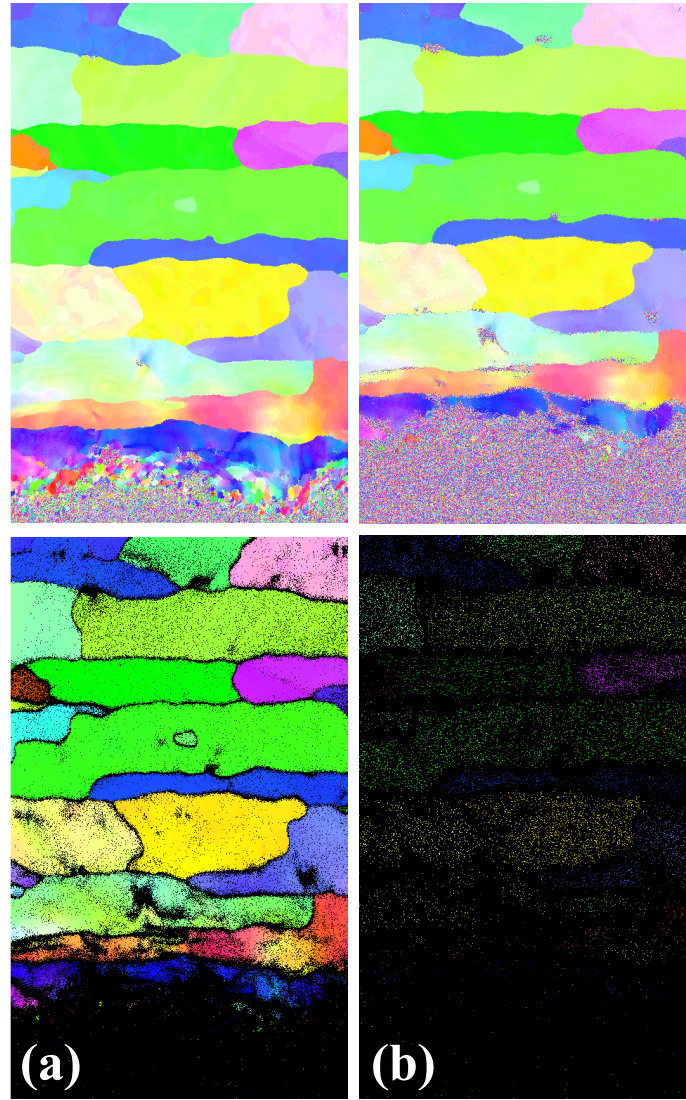
Figure 5.4: IPF-Z map for Dictionary Indexing (top panel) v/s commercial Hough transform-based Aztec™ software (bottom panels) for (a) low gain and (b) high gain settings at 5 keV acceleration voltage. Other acquisition conditions are listed in the text.

orientation in recrystallization site selection during recrystallization and grain growth.

Low symmetry and multiphase: Forsterite/Clinopyroxene-Garnet-Melt

The final case study for the EBSD modality is an orthorhombic forsterite sample and a multiphase geological system containing clinopyroxene (cpx;monoclinic), garnet (grt;cubic) and melt (amorphous) (all data courtesy Dr. Katharina Marquardt, Univ. of Bayreuth). The forsterite sample is an interesting case study for the dictionary method because of its low symmetry and known issues with indexing patterns as its pseudosymmetric variant when
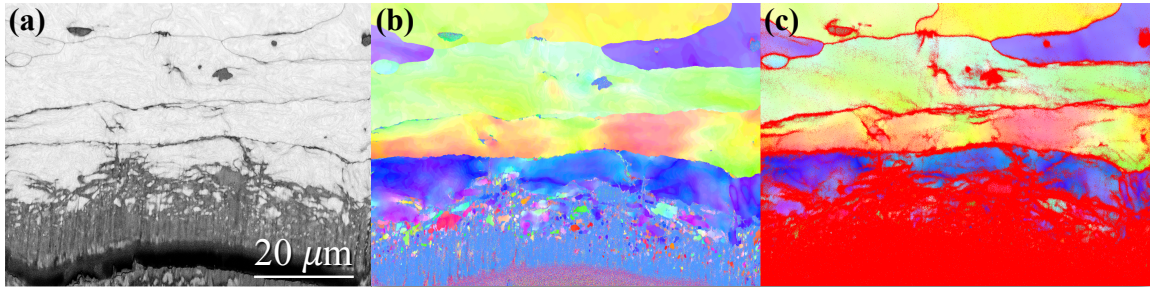
Figure 5.5: (a) Orientation Similarity Map (OSM) of shot peened region. IPF-Z map using (b) the dictionary method and (c) hough transform-based commercial Aztec^{TM} software. The dictionary approach reveals the microstructure at the shot peened surface in exquisite detail. The acceleration voltage was set to 10 keV. Other acquisition parameters are listed in the text.

the conventional Hough based methods are used. The cpx-grt-melt mixture is interesting not only as a very commonly studied multi-phase geological system but also because the post-processing cleanup procedures cannot be employed due to the amorphous melt phase. Fig. 5.6 shows the effect of the image processing routines on the ADP map. The raw background subtracted EBSD patterns are shown in Fig. 5.6(e). Fig. 5.6(a) shows the ADP map for the background corrected raw patterns. The histogram of the pixel intensities is shown in red in Fig. 5.6(b). The image histogram after application of the Adaptive Histogram Equalization (AHE) filter is shown in blue. The AHE filter distributes the image intensity over the maximum possible range and enhances the contrast in the diffraction patterns. The ADP map after applying the AHE filter is shown in Fig. 5.6(c). An interesting region where the diffraction information from the crystal and melt overlap is shown in Fig. 5.6(d). The slight variations in the gray level are caused by the amorphous melt pattern superimposing a weaker pattern of a garnet. This visualizes the third dimension captured by the interaction volume of the electron beam within the sample interior.

Fig. 5.7 shows the montage of results for the forsterite sample. The raw EBSD patterns shown in Fig. 5.7(e) were acquired on a FEI Quanta SEM using a probe current of 2 nA, 30 kV acceleration voltage, and a step size of $0.2\mu m \times 0.2\mu m$. The microscope is equipped with a DigiView 5 camera with $1395 \times 1040 \times 12$ bit resolution and the EDAX/TSL OIM^{TM} software (version 7.0; EDAX/ TSL, Draper, UT, USA). Patterns were captured with 4×4 binning on the camera. A maximum camera gain, background removal but no image processing were applied. Forsterite was the only candidate phase while performing the indexing using
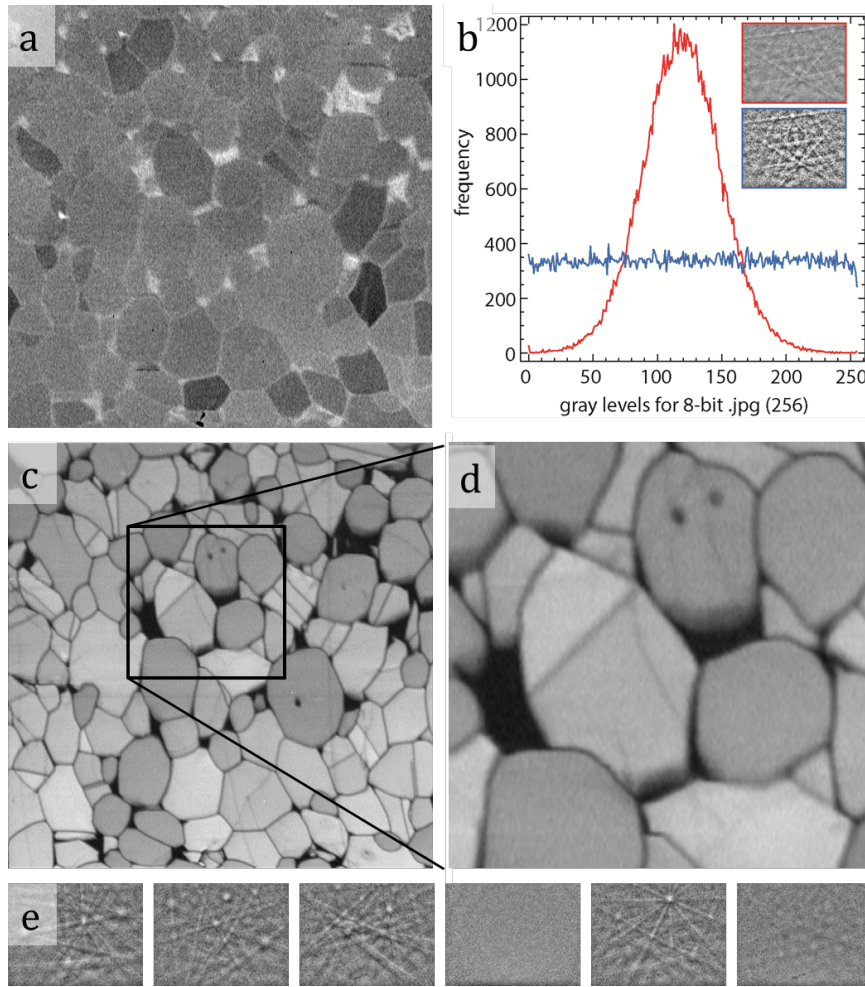
Figure 5.6: Illustration of image processing prior to nearest neighbor similarity map calculation. (a) Average dot-product (ADP) map for the raw background subtracted patterns, and (b) shows a histogram (red) for a background-subtracted EBSP outlined in red, along with the EBSP and histogram after adaptive histogram equalization in blue and outlined in blue. (d) ADP map after applying adaptive histogram equalization before calculating the average dot products. (d) Magnified region from (c), with an interesting region where backscatter information of crystal and melt overlap. The lowest row, e) displays exemplary raw EBSPs.

both the TSL software as well as the dictionary method. The raw IPF-Z map using the TSL software and an enlarged view of a small region of interest is shown in Fig. 5.7(a). The corresponding IPF maps post clean up is shown in Fig. 5.7(b) with the grain boundaries highlighted in white. The cleanup procedure produces unphysical "phantom" grains inside one of the grains as shown in the enlarged view. The results of indexing using the dictionary method is shown in Fig. 5.7(c). The grains boundaries are sharply delineated with consistent results across the grain boundary as well as absence of any "phantom" grains. Additionally, no post processing cleanup of the raw IPF map is needed when the dictionary approach
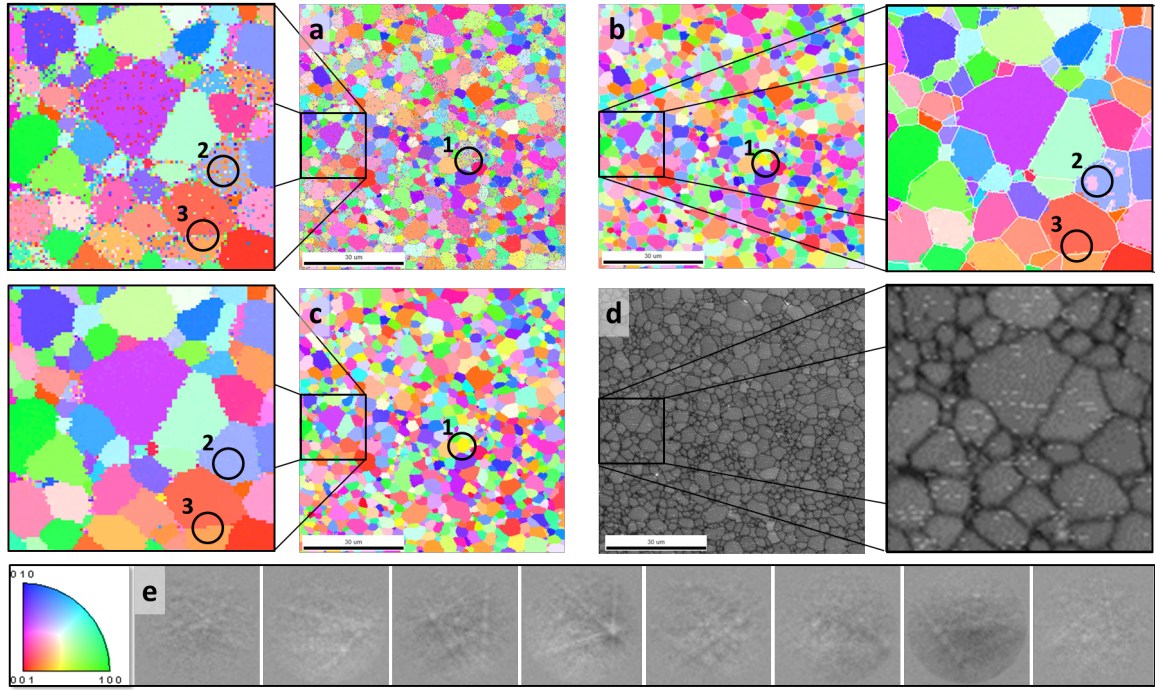
Figure 5.7: Comparison of OIM indexing (upper row) and data fitting using the dictionary approach (lower row). In both examples the EBSP were indexed with forsterite being the only phase. Representative EBSPs are depicted in the third row. a) OIM indexing, raw data, on the left an enlargement of the data is shown. b) Cleaned OIM data set, highlighting the grain boundaries in white. c) Same data set as in a, but indexed using the dictionary approach, note the absence of randomly -indexed pixels in the data set and the consistency of indexing across grain boundaries and in the crystal interior; examples are encircled in the enlargement of a and c. d) Grain boundaries highlighted (dark) using the dictionary data. Displayed is the average dot product map (ADP) that shows average dot product value for each pixel the of the EBSD pattern with its four nearest neighbors. In the third row (e) the color legend and typical EBSD patterns are displayed. The blow-ups of the panels a,b,c, and d are on the left and right hand side of the respective pannels (Patterns courtesy Dr. Katharina Marquardt, Univ. of Bayreuth).

is used. Fig. 5.7(d) shows the Average Dot Product (ADP) map. The grain boundaries are darked than the grain interior points. Furthermore, the charging effects can be seen as bright spots in the ADP map.

Fig. 5.8(a) shows the disorientation distribution of the grains indexed using the TSL OIM$^{\text{TM}}$ package with and without pseudosymmetry correction. The distribution for a random texture is shown on the same curve as a guide. A similar disorientation distribution map of the grains indexed using the dictionary method is shown in Fig. 5.8(b). The distribution closely follows a random texture as expected for this system.

A raw EBSD phase map collected using the HKL system is displayed in Fig. 5.9(a). In the presence of melt at the interfaces, data cleanup is not recommended. Fig. 5.9(e) shows
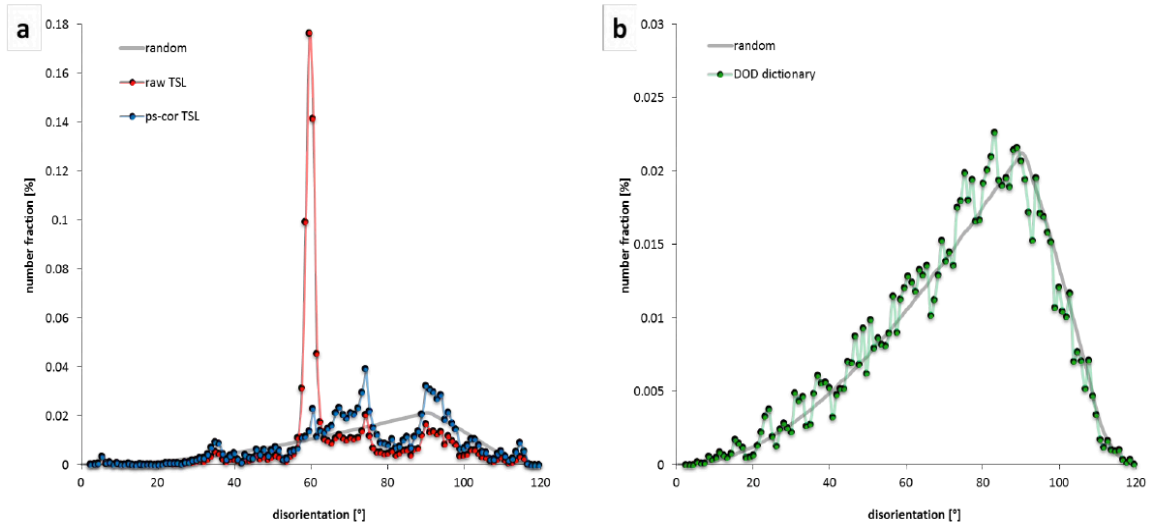
Figure 5.8: Disorientation distribution plots resulting from the different analyses approaches, a) OIM raw indexing (red) and OIM after pseudo-symmetry correction (blue); b) dictionary approach raw data (green), no second graph is displayed as no corrections apply to the dictionary; c) discrepancy in indexing between DI and OIM displayed as disorientation between the respectively indexed pixels. The disorientation between two pixels indexed using the DI or Hough-transform based methods is minimal if the same or similar results are obtained. Different indexing results of same pixels are related to pseudo-symmetric relations as well as other issues such as the assignment of grain boundary pixels to one or the other grain (Patterns courtesy Dr. Katharina Marquardt, Univ. of Bayreuth).

the phase map derived using the four individual highest dot product maps displayed in Fig. 5.9(f)-(i) for cpx, grt, melt pools and grt-cpx phase boundaries, respectively. The joint histogram in Fig. 5.9(b) shows the dot product values for the best fit for clinopyroxene and garnet; there are 250,000 points in this scatter plot. The two dominant clusters correspond to high dot products obtained using the garnet dictionary and the clinopyroxene dictionary, the smaller cluster to the lower left corresponds to EBSD patterns that have a poor match against both dictionaries; those points are assigned to the melt phase. Points above the diagonal of the joint histogram have a larger best match with respect to garnet and are hence assigned to the garnet phase (red) in the phase map (Fig. 5.9(e)). The remaining points have a larger best match for clinopyroxene and are represented in blue in the phase map. The curves along the horizontal and vertical axes in the joint histogram represent the projections of the histogram onto the clinopyroxene and garnet axes. Note that the clinopyroxene and garnet point clouds consist of overlapping blobs that correspond to the individual grains in the microstructure. Overlap patterns obtained near grain boundaries typically correspond to points in between the three major clusters of the joint histogram.
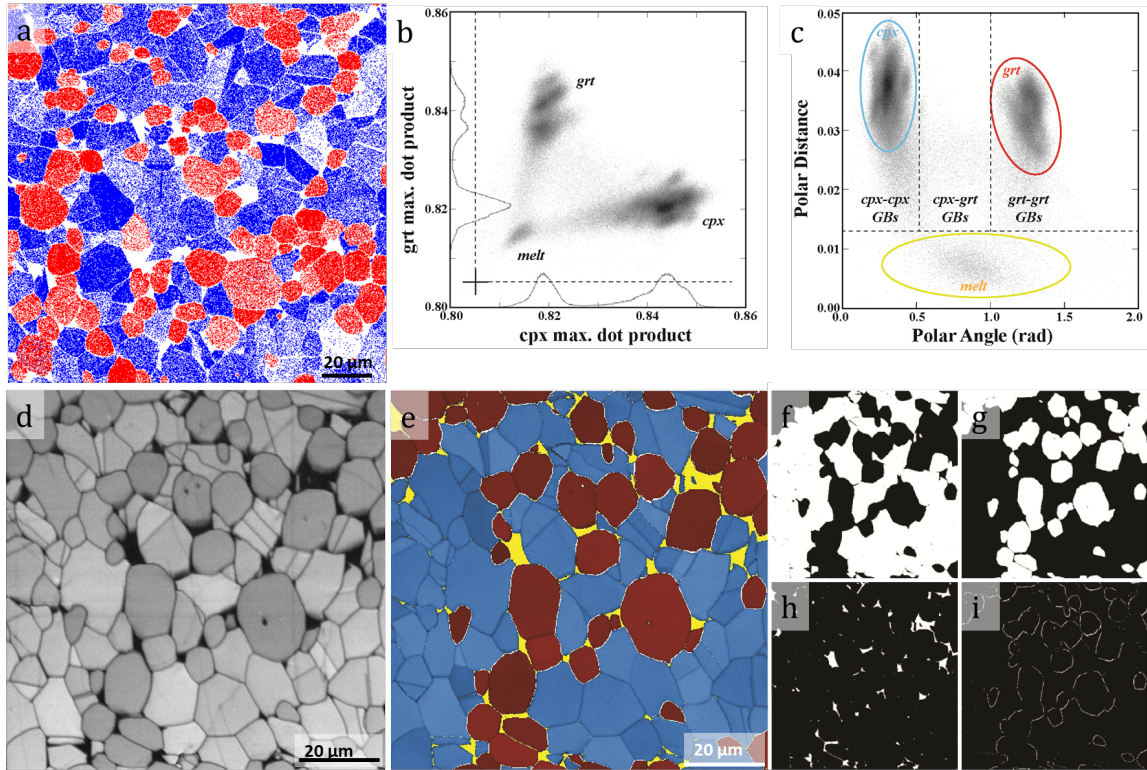
Figure 5.9: Phase identification using different indexing routines. a) indexing using Hough transform-based indexing in HKL, the map was acquired next to the map displayed in (d),(e),(f),(g),(h),(i), using the same settings as for the later. 44% of pixels stay without a solution. Post processing is largely prevented by the presence of the melt phase. b) Indexing by means of DI. The dot product values of garnet and clinopyroxene are plotted versus each other. (c) Plot of the polar distance versus the polar angle determined using the DI approach. The three phases can be clearly separated. d) average dot product map obtained from DI indexing. Grain, phase and twin boundaries are nicely delineated. e) Phase identification in a 2D map representation using the differentiation obtained from b and c respectively. Blue: cpx; Red: Garnet, Yellow: Amorphous (melt) phase and white: wetted Grt-Cpx phase boundaries. (f)-(i) Dictionary indexing confidence index map (DI CI). Light colors correspond to high dot products, dark are low (i.e., poor or no pattern matches); the dot product for experimental images vs. the cpx dictionary is displayed in f. g) Garnet DI CI, (h) Melt pools DI CI, (i) Grt-Cpx-phase boundaries (Patterns courtesy Dr. Katharina Marquardt, Univ. of Bayreuth).

The color map in Fig. 5.9(e) is obtained by merging Fig. 5.9(f)-(i) together with different color values. The polar representation of the joint histogram in Fig. 5.9(c) provides a better separation between the clinopyroxene and garnet phases and the melt phase, and was used to obtain the binary maps in panels Fig. 5.9(f) through (i). The lines limiting the fields between the three phases were chosen at the local point density minimum, and for the clinopyroxene garnet mixed patterns attributed a width of 0.5 rad of the polar angle.

Fig. 5.10 displays the average dot product for the top fifty matches for each sampling point of the partially molten residual eclogite averaged over the complete data set as a
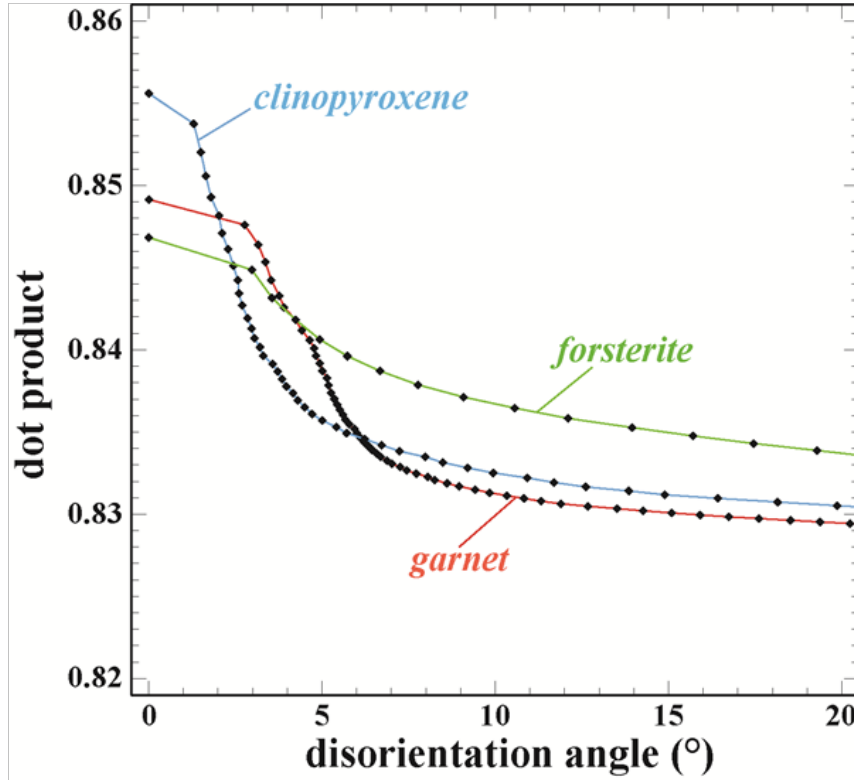
Figure 5.10: Graph showing the dot product values obtained by multiplying an experimental EBSP with the dictionary pattern versus the disorientation between the experimental EBSP and the simulated EBSP (Patterns courtesy Dr. Katharina Marquardt, Univ. of Bayreuth).

function of the disorientation angle between the top match and the lower matches for both the garnet (red) and clinopyroxene (blue) phases. The orientation for which the highest dot product occurs is used as the orientation assigned to the experimental pattern. The next nearest matches all have lower dot products and correspond to a gradually increasing disorientation with respect to the best match pattern. For disorientations larger than about 10°, the dot product values level out and oscillate around a background value.

Accuracy and Precision

Finally, we will conclude this section with a review of the accuracy and precision of the dictionary method compared to the Hough transform based method. For this study, 1000 simulated Ni patterns with added Poisson noise were used. The patterns were generated for a set of random orientations and realistic detector parameters. The patterns were indexed using both the dictionary method and the Hough transform method. The maximum, mini-
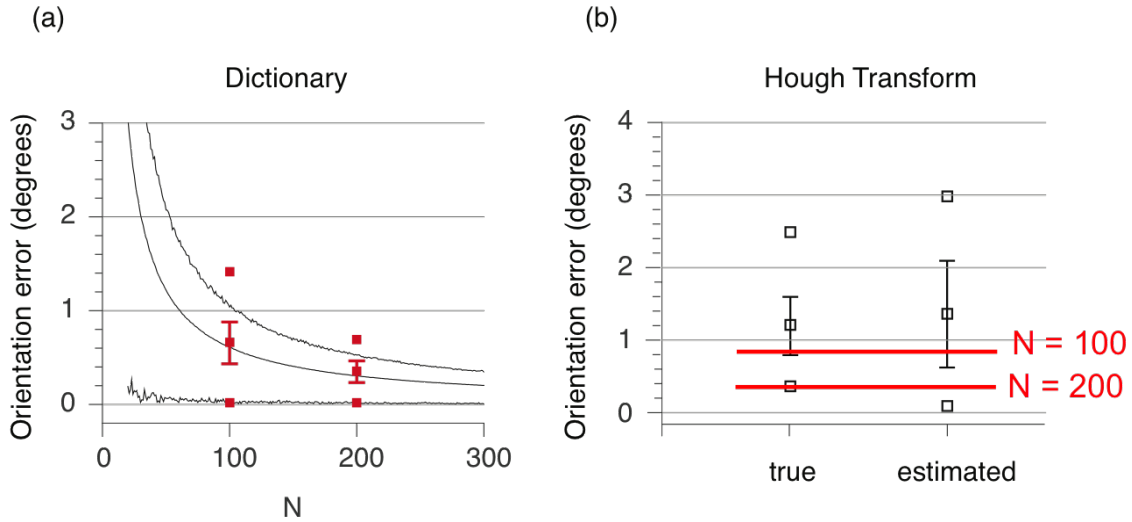
Figure 5.11: Maximum, minimum and mean error in orientation determination for simulated patterns using (a) dictionary of different sizes and (b) Hough transform method with true and estimated pattern centers. The mean error from dictionary is marked in red.(Plot courtesy Dr. Farangis Ram, Carnegie Mellon University)

mum and mean error in orientation using the two methods are shown in Fig. 5.11 (courtesy Dr. Farangis Ram, CMU). The dictionary samples the orientation space using the cubochoric sampling method, where N is the number of sampling points on the semi-edge of the cube. For different values of N, the maximum, minimum and mean disorientation between neighboring points on the grid are shown by the black curves in Fig. 5.11(a). For the dictionary approach, the maximum, minimum and average error in orientation closely follows the maximum, minimum and mean disorientation between neighboring points on the cubochoric grid, which considers only the geometry of the cubochoric space. As the number of sampling points along the cube semi-edge, N, increases, the angular accuracy of the method increases. Fig. 5.11(b) shows the accuracy of the Hough transform method for the same patterns. When the true detector parameters are used, the Hough transform has a higher mean error than the dictionary method (marked by the two red lines). The Hough transform method shows a larger error in orientation if estimated detector parameters are used.

The true detector parameters are seldom known for an experiment and it is important to study the effect of error in pattern center on the final error in orientation determination for the dictionary approach. Fig. 5.12 shows the minimum, maximum and mean error
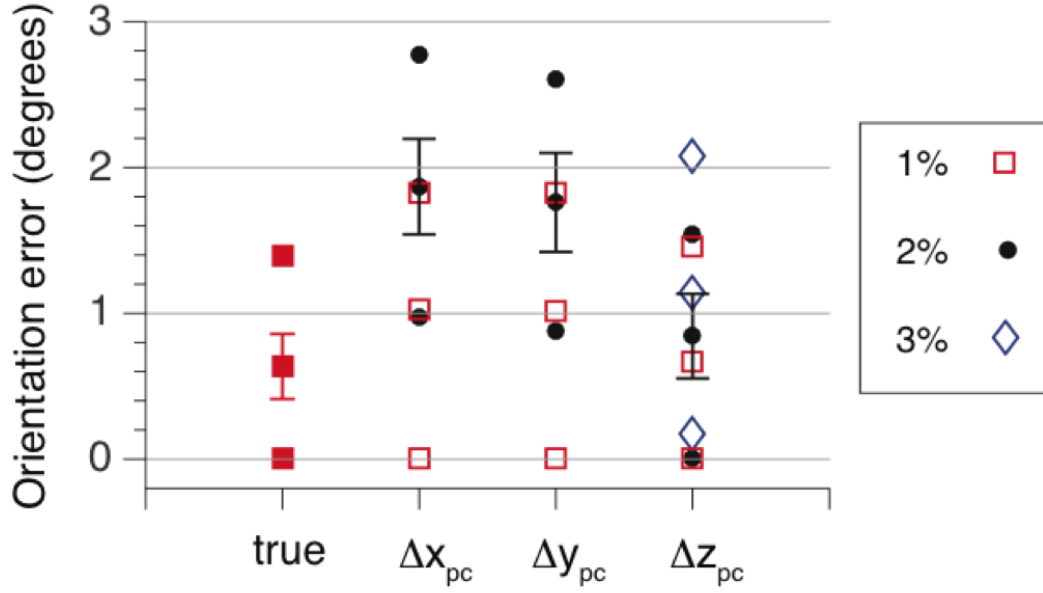
Figure 5.12: Maximum, minimum and mean error in orientation determination for simulated patterns with varying errors in pattern centers.(Plot courtsey Dr. Farangis Ram, Carnegie Mellon University)

for various levels of error in the pattern centers. Unsurprisingly, the error in orientation increases as the error in pattern center location increase. Note that the orientation error is less sensitive to errors in the Z pattern center than the X and Y pattern centers.

Fig. 5.13(a)-(b) shows the effect of pattern size on the orientation error for 0.4% and 1.0% cumulative error in the projection centers respectively. It is interesting to note that regardless of the error in projection centers a 25×25 pattern is sufficient to attain the minimum orientation error.

Fig. 5.14(a)-(c) shows a summary of the effect of error in projection center and specimen tilt on orientation error on the minimum, mean and maximum indexing error respectively. The patterns are 25×25 pixels in size with a $PNSD \approx 45$ dB. The mean orientation error increases more sharply with an error in the specimen tilt than with an error in the projection geometry. The standard deviation of the error does not exceed 0.3°. This concludes our discussion of dictionary based indexing for EBSD modality.

5.1.2 Electron Channeling Patterns

The ECP modality lacks some of the automation of the EBSD modality in terms of pattern acquisition and analysis. Therefore, it is not possible to compare the results of the
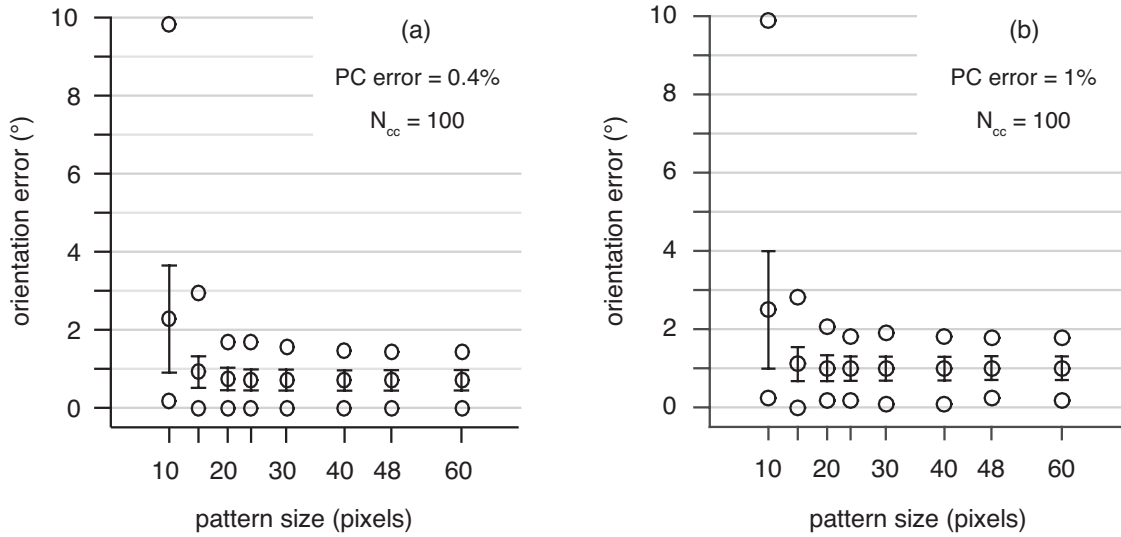
Figure 5.13: The effect of the measured pattern size on orientation error when there is an error in pattern projection center. $PSNR \approx 45$ dB. A trio of vertically aligned data points displays the minimum, mean, and maximum of error in orientations. Each error bar is two standard deviations long. 40 on the horizontal axis, for example, stands for a 40×40 pixel pattern size (courtesy Dr. Farangis Ram, Carnegie Mellon University).
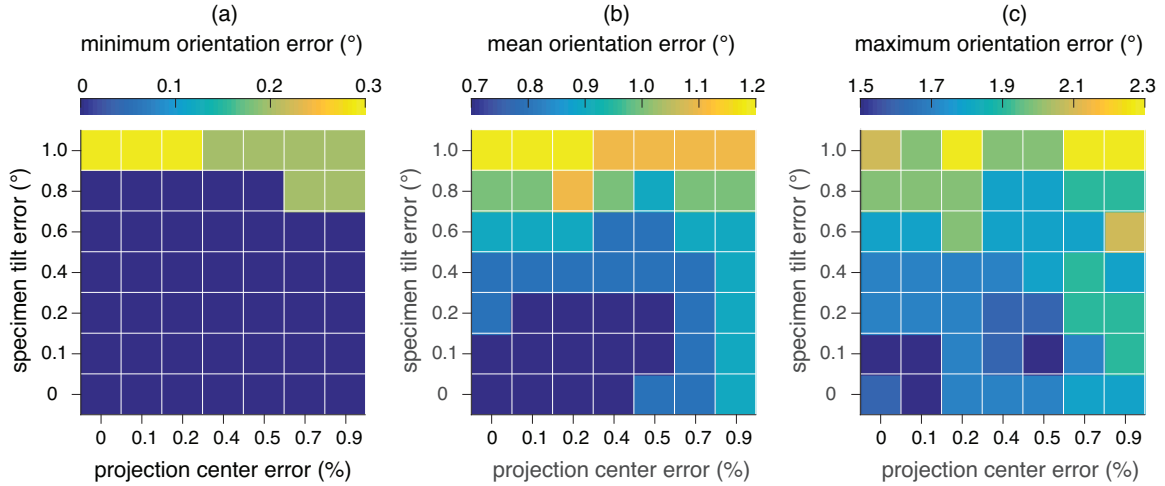
Figure 5.14: The effect of error in detector geometry on orientation error. The standard deviation of orientation error does not exceed $0.3°$. $N_{cc} = 100$. Patterns are 25×25 pixels in size and their $PSNR \approx 45$ dB (courtesy Dr. Farangis Ram, Carnegie Mellon University).

dictionary indexing directly to an already existing package. Hence, we resort to comparing the simulated channeling patterns for the Euler angles after applying dictionary indexing to experimental channeling patterns. For this study, four channeling patterns were recorded from different grains in a polycrystalline Si sample, under identical microscope acquisition conditions. One of these pattern was used to determine the detector parameters, while the other three patterns served as the experimental dataset. The detector parameters were as
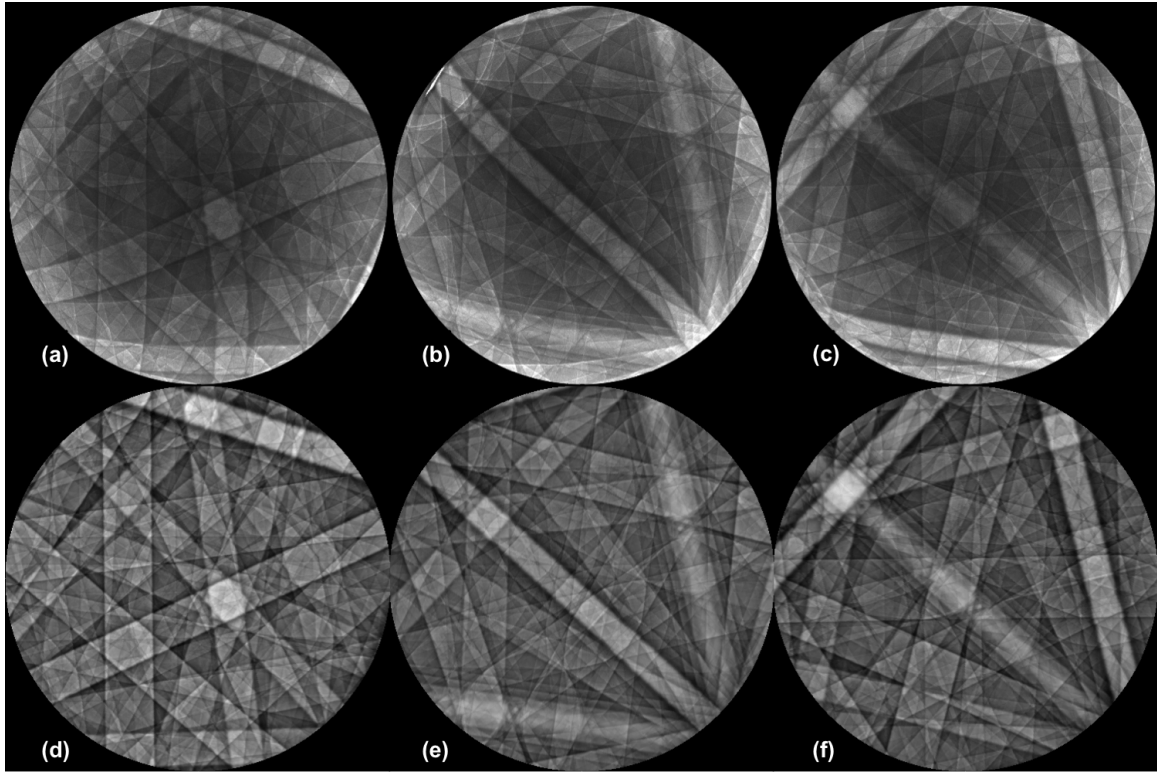
Figure 5.15: Experimental channeling patterns (top row) for three different grain in Si sample. Simulated channeling patterns for Euler angles obtained from the dictionary approach for the respective patterns. (d) $(108.42°, 19.84°, 277.06°)$ (e) $(121.07°, 46.11°, 203.82°)$ (f) $(302.98°, 37.91°, 63.28°)$

follows: $W = 8$mm, $R_{in} = 2$mm, $R_{out} = 5$mm, $\omega = 0°$, $\theta_c = 14.36°$. The experimental patterns used for the study are shown in Fig. 5.15(a)-(c). The results of applying the dictionary approach are shown in Fig. 5.15(d)-(f). The Euler angles (numbers in figure description) reproduces the experimental patterns accurately. However, such an analysis is only visual and appropriate quantification of results is needed.

In the absence of a commercial automated pattern acquisition and indexing system similar to those available for EBSD analysis, we must use a different validation technique. Also, the Euler angles obtained by commercial EBSD packages can not be compared directly to the ones obtained from our dictionary approach since they use different reference frames and fundamental zones. Therefore, to validate our indexing method, in addition to comparing the experimental and simulated patterns for the Euler angles obtained from the dictionary method, the reconstructed misorientations between pairs of patterns having known misorientations were determined. Channeling patterns from a single grain in semiconductor grade

poly-crystalline Silicon with large grains (500 μm) were recorded on a TESCAN MIRA 3 FE-SEM equipped with a rocking beam setup, with $0°$, $+5°$ and $-5°$ sample tilts and a working distance of 9.63 mm; the patterns are shown in Fig. 5.16(a)-(c). There is excellent agreement between the experimental and simulated patterns. The opening angle of the cone was obtained using the BOBYQA algorithm and found to be $11.42°$. The Euler angles obtained from the dictionary approach and the angles after further refinement are shown in Table 5.3.

The orientation refinement was also performed using the BOBYQA DFO algorithm (see section 5.2). The simulated patterns for the refined Euler angles are shown in Fig. 5.16(d)-(f). No noise or distortions were applied and the intensity of the simulated patterns was rescaled to match the experimental patterns. The Euler angles obtained after applying the dictionary method and post refinement are shown in Table 5.2 The misorientation between

ID	Stage Tilt (°)	Dictionary (°)	Refined (°)
1	0	(330.69, 26.11, 38.18)	(333.66, 26.43, 38.26)
2	+5	(338.85, 30.91, 34.85)	(336.85, 30.97, 34.08)
3	-5	(327.61, 21.75, 43.67)	(328.51, 21.96, 43.89)

Table 5.2: Euler triplet for the tree sample tilts obtained from the dictionary method and after refinement using the BOBYQA algorithm.

pairs of Euler angles obtained from the dictionary and after refinement is shown in Table 5.3. The misorientations for the Euler angles from the dictionary approach are slightly different from the true misorientations (reported in the table). This difference can be attributed to the discrete nature of the orientation sampling such that the exact orientation was not present in the dictionary. However, after refinement, the misorientation is in near perfect agreement with the true values.

IDs	Dictionary (°)	Refined (°)	True (°)
(1,2)	7.26	4.98	5.0
(1,3)	5.26	5.03	5.0
(2,3)	10.47	9.99	10.0

Table 5.3: Disorientation for the Euler triplet pairs for the dictionary angles and the refined angles along with the true values.
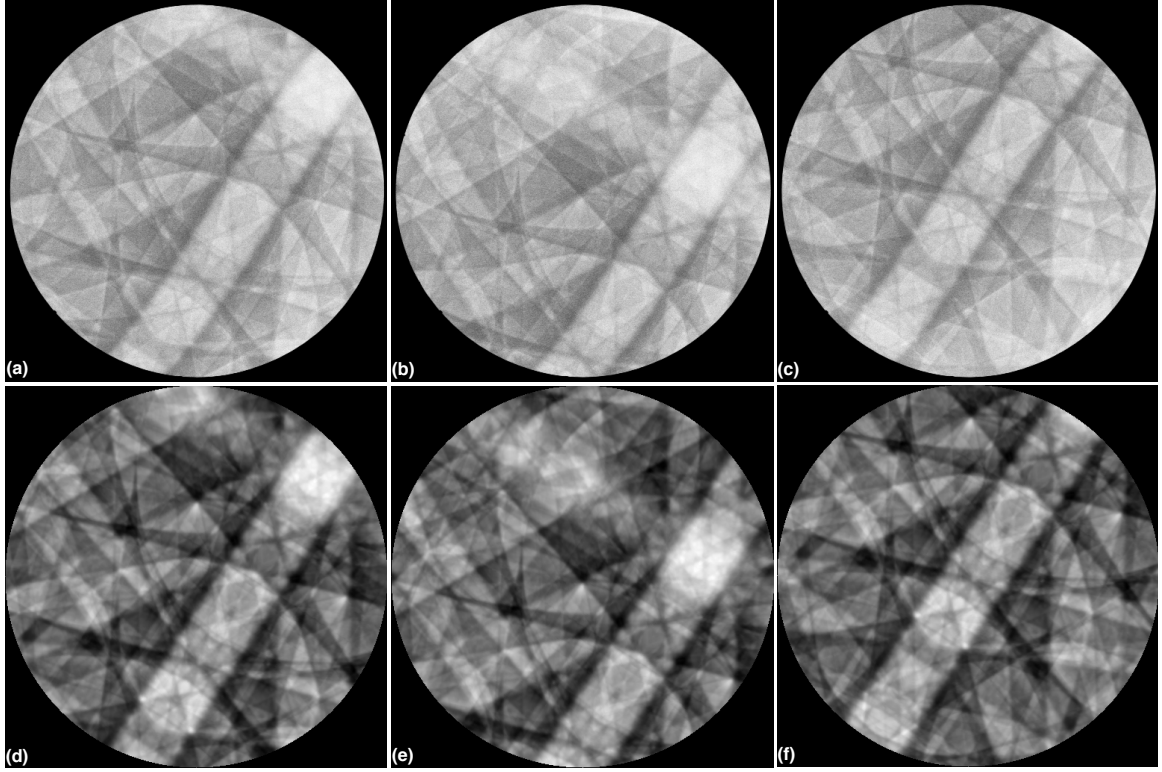
Figure 5.16: Experimental channeling patterns for (a) 0° (b) +5° and (c) −5° stage tilt. (d)-(f) corresponding simulated channeling patterns for (a)-(c). Detector parameters and Euler angles in text and Table 5.3.

Error Analysis

The dictionary approach uses a uniformly sampled grid in orientation space to generate the dictionary. As mentioned previously, it is not necessary and highly unlikely that the experimental pattern will lie on a sampled grid point. Furthermore, the dictionary method requires the detector parameters as its input. Therefore, it is important to study the error introduced in the final indexing as a function of the sampling step size and the error in the initial detector parameters. A set of $1,000$ random orientations was generated and simulated channeling patterns for Silicon at 10 kV and $\theta_c = 15°$ were computed. These patterns were indexed using the dictionary approach for different sampling step sizes and different error levels in the initial detector parameters. The disorientation angle between the orientation given by the dictionary approach and the true orientations was then taken as a measure of the error. The mean disorientation error of the $1,000$ patterns along with the standard deviation are reported as the efficacy of the method. It is important to note that due to the

limited capture angle in a typical channeling pattern $(20° - 30°)$ compared to an electron backscatter diffraction pattern $(70° - 80°)$, there is a small fraction of orientations which are mis-indexed to its pseudosymmetric orientation variant rotated by $(60°[111])$. This is particularly evident from the fact that the fraction of mis-indexed points decreases with increasing capture angle as shown in Fig. 5.17. This problem can be completely alleviated if a sufficiently fine sampling grid is used to generate the dictionary; however, this makes the method computationally more expensive. For the error analysis in this work, we have ignored the small fraction of orientations which were mis-indexed.

Fig. 5.18(a) shows the orientation error as a function of the number of sampling points along the cubochoric semi-edge. Since the dictionary is generated at the sampling grid points, decreasing the sampling step size leads to more patterns in the dictionary. This decreases the orientation error, but increases the computational cost of the method. As shown previously, the better approach is to use a moderate sampling step size ($N \sim 100$) and then refine the orientations using the DFO optimization algorithm. Fig. 5.18(b) shows the orientation error as a function of the error in the input detector parameters for $N = 100$ sampling points along the cubochoric cube semi-edge. For the true detector parameters, the orientation error is about $1.0°$ with $0.5°$ standard deviation. The method is relatively insensitive to increasing error in the input detector parameters up to about 5% error. The error increases beyond that point and the method fails catastrophically for about 8% error in the input detector parameter.

Automated indexing of channeling patterns has important consequences for quantitative defect characterization in the scanning electron microscope using the Electron Channeling Contrast Imaging (ECCI) modality. For example, the $\mathbf{g} \cdot \mathbf{b}$ or $\mathbf{g} \cdot \mathbf{b} \times \mathbf{u}$ analysis for the identification of the Burger's vector of dislocations requires accurate knowledge of the crystal orientation. Further, with the advent of fully scriptable microscopes, such an analysis can be very easily automated. The TESCAN MIRA 3 FE-SEM offers such an opportunity with full control over the microscope stage. The microscope was scripted to scan a region of interest and record channeling patterns from each scanning point. The collected channeling patterns were indexed using the dictionary approach. Fig. 5.19(a) shows the region of interest (ROI) on a large grained Si sample. The acquisition conditions were as follows:
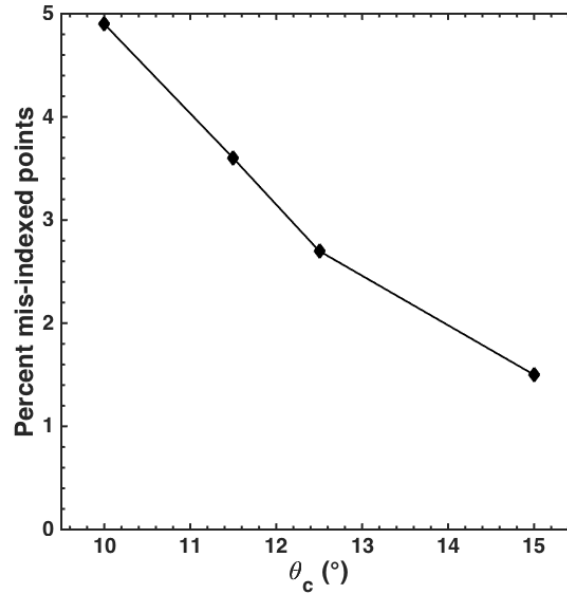
Figure 5.17: Percent of mis-indexed points as a function of the semi-capture angle.
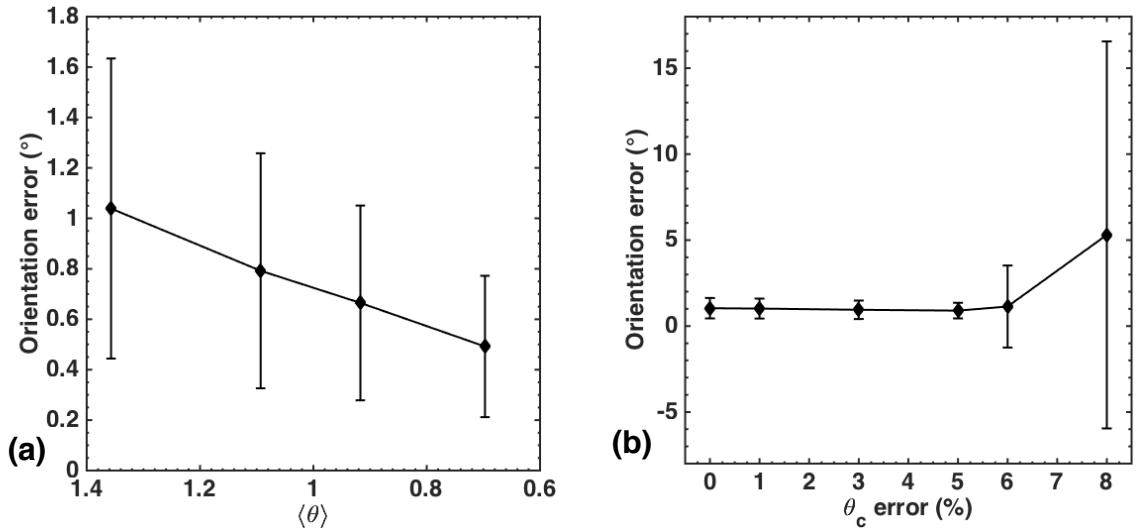
Figure 5.18: (a) Orientation error as a function of mean sampling step size and (b) error in input detector parameters.

acceleration voltage $V = 30$ kV, Working distance, WD $= 15.0$ mm, semi-capture angle, $\theta_c = 10.3°$ and sample tilt $\sigma = 0°$, step size $= 50\mu$m. Fig. 5.19(b)-(c) shows the IPF map after using dictionary indexing on the collected channeling pattern and the IPF map from the same ROI using a commercial EBSD system. The two maps are in very good agreement. The drawback of performing orientation mapping using channeling patterns is due to its limited spatial resolution and larger acquisition times. However, the ability to
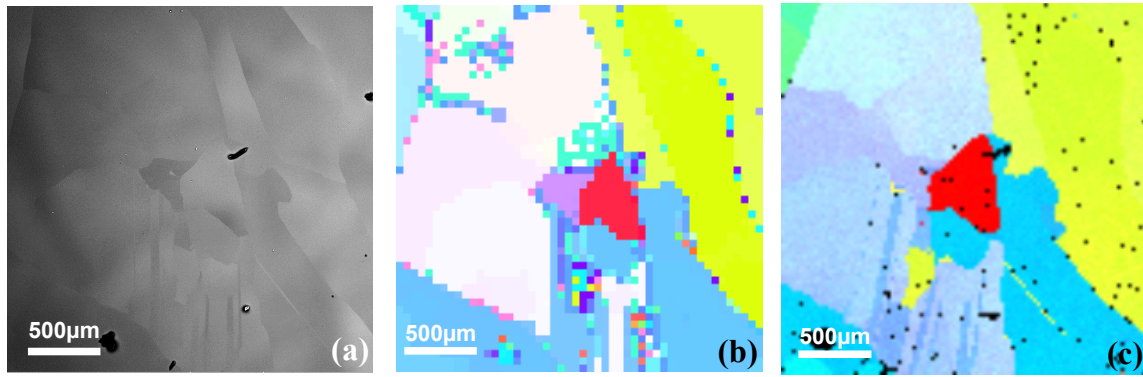
Figure 5.19: (a) Backscatter image of region of interest (ROI) on a large grained Si sample (b) IPF map using dictionary approach on channeling patterns collected from the ROI and (c) IPF map using commercial EBSD system in the same ROI. Acceleration voltage was set to 30 keV.
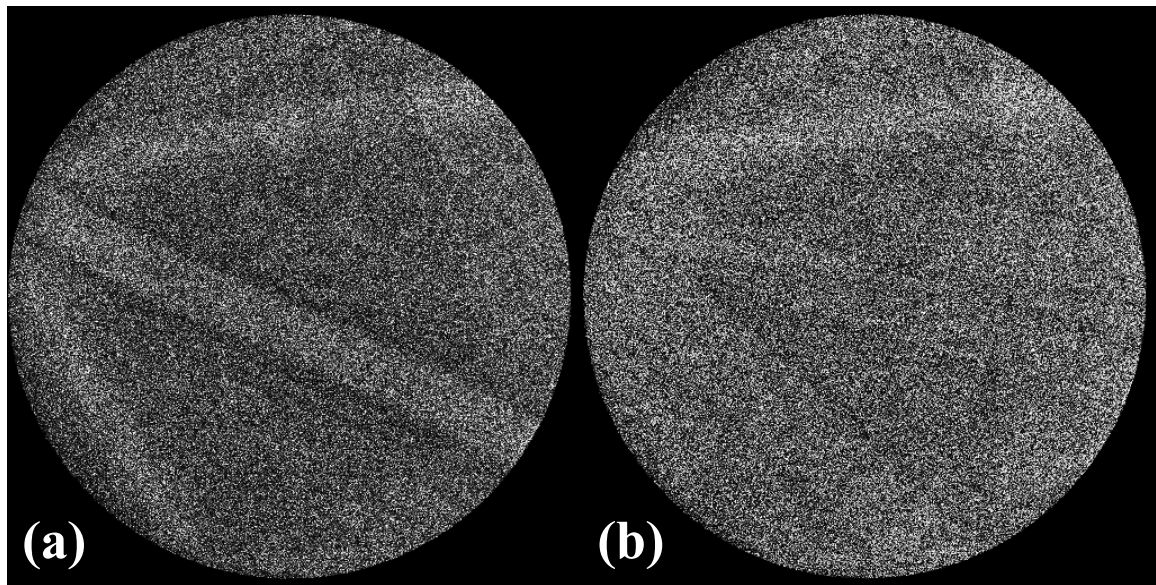
Figure 5.20: Representative channeling patterns collected from ROI shown in Fig. 5.19(a). Acquisition parameters are listed in the text.

index an arbitrary orientation using channeling patterns opens up new possibilities not just for defect imaging, but also for samples incompatible with the high tilt EBSD geometry. Fig. 5.20(a)-(b) presents representative channeling patterns acquired from the ROI showing that the algorithm was able to index patterns with high levels of noise and distortion.

5.1.3 Precession Electron Diffraction

Precession Electron Diffraction patterns were recorded for a 50% cold rolled Cu sample (Data courtsey Asher Leff and Dr. Mitra Taheri, Drexel University). The dictionary approach was used to index these patterns. The result is shown in Fig. 5.21(a). Since the
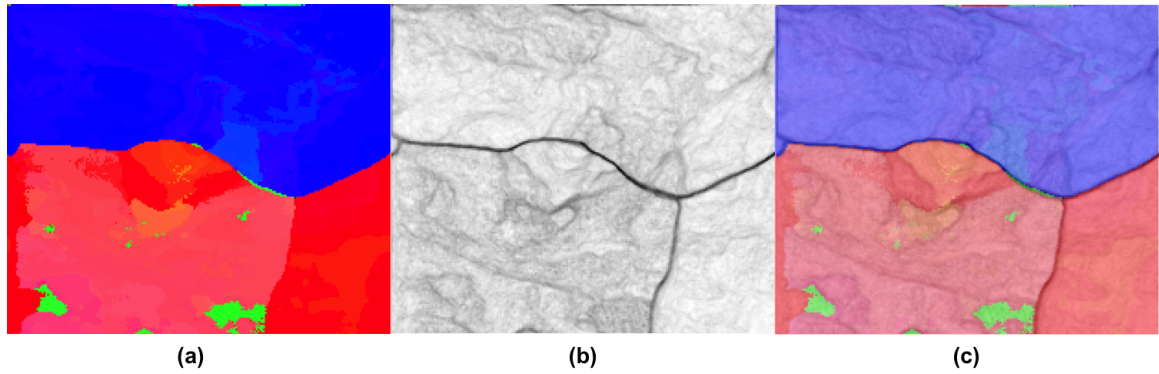
Figure 5.21: (a) IPF map of 50% cold rolled Cu (b) average common nearest-neighbor match map clearly highlighting the sub-grain structure of the highly deformed sample and (c) overlay of the two images.

microstructure is highly deformed, the IPF shows subtle orientation variations within each grain. The areas marked in green are incorrectly indexed due to very noise diffraction patterns from these regions. Fig. 5.21(b) shows the average common nearest-neighbor map for the scan area. In addition to clearly delineating the grain boundaries as shown before, the map also shows contrast withing each grain, which is likely caused by the deformation fields in each grain. The overlay of Fig. 5.21(a)-(b) two images is shown in Fig. 5.21(c). There is high correspondence between the contrast variation in the average common nearest-neighbor match map and the IPF map suggesting that the average common nearest-neighbor match map is indeed showing the deformation field within each grain.

5.2 Orientation Refinement

The typical angular resolutions for the above mentioned techniques range anywhere between $0.1° - 1°$, depending on the acquisition and indexing conditions [111–113]. For some of these diffraction modalities, additional post-processing techniques, such as cross-correlation, which uses an experimental reference pattern, can improve the angular resolution further [114], the only drawback being the lack of control over any parameters giving rise to the diffraction pattern. The availability of accurate and reliable forward models for these diffraction modalities can overcome this hurdle; the forward models can be used to predict the outcome of a diffraction experiment, given a particular sample and detector geometry. The forward models have enabled new approaches for the quantitative extraction

of information from diffraction patterns, by matching them against a controlled set of simulated diffraction patterns with known parameters. In this section, we will focus only on crystal orientations but the extension of this approach to the extraction of other parameters (e.g., the c/a ratio in martensitic steels, or a general solution to pseudo-symmetry related indexing problems) is quite straightforward.

This section is organized as follows: section 5.2.1 introduces the general orientation refinement strategy for an arbitrary diffraction modality, given an accurate physics-based forward model. Two different neighborhood search strategies are presented: a brute force search in the "cubochoric" orientation representation, and a derivative-free optimization (DFO) algorithm. Sections 5.2.2 and 5.2.3 present the results of the application of these algorithms to a set of $1,000$ simulated EBSD patterns as well as to an experimental data set for partially recrystallized 90/10 Brass. Strategies to refine orientations derived from dictionary indexing for a large area EBSD scan are also presented.

5.2.1 Algorithm

A flowchart showing the proposed orientation refinement algorithm is shown in Fig. 5.22. This algorithm relies on the availability of a Generalized Forward Projector (GFP) for the diffraction modality. The GFP is a physics-based model that predicts the results of the diffraction experiment, given a set of instrument, sample and detector parameters. The strength of the coupling between the diffraction probe and the material under investigation can change significantly depending on the nature of the probe, leading to different levels of complexity for the GFP. For example, a weakly coupled probe, such as an x-ray photon, can be described quite simply by a kinematical application of Bragg's law. On the other extreme, strongly coupled probes, such as high energy electrons, require a full relativistic quantum mechanical description to capture the relevant physics, i.e., dynamical elastic scattering. In the majority of these cases, there is no analytical solution available and numerical methods need to be implemented with a computational complexity directly correlated with that of the GFP.

In addition to the GFP, the refinement algorithm requires as input the approximately indexed experimental diffraction patterns as well as an accurate knowledge of the diffraction
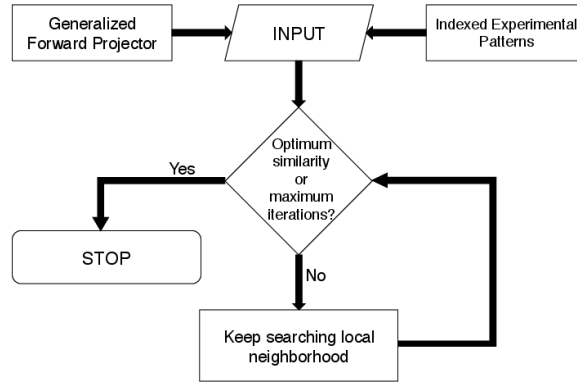
Figure 5.22: Flowchart schematic for an orientation refinement algorithm for a diffraction modality with an accurate forward model.

geometry. The algorithm treats the orientation as the tunable parameter and searches a local neighborhood in orientation space to optimize a similarity metric between the predicted and experimental diffraction patterns. The algorithm is terminated when a local optimum is found or if the algorithm has performed the maximum number of iterations. There are a variety of choices for the similarity/dissimilarity metric, including the normalized dot product, the p-norm of the difference vectors, first and higher order mutual information, and so on [115]. In this paper, we have chosen the normalized dot product as the similarity metric because of its computational efficiency and simplicity. Note that the similarity metric may have a very complex "energy" landscape with respect to the orientation and detector parameters, so that convergence to the global optimum can not be guaranteed in general; convergence to the correct orientation can depend strongly on the initial starting orientation. Therefore, it is of paramount importance to guarantee that the initial guess lies in the "local" neighborhood of the correct orientation. It has been shown using simulated Electron Back-Scatter diffraction Patterns (EBSPs) in [116] that for normalized dot products as the similarity metric, this neighborhood has a radius of about $3° - 5°$ misorientation with respect to the correct orientation value. A detailed study of the behavior of different similarity metrics on the convergence properties of the algorithm is outside the scope of the present study and will be carried out as part of our future work. In this paper, we limit ourselves to orientation refinement for the SEM-based EBSD and ECP modalities, with the extension to other diffraction modalities being relatively straightforward. It is important to emphasize that the refinement algorithms require that all experimental diffraction patterns

be saved during acquisition, which has only recently become possible for the commercial EBSD implementations.

Search Algorithms

The forward models described above for both the EBSD and ECP modalities do not have analytical expressions for the variation of back-scatter yield as a function of the detector parameters and crystal orientation. This limits potential optimization approaches to search algorithms, such as the brute force search, particle swarm optimization etc.; surrogate function based Derivative Free Optimization (DFO) algorithms, such as Nelder-Mead simplex and Bound Optimization by Quadratic Approximation (BOBYQA); or probabilistic methods, such as simulated annealing and its variants. It was found using trial and error that the best convergence was achieved using the brute force and DFO-based search algorithms. For the present study, we evaluated both the brute force search and the BOBYQA algorithms; they are described briefly in the following sub-sections.

Brute Force search Let the operator $\mathcal{M}\left(\mathbf{g}_1, \mathbf{g}_2\right)$ represent the misorientation angle between two orientations $\mathbf{g}_1$ and $\mathbf{g}_2$ and let M_0 be the search radius (in degrees) in orientation space. For a given orientation $\mathbf{g}$, let $\mathcal{S}_{\mathbf{g}}$ be the set of all orientations that lie within the search radius, i.e., $\mathcal{S}_{\mathbf{g}} = \{\mathbf{g}' \mid \mathcal{M}\left(\mathbf{g}, \mathbf{g}'\right) \leq \mathrm{M}_0\}$. If we denote by ϵ the experimental pattern to be indexed, and by $\mathcal{H}\left(\mathbf{g}, \mathbf{X}\right)$ a simulated pattern, using the forward model, for orientation $\mathbf{g}$ and detector parameters $\mathbf{X}$, then the brute force search algorithm seeks to find the orientation $\mathbf{g}_M \in \mathcal{S}_{\mathbf{g}}$ for which the dot product $\mathcal{D}\left(\mathcal{H}\left(\mathbf{g} \mid \mathbf{X}\right), \epsilon\right)$ is maximized, by testing each element in the set $\mathcal{S}_{\mathbf{g}}$. It is customary to represent all diffraction patterns as unit vectors, to facilitate interpretation of the dot product.

To avoid an overly large number of forward model evaluations, we choose a subset $\mathcal{S}_{\mathbf{g}}' \subset \mathcal{S}_{\mathbf{g}}$ of all possible orientations in $\mathcal{S}_{\mathbf{g}}$ such that $\mathcal{S}_{\mathbf{g}}'$ uniformly samples the set $\mathcal{S}_{\mathbf{g}}$ with a 3D grid characterized by a parameter η, which determines the cardinality of the set $\mathcal{S}_{\mathbf{g}}'$. In our implementation, we use the following method to uniformly sample misorientation space:

- Uniformly sample orientations around the identity orientation up to some misorien-

tation M_0 using the cubochoric orientation representation; note that this sampling is performed on a uniform grid in the cubochoric representation, and that η is the number of sampled orientations along the semi-edge of the cubic sampling volume.

- Transform the uniformly sampled misorientations to the orientation of interest, $\mathbf{g}$, using the composition rule in the Rodrigues representation.

Extensive details of this approach can be found in [116]. The cardinality of the subset $\mathcal{S}_{\mathbf{g}}'$ thus generated is $|\mathcal{S}_{\mathbf{g}}'| = (2\eta + 1)^3$. Using this sampling subset, the brute force search then proceeds as follows:

- An initial search radius, M_0 is chosen. If the initial indexing was performed using the dictionary indexing approach, then M_0 is chosen as half the mean misorientation between the cubochoric neighbors. A typical value of M_0 is about $0.7°$.

- A uniform sampling of misorientation space is performed around the initial indexed orientation $\mathbf{g}$ as described above, such that there are $(2\eta + 1)^3$ orientations to be tested. Typically, η is set to 1 or 2.

- The orientation $\mathbf{g}'$ with the highest dot product is chosen from the set of $(2\eta + 1)^3$ orientations. This orientation will be the initial point for the next iteration.

- The search radius is halved, i.e., $M_0/2 \leftarrow M_0$ and the search is repeated. This iteration is carried out P times; typically, P is set to 3.

- At the end of P iterations, the orientation with the highest dot product, $\mathbf{g}_M$ is assigned as the orientation corresponding to the diffraction pattern.

Note that after P iterations, the search radius is reduced to $M_0/2^{P-1}$. This suggests that, if the initial dictionary indexing is performed using η_{DI} samples, then at the end of the brute force search, the effective number of samples is given by $2^{P-1}\eta_{DI}$. This approach requires calling the computationally expensive forward model operator, $\mathcal{H}$, exactly $P(2\eta + 1)^3$ times, i.e, 375 times for $P = 3$ and $\eta = 2$, for each experimental diffraction pattern with a guaranteed convergence to the highest dot product in the search set $\mathcal{S}_{\mathbf{g}}'$. The computationally expensive nature of this method makes it relatively unsuitable for very large

scale datasets, although this problem can be partially alleviated using massive parallelization using MPI/OpenMP or GPU based implementations.

Derivative Free Optimization Since the brute force search described previously is computationally expensive, a computationally more tractable approach is required. Since the derivatives of the forward model, $\mathcal{H}$, are not known analytically, surrogate function-based DFO algorithms are suitable for this optimization problem. This section provides a very brief description of the algorithm; the more mathematically inclined readers should consult the original article [117].

Consider a function $\mathcal{F}(\mathbf{X}), \mathbf{X} \in \mathbb{R}^n$, which we wish to optimize, subject to the bounds $\mathbf{A} \leq \mathbf{X} \leq \mathbf{B}$; the function is specified as a "black-box" with input $\mathbf{X}$. The derivatives of $\mathcal{F}$ with respect to the input variables are not known analytically. DFO methods typically approximate $\mathcal{F}$ in the region $||\mathbf{X}|| \leq \Delta_k$ by means of a substitute function, $\mathcal{Q}$, such that $\mathcal{Q}(y_j) = \mathcal{F}(y_j),\ j = 1, 2, \cdots, m$ for each interpolating point y_j. As its name suggests, BOBYQA uses a quadratic approximation for interpolation. The interpolating points are chosen and adjusted automatically. However, the number of points used for interpolation, m, is typically a constant with $m = 2n + 1$ being a good choice. For the k-th iteration, the neighborhood in which the function $\mathcal{Q}$ is a good approximation for $\mathcal{F}$ is given by Δ_k. There is a lot of freedom in the selection of $\mathcal{Q}$ which only needs to satisfy the interpolation conditions which require choosing $\mathcal{Q}$ such that the Fröbenius or L^2 norm of the change in the second order derivatives, $||\nabla^2 \mathcal{Q}_{k+1} - \nabla^2 \mathcal{Q}_k||$, is minimized. The radius Δ_k of the trust region for each iteration k is also adjusted automatically. The initial and final values, ρ_{i} and ρ_{f} are selected by the user. The ratio $(\rho_{\mathrm{f}}/\rho_{\mathrm{i}})$ is a good measure for how quickly the algorithm terminates and how accurate the final result is; a lower value of this ratio leads to a more accurate final result but slower convergence time and a higher value leads to a less accurate result but faster performance. To balance performance and accuracy, a good choice for these parameters is $\rho_{\mathrm{i}} = 10^{-1}$ and $\rho_{\mathrm{f}} = 10^{-5}$, respectively. In our implementation, the function $\mathcal{F} \equiv \mathcal{H}$ which is the forward model for the diffraction modality and $\mathbf{X} \equiv \mathbf{g}$, the crystal orientation. The optimization is then performed using the Bunge Euler angle representation of the orientation $\mathbf{g}$. This technique generally converges in about 50 to 100

evaluations of the forward model $\mathcal{H}$ and is computationally more efficient than the brute force approach. However, convergence to the optimum value can not be guaranteed since the method can get stuck in a local minimum or the interpolating function, $\mathcal{Q}$, might not be a sufficiently good approximation in the region of interest.

5.2.2 Applications to Synthetic Data Sets

Simulated EBSD Patterns   To test the accuracy of the algorithms, a set of $1,000$ EBSD patterns for Nickel were generated using random orientations and the following parameters: electron acceleration voltage, $V = 20$ kV; sample tilt $\sigma = 70°$; camera elevation $\theta_c = 10°$; projection center $(x^*, y^*, z^*) \equiv (0.5070, 0.7230, 0.5613)$; detector size in pixels $(n_x, n_y) \equiv (480, 480)$; physical size of a detector pixel $\delta = 59.2$ μm; and a pattern binning factor of $8\times$. These patterns were considered to be the "experimental" patterns and were indexed using the dictionary indexing approach, using varying levels of error in the input projection centers. The results were refined using both algorithms described in the previous section. The mean disorientation for the thousand patterns is considered as a measure for the efficacy of the algorithm.

Fig. 5.23 shows refinement results for an initial indexing by the dictionary indexing approach and a subsequent refinement using the brute force search and BOBYQA approaches. The top graph represents results for patterns with a peak signal-to-noise ratio of 65 dB, the bottom graph for 45 dB. The horizontal axis shows varying levels of error (in units of percent of the full detector width) in all three projection center components. The results show that the orientation error is reduced only if the projection center errors are within $\pm 1\%$. For larger errors, even though the confidence index (the highest dot product between simulated and experimental patterns, which is considered as a proxy for disorientation) increases, the orientation error also increases. The results for the brute force search and BOBYQA method are nearly identical with the mean orientation error within $0.05°$ disorientation from the true value. The asymmetry in the disorientation error is less evident for lower errors in the projection center components, but becomes more pronounced as these errors increase. In terms of computational speed, the BOBYQA method outperforms the brute force search by almost an order of magnitude. For the parameters listed above, the
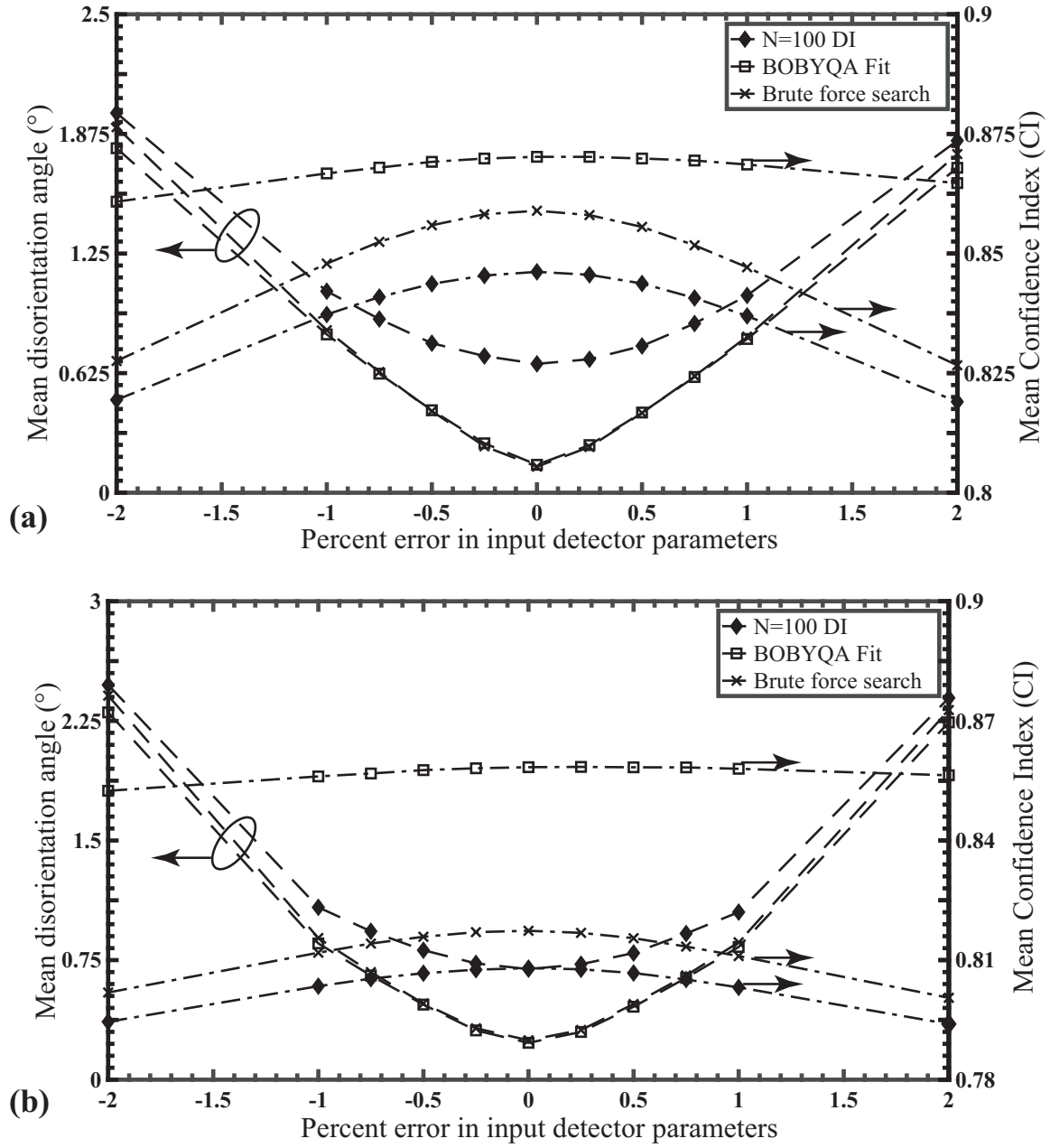
Figure 5.23: Disorientation in degrees (left axis) and confidence index (right axis) as a function of percent error in detector parameters x^*, y^* and z^* when the initial indexing was performed using the dictionary method. The simulated patterns have a peak signal-to-noise ratio of (a) 65 dB and (b) 45 dB.

BOBYQA method refined approximately 72 patterns per second compared to 9 patterns per second using the brute force search. Since the two search methods produce identical results, in the remainder of this paper we only show results for the computationally less expensive BOBYQA method.

In the dictionary indexing approach, dot products are computed for each experimental

pattern with respect to all the dictionary patterns; those dot products are then ranked from highest to lowest, and the top 30-50 values are stored, along with the corresponding orientations. In Fig. 5.23, only the orientation corresponding to the top dot product value was used to determine the mean disorientation angle. In Fig. 5.24, the orientations corresponding to the top 20 best matches were averaged using a quaternion-based averaging algorithm [118], and subsequently refined using both refinement algorithms. Comparison with Fig. 5.23(a) and (b) shows that the orientation averaging process itself lowers the disorientation substantially (note the different vertical scale bars), and that subsequent refinement produces only a small improvement. Hence, application of the orientation averaging procedure for sampling locations inside grains will, in general, improve the orientation accuracy. Near grain boundaries, however, the list of best matches is likely to contain the orientations of both grains, due to the overlapping EBSD patterns, so that the averaging process should not be applied. At grain boundaries, the correct approach would be to refine the pattern against the highest ranked matches for both grain orientations, and then select the refinement that has the highest similarity metric, i.e., the highest dot product.

Simulated Electron Channeling Patterns

The methodology described in the previous section was also used to test the efficacy of the refinement algorithm for electron channeling patterns. A set of $1,000$ ECPs for Silicon was generated using random orientations and the following parameters: acceleration voltage $V = 10$ kV; sample tilt $\sigma = 0°$; working distance $W = 8.0$ mm; semi-capture angle $\theta_c = 15.0°$; and pattern size in pixels $n_{pix} = 512$. The patterns were indexed using the dictionary method [119] with varying levels of error in θ_c and refined using the BOBYQA method. The results of such a refinement are shown in Fig. 5.25. In the case of channeling patterns, the algorithm decreases the orientation error for any error in θ_c of up to $\pm 5\%$. The indexing is less sensitive to the detector parameters than in the case of EBSD patterns with a mean orientation error of about $0.08°$ after refinement for the true detector parameter and less than $0.25°$ for a detector parameter error of $\pm 5\%$.
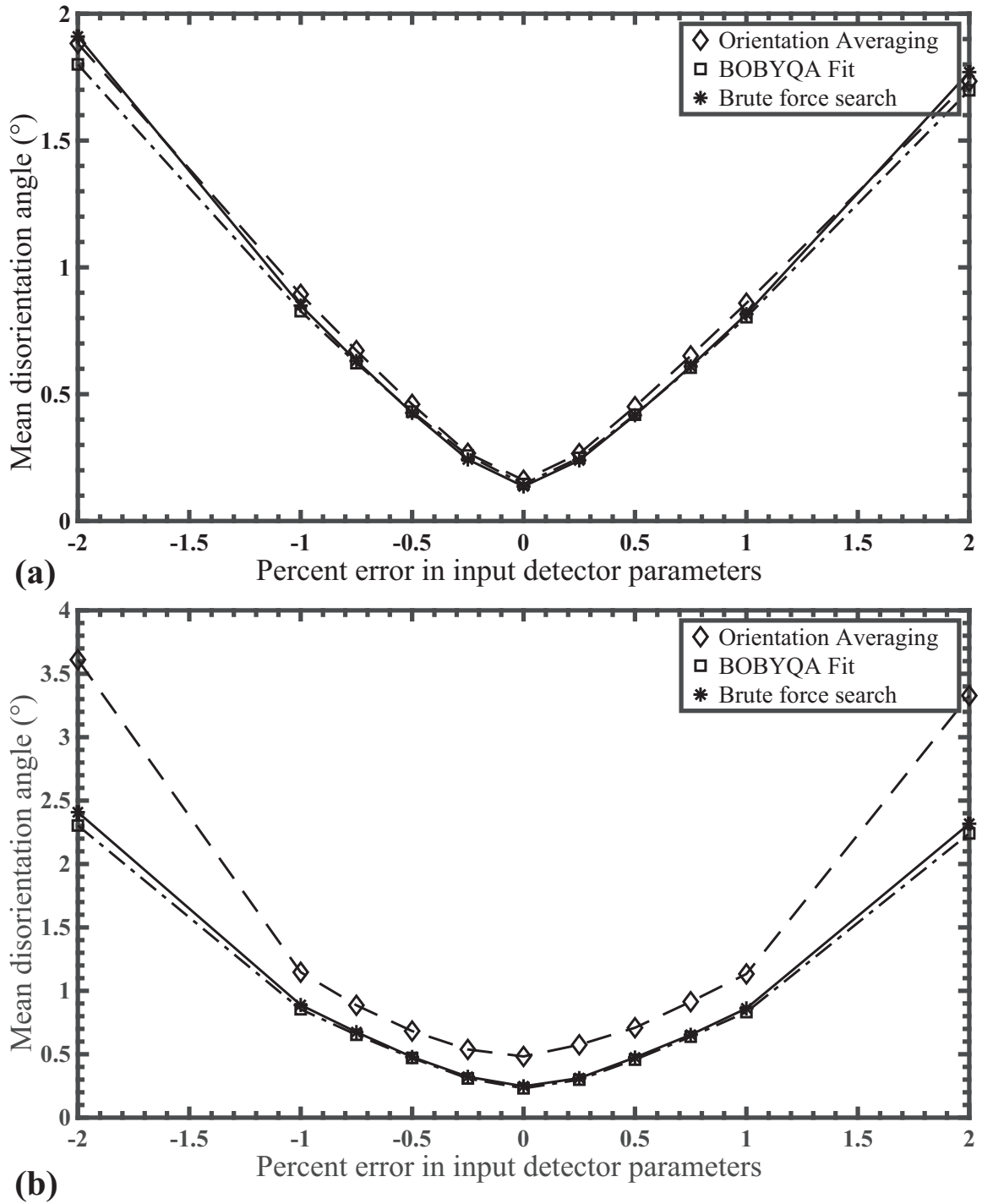
Figure 5.24: Comparison of disorientation in degrees as a function of percent error in detector parameters x^*, y^* and z^* for orientation averaging and orientation refinement. The simulated patterns have a peak signal-to-noise ratio of (a) 65 dB and (b) 45 dB.
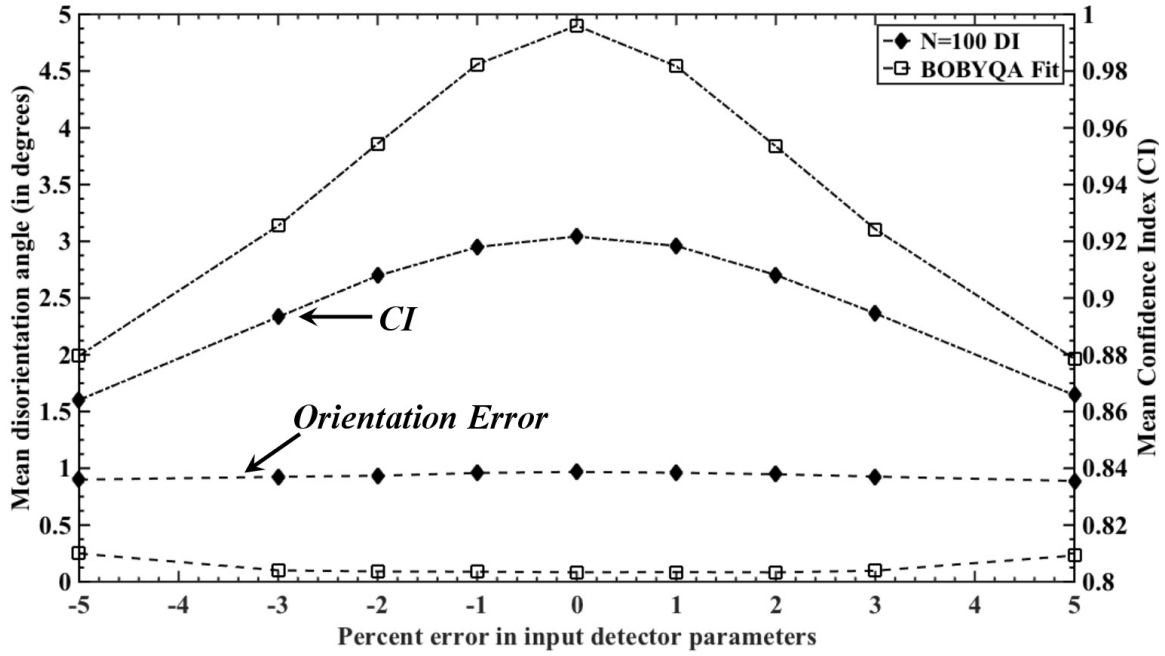
Figure 5.25: Disorientation in degrees (left axis) and confidence index (right axis) as a function of percent error in detector parameters θ_c with the initial indexing performed using the dictionary method.

5.2.3 Applications to Experimental EBSD Data Sets

Partially Recrystallized 90/10 **Brass.**

The refinement algorithm was applied to an experimental EBSD scan collected on a partially recrystallized 90/10 Brass sample. The acquisition conditions were as follows: electron beam acceleration voltage, $V = 10$ kV; sample tilt $\sigma = 70°$; scan step size 0.5 μm; static background subtraction and $8\times$ binning, resulting in a pattern size of 60×60 pixels. The indexing was performed using both the commercial EDAX OIM™ 8 software and the dictionary indexing approach and subsequently refined using the BOBYQA method. Fig. 5.26 presents the results of the refinement. Fig. 5.26(a)-(c) show the (100), (010) and (001) Inverse Pole Figures (IPFs), respectively, after application of the refinement algorithm. The IPFs show significant orientation gradients resulting from lattice rotations due to the high deformation. Fig. 5.26(d) shows the Orientation Similarity Map (OSM) obtained from the dictionary indexing method, clearly delineating the recrystallized grains. The OSM is qualitatively similar to the kernel average misorientation (KAM) map, with brighter regions showing higher similarity in orientation between neighboring sampling points. As stated earlier, the dictionary indexing approach produces a list of the top k matches for each

diffraction pattern. The intensity at a certain pixel in the OSM is obtained by averaging the number of orientations in common with the top match lists of the neighboring pixels. If the set of top k orientations at a pixel (i, j) is denoted by $\mathcal{N}_{i,j}$, then the OSM intensity at scan pixel (i, j), $\mathcal{I}\left(\text{OSM}\right)_{i,j}$, is defined as

$$\mathcal{I}\left(\text{OSM}\right)_{i,j} = \frac{1}{4}\left(\mathcal{C}_{i,j;i-1,j} + \mathcal{C}_{i,j;i+1,j} + \mathcal{C}_{i,j;i,j-1} + \mathcal{C}_{i,j;i,j+1}\right), \tag{5.1}$$

where $\mathcal{C}_{a,b;c,d} \equiv \#[\mathcal{N}_{a,b} \cap \mathcal{N}_{c,d}]$ and $\#[\mathcal{S}]$ represents the cardinality of the set $\mathcal{S}$. Fig. 5.26(e) shows the point-by-point disorientation map between the results from dictionary indexing and the post-refinement results. Certain recrystallized grains show a larger change in orientation upon refinement; this is most likely due to the discrete nature of the DI orientation sampling, coupled with the fact that recrystallized grains have a rather constant orientation. Most of the scan points inside these grains were indexed as the same orientation in the dictionary; if this orientation was further away from the true orientation, then that particular grain will show up brighter in the disorientation angle map (Fig. 5.26(e)). Such a systematic behavior is not seen for the deformed grains since the orientation varies spatially with each scan point. Finally, Fig. 5.26(f) shows a histogram of the confidence index (CI) for dictionary indexing (dotted curve) and after refinement (solid curve). As expected, in addition to the overall curve shifting to the right indicating a better match, the distribution also becomes narrower. It is important to note that all of these conclusions are contingent upon the availability of accurate detector parameters.

Fig. 5.27 shows the KAM maps for the same scan area using dictionary indexing (a), refinement of dictionary indexing (b) and the commercial OIM™ 8 software (c). The KAM map in Fig. 5.27(a) shows ghost features in regions with high deformation which vanish after the orientations are refined, as shown in Fig. 5.27(b). The KAM map produced after the application of the refinement algorithm matches very well with the one produced by the Hough transform-based method, as shown in Fig. 5.27(c). The ghost features in the unrefined KAM map are an artifact of the discrete orientation sampling used in the dictionary indexing method. Therefore, if the most precise orientations are required from the dictionary method, it becomes imperative to apply one of the refinement algorithms
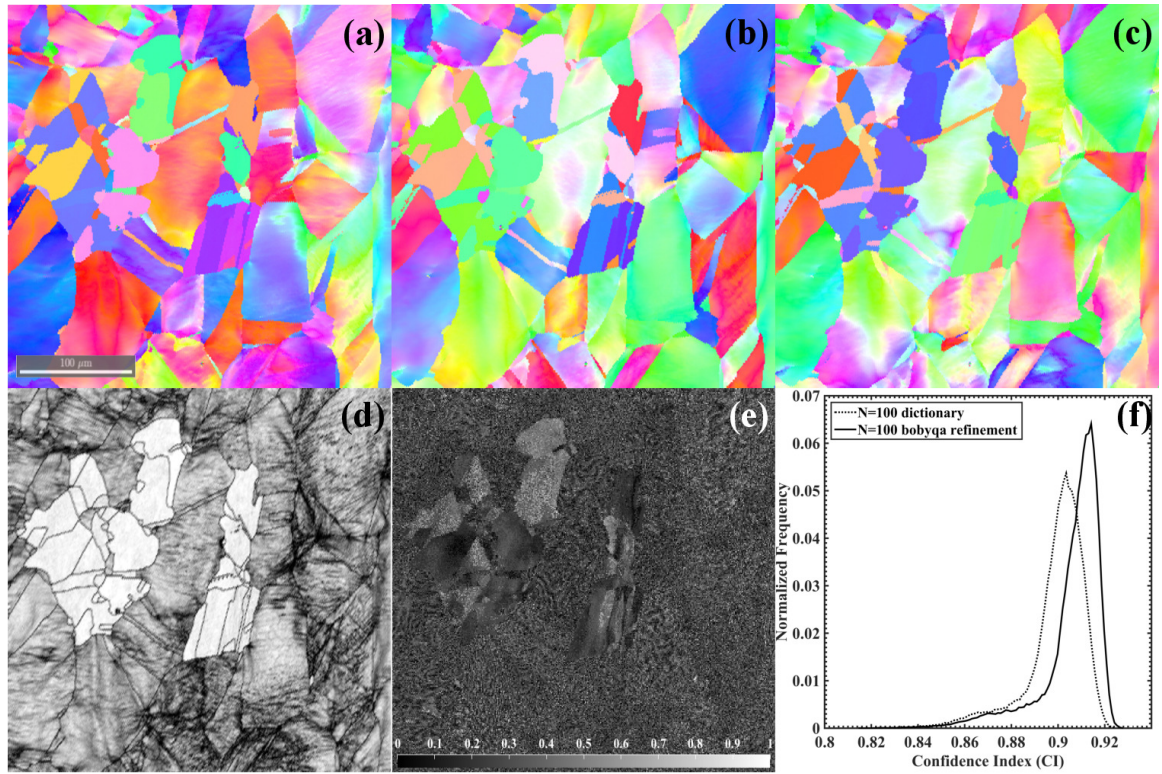
Figure 5.26: EBSD scan for partially recrystallized 90/10 Brass indexed with dictionary indexing and refined with BOBYQA method. (a) IPF-[100] (b) IPF-[010] (c) IPF-[001] (d) Orientation Similarity Map (OSM) showing recrystallized grains (e) Disorientation angle between orientation obtained by dictionary indexing and post refinement and (f) distribution of Confidence Index (CI) after dictionary indexing and post-refinement.
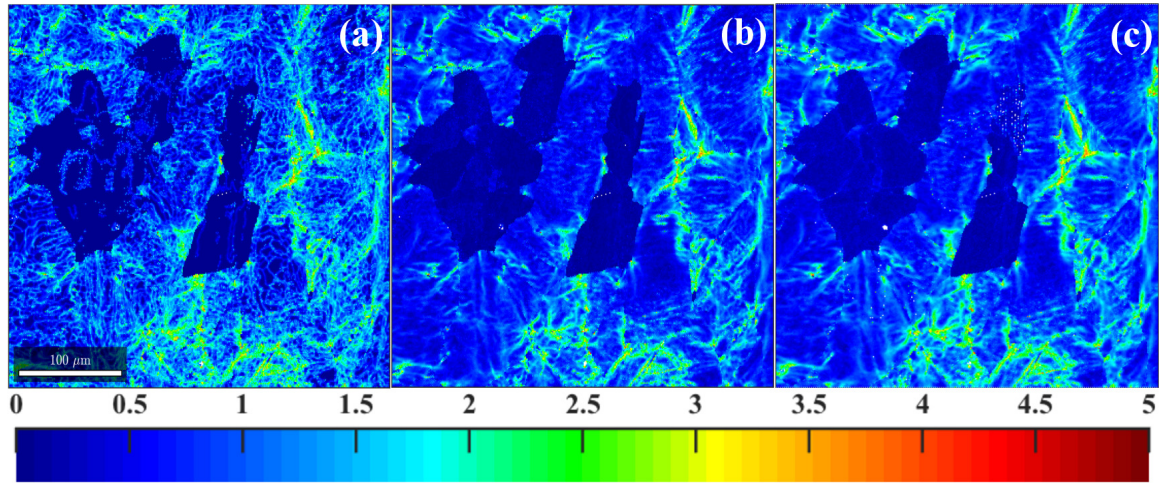
Figure 5.27: KAM maps for partially recrystallized Brass with (a) Dictionary Indexing (b) Refinement of Dictionary Indexing results and (c) Hough transform based Indexing.

described above.

Large Area EBSD Scans

Pattern Center Shift Correction   Unlike the Hough transform-based method, which dynamically corrects for shifts in the projection center caused by beam scanning, the dictionary indexing method uses a fixed pattern center to generate the dictionary and index the patterns; this approximation is necessary to keep the dictionary method computationally tractable. While this approximation is valid for EBSD scans with a small field of view (comparable to the size of a single detector pixel), the projection center shifts appreciably for larger view fields and it becomes imperative to take this into account. It is shown in Appendix C that a small shift in the projection center can be approximated by a rotation; in other words, to first order, a rigid translation of the EBSD pattern across the detector is equivalent to a rotation around an axis normal to the direction of translation. A shift in pattern center can thus be compensated, to first order, by a rotation of the proper angle in the opposite direction. Hence, the sample orientations determined for a large region of interest, using a single pattern center, can be corrected afterwards by application of this rotation.

Consider a scan point with coordinates (i, j) in a rectangular scan ($-M \leq i \leq M$ and $-N \leq j \leq N$, with i the row and j the column number), a step size of Δ along both scan directions, and assume that the dictionary indexing is carried out with a projection center corresponding to the central sampling point, $C \equiv (0, 0)$; the orientation correction factor is then given by the axis angle pair $(\hat{\mathbf{n}}, \omega)$, where

$$
\begin{aligned}
\hat{\mathbf{n}} &= \frac{1}{\rho} \left(-i\delta \cos \alpha, \, j\delta \cos \alpha \cos 2\alpha, \, -i\delta \sin \alpha \right), \\
\cos \omega &= \frac{L - j\delta \cos \alpha \sin 2\alpha}{\sqrt{L^2 - 2j\delta \cos \alpha \sin 2\alpha + (j\delta \cos \alpha)^2 + (i\delta)^2}}.
\end{aligned}
\tag{5.2}
$$

Here, $\rho = \sqrt{(i\delta)^2 + (j\delta \cos \alpha \cos 2\alpha)^2}$, $\alpha = \pi/2 - \sigma + \theta_c$, σ and θ_c are the sample tilt and camera elevation respectively, δ is the physical detector pixel size and L is the sample to scintillator distance. The above correction approach was applied to a simulated Nickel EBSD data set. The sample was assumed to be a single crystal such that the orientation remains constant for all scan points. The EBSD data set was generated for a 15 kV electron

beam; sample tilt $\sigma = 70°$; camera elevation $\theta = 10°$; projection center of the central sampling point, $(x^*, y^*, z^*) \equiv (0.50, 0.7083, 0.4464)$; physical detector pixel size $\delta = 70.0\ \mu m$; detector size in pixels $(n_x, n_y) \equiv (480, 480)$; no pattern binning; orientation $(\phi_1, \Phi, \phi_2) \equiv (270.0°, 45.0°, 45.0°)$; and a field of view of $W \times H = 2 \times 3\ \mathrm{mm}^2$ with a sampling step size set to 20 μm in both scan directions. A schematic of the scan setup is shown in Fig. 5.28; representative EBSPs from the central sampling point, denoted by the coordinate $(0, 0)$, and the four corners are shown as well. The location of the projection center for the central sampling point, $(0, 0)$ is marked by the yellow cross in all the diffraction patterns. The EBSPs at the corners clearly show an appreciable pattern shift caused by the projection center change and the assumption of a fixed projection center for a large area scan is clearly not valid.

The synthetic EBSD data set was indexed using the dictionary indexing method with the projection center of the central sampling point as input. The disorientation angle between the DI results for each scan location and the known crystal orientation is shown in Fig. 5.29(a). The disorientation map clearly shows the effect of the discrete sampling of orientation space on the final results. The result of the DI approach was then refined using the BOBYQA algorithm, and the disorientation map between the refined angles and the known orientation is shown in Fig. 5.29(b). As expected, the refinement algorithm produces a smooth disorientation map. The maximum disorientation error between the refined and true orientation is about 6.5° in the corners of the region of interest. This falls outside the range of $0° - 3°$ for which the dot product similarity metric is sensitive to disorientations and the refinement algorithm with a dynamically corrected pattern center is not expected to work. However, after applying the corrections described in eq. 5.2 to the refined orientations, the maximum disorientation in the field of view decreases to about 1.3°, with most scan points having errors well below 1°, as shown in Fig. 5.29(c). This is well with the convergence radius of the refinement algorithm and the refinement algorithm can be applied again, this time using the correct projection center for each sampling point.

Thus, for large EBSD scans, a three step refinement process is required; the first step overcomes the artifacts of a discretely sampled orientation space, the second step corrects the
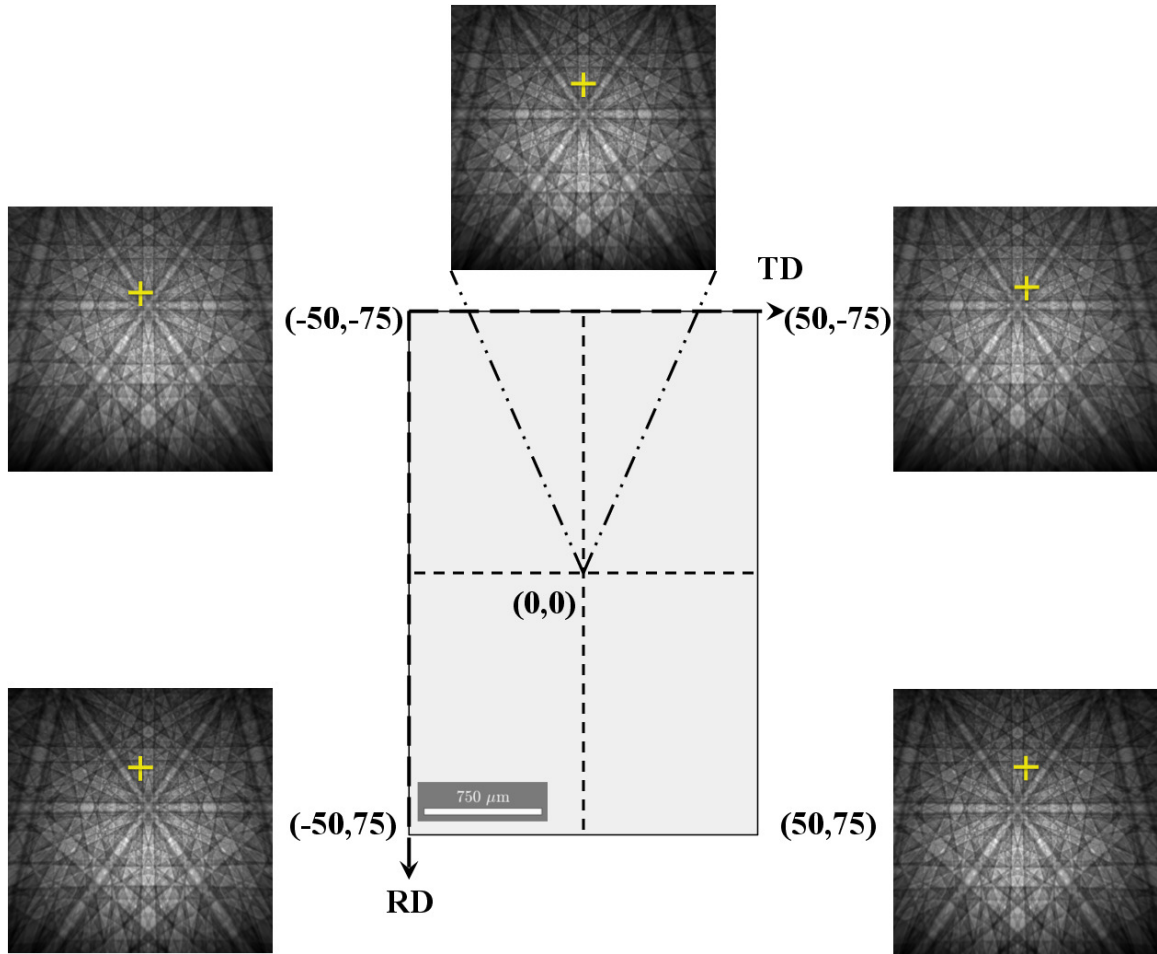
Figure 5.28: Schematic of the scan setup for the simulated large area EBSD data set with the corresponding diffraction pattern. The yellow cross shows the projection centers for the central scan point in all the diffraction patterns showing appreciable shifts in the diffraction pattern.

orientations for the use of a fixed projection center, and the final step refines the orientations using the correct projection centers. The results of this procedure are shown in Fig. 5.29(d); the orientations cluster around the exact value with the maximum disorientation in the field of view being $0.24°$; the average disorientation is $0.008° \pm 0.007°$. It is unclear at this point why the disorientation for certain isolated sampling points remains significantly higher than the average value; it is possible that the refinement algorithm becomes stuck in a local minimum of the cost function.

Corrections for Large Area Experimental Data Sets Fig. 5.30 shows an experimental relative disorientation angle map for a large-grained Fe-3%Si specimen, obtained using the Hough-based indexing approach. The measured area has two grains, and the larger
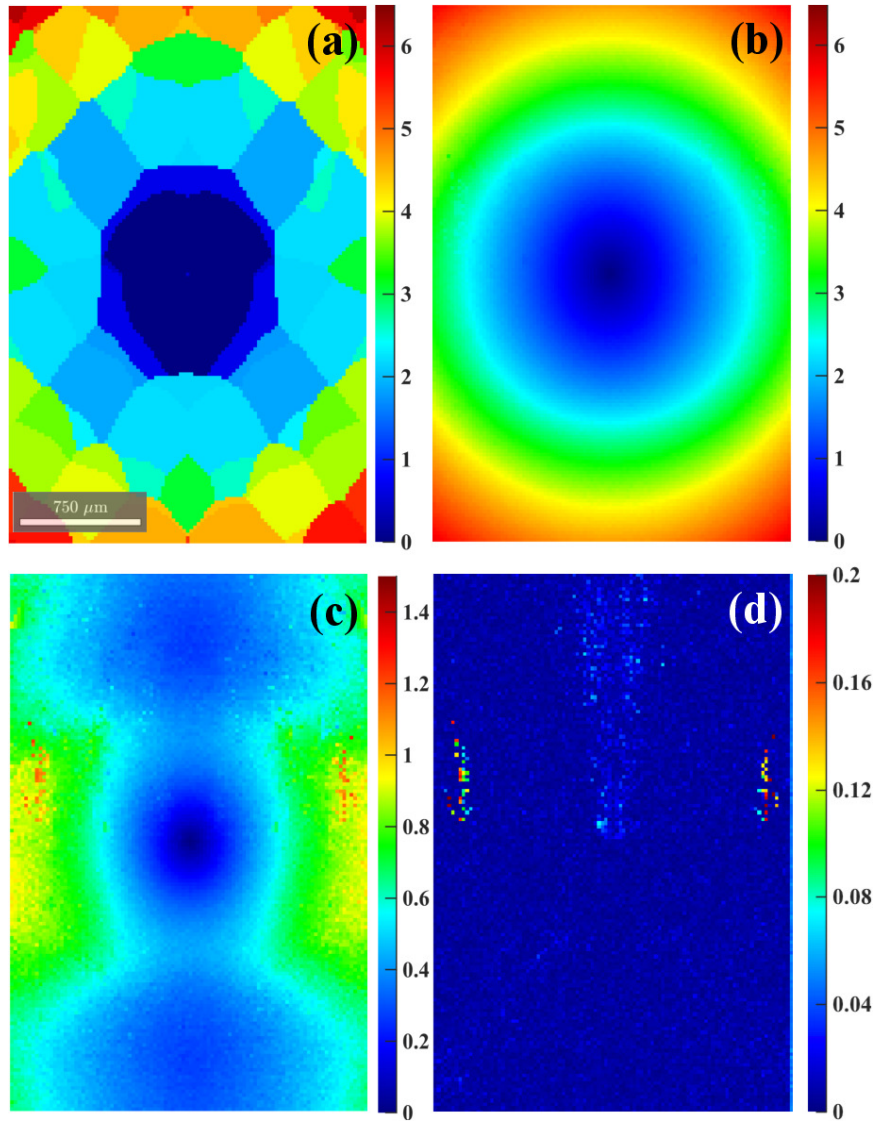
Figure 5.29: Disorientation angle in degrees with the center pixel with (a) Dictionary approach (b) Orientation refinement using BOBYQA (c) pattern center correction to refined orientations and (d) refinement using correct pattern centers and Euler angles obtained from (c). The dictionary result in (a) shows a patch work of regions with constant disorientation angle; this is due to the discrete sampling of orientation space that underlies the dictionary indexing approach.

grain is used for this analysis. In Fig. 5.30(a), the maximum disorientation with respect to the top left corner is 2°. The map shows several sets of parallel linear contours arranged in an "argyle"-style pattern; the disorientation across each contour line is about 0.5°.

The argyle pattern becomes finer when the Hough resolution increases, as shown in Fig. 5.30(b). It is important to note that the argyle pattern effect is not caused by not accounting for the variation of the EBSP projection center across the map; the shift of the projection center was dynamically corrected in the acquisition software.
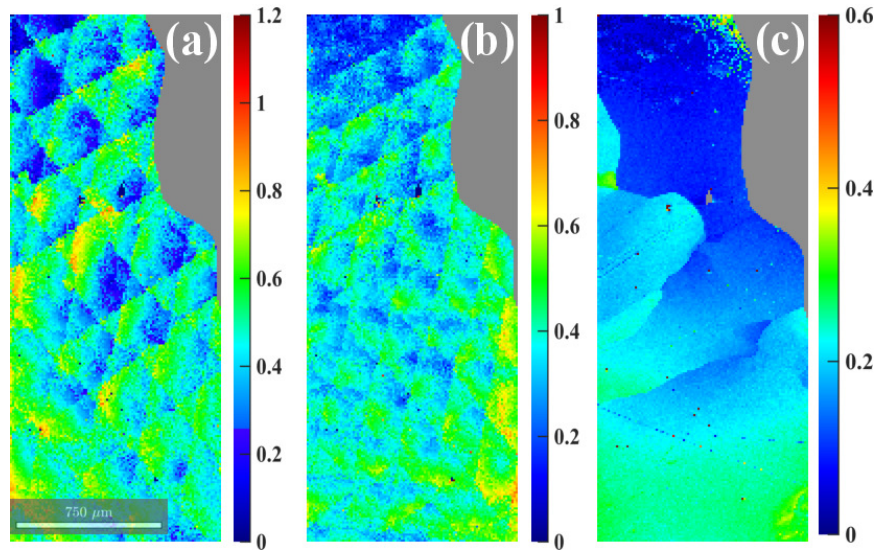
Figure 5.30: The argyle pattern in the disorientation map of a single crystal indexed by the Hough transform based algorithm.—The color represents the angle of disorientation with respect to the point at the top left corner of the map. The projection center is varied according to the position of the scan point. The map is acquired from Fe-3%Si on a 1×2.6 mm^2 surface area, with a step size of 10 μm. The maps in (a) and (b) only differ in their Hough resolution: (a) $\rho = 160$ pixels and $\theta = 0.5°$ and (b) $\rho = 200$ pixels and $\theta = 0.5°$. (c) represents the disorientation map after refinement of the Hough-based orientations.

An argyle pattern appears in an experimental relative disorientation angle map when: (1) indexing is carried out using the Hough transform based algorithm and (2) the size of a single grain exceeds 100 μm. The linear disorientation contours that form the argyle pattern in Fig. 5.30 are aligned with the traces of crystal lattice planes, suggesting that they are related to individual Kikuchi bands. Their position on the map, their spatial frequency, their orientation, and the extent of the angle of disorientation across them depends on the Hough resolution and on the number and orientation of the Kikuchi bands that are used for indexing.

To examine this effect more closely, we applied the Hough transform based indexing algorithm to the synthetic Nickel single crystal data set described in the previous section (see Fig. 5.28). The disorientation map of this synthetic material was then computed based on the orientations obtained by the Hough algorithm (which employs a dynamical pattern center correction). As shown in Fig. 5.31, the argyle pattern appears again, and is more regular and pronounced compared to the experimental Fe-3%Si case shown in Fig. 5.30. This is due to: (1) the higher sharpness of the simulated patterns and (2) the fact that the
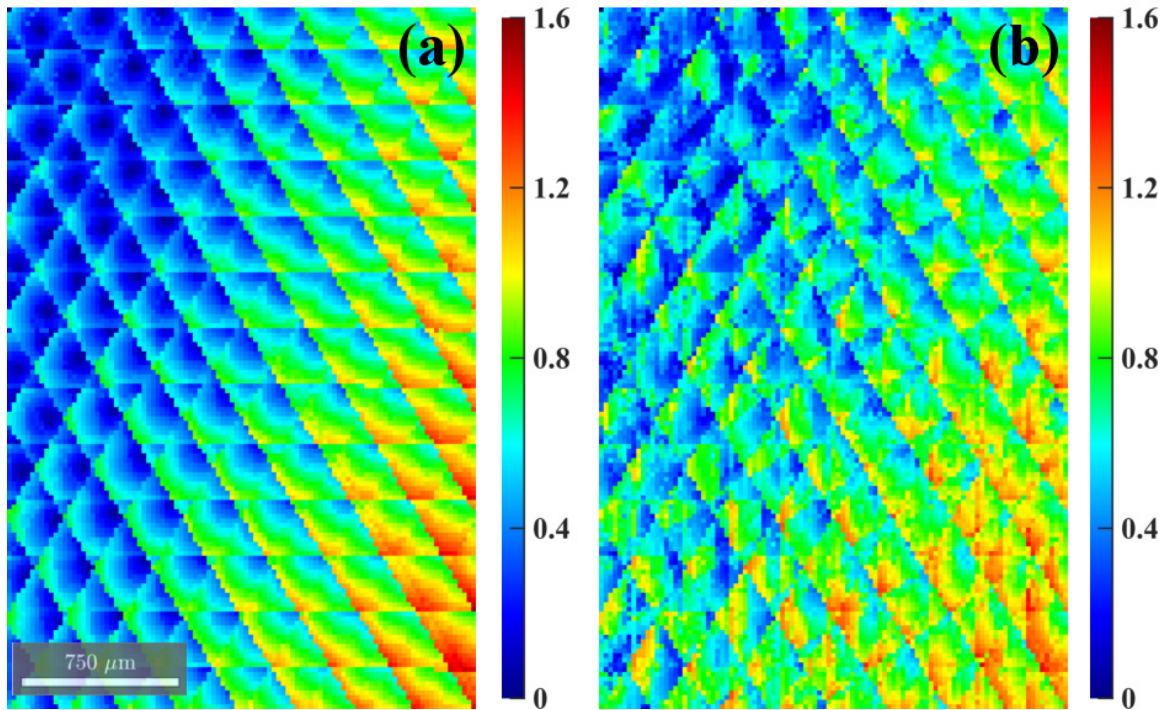
Figure 5.31: The argyle pattern in the disorientation map of a synthetic Ni single crystal indexed by the Hough transform based algorithm.—The color represents the angle of disorientation with respect to the point at the top left corner of the map. The projection center is varied according to the position of the scan point. The surface area is 2×3 mm^2, and the step size is 20 μm. Both maps have the same Hough resolution: $\rho = 160$ pixels and $\theta = 0.5°$. The maps in (a) and (b) only differ in the number of Kikuchi bands that are used for indexing: (a) 10 bands and (b) 4 bands.

Fe-3%Si single crystal is composed of a few sub-grains that are slightly rotated with respect to the mean orientation of the grain. The Hough transform based indexing cannot clearly resolve them because its resolution is not high enough. However, their boundaries partly overlay the argyle pattern and diminish its regularity compared to the synthetic argyle pattern. The sub-grains are revealed by the dictionary indexing based refinement algorithm proposed in this paper. The difference between the argyle patterns in Fig. 5.31(a) and (b) is the result of the different number of Kikuchi bands used for indexing: 10 bands in (a) versus 4 bands in (b). When the number of Kukuchi bands used for indexing increases, the number of parallel disorientation contour sets increases and the argyle pattern becomes more intricate.

The disorientation contour lines are the result of discrete jumps in the detected positions of Hough peaks; in the indexing algorithm, the Hough peak positions are determined to the nearest pixel, which causes discrete jumps when a peak moves onto a neighboring Hough

pixel. This discretization error occurs in a different way for each Kikuchi band which explains why the resulting disorientation map shows contours that are parallel to individual lattice plane traces. This is the result of the discreteness of Hough space and can only be mitigated by increasing the resolution. This, however, changes the shape of the K-cluster (the representation of a Kikuchi band in Hough space) and its peak will no longer be at its center but at one of its corners, which increases the error in the detected plane trace. At present, there is no easy solution to avoid the appearance of the disorientation contour lines in Hough-based large area EBSD scans. Care must be taken not to misinterpret these artifacts for microstructural features, such as sub-grain boundaries or crystal slip traces.

When the Fe-Si data set shown in Fig. 5.30(a) is refined using the BOBYQA algorithm, the complete argyle pattern is removed from the disorientation map resulting in the map shown in Fig. 5.30(c) (disorientations with respect to the top left point in the map). The orientations change by only a fraction of a degree across the field of view, and the sub-grain boundaries become prominent features in the map. Fig. 5.32 shows the result of applying dictionary indexing to the Fe-Si data set: (a) shows the dictionary indexing result which exhibits a patch work of regions of constant disorientation due to the discrete sampling of orientation space. In (b), the orientations of (a) are refined using the BOBYQA algorithm, and they show the typical pattern expected for large area indexing with respect to a fixed pattern center. Application of the orientation corrections results in the disorientation map shown in Fig. 5.32(c), and a final refinement produces the map in (d). Note that the disorientations in this figure are plotted with respect to the center of the region of interest; when the top left point is used as the reference, the resulting refined disorientation map becomes virtually identical to that shown in Fig. 5.30(c).
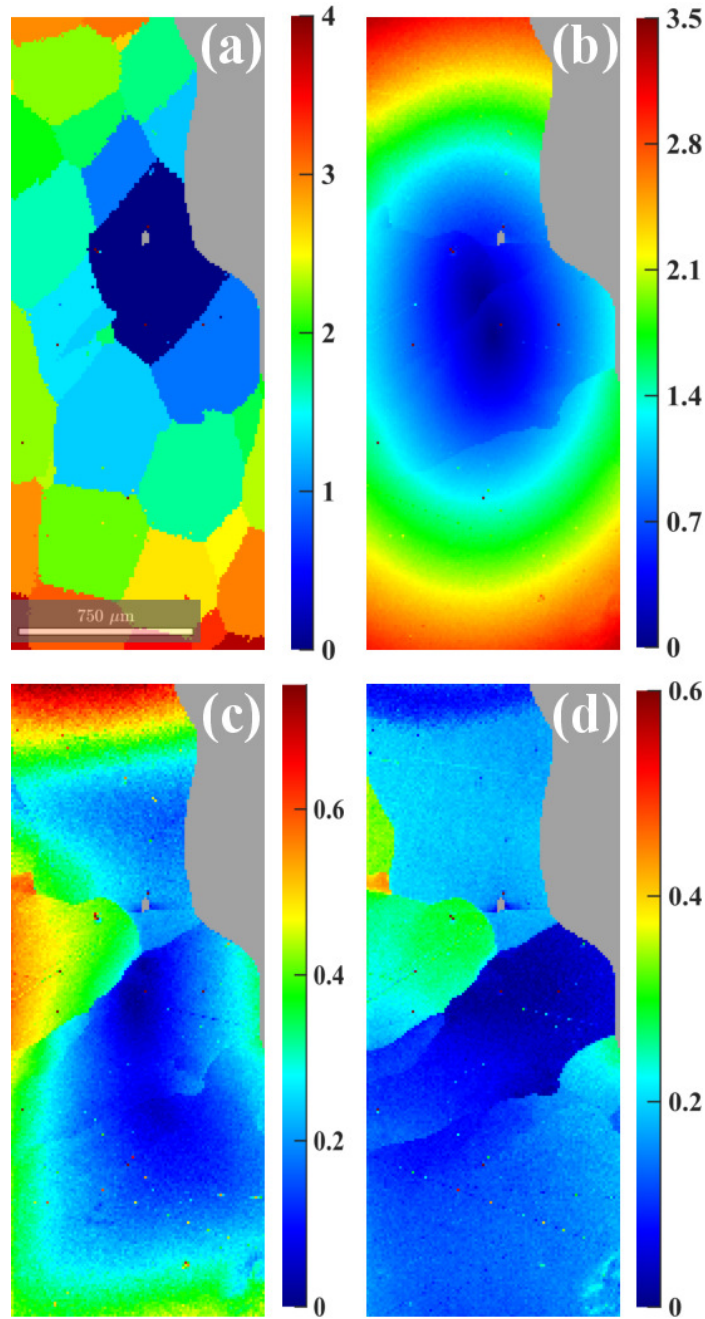
Figure 5.32: (a) Dictionary Indexing (b) Orientation refinement without single pattern center (c) pattern center correction to refined orientations and (d) refinement using correct pattern centers and Euler angles obtained from (c).

5.3 Pole Figure Inversion

The central problem of quantitative texture analysis involves the determination of the Orientation Distribution Function (ODF) to characterize a particular poly-crystalline material system. The ODF can then subsequently be used to compute orientation-averaged

anisotropic properties, such as the effective elastic moduli, electrical conductivity, and so on. Since the ODF is such a central quantity for materials properties, there has been a lot of work in this area, going back many decades. The ODF can be determined directly from orientations measured at discrete locations using Electron Back-Scatter Diffraction (EBSD), which provides a high spatial resolution but makes the study of bulk texture slow and somewhat cumbersome, or indirectly from x-ray or neutron diffraction pole figures (PFs).

The extraction of the ODF from PFs, also known as "pole figure inversion," has a rich literature and has been studied extensively using both series expansion methods and discrete methods [120–125]. It is also well known that the pole figure inversion problem has many parallels with the standard tomography problem. The tomography community has made giant leaps in solving ill-conditioned tomographic inverse problems, of which pole figure inversion is a special case, in the past few decades moving from algebraic methods such as Algebraic Reconstruction Technique (ART) and Successive Iterative Reconstruction (SIRT) to Model-based Iterative Reconstruction (MBIR) [126]. However, these new techniques are not known or haven't been used in the materials characterization community. This, together with the recent advances in orientation representations and sampling [75, 127–129] has laid the foundation for implementing these new methods to a very old problem and revisiting the pole figure inversion problem to explore the applicability of these new approaches may be a fruitful exercise.

In this section, we apply a combination of novel orientation parametrizations with model-based iterative tomographic reconstruction (MBIR) algorithms to generate ODFs based on experimental texture data, in particular pole figures. We begin, in section 5.3.1, with an overview of the pole figure inversion problem, followed in section 5.3.2 by a description of the cubochoric orientation representation and modified equal-area Lambert projections. In section 5.3.3, we describe the bayesian concepts underlying the MBIR approach and introduce both the forward and prior models that are needed to create together the MBIR algorithm. In section 5.3.4, we describe the results of ODF reconstructions for both synthetic model data, and an experimental data set for a Ti-6Al-4V EBSD data set, and we conclude the section with a brief discussion of the MBIR pole figure inversion approach.

5.3.1   Background

The orientation of a crystal is represented by a passive 3D rotation, $\mathbf{g}$, which maps the specimen's right-handed Cartesian coordinate frame, $\mathbf{e}^s \equiv (\mathbf{e}_1^s, \mathbf{e}_2^s, \mathbf{e}_3^s)$ onto a right-handed Cartesian coordinate system attached to the crystal, $\mathbf{e}^c \equiv (\mathbf{e}_1^c, \mathbf{e}_2^c, \mathbf{e}_3^c)$, such that $\mathbf{e}_i^s = \mathbf{g}_{ij}\mathbf{e}_j^c$; in this representation, the orientation $\mathbf{g}$ corresponds to a 3×3 special orthogonal matrix, i.e., an element of $SO(3)$.

For any plane normal $\mathbf{h}$ in the crystal frame, there is a direction $\mathbf{y}$ in the specimen frame, such that $\mathbf{h} = \mathbf{g}\,\mathbf{y}$. The orientation distribution function (ODF) is defined as a functional mapping $f : SO(3) \to \mathbb{R}^+$ and defines the relative frequencies of the crystal orientations in a given sample [120, 130]. The ODF f is normalized such that

$$\int_{\mathbf{g} \in SO(3)} f(\mathbf{g})\mathrm{d}\mathbf{g} = V_{SO(3)}. \tag{5.3}$$

A truly random texture has a constant value of f everywhere; since f does not sum to unity, it is not a probability distribution.

The fundamental equation of texture relates the diffracted intensity for a specimen direction $\mathbf{y}$ in the pole figure for the planes $\mathbf{h}$ to the ODF, $f(\mathbf{g})$, by the relations [131]

$$\mathcal{P}(\mathbf{y};\mathbf{h}) = \frac{1}{2}\big[\mathcal{I}\,(\mathbf{y};\mathbf{h}) + \mathcal{I}\,(\mathbf{y};-\mathbf{h})\,\big]; \tag{5.4}$$

$$\mathcal{I}\,(\mathbf{y};\mathbf{h}) = \frac{1}{2\pi}\int_\Lambda f(\mathbf{g})\mathrm{d}\mathbf{g}. \tag{5.5}$$

where the integration path Λ corresponds to the set of orientations for which:

$$\Lambda \equiv \{\mathbf{g}|\mathbf{g}\,\mathbf{h} = \mathbf{y}\}. \tag{5.6}$$

The integration is carried out for all the orientations which bring $\mathbf{h}$ to $\mathbf{y}$, since these orientations contribute to the intensity in the pole figure for that particular specimen direction. A proper weighting of $\mathcal{P}(\mathbf{y};\mathbf{h})$, which describes the relative frequency of orientations contributing to the pole figure, will produce the intensity of the beam diffracted by the pole $\mathbf{h}$

into the specimen direction $\mathbf{y}$. Mathematically, this can be stated as follows:

$$I(\mathbf{y}; \mathbf{h}) = \frac{\rho(\mathbf{h})\mathcal{P}(\mathbf{y}; \mathbf{h})}{\sum_{\mathbf{h}} \rho(\mathbf{h})}. \tag{5.7}$$

where $\rho(\mathbf{h})$ represents the structure factor for reflection by the reciprocal lattice vector $\mathbf{h}$.

5.3.2 Discretization

As stated in eq. 5.5, the pole figure intensity for a sample direction $\mathbf{h}$ requires the integration of the orientation distribution function, $f(\mathbf{g})$, along a particular path Λ in orientation space. It has been shown by Schaeben and van den Boogaart [132] that this integral is the totally geodesic Radon transform in any representation used for $SO(3)$; for instance, the path is a straight line in Rodrigues space [124], a parameterized harmonic curve in Euler space [133], and an ellipse in quaternion space, as shown explicitly in Appendix D. Typically, for direct pole figure inversion methods, ODFs are binned either in Euler angles, using a fixed angular bin size, or in Rodrigues space using a finite element technique. While these representations have been widely successful in reconstructing ODFs, there are a number of problems associated with them. Firstly, these spaces are not uniform representations of orientation space, so equi-angular or FEM-based binning leads to cells corresponding to different orientation volumes. Furthermore, these spaces are not hierarchical and refining the results using a finer sampling grid is generally not possible. Similarly, direct PF inversion methods also involve discretization of the PF space, which is the space of all points on the unit sphere, $\mathbb{S}^2$. Once again this is typically done by taking equal-angle bins for the declination and azimuthal angles, and this approach suffers from the same problem as the Euler angle space, namely that the discretization is not uniform in $SO(3)$.

A recently introduced orientation representation known as the "cubochoric" representation possesses the desirable properties of being both hierarchical and an equal-volume mapping onto $SO(3)$, so it is in principle better suited as the orientation representation of choice for pole figure inversions. In addition, a recently designed projection scheme to map uniform grids on a square to uniform grids on the unit sphere, $\mathbb{S}^2$, [73] could serve as an efficient and effective alternative method for the discretization of PF space.

Cubochoric Representation

As mentioned in earlier chapters, the cubochoric representation of 3D orientations is obtained by an equal-volume mapping of the homochoric ball $\mathbb{B}_h^3$ with volume π^2 onto a cube C of the same volume. Rotations with rotation angle $\omega = \pi$ lie on the surface of the homochoric ball $\mathbb{B}_h^3$ and are mapped onto the surface of the cube C; the identity rotation lies at the center of the cube. The homochoric ball itself is a generalization of the well known equal-area Lambert projection from the two-sphere $\mathbb{S}_+^2$ onto a disc; the higher order Lambert projection maps the homochoric ball $\mathbb{B}_h^3$ onto $\mathbb{S}_+^3$, the quaternion northern hemisphere, in a volume-preserving mapping. Therefore, a uniform cubic grid in cubochoric space provides a way to bin orientations such that each voxel has both a regular cube shape, as well as an equal volume, resulting in a truly uniform discretization of $SO(3)$. It is also interesting to note that the equal-volume nature of the cubochoric space implies that a fast tri-linear interpolation scheme can be used to distribute intensities at the discrete nodes during the reconstruction. The reader is referred to [74] for details.

Modified Lambert Equal Area Projection

The modified Lambert projection is an equal-area mapping between the northern hemisphere of the unit sphere, $\mathbb{S}^2$, and a square, S, with the same area 2π. The north pole is mapped to the center of the square and the equator onto its edges. This mapping is carried out in two steps; the first step maps points on a square with edge length $\sqrt{2\pi}$ to points in a disc $\mathbb{B}^2$ with the same area. The second step uses the well known equal area Lambert projection to map the points from the disc onto points of northern hemisphere $\mathbb{S}_+^2$ of the sphere $\mathbb{S}^2$. Since this is an area preserving mapping, it provides an efficient algorithm to generate uniform grids on the sphere by generating a uniform grid on a square. The reader is referred to [134] for further details.

5.3.3 MAP Estimate

The maximum *a posteriori* (MAP) estimate is a widely used Bayesian statistics estimator which maximizes the posterior probability, leading to the most probable solution given the input information. The MAP estimator can also be interpreted as a *maximum likelihood*
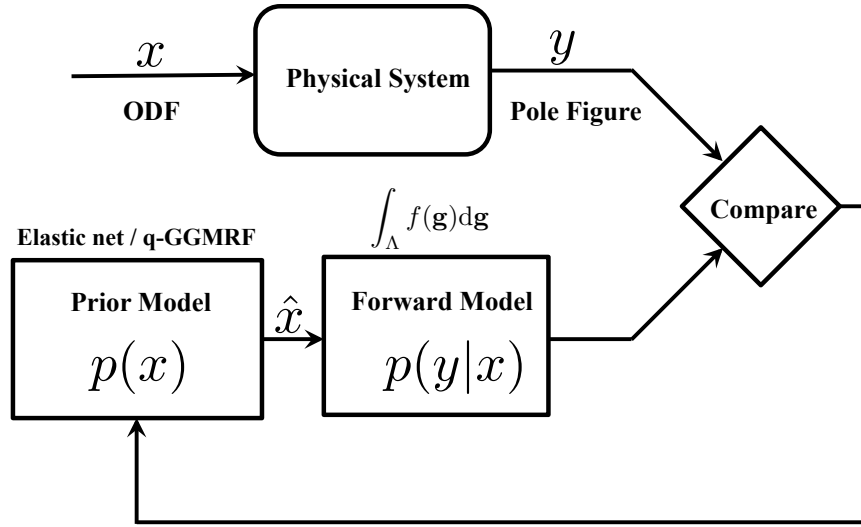
Figure 5.33: Schematic for model based iterative reconstruction technique.

estimator or least squared error estimator with a regularization or penalization term to stabilize the optimization problem. Suppose that we wish to estimate the quantity of interest, x, from a set of measured data, y; if $p(x|y)$ represents the posterior probability, then by Bayes' theorem,

$$p(x|y) = \frac{p(y|x)p(x)}{p(y)}. \tag{5.8}$$

The MAP estimate seeks to maximize $p(x|y)$, i.e., it seeks to find the most probable value for the quantity of interest given the observed data. Since the logarithm is a monotonic function, the problem of maximizing $p(x|y)$ is the same as minimizing the negative log of that function. Additionally, we neglect $p(y)$ since it is independent of x. Therefore, for a vector $x \in \mathbb{R}^N$, the MAP estimate is given by

$$\hat{x}_{MAP} = \underset{x \in \mathbb{R}^N}{\arg\min}\{-\log p(y|x) - \log p(x)\} \tag{5.9}$$

The first term in the MAP estimate, $\log p(y|x)$, is referred to as the forward model and the second term is the prior distribution or the prior model of x. The overall scheme of the MAP estimate is shown in Fig. 5.33

There have been a variety of prior models used in literature such as the L1 norm, L2 norm etc. Notably, with the assumption that x is a Markov Random Field (MRF), it can be shown using the Hammersley-Clifford theorem that the prior model, $p(x)$, will have

the form of a Gibbs distribution [135, 136]. While there is no physical requirement on the ODF to be an MRF, this assumption forces neighboring pixels to be similar and gives good approximations in a variety of other physical science problems. A wide variety of such prior distributions gave been used in the literature [137–140]; the q-Generalized Gaussian Markov Random Field (q-GGMRF) has been particularly successful in tomographic reconstruction problems [141–143]. To formulate the overall cost function appropriate for ODF estimation, we need to provide expressions for both the conditional probability and the prior model terms in equation 5.9. It is interesting to note that the prior distribution, $p(x)$ can also be interpreted as a regularization term to stabilize the MAP estimate. If the prior distribution, $p(x)$ is ignored, then the MAP estimate reduces to the Maximum Likelihood (ML) estimator. The optimization problem then reduces to

$$\hat{x}_{ML} = \arg\min_{x \in \mathbb{R}^N}\{-\log p(y|x)\} \tag{5.10}$$

Forward model

As discussed previously, the pole figure intensity for a particular sample direction $\mathbf{y}$ and pole $\mathbf{h}$ is given by the equation 5.7; we will denote this by the operator $\mathcal{H}$. Given the ODF, $\mathbf{X}$ the operator, $\mathcal{H}$ predicts the pole figure intensity, $\mathcal{I}$ for that particular sample direction and pole. Since the pole figure intensity is obtained by a linear integral operation given by eq. 5.5, $\mathcal{H}$ is also linear in the ODF. The line integral for a sample direction $\mathbf{y}$ and pole $\mathbf{h}$ can be discretized as

$$\mathcal{I}(\mathbf{y};\mathbf{h}) = \sum_{i \in \mathcal{S}} X_i \Delta_i \tag{5.11}$$

Here, $\mathcal{S}$ represents the set of orientations which maps the pole $\mathbf{h}$ to the sample direction $\mathbf{y}$. It is also important to note that the set $\mathcal{S}$ only has orientations in the fundamental zone dictated by crystallographic symmetry. It is interesting to note that if the ODF is discretized using the cubochoric representation, then the differential volume in orientation space, $\Delta_i = \Delta \quad \forall i \in [1, N]$. The operator $\mathcal{H}$ can be represented as a matrix, $\mathcal{A}$ with the rows of matrix representing the line integral for different sample directions, $\mathbf{y}$ and pole $\mathbf{h}$. If

N_P represents the number of pole figures and N_K represents the number of sample direction measurement in each pole figure, then the total number of rows of $\mathcal{A}$, $n_{\mathcal{A}}^R$ which is the same as the total number of experimental measurements, $\mathbf{P}$ and is given by $n_{\mathcal{A}}^R = N_K \times N_P$. The variance in detector x-ray counts is typically modeled using Poisson statistics. It can be shown, using the variance stabilizing property of the square root transformation of a Poisson random variable, that the variance is well approximated by a constant variance Gaussian distribution [144]. The conditional probability of the pole figure intensity being $\mathbf{P}$ given an ODF $\mathbf{X}$, can be written as

$$p\left(\mathbf{P}|\mathbf{X}\right) \sim \exp\left\{-\frac{1}{2\sigma_w^2}||\mathcal{A}\mathbf{X} - \mathbf{P}||_2^2\right\}. \tag{5.12}$$

There are constant factors in front of the probability distribution and thus $\sim$ has been used. The problem of inverting a pole figure is exactly determined if $\mathcal{A}$ is a square matrix, i.e. the number of pole figure measurements is equal to the number of elements in the discrete ODF. However, this is not the case and the problem can only be solved in the "least-square sense".

Prior Model

In the last section, the problem of pole figure inversion was set up as a linear least square regression problem. It is a convex optimization problem with guaranteed solutions. However, it is also well known that such linear least square regression leads to over-fitting in absence of some regularization (prior information) to stabilize the solution. There are a variety of regularization models to choose from. In this chapter, we evaluate the elastic net and q-Generalized Gaussian Markov Random Field (q-GGMRF) regularization.

Elastic Net Prior   The elastic net prior model is a bridge between the ridge regression, which considers the $L2$ norm of the solution vector as the prior term and LASSO, which considers the $L1$ norm of the solution vector as prior model. Ridge regression ensures a small $L2$ norm of the solution vector which avoids the solution dominated by a few large values. LASSO on the other hand ensures sparsity in the solution. The prior probability

distribution, $p(x)$ is modeled as a weighted sum of the $L1$ and $L2$ norm of x.

$$p(\mathbf{X}) \sim \exp\left\{ -\frac{\lambda}{2\sigma_x^2}\left(\alpha||\mathbf{X}||_1 + \frac{(1-\alpha)}{2}||\mathbf{X}||_2^2 \right) \right\}. \tag{5.13}$$

For $\alpha = 1$, the prior model is the same as the $L1$ norm, while for $\alpha = 0$, the prior model approaches ridge regression. Again, the constant factors in front of the probability distribution have been ignored.

q-**Generalized Gaussian Markov Random Field**   The prior probability distribution can also be modeled using the q-Generalized Gaussian Markov Random Field (q-GGMRF). The main strength of this prior model draws from its property to correlate neighboring pixels. Thus, the parameters of this model can be adjusted depending on the nature of the experimental data, to account for sharp or diffuse boundaries. This prior model also offers the additional benefit of having a bounded second derivative, such that the substitute method can be used for an efficient implementation of the MAP estimator [145]. Let $\mathcal{N}$ be the set of all neighboring pixels in an image and $g_{i,j}$ be the normalized weighting kernel for each such neighboring pixel which is inversely proportional to distance such that $\sum_{i,j} g_{i,j} = 1$, then the probability density function is given by:

$$p(\mathbf{X}) = \frac{1}{Z}\exp\left\{ -\sum_{\{i,j\}\in\mathcal{N}} g_{i,j}\,\rho(X_i - X_j) \right\}, \tag{5.14}$$

with

$$\rho(\Delta) = \frac{|\Delta|^p}{p\sigma_x^p}\left(\frac{|\frac{\Delta}{T\sigma_x}|^{q-p}}{1 + |\frac{\Delta}{T\sigma_x}|^{q-p}} \right). \tag{5.15}$$

Here, Z is a normalizing constant and p, q, c and σ_x are the prior model parameters. Typically $1 \leq p \leq q \leq 2$ is used to ensure convexity of $\rho(\cdot)$. In this chapter, q has been set to 2; for this value of q, $p = 1$ corresponds to sharp edge prior model for the MAP estimate and $p = 2$ corresponds to diffuse edges in the final reconstruction. Thus the q-GGMRF model provides a flexible prior model to capture a wide range of textures in various material systems.

Optimization Problem

Maximum Likelihood estimator   For a set of pole figure measurements denoted by the column vector $\mathbf{P}$, using eq. 5.10, the maximum likelihood estimator for the problem of inverting the pole figure is simplified to the following optimization problem

$$\underset{\mathbf{X}}{\text{minimize}} \ ||\mathcal{A}\mathbf{X} - \mathbf{P}||_2^2 \quad \text{subject to} \ \begin{cases} \mathbf{X} \geq 0; \\ \Delta||\mathbf{X}||_1 = \frac{\pi^2}{\mathcal{O}_\mathcal{N}} \end{cases} \tag{5.16}$$

Here, $\mathcal{O}_\mathcal{N}$ denotes the order of the rotational symmetry group of the crystal. This is a convex optimization problem and the solution is guaranteed. However, it is well known that the solution typically over-fits the data with a few values dominating the solution. These issues can be ameliorated using prior models to stabilize the solution and prevent over-fitting.

Elastic net prior   As stated in eq. 5.13, the elastic net prior uses a combination of L1 and L2 norm of the solution vector as prior models. Plugging the Gaussian model for $p(x|y)$ and the elastic net prior for $p(x)$ in eq. 5.9 (ignoring the constant factors) reduces the pole figure inversion to the following optimization problem

$$\underset{\mathbf{X}}{\text{minimize}} \ \frac{1}{2\sigma_w^2}||\mathcal{A}\mathbf{X} - \mathbf{P}||_2^2 + \frac{\lambda}{2\sigma_x^2}\left(\alpha||\mathbf{X}||_1 + \frac{(1-\alpha)}{2}||\mathbf{X}||_2^2\right) \quad \text{subject to} \ \begin{cases} \mathbf{X} \geq 0; \\ \Delta||\mathbf{X}||_1 = \frac{\pi^2}{\mathcal{O}_\mathcal{N}} \end{cases} \tag{5.17}$$

This is again a convex optimization problem with guaranteed convergence. The $L2$ norm ensures that a few large numbers don't dominate the solution vector while the $L1$ norm ensures sparsity in the final solution. There are a variety of methods to determine the weight factors for the prior models such as the *discrepancy principle* [146], generalized cross-validation [147], L-curve method described in [148] etc. independent of the user. For this work, we will be using a combination of the L-curve method and trial and error to determine these parameters. A more complete approach to determining these parameters will be undertaken as part of the future work.

q-**GGMRF prior** Substituting the *q*-GGMRF prior distribution in eq. 5.9 gives the following optimization problem for the pole figure inversion problem

$$
\underset{\mathbf{X}}{\text{minimize}} \ \frac{1}{2\sigma_w^2} ||\mathcal{A}\mathbf{X} - \mathbf{P}||_2^2 + \sum_{\{i,j\}\in\mathcal{N}} g_{i,j}\rho\left(X_i - X_j\right) \quad \text{subject to} \ \begin{cases} \mathbf{X} \geq 0; \\[2mm] \Delta||\mathbf{X}||_1 = \frac{\pi^2}{\mathcal{O}_\mathcal{N}} \end{cases} \tag{5.18}
$$

The various parameters of the distribution are listed in section 5.3.3. These parameters can be adjusted to give smooth diffuse or sharp boundaries in the final reconstruction. However, this form of the cost function is non-convex and difficult to minimize. To simplify the problem as well as speed up the convergence, the substitute function approach is used, which leads to a closed form update for the ODF. A symmetric bound method is used to construct the substitute function with the original cost function being bounded from above by the substitute function. At any point Δ', the substitute function, $\rho(\Delta; \Delta')$ is given as

$$
\rho(\Delta; \Delta') = \frac{a_2}{2}\Delta^2. \tag{5.19}
$$

Here, a_2 is determined by matching the gradients of $\rho(\Delta)$ and $\rho(\Delta; \Delta')$ at the point Δ'. This leads to the following form of the substitute function:

$$
\rho(\Delta; \Delta') = \begin{cases} \frac{\rho'(\Delta')}{2\Delta'}\Delta^2 & \Delta \neq 0; \\[3mm] \frac{\rho''(0)}{2}\Delta^2 & \Delta = 0. \end{cases} \tag{5.20}
$$

Using this form of the substitute function, the new optimization problem is

$$
\underset{\mathbf{X}}{\text{minimize}} \ \frac{1}{2\sigma_w^2} ||\mathcal{A}\mathbf{X} - \mathbf{P}||_2^2 + \sum_{\{i,j\}\in\mathcal{N}} \tilde{g}_{i,j}\left(X_i - X_j\right)^2 \quad \text{subject to} \ \begin{cases} \mathbf{X} \geq 0; \\[2mm] \Delta||\mathbf{X}||_1 = \frac{\pi^2}{\mathcal{O}_\mathcal{N}} \end{cases} \tag{5.21}
$$

where,

$$
\tilde{g}_{i,j} = \begin{cases} g_{ij}\dfrac{|X_i - X_j)|^{p-2}}{2\sigma_x^p} \dfrac{\left|\frac{X_i - X_j)}{T\sigma_x}\right|^{q-p}\left(\frac{q}{p} + \left|\frac{X_i - X_j)}{T\sigma_x}\right|^{q-p}\right)}{\left(1 + \left|\frac{X_i - X_j)}{T\sigma_x}\right|^{q-p}\right)^2} & \Delta \neq 0; \\[8mm] g_{ij}\dfrac{1}{p\sigma_x^p} & \Delta = 0. \end{cases} \tag{5.22}
$$

The details of these calculations can be found in [149].

Pole	cubochoric RP error	MTEX RP error
$(2, 0, 0)$	3.3×10^{-3}	5.5×10^{-2}
$(2, 2, 0)$	2.8×10^{-3}	4.9×10^{-2}
$(1, 1, 1)$	1.8×10^{-3}	4.4×10^{-2}

Table 5.4: $L2$ error between input and reconstructed pole figures using current method and MTEX (default parameters).

5.3.4 Results

It has been very aptly put by J. Kallend in chapter 3 of [150] that

"All of the methods described are capable of producing a solution that is a good fit to the available experimental data" and

"the reader should be wary of tests claiming to show that one algorithm is better than another based on the analysis of model functions".

This is particularly true if the only metric used for the efficacy of an algorithm is the residual norm between the experimental and recalculated pole figures. In this section, we will present the results of the algorithm on both simulated and experimental data, using both complete and incomplete pole figures. In addition to comparing the residual norm, we will be using the 3D visualization techniques described in [129] to compare the final reconstructions of the ODF to the input ODF.

Model Pole Figures: Cube Texture in Ni

The initial ODF was generated using the free open-source MTEX toolbox. The initial ODF (all 24 equivalent orientations) in stereographic vector space is shown in Fig. 5.36(a). The 3 pole figures (Miller indices indicated above each pole figure) used for the ODF reconstruction are shown in Fig. 5.35(a). The reconstruction was performed using the elastic net prior.

Elastic net prior   The pole figure inversion was carried out for a number of different regularization parameters, λ and α. Given a true ODF, $\mathbf{X}_{\text{True}}$ and an estimate of the ODF, $\mathbf{X}_{\text{est}}$, the reconstruction error, R is defined as

$$R = \frac{||\mathbf{X}_{\text{True}} - \mathbf{X}_{\text{est}}||_2}{||\mathbf{X}_{\text{True}}||_2} \tag{5.23}$$
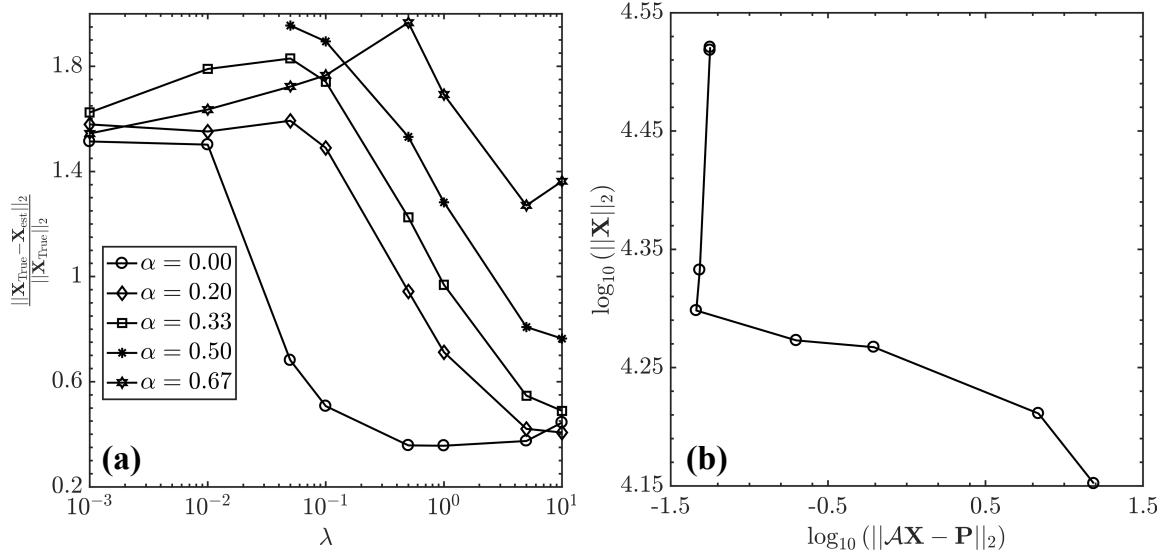
Figure 5.34: (a)Reconstruction error for different regularization parameters. The parameters $\lambda = 0.5$ and $\alpha = 0$ (pure ridge regression) gave the least reconstruction error of 0.356 and (b) L-curve analysis for the dataset showing an inflection point for the same set of regularization parameters.

Here, $||\cdot||_2$ represents the $L2$ norm of a vector. Fig. 5.34(a) shows the reconstruction error for a number of different parameters. $\lambda = 0.5$ and $\alpha = 0$ gave the least reconstruction error of 0.356. This set of parameters correspond to pure ridge regression and thus an L-curve analysis can also be performed. Fig. 5.34(a) shows the plot of the $L2$ norm of the solution vector with the residual error between the input and reconstructed pole figures for different values of λ ($\alpha = 0$). An appropriate set of regularization parameters achieve a good compromise between small $L2$ norm and low residual error. This corresponds to the inflection point in the characteristic L shape. Unsurprisingly, the inflection point in the L-curve corresponds to the same set of regularization parameters as the lowest reconstruction error ($\lambda = 0.5, \alpha = 0$). this gives us an independent way to obtain the regularization parameters for an arbitrary dataset.

The reconstructed pole figures and the difference with the input pole figure are shown in Fig. 5.35(b)-(c) respectively. The $L2$ error as calculated by MTEX between the input and reconstructed pole figures are shown in table 5.4. The reconstructed ODF in stereographic vector space (all equivalent orientations) is shown in Fig. 5.36(b).
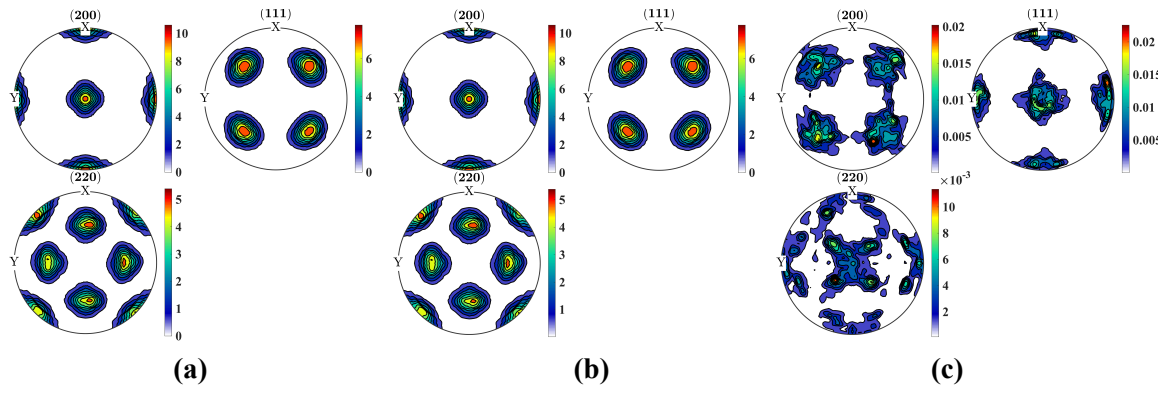
Figure 5.35: Pole figures for cube texture in Nickel (a) Input (b) reconstructed and (c) difference between input and reconstructed.

(a) **(b)**
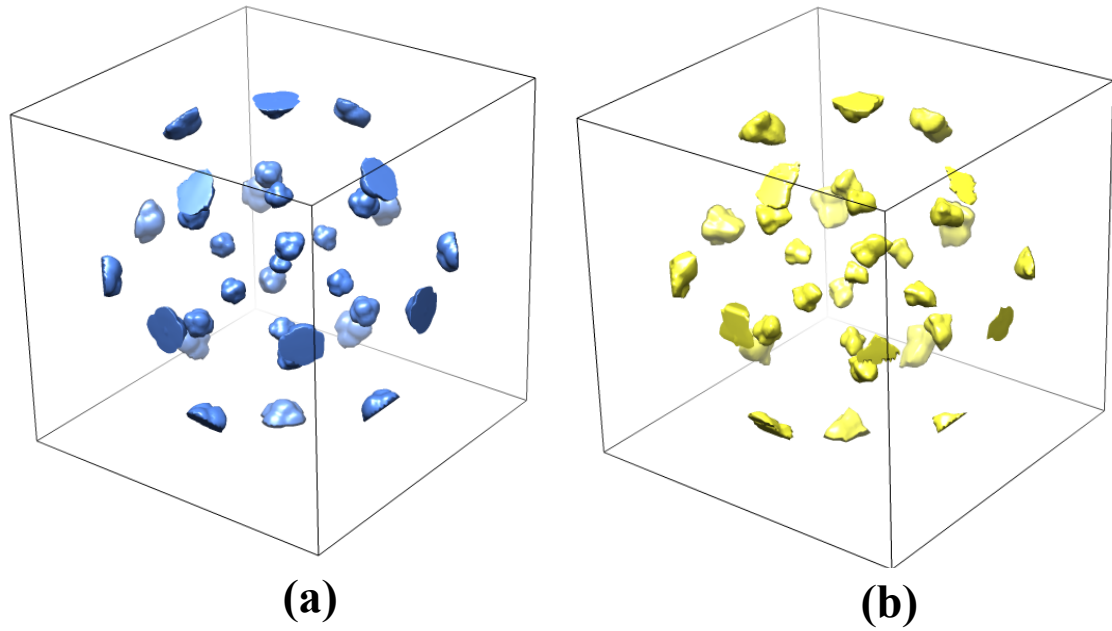
Figure 5.36: Cube texture in stereographic vector space (a) Input and (b) reconstructed

Complete Pole Figures: α-Ti

EBSD scans were performed on a two phase Ti-64 alloy containing both hexagonal α and cubic β phases. The total number of scan points were in excess of 1×10^6 with the number of grains exceeding 5×10^3 ensuring that the ODF can be estimated from the EBSD data with a fair degree of confidence. This ODF was used to generate pole figures for the α-Ti phase which were subsequently inverted to recalculate the ODF for this phase. The input ODF for the α-Ti phase is shown in Fig. 5.39(a). The black dots show the boundary of the stereographic sphere (radius 1).

Pole	cubochoric RP error	MTEX RP error
$(0,0,0,1)$	3.2×10^{-4}	3.2×10^{-2}
$(1,1,\bar{2},0)$	5.2×10^{-4}	3.5×10^{-2}
$(1,0,\bar{1},0)$	5.3×10^{-4}	3.14×10^{-2}
$(1,0,\bar{1},1)$	8.3×10^{-4}	12.4×10^{-2}

Table 5.5: $L2$ error between input and reconstructed pole figures using current method and MTEX (default parameters).
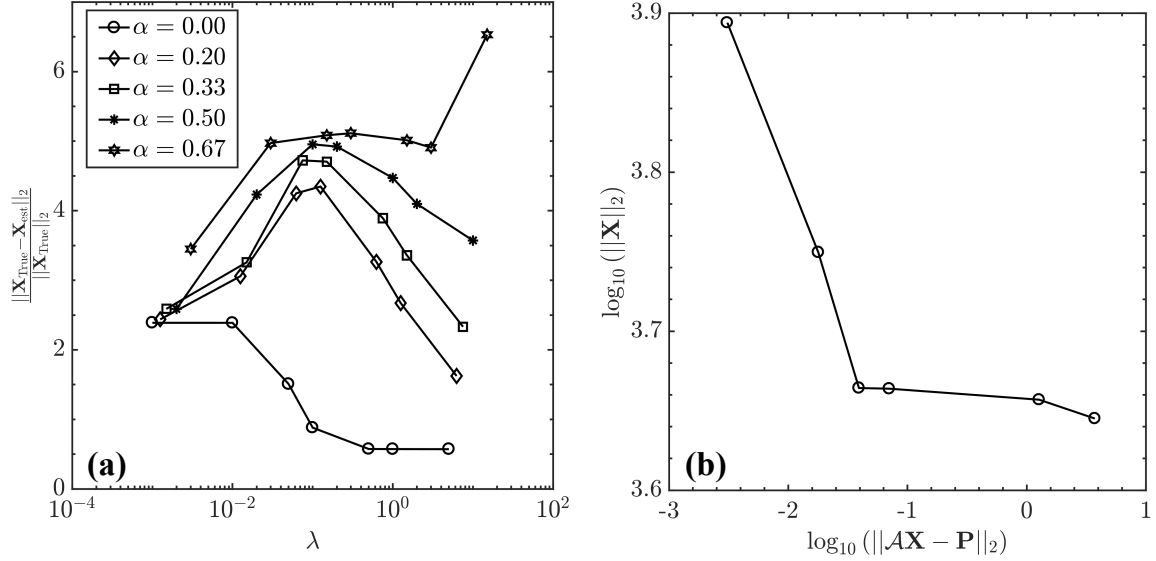
Figure 5.37: (a)Reconstruction error for different regularization parameters. The parameters $\lambda = 1.0$ and $\alpha = 0$ (pure ridge regression) gave the least reconstruction error of 0.573 and (b) L-curve analysis for the dataset showing an inflection point for the same set of regularization parameters.

The reconstruction error (see definition above) for a range of different λ and α values are shown in Fig. 5.37(a). The regularization parameters for the best reconstruction, i.e. least error were found to be $\lambda = 1.0$ and $\alpha = 0$. This set of parameters correspond to a pure ridge regression with no linear term. This makes it amenable to perform the L-curve analysis for this dataset. The log of the residual error in pole figures is plotted against the $L2$ norm of the solution vector for different values of regularization parameters. The curve shows a characteristic L shape, with the best compromise between low reconstruction error and smaller $L2$ norm of the solution vector found at the inflection point. This is shown in Fig. Fig. 5.37(b). Similar to the model cube texture, the inflection point also corresponds to $\lambda = 1.0$, which is identical to the parameters for least reconstruction error.

The reconstructed pole figures and the difference with the input pole figure are shown in Fig. 5.38(b)-(c) respectively. The $L2$ error as calculated by MTEX between the input and
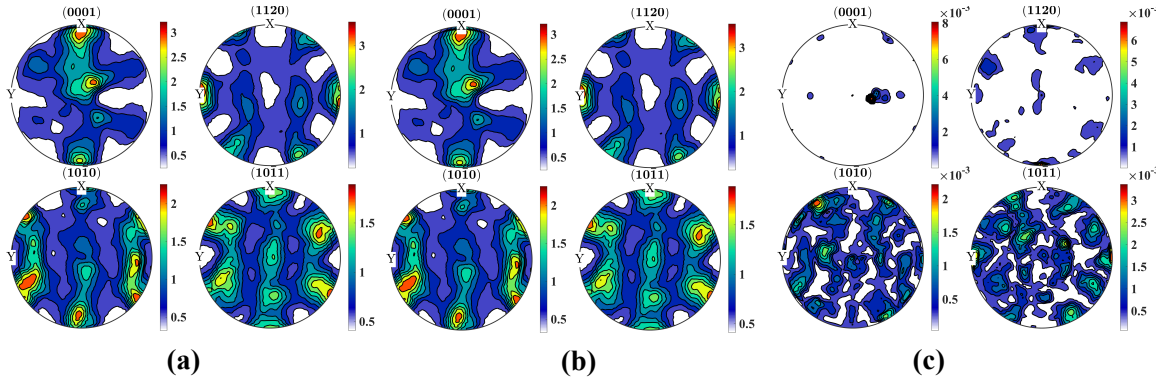
Figure 5.38: Pole figures for cube texture hexagonal α-Ti (a) Input (b) reconstructed and (c) difference between input and reconstructed.
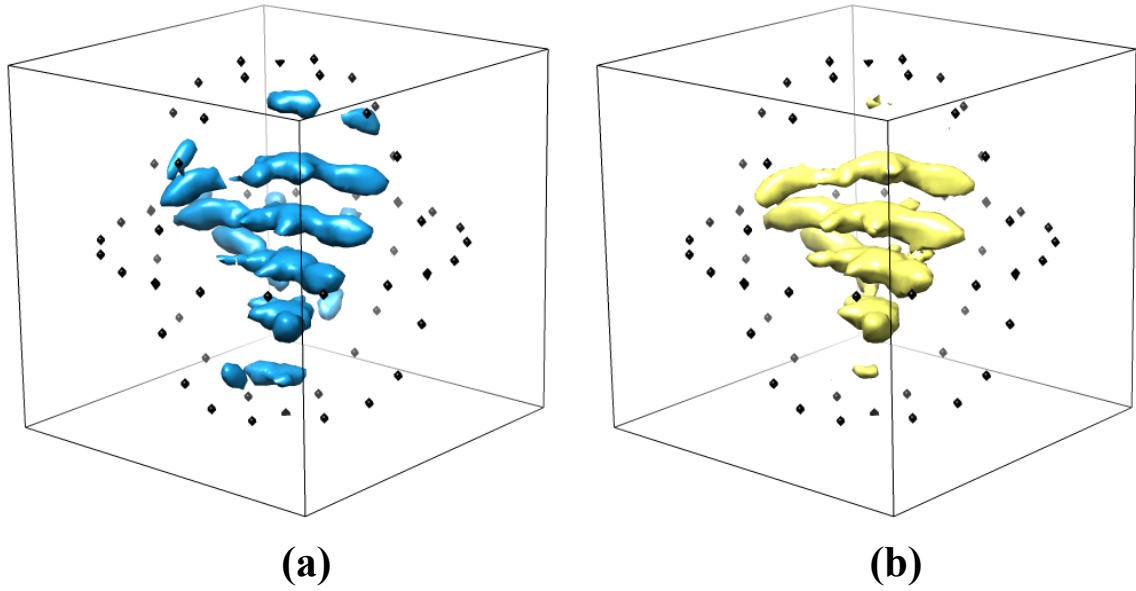
Figure 5.39: Texture in α-Ti (a) Input and (b) reconstructed.

reconstructed pole figures are shown in table 5.5. The reconstructed ODF in stereographic vector space (all equivalent orientations) is shown in Fig. 5.39(b). The black dots show the boundary of the stereographic sphere (radius 1).

5.4 Conclusion and Discussion

In this chapter, we presented results for the use of forward models to materials characterization. The forward models for electron scattering were used to develop a new indexing scheme for three different diffraction modalities: Electron Backscatter Diffraction, Electron Channeling Patterns and Precession Electron Diffraction. A forward model for predicting

pole figure intensities employing the new cubochoric representation was developed. This forward model in conjunction with the Model based Iterative Reconstruction approach from the tomography community was used to develop a new direct method for pole figure inversion.

It was hypothesized that the forward model based dictionary method will perform better than the Hough transform based methods for the following cases:

- **High gain/Fast acquisition conditions**: The dictionary method will give superior results compared to the commercial package when high gain or fast acquisition conditions are used, or if the pattern quality is low. As a case study for this claim, indexing results for a Nickel dataset were presented where scans were collected from the same region of interest but with varying levels of gain and exposure time to maintain the same exposure level. At 25 dB of noise when the Hough transform based method gives 0% indexing success rate, the dictionary method was still able to index ∼ 75% of the scan points.

- **Low keV/Highly deformed sample**: The dictionary method will outperform the commercial methods in terms of the indexing success rate when low acceleration voltages are used to improve the spatial resolution. To verify this claim, the dictionary method was employed on a shot peened Aluminum dataset with significant stored deformation at 5 keV. The dictionary produced superior results both close to the grain boundaries as well as close to the highly deformed shot peened regions, resolving extremely fine microstructural features.

- **Low symmetry/multi-phase melt**: The dictionary approach will show a significant improvement over the commercial package, not only in terms of indexing success rate and phase identification but also in erroneous indexing of diffraction patterns as one of its pseudosymmetric variants for low symmetry crystals. This claim was tested for two challenging geological samples, namely orthorhombic Forsterite and a multi-phase mixture of monoclinic Clinopyroxene (cpx), cubic Garnet (grt) and amorphous melt. The presence of the melt in the latter sample also limits the use of post processing cleanup procedure. The dictionary approach showed a much better indexing success

rate and was able to resolve fine microstructural features in both the samples. The method was also able to completely segment the cpx-grt-melt mixture in its constituent phases along with identification of cpx-grt phase boundaries as well as wetted cpx and grt grains (cpx-melt and grt-melt phase boundaries).

The dictionary approach was also able to index electron channeling patterns. This is the first automated method to index an arbitrary electron channeling pattern of arbitrary symmetry. The proof of concept was demonstrated for patterns from a polycrystalline Si sample with the results in excellent agreement with the calibrated values. An error analysis is performed using a set of $1,000$ simulated patterns with random orientations. The results show that the method produces a mean orientation error of $1°$ with $0.5°$ standard deviation for the true detector parameters and $N = 100$ points along the cubochoric cube semi-edge, corresponding to a mean sampling step size of $1.4°$. Increasing the number of sampling points decreases the error. The mean orientation error is insensitive to an error in the detector parameters up to about 5% error in detector parameter.

Indexing results of applying the dictionary approach to precession electron diffraction patterns from a highly deformed Cu sample were also shown. The method was able to resolve subtle variations in the orientation within the grain. The orientation similarity map (OSM) clearly delineates the grain boundaries and shows contrast within each grain with the deformation field being a likely reason for the contrast variation.

The dictionary approach offers a unified method to indexing diffraction patterns. The basic ingredients of the algorithm involve a generalized forward projector and detector model, specific to the diffraction modality and uniform sampling of orientation space, which is independent of the modality. The problem of indexing was reformulated from an *inverse problem* to a *forward problem*. This reformulation guarantees that the indexing problem will always have a unique solution, since there will always be a highest dot product. However, the drawback with the dictionary approach is in its computational cost. The orientation space is enormous; even for cubic symmetry and a modest angular resolution of about $1.4°$, the dictionary method requires calculation of 333,227 patterns. For lower symmetry and higher angular resolution, the number of patterns in the dictionary can easily exceed a

million. Thus, significant efforts need to be made to make the dictionary approach more computationally efficient. The dictionary approach can complement the Hough transform based methods to give high fidelity IPF maps, as well as phase, grain boundary and topographic information about underlying microstructure.

Two algorithms to refine approximately known orientations for any diffraction modality were presented. The technique relies on the availability of an accurate forward model, which captures the relevant physics of the diffraction experiment, a reasonably accurate initial starting value and a method to effectively and efficiently search the local orientation neighborhood to optimize a similarity metric between the experimental and computed diffraction patterns. Two such search methods, namely the brute force search and a Derivative Free Optimization (DFO) approach were described. The results of both algorithms were presented for two different electron diffraction modalities: Electron Back-scatter Diffraction (EBSD) and Electron Channeling Patterns (ECP).

The accuracy of the method was evaluated using a set of $1,000$ simulated diffraction patterns with known orientations sampled randomly, and indexed both using the dictionary method and the Hough transform method. For the EBSD modality, the algorithms reduce the orientation error for up to a $\pm 1\%$ error in the input detector parameters (projection center coordinates), while the ECP modality is largely insensitive up to $\pm 5\%$ error in the input detector parameter (capture angle). Thus, unsurprisingly, accurate detector parameters are necessary for the algorithm to converge to the correct values. While the dictionary method has many advantages over the Hough transform-based methods, including robustness to noise in diffraction patterns, the dictionary method suffers from the drawback of a discretely sampled orientation space. This problem is exacerbated in the case of deformed materials where there are gradients in the orientation within each grain which are manifested as orientation contours in the IPF and KAM maps. The proposed refinement algorithms were able to overcome these discrete sampling artifacts.

The refinement is performed assuming knowledge of accurate detector parameters. However, for large area EBSD scans, the projection center is not constant and changes appreciably across the scan area. A simple correction factor was introduced to handle this case and correct the orientations. The correction method was applied to a simulated large area single

crystal EBSD scan with a 2×3 mm^2 field of view, showing very good results. In conclusion, the refinement algorithms introduced here rely on an accurate knowledge of the detector parameters and the initial indexing is especially crucial for the dictionary based indexing of diffraction patterns, which, for large scan areas, suffers from the obvious drawback of a discretely sampled orientation space.

Finally, a new model based method to invert pole figures using the equal-volume cubochoric projection is introduced. The tomography community has made giant leaps in solving ill-conditioned tomographic inverse problems, of which pole figure inversion is a special case, in the past few decades moving from algebraic methods such as Algebraic Reconstruction Technique (ART) and Successive Iterative Reconstruction (SIRT) to Model-based Iterative Reconstruction (MBIR). However, these new techniques are not known or have not been used in the materials characterization community. This, together with the recent advances in orientation representations and sampling has laid the foundation for implementing these new methods to a very old problem. The proof of concept of this method is shown for synthetic cube texture and complete pole figure for α-Ti using EBSD data. It is noted that more work needs to be done to implement the complete model based approach using Markov random fields as prior models.

In conclusion, forward models greatly improve our ability to solve inverse problems and offer a new and exciting avenue for devising new analysis tools and techniques for materials characterization.

CHAPTER VI

Future Work

In the previous chapters, we have introduced the dictionary approach, a new method to index diffraction patterns uses all available pixels in the image. We discussed all the pieces required for the dictionary-based algorithm to work correctly. This includes the generalized forward projector, the detector and noise model and finally a scheme to uniformly sample orientation space. The approach was shown to work for three different diffraction modalities, Electron Backscatter Diffraction, Electron Channeling Patterns and Precession Electron Diffraction. We were also able to extract additional information about the underlying microstructure using the dictionary approach. Further, we proposed a model based iterative reconstruction method for inverting pole figures to calculate the orientation distribution function. However, there are a number of challenges and bottlenecks which need to be addressed. In this chapter we will discuss some new directions of study which build on the work carried out as part of this thesis.

6.1 Short Term

6.1.1 MBIR implementation for Pole Figure Inversion

The new implementation for inverting pole figures to calculate the orientation distribution function using the hierarchical and refinable cubochoric representation and the elastic net prior model has shown promising results. This implementation uses sparse matrix operations with minimal computational overhead associated with finer grids for discretization of orientation space. The pole figure inversion problem has also been formulated using the q-generalized Gibb's Markov Random Field prior model. This model needs to be imple-

mented and the results need to be compared to the elastic net prior model as well as other existing methods including the harmonic function based implementation used in MTEX as well as the direct Euler space method in popLA.

6.1.2 Detector Parameters

The dictionary method requires accurate detector parameters in order to correctly index diffraction modalities. The proposed algorithm uses a derivative free optimization techniques to accurately estimate these parameters. However, if the initial guess is not accurate, the algorithm fails to converge to the correct values. There are two potential reasons for this:

- The objective function used in the method (dot product) may not be the best proxy for the discrepancy between experimental and simulated patterns;

- Another type of optimization algorithms might be more suitable for this problem.

It was found using numerical experiments that mutual information has a deeper well in the energy landscape for pattern optimization. It was also found that a direct search method such as the Hooke algorithm [151] performed better than the currently implemented Nelder-Mead/BOBYQA methods. The implementation of these algorithms and a comparative study with the existing implementation constitutes another important aspect which can be finished in the short term.

6.1.3 Dictionary Indexing of Transmission Kikuchi Diffraction Patterns

The forward model for the TKD modality shows very good correspondence with the real experimental patterns. The extension of the dictionary indexing algorithm to the TKD modality is straightforward. Some preliminary work to this effect has already been undertaken and shown promising results; the method needs to be tested. Since the patterns looks very similar to the EBSD modality, it is expected that much of the benchmarks in terms of angular accuracy and error analysis as well-as the efficacy of the method including robustness against noise and low symmetry patterns holds for these patterns. However, a comprehensive study of the dictionary method to establish these bounds quantitatively needs to be undertaken.

6.2 Medium Term

6.2.1 Computational Efficiency

One of the biggest hurdles associated with the dictionary approach is the computational time required. The forward model has two distinct steps for the EBSD, ECP and TKD modalities: Monte Carlo trajectory simulations and master diffraction pattern calculation, followed by pattern interpolation. The Monte Carlo simulations assumed that the incident electrons are independent and do not interact with each other. Therefore, the algorithm is easily implementable on a Graphics Processing Unit (GPUs). This has already been done, bringing down the typical computation time for 2×10^9 electrons from about 14 hours to about 5 minutes. This is an impressive speedup of more than $150\times$. The master pattern computation, on the other hand, is parallelized using the OpenMP approach and can take anywhere from a few minutes for high symmetry elemental crystals, such as Nickel and Silicon, to days for lower symmetry and complex crystal structures having a large unit cell. While a more efficient implementation of this on a GPU with a high level of parallelism might decrease the compute times, it is the authors opinion that this will not make the method "on-line" and at par with the commercial methods.

An interesting candidate for improving the efficiency of the methods and making it "on-line" is a convoluted neural networks based deep learning algorithm. These algorithms have been shown to learn highly non-linear functions with powerful predictive abilities. The most important requirement for neural networks to get adequate predictive performance is large amounts of data for training the model. This is not a barrier for our purpose as accurate forward models exist for these diffraction modalities and there is no shortage of simulated data. This is very similar to how self-driving cars were initially trained on physics based game engines before training in real world scenarios. The broad goal of the model will be to learn the diffraction patterns for different material systems (symmetries), acceleration voltages, detector parameters, orientations etc. However, learning the orientation information will be the first goal and other information will be learned incrementally. The hope is that given sufficient training data, such a neural network based model will be able to predict orientations. Some very preliminary numerical experiments using Google's TensorFlow

package on the nVIDIA 1080 GTX GPU suggest an indexing speed of about 1500 patterns per second for a 60×60 binned pattern for cubic Nickel. However, much work needs to be done in optimizing this approach to match the efficacy of the dictionary method and generalizing it to include other variable parameters in the model.

6.2.2   Electron scattering calculations for multiphase system

The prediction of diffraction patterns in the case where the electron interacts with multiple crystals is of great interest to researchers in the areas of thin films and semiconductors. This diffraction pattern is expected to be a function of the geometry of the system. A forward model for predicting the diffraction pattern might provide a non-destructive method of extracting these quantities. The problem boils down to a boundary value problem of smoothly matching the wavefunctions at the crystal interfaces. While some preliminary work has been done in this area, much needs to be done to have an accurate forward model.

6.2.3   Predicting pseudosymmetry in an arbitrary crystal

As shown in previous chapter, the results from the dictionary approach were free from pseudosymmetric artifacts introduced typically in lower symmetry systems. The dictionary approach can be used to predict the possible pseudosymmetric variants using a "dictionary-on-dictionary" run. The top k matches from the dictionary-on-dictionary indexing are expected to be clustered around the same orientation as well as close to the pseudosymmetric variant. The origins of pseudosymmetry in the indexing results using Hough transform needs to be investigated in more depth. We hypothesize that this might be due to the use of kinematical structure factors for choosing the candidate bands. The use of dynamical band intensities as a selection criteria might be able to alleviate such artifacts.

6.2.4   Contrast inversion in electron diffraction modalities

Contrast inversion of certain bands in the EBSD and TKD modality is a well documented phenomenon. Fig. 6.1(a)-(d) shows EBSD patterns for Silicon at 20 kV acceleration voltage at sample tilts of $64°$, $60°$, $56°$ and $52°$ respectively. Decreasing the sample tilt leads to an a contrast inversion in certain bands, some of which are pointed out by the arrows. There have been some attempts to explain this phenomenon using dynamical diffraction [152].
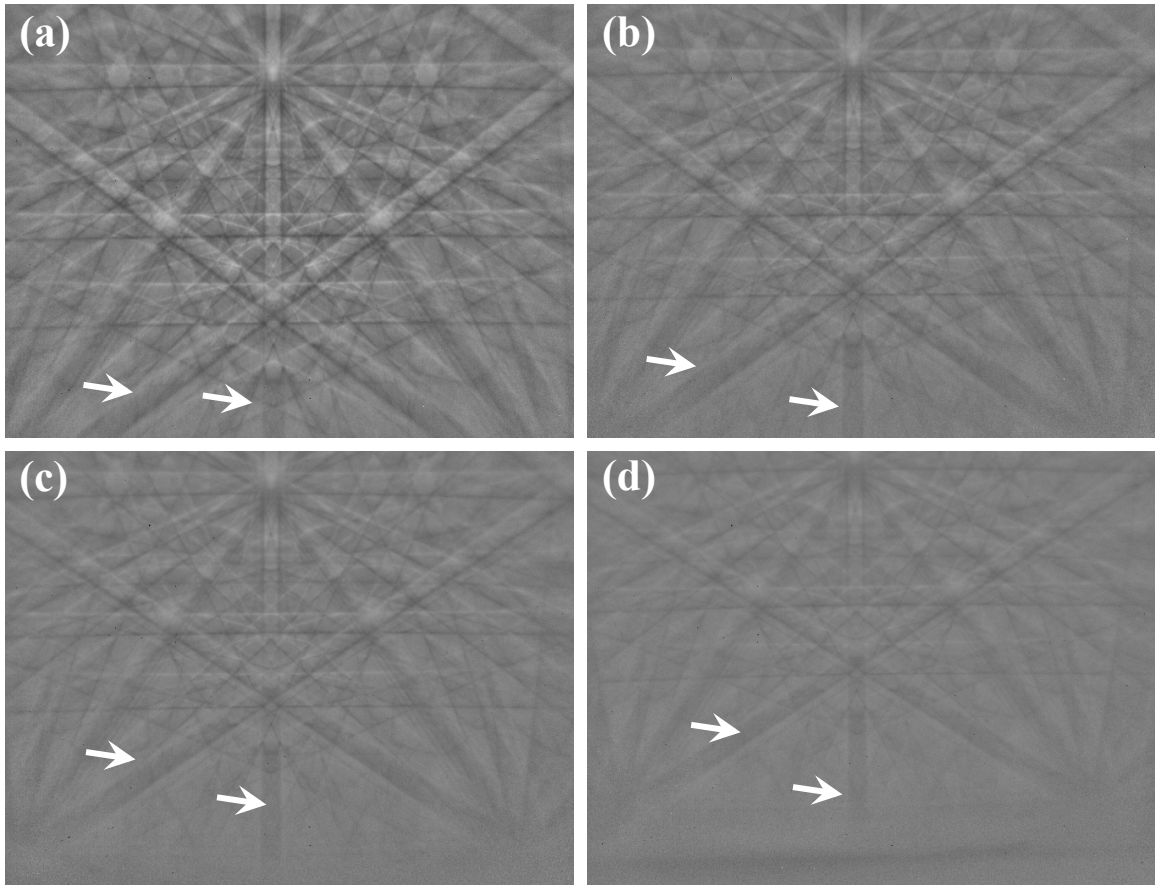
Figure 6.1: Electron Backscatter Difraction pattern from Silicon at 20 kV microscope acceleration voltage at different sample tilts (a) 64° (b) 60° (c) 56° and (d) 52°. (Patterns courtesy Dr. Gert Nolze, Bundesanstalt fuer Materialforschung und -pruefung)

However, these theoretical developments rely on artificially changing the information depth of electrons in the crystal. To the best of the author's knowledge, there are no physically motivated models which can give rise to these contrast inversions.

6.3 Long Term

6.3.1 Automated Defect Imaging in the SEM

Defect analysis using a Scanning Electron Microscope (SEM), commonly known as Electron Channeling Contrast Imaging (ECCI), has received much attention in the recent past. Traditional defect analysis has for decades relied on TEM modalities, such as the bright field-dark field and weak beam imaging, and Scanning Transmission Electron Microscopy (STEM) diffraction contrast imaging methods. While the spatial resolution of ECCI is

somewhat lower than that of the TEM based methods, ECCI provides more flexibility in sample preparation and data acquisition from bulk samples. The method relies on the variation of backscatter yield near lattice defects. To achieve quantitative defect analysis, the exact diffraction conditions need to be known, which, in turn, requires accurate determination of the crystal orientation. Since ECPs are difficult to index, there have been efforts to integrate ECCI with the Electron Backscatter Diffraction (EBSD) method for orientation mapping [51]. However, the dictionary approach can eliminate the use of extra hardware by opening the possibility of indexing an arbitrary ECP. Furthermore, with the advent of fully scriptable microscopes for stage control and data acquisition, it has become possible to automate the data collection process for rapid ECCI-based defect characterization and analysis. The TESCAN-MIRA3 SEM with beam rocking apparatus is fully scriptable using the SharkSEM remote control library, which can be used for automated data acquisition by controlling both the stage and the detectors (secondary and backscatter). The ultimate aim of this exercise is to automate data collection in the ECCI modality by indexing the ECP and achieving multiple two beam orientations by autonomous navigation in orientation space using sample tilt and rotation. This will enable high-throughput collection of large numbers of defect images from different regions in the sample.

While the dictionary algorithm has been successful in indexing channeling patterns, the method is a post-processing tool in principle. Even with the hybrid OpenCL/OpenMP implementation of the dictionary method, real time indexing capabilities have not been achieved. At this point, convoluted neural network based deep learning seems to be the only approach to make the real time indexing of channeling patterns viable. Designing such a model for an arbitrary material system, inexact knowledge of the microscope geometry along with full integration into the current microscope software seems to be a formidable challenge. However, real time indexing of channeling patterns would open up a plethora of new possibilities for materials characterization in the SEM and is a worthwhile exercise.

6.3.2 Rethinking the EBSD geometry

The motivation of tilting the sample to 70° while designing the EBSD system was to improve the backscatter yield of the sample. While this geometry works, it is complicated and

highly prohibitive for certain samples. It would be desirable to perform EBSD with a nearly horizontal sample with a simpler and more flexible geometry. With continual improvements in electronics and the advent of high dynamic range electron detectors capable of imaging a direct electron beam with single electron sensitivity [153], this no longer remains a strict requirement. These detectors together with the robustness against noise of dictionary indexing can be used to re-design the EBSD geometry. This might have important consequence for Focussed Ion Beam (FIB) based 3-D materials characterization technique making the geometry simpler and potentially reducing the stage movements required for milling and acquisition of diffraction patterns.

APPENDIX A

Uniform sampling of Misorientation space

In this section, we derive the equation of the iso-misorientation surface with respect to an arbitrary Rodrigues vector $\boldsymbol{\rho} = \tan(\frac{\omega}{2})\hat{\mathbf{n}}$; this amounts to finding the locus of points such that the modulus of the Rodrigues vector representing the misorientation between any point on the surface and the point of interest is a constant. Let $\boldsymbol{\tau}$ represent any Rodrigues vector that has a constant misorientation angle μ with respect to the point $\boldsymbol{\rho}$. It is well known that the combination rule for Rodrigues vectors is different from the traditional parallelogram law of vector addition. Two Rodrigues vectors, $\boldsymbol{\rho}_A$ and $\boldsymbol{\rho}_B$, with $\boldsymbol{\rho}_B$ applied after $\boldsymbol{\rho}_A$, combine according to the law:

$$\{\boldsymbol{\rho}_A, \boldsymbol{\rho}_B\} = \frac{\boldsymbol{\rho}_A + \boldsymbol{\rho}_B - \boldsymbol{\rho}_A \times \boldsymbol{\rho}_B}{1 - \boldsymbol{\rho}_A \cdot \boldsymbol{\rho}_B}. \tag{A.1}$$

The Rodrigues vector corresponding to the misorientation between $\boldsymbol{\rho}_A$ and $\boldsymbol{\rho}_B$ is simply the vector that maps $\boldsymbol{\rho}_B$ onto $\boldsymbol{\rho}_A$, namely

$$\boldsymbol{\rho}^{mis} = \{\boldsymbol{\rho}_B, -\boldsymbol{\rho}_A\} = \frac{\boldsymbol{\rho}_B - \boldsymbol{\rho}_A + \boldsymbol{\rho}_B \times \boldsymbol{\rho}_A}{1 + \boldsymbol{\rho}_B \cdot \boldsymbol{\rho}_A}. \tag{A.2}$$

Substituting $\boldsymbol{\rho}_B$ by $\boldsymbol{\tau}$ and $\boldsymbol{\rho}_A$ by $\boldsymbol{\rho}$, we obtain for the modulus of the misorientation Rodrigues vector:

$$|\boldsymbol{\rho}^{mis}| = \left| \frac{\boldsymbol{\tau} - \boldsymbol{\rho} + \boldsymbol{\tau} \times \boldsymbol{\rho}}{1 + \boldsymbol{\tau} \cdot \boldsymbol{\rho}} \right| = c \equiv \tan \frac{\mu}{2}. \tag{A.3}$$

Squaring both sides of the equation (A.3) we obtain:

$$\frac{|\boldsymbol{\tau}|^2 + |\boldsymbol{\rho}|^2 + |\boldsymbol{\tau} \times \boldsymbol{\rho}|^2 - 2\boldsymbol{\tau} \cdot \boldsymbol{\rho}}{(1 + \boldsymbol{\tau} \cdot \boldsymbol{\rho})^2} = c^2. \tag{A.4}$$

Setting $\tau^2 \equiv |\boldsymbol{\tau}|^2$ and $\rho^2 \equiv |\boldsymbol{\rho}|^2$ and using $|\boldsymbol{\tau} \times \boldsymbol{\rho}|^2 = \tau^2\rho^2 - (\boldsymbol{\tau} \cdot \boldsymbol{\rho})^2$ we have:

$$(1 + c^2)(\boldsymbol{\tau} \cdot \boldsymbol{\rho})^2 + 2(1 + c^2)\boldsymbol{\tau} \cdot \boldsymbol{\rho} - (1 + \rho^2)\tau^2 - \rho^2 + c^2 = 0. \tag{A.5}$$

This equation has both quadratic and linear terms in the components of $\boldsymbol{\tau} = (\tau_x, \tau_y, \tau_z)$, which indicates that the iso-misorientation surface is a quadratic surface in Rodrigues space. Introducing a coordinate translation vector $\mathbf{v}$, one can determine the components of $\mathbf{v}$ such that the terms linear in the components of $\boldsymbol{\tau}$ in equation A.5 vanish. This leads to

$$\mathbf{v} = \frac{1 + \cos\omega}{\cos\mu + \cos\omega}\boldsymbol{\rho}. \tag{A.6}$$

The remaining equation can then be formulated in matrix form as:

$$(\boldsymbol{\tau} - \mathbf{v})^T \mathcal{K}(\boldsymbol{\tau} - \mathbf{v}) = 1, \tag{A.7}$$

where the matrix $\mathcal{K}$ is symmetric with elements κ_{ij} given by:

$$\kappa_{ii} = \alpha(1 + \rho^2 - (1 + c^2)\rho_i^2); \tag{A.8}$$

$$\kappa_{ij} = -\alpha(1 + c^2)\rho_i\rho_j \qquad (i \neq j), \tag{A.9}$$

with

$$\alpha = \frac{1 - c^2\rho^2}{c^2(1 + \rho^2)^2}. \tag{A.10}$$

The matrix $\mathcal{K}$ has eigenvalues:

$$\lambda_1 = \lambda_2 = \text{sign}\,(\pi - (\omega + \mu))\sqrt{\frac{1 - \cos\mu}{\cos\mu + \cos\omega}}; \tag{A.11}$$

$$\lambda_3 = \left|\frac{\sin\mu}{\cos\mu + \cos\omega}\right|, \tag{A.12}$$

and the orthonormal eigenvectors of $\mathcal{K}$ are given by the columns of the eigenvector matrix E_{ij} (with $s \equiv \sqrt{\rho_x^2 + \rho_z^2}$):

$$
E_{ij} = \begin{pmatrix} -\frac{\rho_z}{s} & -\frac{\rho_x \rho_y}{\rho s} & \frac{\rho_x}{\rho} \\ 0 & \frac{s}{\rho} & \frac{\rho_y}{\rho} \\ \frac{\rho_x}{s} & -\frac{\rho_y \rho_z}{\rho s} & \frac{\rho_z}{\rho} \end{pmatrix}. \tag{A.13}
$$

The prefactor in equation (A.11) can be equal to $+1$ or -1, depending on the values of μ and ω. The transition from $+1$ to -1 occurs when $\tan(\mu/2) = \tan((\pi - \omega)/2)$ or $\mu + \omega = \pi$. Consequently, the iso-surface shape changes from an ellipsoid to a hyperboloid of two sheets (with two negative and one positive eigenvalues). We will treat the case $\mu + \omega = \pi$ separately, since the translation vector $\mathbf{v}$ goes to infinity in that case. Noting that $\tan(\omega/2) \tan(\mu/2) = 1$ and substituting $\tan(\omega/2)$ by k, we obtain a quadratic surface described by the matrix equation $\boldsymbol{\tau}^T \mathcal{K} \boldsymbol{\tau} = 0$, where $\boldsymbol{\tau} = (\tau_x, \tau_y, \tau_z, 1)$ is a homogeneous vector; setting $\alpha = 1 + k^2$, the 4×4 matrix $\mathcal{K}$ has elements κ_{ij} defined by:

$$
\begin{aligned}
\kappa_{ii} &= \alpha(1 - n_i^2) & (i \leq 3), \tag{A.14} \\
\kappa_{ij} &= -\alpha n_i n_j & (i \neq j, i, j \leq 3), \tag{A.15} \\
\kappa_{ij} &= -\alpha \frac{n_l}{k} & (l = \inf\{i,j\}, \sup\{i,j\} = 4), \tag{A.16} \\
\kappa_{44} &= \alpha \frac{(k^2 - 1)}{k^2}. \tag{A.17}
\end{aligned}
$$

We also define another matrix, $\mathcal{L}$, as the 3×3 submatrix of $\mathcal{K}$, such that $\lambda_{ij} = \kappa_{ij} (i, j = 1, 2, 3)$. The eigenvalues of $\mathcal{L}$ are

$$
\lambda_1 = \lambda_2 = \alpha; \tag{A.18}
$$

$$
\lambda_3 = 0, \tag{A.19}
$$

and the eigenvector matrix is again given by E_{ij} (eq. A.13). Since $\text{rank}(\mathcal{K}) = 4$, $\text{rank}(\mathcal{L}) = 2$, and $\det(\mathcal{K}) < 0$, the quadratic surface is an elliptic paraboloid for the special case of $\omega + \mu = \pi$ [154]; because the two non-vanishing eigenvalues are equal, the cross-section of the quadratic surface normal to the third eigenvector is circular, as it is for the general case of the spheroid when $\omega + \mu \neq \pi$.

For numerical computations, one can make use of equation (A.3), but care must be taken with the denominator: if $\omega + \mu = \pi$, then the misorientation Rodrigues vector for the point $\boldsymbol{\tau}$ for which $\boldsymbol{\tau} \cdot \boldsymbol{\rho} = -1$ must be set to a vector parallel to $\boldsymbol{\rho}$ with infinite length (i.e., a $180°$ rotation around $\hat{\boldsymbol{\rho}}$). This is the only singular point.

APPENDIX B

Correction Factor for Monte Carlo Interpolation

In this document, we seek the generalization to the correction factor that has been described in chapter III. We seek to find the general expression for the area of the ellipse formed due to intersection of a cone with a plane, which is akin to finding the semi-major and semi-minor axes of the ellipse. We will make use of ideas from quadratic surfaces in this derivation. It is well known that the intersection of a plane with a cone leads to a quadratic curves. An examples of this is shown in Fig. B.1. We are interested in the case when the conic section is an ellipse.

The general equation of a cone with the unit vector along the axis given by $\hat{\mathbf{n}}$ is given by the following equation

$$\hat{\mathbf{r}} \cdot \hat{\mathbf{n}} = \cos \alpha. \tag{B.1}$$

Here, $\hat{\mathbf{r}}$ is the unit vector for any point on the cone and α is the opening angle of the cone.

In cartesian coordinates, $\hat{\mathbf{r}} = \frac{(x,y,z)}{\sqrt{x^2+y^2+z^2}}$. Also assuming $\hat{\mathbf{n}} = (n_1, n_2, n_3))$ with $n_1^2 + n_2^2 + n_3^2 = 1$, the equation of the cone reads as

$$n_1 x + n_2 y + n_3 z = \sqrt{x^2 + y^2 + z^2} \cos \alpha. \tag{B.2}$$

Consider the geometry shown in Fig. B.2. The unit vector along the cone axis is given by $\hat{\mathbf{n}} = (\cos \phi \sin \theta, \sin \phi \sin \theta, \cos \theta)$ and the plane is given by the equation $z = L$. In such a case, the equation of the ellipse can be calculated by finding the curve of intersection of the cone and the plane. This is a trivial but tedious problem. Substituting $z = L$ in equation
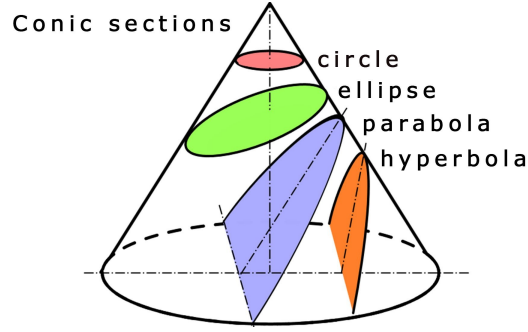
Figure B.1: Different conic sections formed by intersection of a cone and plane.
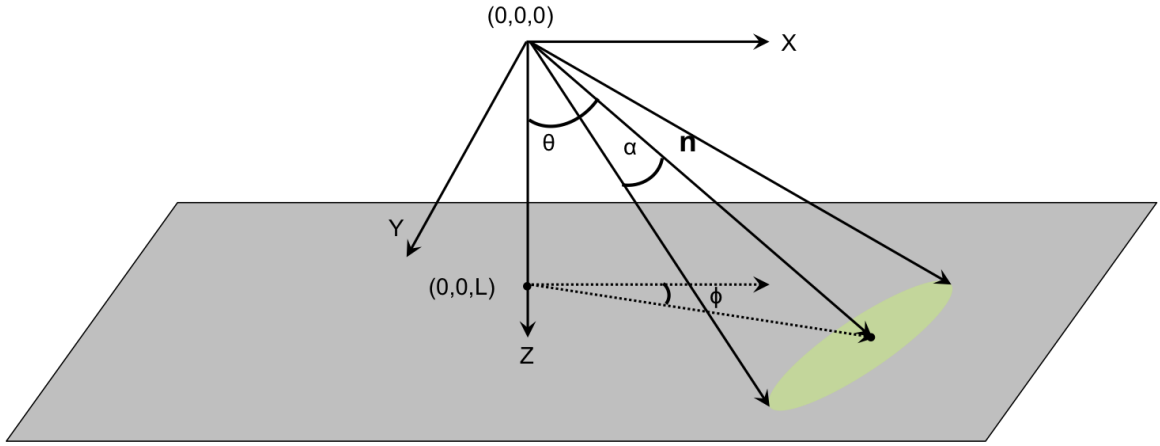
Figure B.2: Geometry of the problem.

B.2, we get

$$n_1 x + n_2 y + n_3 L = \sqrt{x^2 + y^2 + L^2} \cos \alpha. \tag{B.3}$$

We will denote $\cos \alpha$ as μ. We introduce dimensionless coordinates such that $x_d = x/L, y_d = y/L, z_d = z/L$. Squaring both sides and collecting terms, we end up with the general parabolic curve having the equation

$$(\mu^2 - n_1^2)x_d^2 - 2n_1 n_2 x_d y_d + (\mu^2 - n_2^2)y_d^2 - 2n_1 n_3 x_d - 2n_2 n_3 y_d + (\mu^2 - n_3^2) = 0 \tag{B.4}$$

Note that squaring the term introduces extra solutions for the problem. Those solutions correspond to the cone at an angle $\pi - \alpha$ to the unit vector $\hat{\mathbf{n}}$. The determinant of this quadratic surface, D is given by

$$D = 4n_1^2 + n_2^2 - 4(\mu^2 - n_1^2)(\mu^2 - n_2^2) \tag{B.5}$$

After some trivial algebra, D reduces to

$$D = -4\mu^2(\mu^2 + n_1^2 + n_2^2) \tag{B.6}$$

$$D < 0 \; \forall \; \hat{\mathbf{n}} \; \in \; \mathbb{S}_1^2, \mu \in [-1, 1] \tag{B.7}$$

The sign of the determinant, D guarantees that the conic section is always an ellipse. In order to find the correction factor $\gamma(\hat{\mathbf{n}})$, we need the semi-major and semi-minor axes of the ellipse defined by equation B.4. This can be done by bringing the ellipse in canonical form. The equation of the ellipse using homogeneous coordinates can be written as $\mathbf{x}^T \mathcal{A}\mathbf{x} = 0$, where the matrix $\mathcal{A}$ is a 3×3 matrix given by

$$\mathcal{A} = \begin{pmatrix} \mu^2 - n_1^2 & -n_1 n_2 & -n_1 n_3 \\ -n_1 n_2 & \mu^2 - n_2^2 & -n_2 n_3 \\ -n_1 n_3 & -n_2 n_3 & \mu^2 - n_3^2 \end{pmatrix}$$

Let $\mathcal{B}$ be the 2×2 sub-matrix of $\mathcal{A}$ given by

$$\mathcal{B} = \begin{pmatrix} \mu^2 - n_1^2 & -n_1 n_2 \\ -n_1 n_2 & \mu^2 - n_2^2 \end{pmatrix}$$

If the eigenvalues of $\mathcal{A}$ are given by $(\lambda_1, \lambda_2, \lambda_3)$ and the eigenvalues of $\mathcal{B}$ is given by (δ_1, δ_2), then the semi-major and semi-minor axis axis are given by (assuming $\delta_1 > \delta_2$)

$$\begin{aligned} a &= \sqrt{\frac{-\lambda_1 \lambda_2 \lambda_3}{\delta_2^2 \delta_1}} \\ b &= \sqrt{\frac{-\lambda_1 \lambda_2 \lambda_3}{\delta_1^2 \delta_2}} \end{aligned} \tag{B.8}$$

The details can be found in [155]. The eigenvalues are given by the expressions

$$\begin{aligned} \lambda_1 &= \mu^2 \\ \lambda_2 &= \mu^2 \\ \lambda_3 &= \mu^2 - 1, \end{aligned} \tag{B.9}$$
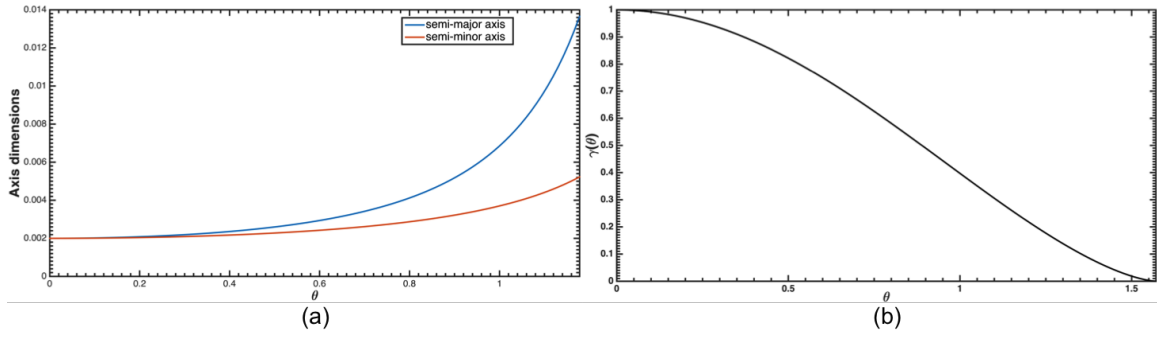
Figure B.3: (a) Semi-major and semi-minor axis of the ellipse and (b) correction factor as a function of polar angle away from pattern center.

and,

$$\delta_1 = \mu^2$$
$$\delta_2 = \mu^2 + n_3^2 - 1. \tag{B.10}$$

Thus, the correction factor $\gamma(\hat{\mathbf{n}})$ is then given by the ratio of area of the circle at the pattern center to the area of the ellipse around an arbitrary unit vector $\hat{\mathbf{n}}$. After some trivial algebra, the expression simplifies to

$$\gamma(\hat{\mathbf{n}}) = \frac{(\mu^2 + n_3^2 - 1)^{3/2}}{\mu^3}. \tag{B.11}$$

Note that the correction factor is independent of the x and y components of the unit vector $\hat{\mathbf{n}}$, which indicates that there is circular symmetry with respect to the pattern center. The plot of the semi-major and semi-minor axes as a function of θ such that $n_3 = \cos\theta$ is shown in Fig. B.3(a) ($\mu = 0.996195$ corresponding to $\alpha = 5°$). The plot of the correction factor as a function of the polar angle θ, such that $n_3 = \cos\theta$ is given in Fig. B.3(b) ($\mu = 0.996195$ corresponding to $\alpha = 5°$)

APPENDIX C

Correction factor for Large Area EBSD Scans

A schematic with the EBSD setup is shown in Fig. C.1. As the beam is rastered from point O to O′, the projection center shifts from point P to P′. It is trivial geometry to show that Δy_{PC} and Δx_{RD} are related as

$$\Delta y_{\text{PC}} = \Delta x_{\text{RD}} \cos \alpha. \tag{C.1}$$

Here, $\alpha = \pi/2 - \sigma + \theta_c$ (see Fig. C.1 for definition of σ and θ_c). The shift in the projection center in the transverse direction (TD) is equal in magnitude but in the opposite direction to the beam shift, i.e. $\Delta x_{\text{PC}} = -\Delta x_{\text{TD}}$. As shown in the figure, we seek a rotation which maps the projection center from the new position to the old position. Assuming that D is the origin of the detector frame, the coordinates of the old projection center, P are given by $(x_{\text{PC}}, y_{\text{PC}}, 0)$, the coordinates for the new projection center, P′ for a beam shift of Δx_{sample} and Δy_{sample} in the RD and TD respectively are given by the expression

$$
\begin{aligned}
x_{\text{PC}}^{\text{new}} &= x_{\text{PC}} - \Delta x_{\text{TD}}, \\
y_{\text{PC}}^{\text{new}} &= y_{\text{PC}} - \Delta x_{\text{RD}} \cos \alpha.
\end{aligned}
\tag{C.2}
$$

Note that the sample to scintillator distance, OP also changes as the beam is rastered across the sample to the point O'. The new sample to scintillator distance, $O'P'$ denoted by L' is given by

$$L' = L - \Delta x_{\text{RD}} \sin \alpha \tag{C.3}$$

179
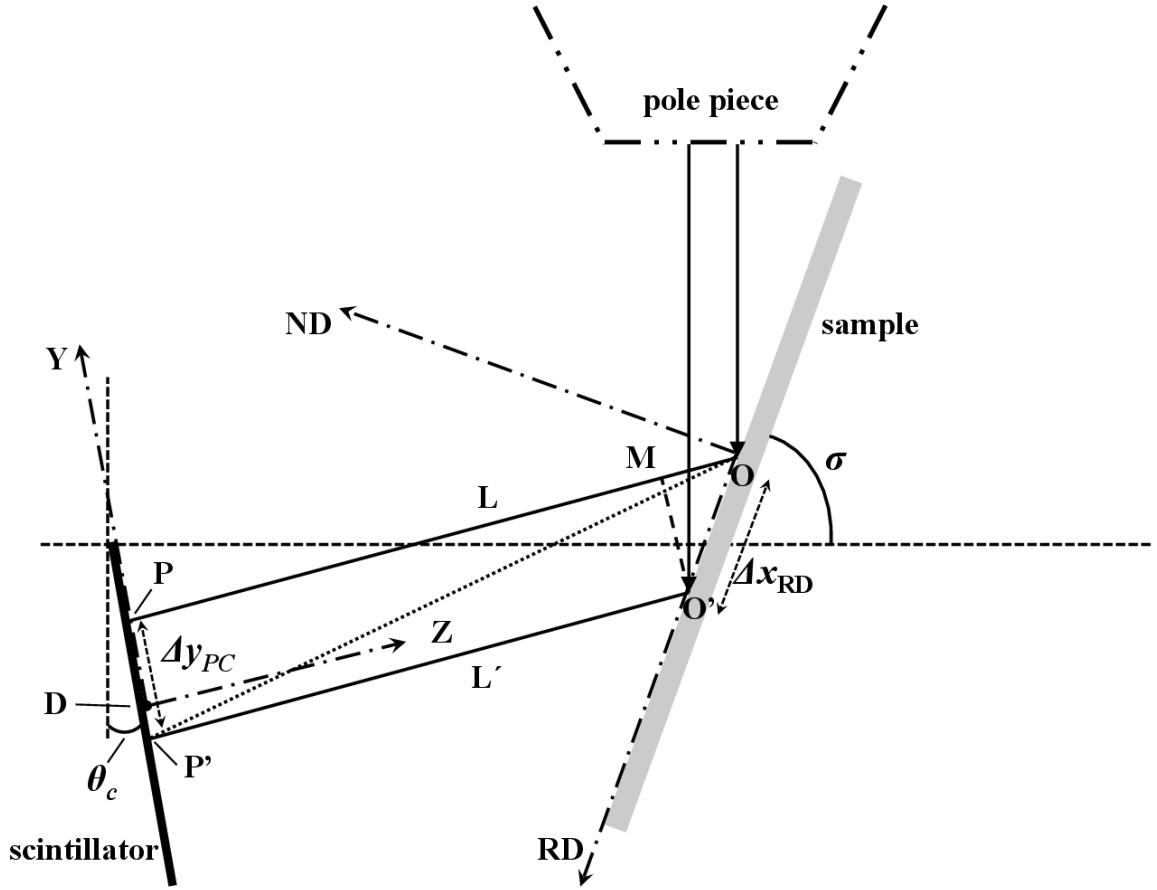
Figure C.1: Schematic of an experimental EBSD geometry when beam is rastered on the sample.

For a projection center coordinate of (X_{PC}, Y_{PC}) on the detector, the position vector, $\mathbf{r} \equiv (\mathrm{r}_x, \mathrm{r}_y, \mathrm{r}_z)$ for any scintillator pixel (X_s, Y_s) in the sample reference frame is given by [156]:

$$
\begin{aligned}
\mathrm{r}_x &= \frac{1}{\rho}\left[(Y_{PC} - Y_s)\delta \cos\alpha + L \sin\alpha\right], \\
\mathrm{r}_y &= \frac{-1}{\rho}(X_{PC} - X_s)\delta, \\
\mathrm{r}_z &= \frac{1}{\rho}\left[-(Y_{PC} - Y_s)\delta \sin\alpha + L \cos\alpha\right].
\end{aligned}
\tag{C.4}
$$

Here, δ is the physical detector pixel size, L is the distance between the illumination point and the scintillator, $\rho = \delta\sqrt{(Y_{PC} - Y_s)^2 + (X_{PC} - X_s)^2 + (L/\delta)^2}$. For a change in projection center of $(\Delta X_{PC}, \Delta Y_{PC})$, it is straightforward to compute the new position vector, $\mathbf{r}'$, for any pixel (X_s, Y_s) on the detector by replacing the old projection center with the new

one. The change in the position of any point on the detector due to a change in the projection center is then given by $\Delta \mathbf{r} = \mathbf{r}' - \mathbf{r}$. We now seek a rotation, $\mathbf{g}_c$, in the sample reference frame which brings the Kikuchi bands, displaced due to the pattern center shift, on top of each other. Since each pixel on the detector has a different $\Delta \mathbf{r}$, an exact mapping of all position vectors is not possible using a single rotation, $\mathbf{g}_c$. Only one position vector on the whole detector can be exactly mapped back to its old position so we must choose which vector this will be. Obvious choices include mapping the central pixel of the detector, the old and new projection centers or the corners of the patterns. Using trial and error, it was found that the rotation which produces the best correction across the entire field of view maps the new projection center to the old one. This rotation is straightforward to express in the axis-angle pair representation $(\hat{\mathbf{n}}, \omega)$:

$$
\begin{aligned}
\hat{\mathbf{n}} &= \frac{\mathbf{r}'_{PC} \times \mathbf{r}_{PC}}{|\mathbf{r}'_{PC} \times \mathbf{r}_{PC}|}, \\
\cos \omega &= \frac{\mathbf{r}'_{PC} \cdot \mathbf{r}_{PC}}{|\mathbf{r}'_{PC}| \, |\mathbf{r}_{PC}|}.
\end{aligned}
\tag{C.5}
$$

The vectors $\mathbf{r}'_{PC}$ and $\mathbf{r}_{PC}$ are given by the following expressions:

$$
\begin{aligned}
\mathbf{r}_{PC} &= (\sin \alpha, 0, \cos \alpha), \\
\mathbf{r}'_{PC} &= \frac{1}{\rho'} (\Delta Y_{PC} \delta \cos \alpha + L \sin \alpha, \Delta X_{PC} \delta, -\Delta Y_{PC} \delta \sin \alpha + L \cos \alpha).
\end{aligned}
\tag{C.6}
$$

Here, $\rho' = \delta \sqrt{\Delta X_{PC}^2 + \Delta Y_{PC}^2 + (L/\delta)^2}$. For small changes in the pattern center, the new position vector, $\mathbf{r}'_{PC}$, can be approximated using a Taylor series expansion. The position vector of the new projection center is then given to first order by:

$$
\mathbf{r}'_{PC} = \mathbf{r}_{PC} + \left. \frac{\partial \mathbf{r}_{PC}}{\partial X_{PC}} \right|_{X_s = X_{PC}^0} \Delta X_{PC} + \left. \frac{\partial \mathbf{r}_{PC}}{\partial Y_{PC}} \right|_{Y_s = Y_{PC}^0} \Delta Y_{PC}.
\tag{C.7}
$$

X_{PC}^0 and Y_{PC}^0 are the projection centers in the detector frame, P for illumination point O

(see Fig. C.1). Evaluation of the partial derivatives results in the following expressions:

$$
\begin{aligned}
\frac{\partial \mathbf{r}_{PC}}{\partial X_{PC}}\bigg|_{X_s=X_{PC}^0} &= \left(0, \frac{-1}{L}, 0\right), \\
\frac{\partial \mathbf{r}_{PC}}{\partial Y_{PC}}\bigg|_{Y_s=Y_{PC}^0} &= \left(\frac{\cos\alpha}{L}, 0, \frac{\sin\alpha}{L}\right).
\end{aligned}
\tag{C.8}
$$

Substituting these expressions in equations C.7 and C.5, the approximate first order rotation to compensate for a shift in the projection center is given by:

$$
\begin{aligned}
\hat{\mathbf{n}} &= \frac{1}{\rho_c}\left(-\Delta X_{PC}\cos\alpha, -\Delta Y_{PC}\cos 2\alpha, \Delta X_{PC}\sin\alpha\right), \\
\cos\omega &= \frac{L + \Delta Y_{PC}\delta\sin 2\alpha}{\sqrt{L^2 + 2L\Delta Y_{PC}\delta\sin 2\alpha + (\Delta X_{PC}\delta)^2 + (\Delta Y_{PC}\delta)^2}}.
\end{aligned}
\tag{C.9}
$$

Here, $\rho_c = \sqrt{(\Delta X_{PC})^2 + (\Delta Y_{PC}\cos 2\alpha)^2}$. Note that for the special case of $\Delta X_{PC} = \Delta Y_{PC} = 0$, both $\hat{\mathbf{n}}$ and ω vanish, as expected; for this case, the axis-angle pair must be set equal to the identity rotation. It is evident from equation C.9 that the validity of this approximation depends on the parameters $\Delta X_{PC}\delta/L$ and $\Delta Y_{PC}\delta/L$ being small.

APPENDIX D

Geodesics in stereographic and quaternion vector space

The integration path, Λ in the fundamental equation of texture is described by $\{\mathbf{g}|\mathbf{g}\mathbf{h} = \mathbf{y}\}$. Following the same parametrization of Λ as used in [124], we will write all the quaternion which maps $\mathbf{h}$ to $\mathbf{y}$, $\tilde{q}$ as a composition of two quaternions, q_0 and q such that $\tilde{q} = q \star q_0$. q_0 is the smalles rotation which maps $\mathbf{h}$ to $\mathbf{y}$ and q represents all rotations about $\mathbf{y}$. Each of these quaternions is given by

$$
\begin{aligned}
q_0 &= \left(\cos\left(\frac{\omega}{2}\right), \sin\left(\frac{\omega}{2}\right) \frac{\mathbf{h} \times \mathbf{y}}{|\mathbf{h} \times \mathbf{y}|} \right), \\
q &= \left(\cos\left(\frac{\phi}{2}\right), \sin\left(\frac{\phi}{2}\right) \frac{\mathbf{y}}{|\mathbf{y}|} \right).
\end{aligned}
\tag{D.1}
$$

Here, ω is the angle between $\mathbf{h}$ and $\mathbf{y}$ and ϕ is the variable parameter in the range $[0, 2\pi]$. After some trivial algebra and using $\mathbf{h} \cdot \mathbf{y} = |\mathbf{h}||\mathbf{y}| \cos\omega$ and $|\mathbf{h} \times \mathbf{y}| = |\mathbf{h}||\mathbf{y}| \sin\omega$, it can be shown that

$$
\tilde{q} = \left(\cos\left(\frac{\phi}{2}\right) \cos\left(\frac{\omega}{2}\right), \right.
\tag{D.2}
$$
$$
\left. \left[\sin\left(\frac{\omega}{2}\right) \left(\frac{\hat{\mathbf{h}} \times \hat{\mathbf{y}}}{\sin\omega}\right) \right] \cos\left(\frac{\phi}{2}\right) + \left[\frac{\hat{\mathbf{h}} + \hat{\mathbf{y}}}{2\cos\left(\frac{\omega}{2}\right)} \right] \sin\left(\frac{\phi}{2}\right) \right)
$$

Inspecting the vector part of the quaternion, $\tilde{q}$, it is immediately clear that this is the parametric equation for an ellipse, with the center at the origin, major and minor axis given by the unit vectors $\left(\hat{\mathbf{h}} + \hat{\mathbf{y}}\right)/2\cos\left(\omega/2\right)$ and $\left(\hat{\mathbf{h}} \times \hat{\mathbf{y}}\right)/\sin\omega$ respectively and the major and minor dimensions given by 1 and $\sin\left(\omega/2\right)$. Since ϕ varies from $[0, \pi]$ and the parametrization involves $\phi/2$, the curve will only trace half of the ellipse. In fact, the entire

quaternion can be written in a vectorial equation of the form $\tilde{q} = a\hat{\mathbf{U}} \cos(\phi/2) + b\hat{\mathbf{V}} \sin(\phi/2)$, and represents an ellipse in 4-D space, with $\hat{\mathbf{U}}$ and $\hat{\mathbf{V}}$ representing the 4 dimensional "major" and "minor" axis and a and b representing the dimensions of these axis respectively. Their values are given by

$$
\begin{aligned}
\hat{\mathbf{U}} &= \frac{\left(\cos\left(\frac{\omega}{2}\right), \hat{\mathbf{h}} \times \hat{\mathbf{y}}\right)}{\left|\cos\left(\frac{\omega}{2}\right)\right|\sqrt{3 - 2\cos\omega}}, \\
\hat{\mathbf{V}} &= \frac{\left(0, \hat{\mathbf{h}} + \hat{\mathbf{y}}\right)}{2\cos\left(\frac{\omega}{2}\right)}, \\
a &= \sqrt{\frac{3}{4} - \frac{1}{2}\cos\omega}, \\
b &= 1.
\end{aligned}
\tag{D.3}
$$

Notice that the special case where $\omega = \pi$ needs to be considered separately. Either of $\hat{\mathbf{U}}$ or $\hat{\mathbf{V}}$ could be the major and minor axis since a can be greater than 1 or less than 1. For the special case of $\omega = 2\pi/3$, the ellipse is a circle with $(a, b) = 1$. For the special case of $\omega = \pi$, $\mathbf{h} + \mathbf{y} = 0$. Therefore, the quaternion $\tilde{q}$ can be written as a composition of of the axis-angle pairs $(\hat{\mathbf{n}}, \pi)$ and $(\mathbf{y}, \phi)$, where $\hat{\mathbf{n}}$ is any unit vector such that $\hat{\mathbf{n}} \cdot \mathbf{h} = 0$. After some trivial algebra,

$$
\tilde{q} = \left(0, \hat{\mathbf{n}} \cos\left(\frac{\phi}{2}\right) + \left(\hat{\mathbf{h}} \times \hat{\mathbf{n}}\right) \sin\left(\frac{\phi}{2}\right)\right)
\tag{D.4}
$$

The quaternion, $\tilde{q}$ is a pure quaternion or a *versor*. The ellipse in this case is a circle with unit major and minor axis dimensions. However, it is interesting to note that there is a degeneracy in the choice of the unit vector $\hat{\mathbf{n}}$ and any unit vector in the plane of $\hat{\mathbf{h}}$ will suffice.

BIBLIOGRAPHY

[1] J.J. Fundenberger, E. Bouzy, D. Goran, J. Guyon, H. Yuan, and A. Morawiec. Orientation mapping by transmission-sem with an on-axis detector. *Ultramicroscopy*, 161:17 – 22, 2016.

[2] A. Tarantola. *Inverse Problem Theory and Model Parameter Estimation.* SIAM, Philadelphia, 2004.

[3] R.C. Aster, B. Borchers, and Thurber C.H. *Parameter Estimation and Inverse Problems.* Elsivier, 2013.

[4] N.C. Krieger Lassen, D. Juul Jensen, and K. Conradsen. Image processing procedures for analysis of electron back scattering patterns. *Scanning Microscopy*, 6:115–121, 1992.

[5] N.C. Krieger Lassen. Automatic crystal orientation determination from ebsps. *Micron and Microscopica Acta*, 6:191–192, 1992.

[6] E.F. Rauch and L. Dupuy. Rapid diffraction patterns identification through template matching. *Archives of Metallurgy and Materials*, 50(1):87–99, 2005.

[7] S. Nishikawa and Kikuchi S. Diffraction of cathode rays by calcite. *Nature*, 122:726–726, 1928.

[8] M. N. Alam, M. Blackman, and D. W. Pashley. High-angle kikuchi patterns. *Proceedings of the Royal Society of London A: Mathematical, Physical and Engineering Sciences*, 221(1145):224–242, 1954.

[9] J.A. Venables and C.J. Harland. Electron back-scattering patternsa new technique for obtaining crystallographic information in the scanning electron microscope. *Philosophical Magazine*, 27:1193–1200, 1973.

[10] D.J. Dingley. On-line determination of crystal orientation and texture determination in an SEM. *Proceedings of the Royal Microscopical Society*, 19:74–78, 1984.

[11] D.J. Dingley, M. Longdon, J. Wienbren, and J. Aldernan. On-line analysis of electron backscatter diffraction patterns, texture analysis of polysilicon. *Scanning Electron Microscopy*, 1:451–456, 1987.

[12] K. Z. Baba-Kishi and D. J. Dingley. Backscatter kikuchi diffraction in the sem for identification of crystallographic point groups. *Scanning*, 11(6):305–312, 1989.

[13] P.V.C. Hough. Method and means for recognizing complex patterns, 1962.

[14] Brent L. Adams, Stuart I. Wright, and Karsten Kunze. Orientation imaging: The emergence of a new microscopy. *Metallurgical Transactions A*, 24(4):819–831, 1993.

[15] J. R. Michael and R P Goehner. Crystallographic phase identification in the scanning electron microscope: backscattered electron kikuchi patterns imaged with a ccd based detector. *MSA Bulletin*, 26:168, 1993.

[16] D.L. Barr and W.L. Brown. A channel plate detector for electron backscatter diffraction. *Review of Scientific Instruments*, 66, 1995.

[17] A. Deal, T. Hoogan, and A. Eades. Energy-filtered electron backscatter diffraction. *Ultramicroscopy*, 108, 2008.

[18] A.J. Wilkinson, G. Moldovan, T.B. Britton, A. Bewick, R. Clough, and physical A.I. Kirkland. Direct detection of electron backscatter diffraction patterns. *Physical Review Letters*, 111, 2013.

[19] F.J. Humphreys. Review grain and subgrain characterisation by electron backscatter diffraction. *Journal of Material Science*, 36(16):3833–3854, 2001.

[20] A. Schwartz, M. Kumar, B.L. Adams, and D.P. Field, editors. *Electron Backscatter Diffraction in Materials Science*. Springer, 2009.

[21] D. Dingley. Progressive steps in the development of electron backscatter diffraction and orientation imaging microscopy. *Journal of Microscopy*, 213:214–224, 2003.

[22] T.M. Maitland and A. Gholinia. Advances in high-speed ebsd orientation mapping. *Microscopy and Microanalysis*, 13, Supplement S02, 2007.

[23] Niels Christian Krieger Lassen. *Automated Determination of Crystal Orientations from Electron Backscattering Patterns*. PhD thesis, Technical University of Denmark, 6 1994.

[24] Krieger L.N.C. Source point calibration from an arbitrary electron backscattering pattern. *Journal of Microscopy*, 195(3):204–211, sep 1999.

[25] K. Mingard, A. Day, C. Maurice, and P. Quested. Towards high accuracy calibration of electron backscatter diffraction systems. *Ultramicroscopy*, 111(5):320–329, apr 2011.

[26] C. Maurice, K. Dzieciol, and R. Fortunier. A method for accurate localisation of EBSD pattern centres. *Ultramicroscopy*, 111(2):140–148, jan 2011.

[27] S. Vespucci, G. Naresh-Kumar, C. Trager-Cowan, K.P. Mingard, D. Maneuski, V. O'Shea, and A. Winkelmann. Diffractive triangulation of radiative point sources. *Appl. Phys. Lett.*, 110:124103, 2017.

[28] T.C. Isabell and V.P. Dravid. Resolution and sensitivity of electron backscattered diffraction in a cold field emission gun sem. *Ultramicroscopy*, 67(1-4):59–68, 1997.

[29] D. Dingley. Progressive steps in the development of electron backscatter diffraction and orientation imaging microscopy. *Journal of Microscopy*, 213(3):214–224, 2004.

[30] S.X. Ren, E.A. Kenik, K.B. Alexander, and A. Goyal. Exploring spatial resolution in electron back-scattered diffraction experiments via monte carlo simulation. *Microscopy and Microanalysis*, 4(1):15–22, 1998.

[31] F.J. Humphreys. Characterisation of fine-scale microstructures by electron backscatter diffraction (ebsd). *Scripta Materialia*, 51(8 SPEC. ISS.):771–776, 2004.

[32] S. Zaefferer. On the formation mechanisms, spatial resolution and intensity of backscatter kikuchi patterns. *Ultramicroscopy*, 107(2-3):254–266, 2007.

[33] D.G. Coates. Kikuchi-like reflection patterns obtained with scanning electron microscope. *Philosophical Magazine*, 16(144):1179–1185, 1967.

[34] G. R. Booker, A. M. B. Shaw, M. J. Whelan, and P. B. Hirsch. Some comments on the interpretation of the kikuchi-like reflection patterns observed by scanning electron microscopy. *Philosophical Magazine*, 16(144):1185–1191, 1967.

[35] D. R. Clarke and A. Howie. Calculations of lattice defect images for scanning electron microscopy. *Philosophical Magazine*, 24(190):959–971, 1971.

[36] J. P. Spencer, C. J. Humphreys, and P. B. Hirsch. A dynamical theory for the contrast of perfect and imperfect crystals in the scanning electron microscope using backscattered electrons. *Philosophical Magazine*, 26(1):193–213, 1972.

[37] M. Pitaval, P. Morin, J. Baudry, E. Viaria, and G. Fontaine. Advances in crystalline contrast from defects. *Scanning Electron Microscopy*, 1:439–444, 1977.

[38] P. Morin, M. Pitaval, D. Besnard, and G. Fontaine. Electronchannelling imaging in scanning electron microscopy. *Philosophical Magazine A*, 40(4):511–524, 1979.

[39] J.T. Czernuszka, N.J. Long, E.D. Boyes, and P.B. Hirsch. Imaging of dislocations using backscattered electrons in a scanning electron microscope. *Philosophical Magazine Letters*, 62:227–232, 1990.

[40] B. A. Simkin and M. A. Crimp. An experimentally convenient configuration for electron channeling contrast imaging. *Ultramicroscopy*, 77(1-2):65–75, 5 1999.

[41] J.P. Spencer and C.J. Humphreys. A multiple-scattering transport-theory for electron channeling patterns. *Philosophical Magazine A*, 42:433–451, 1980.

[42] K. Marthinsen and R. Høier. Many-beam effects and phase information in electron channeling patterns. *Acta Crystallographica A*, 42:484–492, 1986.

[43] C.J. Rossouw, P.R. Miller, T.W. Josefsson, and L.J. Allen. Zone axis backscattered electron contrast for fast electrons. *Philosophical Magazine A*, 70:985–998, 1994.

[44] S.L. Dudarev, P. Rez, and M.J. Whelan. Theory of electron backscattering from crystals. *Physical Review B*, 51:3397–3405, 1995.

[45] A. Winkelmann, B. Schröter, and W. Richter. Dynamical simulations of zone axis electron channelling patterns of cubic silicon carbide. *Ultramicroscopy*, 98:1–7, 2003.

[46] D.C. Joy, D.E. Newbury, and D.L. Davidson. Electron channeling patterns in the scanning electron microscope. *Journal of Applied Physics*, 53, 1982.

[47] B.A. Simkin, B.C. Ng, T.R. Bieler, M.A. Crimp, and D.E. Mason. Orientation determination and defect analysis in the near-cubic intermetallic γ-TiAl using SACP, ECCI, and EBSD. *Intermetallics*, 11(3):215–223, 2003.

[48] M.A. Crimp, B.A. Simkin, and Ng B.C. Demonstration of the g · b × u = 0 edge dislocation invisibility criterion for electron channelling contrast imaging. *Philosophical Magazine Letters*, 81:833–837, 2001.

[49] R.J. Kamaladasa and Y.N. Picard. Basic principles and application of electron channeling in a scanning electron microscope for dislocation analysis. *Microscopy: Science, Technology, Applications and Education*, pages 1583–1590, 2010.

[50] N. Schmidt and N. Olesen. Computer aided determination of crystal lattice orientation from electron channeling patterns in the SEM. *Canadian Mineralogist*, 27:15–22, 1989.

[51] I. Gutiérrez-Urrutia, S. Zaefferer, and D. Raabe. Coupling of electron channeling with EBSD: Toward the quantitative characterization of deformation structures in the SEM. *Journal of Materials*, 65(9):1229–1236, 2013.

[52] R. Vincent and P.A. Midgley. Double conical beam-rocking system for measurement of integrated electron diffraction intensities. *Ultramicroscopy*, 53(3):271–282, 1994.

[53] J. Gjønnes, V. Hansen, B. S. Berg, P. Runde, Y. F. Cheng, K. Gjønnes, D. L. Dorset, and C. J. Gilmore. Structure Model for the Phase Al_mFe Derived from Three-Dimensional Electron Diffraction Intensity Data Collected by a Precession Technique. Comparison with Convergent-Beam Diffraction. *Acta Crystallographica Section A*, 54(3):306–319, May 1998.

[54] B.S. Berg, V. Hansen, P.A. Midgley, and J. Gjnnes. Measurement of three-dimensional intensity data in electron diffraction by the precession technique. *Ultramicroscopy*, 74(3):147 – 157, 1998.

[55] M Gemmi, L Righi, G Calestani, A Migliori, A Speghini, M Santarosa, and M Bettinelli. Structure determination of -bi8pb5o17 by electron and powder x-ray diffraction. *Ultramicroscopy*, 84(3):133 – 142, 2000.

[56] Mauro Gemmi, Xiaodong Zou, Sven Hovmöller, Andrea Migliori, Marie Vennström, and Yvonne Andersson. Structure of Ti_2P solved by three-dimensional electron diffraction data collected with the precession technique and high-resolution electron microscopy. *Acta Crystallographica Section A*, 59(2):117–126, Mar 2003.

[57] C.S. Own. *System Design and Verification of the Precession Electron Diffraction Technique.* PhD thesis, Northwestern University, 2005.

[58] C.S. Own, W. Sinkler, and L.D. Marks. Rapid structure determination of a metal oxide from pseudo-kinematical electron diffraction data. *Ultramicroscopy*, 106(2):114 – 122, 2006.

[59] J.-P. Morniroli and A. Redjaimia. Electron precession microdiffraction as a useful tool for the identification of the space group. *Journal of Microscopy*, 227(2):157–171, 2007.

[60] Alexander S. Eggeman and Paul A. Midgley. Refining structures against reflection rank: an alternative metric for electron crystallography. *Acta Crystallographica Section A*, 68(3):352–358, May 2012.

[61] Lukáš Palatinus, Damien Jacob, Priscille Cuvillier, Mariana Klementová, Wharton Sinkler, and Laurence D. Marks. Structure refinement from precession electron diffraction data. *Acta Crystallographica Section A*, 69(2):171–188, Mar 2013.

[62] Damien Jacob, Lukas Palatinus, Priscille Cuvillier, Hugues Leroux, Chiara Domeneghetti, and Fernando Cámara. Ordering state in orthopyroxene as determined by precession electron diffraction. *American Mineralogist*, 98(8-9):1526–1534, 2013.

[63] E.F. Rauch, M. véron, J. Portillo, D. Bultreys, Y. Maniette, and S. Nicolopoulos. Automatic crystal orientation and phase mapping in tem by precession diffraction. *Microscopy and Analysis*, 22(6):S5–S8, 2008.

[64] J.M. Rebled, L.L. Yedra, S. Estrade, J. Portillo, and F. Peiro. Advances in high-speed ebsd orientation mapping. *Ultramicroscopy*, 111:1504–1511, 2011.

[65] P.A. Midgley and A.S. Eggerman. Precession electron diffraction a topical review. *Journal of International Union of Crystallography*, 2(1):126–136, 2014.

[66] D. Viladot, M. véron, M. Gemmi, Peiró, J. Portillo, S. Estradé, J. Mendoza, N. Llorca-Isern, and S. Nicolopoulos. Orientation and phase mapping in the transmission electron microscope using precession-assisted diffraction spot recognition: state-of-the-art results. *Journal of Microscopy*, 252(1):23–34, 2013.

[67] R.R. Keller and R.H. Geiss. Transmission ebsd from 10 nm domains in a scanning electron microscope. *Journal of Microscopy*, 245(3):245–251, 2012.

[68] Patrick W. Trimby. Orientation mapping of nanostructured materials using transmission kikuchi diffraction in the scanning electron microscope. *Ultramicroscopy*, 120:16 – 24, 2012.

[69] Patrick W. Trimby. Orientation mapping of nanostructured materials using transmission kikuchi diffraction in the scanning electron microscope. *Ultramicroscopy*, 120:16 – 24, 2012.

[70] R. van Bremen, D. Ribas Gomes, L.T.H. de Jeer, V. Ocelk, and J.Th.M. De Hosson. On the optimum resolution of transmission-electron backscattered diffraction (t-ebsd). *Ultramicroscopy*, 160:256 – 264, 2016.

[71] Y.Z. Wang, M.G. Kong, Z.W. Liu, C.C. Lin, and Y. Zeng. Effect of microscope parameter and specimen thickness of spatial resolution of transmission electron backscatter diffraction. *Journal of Microscopy*, 264(1):34–40, 2016.

[72] A. Morawiec. Rodrigues parameterization for orientation and misorientation distributions. *Philosophical Magazine A*, 73:1113–1130, 1996.

[73] D. Ro¸sca. New uniform grids on the sphere. *Astronomy and Astrophysics*, 520(A63), 2010.

[74] D. Roşca, A. Morawiec, and M. De Graef. A new method of constructing a grid in the space of 3d rotations and its application to texture analysis. *Modelling and Simulation in Materials Science and Engineering*, 22, 2014.

[75] D. Roşca and G. Plonka. New uniform grids on the sphere. *Journal of Computational and Applied Math*, 236(6), 2011.

[76] S.L. Dudarev and Peng L.M. Effects of bulk resonance diffraction on inelastic scattering of high energy electrons by crystals. *Proceeding of the Royal Society of London A*, 440:117–133, 1993.

[77] S.L. Dudarev and L.M. Peng. Theory of bulk resonance diffraction in theed. *Proceedings of the Royal Society of London A*, 440:95–115, 1993.

[78] S.L. Dudarev, L.M. Peng, and M.J. Whelan. Correlations in space and time and dynamical diffraction of high energy electrons by crystals. *Physical Review B*, 48(13):408, 1993.

[79] S.L. Dudarev, P. Rez, and M.J. Whelan. Theory of electron backscattering from crystals. *Physical Review B*, 51:3397, 1995.

[80] K. Fujiwara. Relativistic dynamical theory of electron diffraction. *Journal of the Physical Society of Japan*, 16(2226-2238), 1961.

[81] E. Humphrey, C. Phatak, A.K. Petford-Long, and M. De Graef. Separation of electrostatic and magnetic phase shifts using a modified transport-of-intensity equation. *Ultramicroscopy*, 139:5–12, 2014.

[82] G.H. Smith and R.E. Burge. The analytical representation of atomic scattering amplitudes for electrons. *Acta Crystallographica A*, 15:182–186, 1962.

[83] P.A. Doyle and P.S. Turner. Relativistic hartreefock x-ray and electron scattering factors. *Acta Crystallographica A*, 24:390–397, 1968.

[84] A. Weickenmeier and Kohl H. Computation of absorptive form factors for high-energy electron diffraction. *Acta Crystallographica A*, 47:590–597, 1991.

[85] D. Rez, P. Rez, and I. Grant. Diracfock calculations of x-ray scattering factors and contributions to the mean inner potential for electron scattering. *Acta Crystallographica A*, 50:481–497, 1994.

[86] M. De Graef. *Introduction to Conventional Transmission Electron Microscopy*. Cambridge Press, 2003 edition, 2003.

[87] D. Van Dyck. The importance of backscattering in high-energy electron diffraction calculations. *Physica Status Solidi (b)*, 77:301–308, 1976.

[88] C. Moler and C. Van Loan. Ninteen dubious ways to compute the exponential of a matrix, twenty-five years later. *SIAM Review*, 45(1), 2003.

[89] F. Bloch. Bemerkung zur elektronentheorie des ferromagnetismus und der elektrischen leitfähigkeit. *Zeitschrift für Physik*, 57:545–555, 1929.

[90] A.J.F. Metherell. Diffraction of electrons by perfect crystals. In Valdrè U. Ruedl E., editor, *Electron Microscopy in Material Science*, pages 401–552. Commision of European communities, Luxemborg, 1975.

[91] D C. Joy. *Monte Carlo Modeling for Electron Microscopy and Microanalysis*. Oxford University Press, 1995.

[92] H. Staub, H. Bethe, J. Ashkin, N.F. Ramsey, and K.T. Bainbridge. *Experimental Nuclear Physics*, volume 1. John Wiley & Sons, 1930.

[93] D.C. Joy and S. Luo. An empirical stopping power relationship for low-energy electrons. *Scanning*, 11(4):176–180, 1989.

[94] K.M. Krishnan. Atomic site and species determinations using channeling and related effects in analytical electron microscopy. *Ultramicroscopy*, 24:125–142, 1988.

[95] Z.L. Wang. *Elastic and Inelastic Scattering in Electron Diffraction and Imaging*. Plenum Press, New York, 1995.

[96] C.J. Rossouw, P.R. Miller, T.W. Josefsson, and L.J. Allen. Zone axis back-scattered electron contrast for fast electrons. *Philosophical Magazine A*, 70:985–998, 1994.

[97] A. Winkelmann, C. Trager-Cowan, F. Sweeney, A.P. Day, and P. Parbrook. Many-beam dynamical simulation of electron backscatter diffraction patterns. *Ultramicroscopy*, 107:414–421, 2007.

[98] Y.N. Picard, M. Liu, J. Lammatao, R. Kamaladasa, and M. De Graef. Theory of dynamical electron channeling contrast images of near-surface crystal defects. *Ultramicroscopy*, 146:71–78, 2014.

[99] P. W. Hawkes and E. Kasper. *Principles of Electron Optics: Wave Optics*, volume 3. Academic Press, New York, 1989.

[100] P. W. Hawkes and E. Kasper. *Principles of Electron Optics: Basic Geometrical Optics*, volume 2. Academic Press, New York, 1989.

[101] M. Szilagyi. *Electron and Ion Optics*. Plenum Press, New York, 1988.

[102] D. Hardin and E.B. Saff. Discretizing manifolds via minimum energy points. *Notices of the AMS*, 51:1186–1194, 2004.

[103] J.A. Nelder and R. Mead. A simplex method for function minimization. *Computer Journal*, 7:308–313, 1965.

[104] M.J.D. Powell. The bobyqa algorithm for bound constrained optimization without derivatives. Technical report, Department of Applied Mathematics and Theoretical Physics, Cambridge University, 6 2009.

[105] L.M. Rios and N.V. Sahinidis. Derivative-free optimization: a review of algorithms and comparison of software implementations. *Journal of Global Optimization*, 56:1247–1293, 2013.

[106] S.M. Pizer, E.P. Amburn, J.D. Austin, R. Cromartie, A. Geselowitz, T. Greer, B.T.H. Romney, J.B. Zimmerman, and K. Zuiderveld. Adaptive histogram equalization and its variation. *Computer Vision, Graphics and Image Processing*, 39:355–368, 1987.

[107] C. Bouman and K. Sauer. A generalized gaussian image model for edge-preserving map estimation. *IEEE Trans. Image Process*, 2(3):296–310, 1993.

[108] H. Derin, H. Elliot, R. Christi, and R. Geman. Bayes smoothing algorithms for segmentation of binary images modeled by markov random fields. *IEEE Transactions on Pattern Analysis and Machine Intelligence*, PAMI-6(6):707–720, 1984.

[109] S. Geman and D. Geman. Stochastic relaxation, gibbs distributions, and the bayesian restoration of images. *IEEE Transactions on Pattern Analysis and Machine Intelligence*, PAMI-6(6):721–741, 1984.

[110] J. Besag. On the statistical analysis of dirty pictures. *Journal of Royal Statistical Society B*, 48(3):259–302, 1986.

[111] A.J. Schwartz, M. Kumar, B.L. Adams, and D.P. Field, editors. *Electron Backscatter Diffraction in Materials Science*. Springer, 2nd. edition, 2009.

[112] U. Lienert, S. F. Li, C. M. Hefferan, J. Lind, R. M. Suter, J. V. Bernier, N. R. Barton, M. C. Brandes, M. J. Mills, M. P. Miller, B. Jakobsen, and W. Pantleon. High-energy diffraction microscopy at the advanced photon source. *JOM*, 63(7):70–77, 2011.

[113] E.F. Rauch and M. Vron. Crystal orientation angular resolution with precession electron diffraction. *Microscopy and Microanalysis*, 22(S3):500501, 2016.

[114] A. J. Wilkinson, G. Meaden, and D. J. Dingley. High resolution mapping of strains and rotations using electron backscatter diffraction. *Materials Science and Technology*, 22(11):1271–1278, 2006.

[115] A.A. Goshtasby. *Image Registration, Advances in Computer Vision and Pattern Recognition*. Springer Verlag, London, 2012.

[116] S. Singh and M. De Graef. Orientation sampling for dictionary-based diffraction pattern indexing methods. *Modeling and Simulation in Material Science and Engineering*, 159:81–94, 2016.

[117] M.J.D. Powell. The bobyqa algorithm for bound constrained optimization without derivatives. Technical report, Department of Applied Mathematics and Theoretical Physics, Cambridge University, 6 2009.

[118] A.J. Hanson. *Visualizing Quaternions*, chapter 18, pages 167–171. Series in Interactive 3D Technology. Elsevier, Amsterdam, 2006.

[119] Saransh Singh and Marc De Graef. Dictionary indexing of electron channeling patterns. *Microscopy and Microanalysis*, 23(1):1–10, 2017.

[120] R.J. Roe. Description of crystallite orientation in polycrystalline materials - iii: General solution to pole figure inversion. *Journal of Applied Physics*, 26:2024–2031, 1965.

[121] H.J. Bunge. *Mathematische Methoden der Texturanalyse*. Akademie-Verlag Berlin, 1969.

[122] H.R. Wenk, editor. *Preferred Orientation in Deformed Metals and Rocks: An Introduction to Modern Texture Analysis.* Academic Press, Orlando FL, 1985.

[123] H. Schaeben. Entropy optimization in quantitative texture analysis. *Journal of Applied Physics*, 64:2236–2237, 1998.

[124] N.R. Barton, D.E. Boyce, and P.R. Dawson. Pole figure inversion using finite elements over rodrigues space. *Textures and Microstructures*, 35:113–144, 2002.

[125] R. Hielscher and H. Schaeben. A novel pole figure inversion method: specification of the mtex algorithm. *Journal of Applied Crystallography*, 41:1024–1037, 2008.

[126] C.A. Bouman and K. Sauer. A generalized gaussian image model for edge-preserving map estimation. *IEEE Transaction on Image Processing*, 2:296–310, 1993.

[127] D. Roşca, A. Morawiec, and M. De Graef. A new method of constructing a grid in the space of 3D rotations and its applications to texture analysis. *Modeling and Simulations in Materials Science and Engineering*, 22:075013, 2014.

[128] S. Singh and M. De Graef. Orientation sampling for dictionary-based diffraction pattern indexing methods. *Modelling and Simulation in Materials Science and Engineering*, 24:085013, 2016.

[129] P.G. Callahan, M. Echlin, T.M. Pollock, S. Singh, and M. De Graef. Three-dimensional texture visualization approaches: theoretical analysis and examples. *Journal of Applied Crystallography*, 50:430–440, 2017.

[130] H.J. Bunge. Presentation of general textures. *Zeitschrift fuer Metallkunde*, 56:872–874, 1965.

[131] H.-J. Bunge. 3 - orientation distributions. In H.-J. Bunge, editor, *Texture Analysis in Materials Science*, pages 42 – 46. Butterworth-Heinemann, 1982.

[132] H. Schaeben and K.G. van den Boogaart. Spherical harmonics in texture analysis. *Tectonophysics*, 370:253–268, 2003.

[133] A. Morawiec and J. Pospiech. Properties of projection lines in the space of the orientation distribution function. *Textures and Microstructures*, 10:243–264, 1989.

[134] D. Roşca. New uniform grids on the sphere. *Astronomy & Astrophysics*, 520:A63, 2010.

[135] J. Besag. Spatial interaction and the statistical analysis on lattice systems. *Journal of the Royal Statistical Society B*, 36:192–326, 1974.

[136] R. Kindermann and J. Laurie Snell. *Markov Random Fields and Their Applications.* American Mathematical Society, Providence, RI, 1980.

[137] A. Buades, B. Coll, and J. M. Morel. A review of image denoising algorithms, with a new one. *Multiscale Modeling & Simulation*, 4(2):490–530, 2005.

[138] A. Wong and J. Orchard. A nonlocal-means approach to exemplar-based inpainting. In *2008 15th IEEE International Conference on Image Processing*, pages 2600–2603, Oct 2008.

[139] K. . Dabov, A. . Foi, V. . Katkovnik, and K. . Egiazarian. Image denoising by sparse 3-d transform-domain collaborative filtering. *Trans. Img. Proc.*, 16(8):2080–2095, August 2007.

[140] K. M. Hanson. Bayesian reconstruction based on flexible prior models. *J. Opt. Soc. Am. A*, 10(5):997–1004, May 1993.

[141] S. V. Venkatakrishnan, L. F. Drummy, M. A. Jackson, M. De Graef, J. Simmons, and C. A. Bouman. A model based iterative reconstruction algorithm for high angle annular dark field-scanning transmission electron microscope (haadf-stem) tomography. *IEEE Transactions on Image Processing*, 22(11):4532–4544, Nov 2013.

[142] S. V. Venkatakrishnan, L. F. Drummy, M. Jackson, M. De Graef, J. Simmons, and C. A. Bouman. Model-based iterative reconstruction for bright-field electron tomography. *IEEE Transactions on Computational Imaging*, 1(1):1–15, March 2015.

[143] J. W. Gibbs, K. A Mohan, E. B. Gulsoy, A. J. Shahani, X. Xiao, C. A. Bouman, M. De Graef, and P. W. Voorhees. The three-dimensional morphology of growing dendrites. *Scientific Reports*, 5, 2015.

[144] N.L. Johnson, A.W. Kemp, and S. Kotz. *Univariate Discrete Distributions.* John Wiley & Sons, 2005.

[145] Z. Yu, J. Thibault, C. Bouman, K. Sauer, and J. Hsieh. Fast model-based x-ray ct reconstruction using spatially nonhomogeneous icd optimization. *IEEE Transaction on Image Processing*, 36:161–175, 2011.

[146] P. W. Hawkes and E. Kasper. *The Theory of Tikhonov Regularization for Fredholm Equations of the First Kind.* Pitman Advanced Pub. Program, Boston/London, 1984.

[147] Gene H. Golub, Michael Heath, and Grace Wahba. Generalized cross-validation as a method for choosing a good ridge parameter. *Technometrics*, 21(2):215–223, 1979.

[148] Per Christian Hansen and Dianne Prost OLeary. The use of the l-curve in the regularization of discrete ill-posed problems. *SIAM Journal on Scientific Computing*, 14(6):1487–1503, 1993.

[149] C.A. Bouman. Model based image processing. 2013.

[150] U.F. Kocks, C.N. Tomé, and H.-R. Wenk, editors. *Texture and Anisotropy.* Cambridge University Press, 2000.

[151] Robert Hooke and T. A. Jeeves. " direct search" solution of numerical and statistical problems. *J. ACM*, 8(2):212–229, April 1961.

[152] Aimo Winkelmann and Gert Nolze. Analysis of kikuchi band contrast reversal in electron backscatter diffraction patterns of silicon. *Ultramicroscopy*, 110(3):190 – 194, 2010.

[153] Mark W. Tate, Prafull Purohit, Darol Chamberlain, Kayla X. Nguyen, Robert Hovden, Celesta S. Chang, Pratiti Deb, Emrah Turgut, John T. Heron, Darrell G. Schlom, and et al. High dynamic range pixel array detector for scanning transmission electron microscopy. *Microscopy and Microanalysis*, 22(1):237249, 2016.

[154] W. H. Beyer. *CRC Standard Mathematical Tables and Formulae.* CRC Press, Boca Raton, 1987.

[155] A.B. Ayoub. The central conic sections revisited. *Mathematics Magazine*, 66(5):322–325, 1993.

[156] Patrick G. Callahan and Marc De Graef. Dynamical electron backscatter diffraction patterns. part i: Pattern simulations. *Microscopy and Microanalysis*, 19(5):12551265, 2013.